Adsorption of Biomacromolecules onto Polysaccharide Surfaces

Xiao Zhang

Dissertation submitted to the faculty of the Virginia Polytechnic Institute and State
University in partial fulfillment of the requirements for the degree of

Doctor of Philosophy
In
Chemistry

Alan R. Esker, Chair
Kevin J. Edgar
Louis A. Madsen
Hervé Marand
Maren Roman

Aug 7, 2014
Blacksburg, Virginia

Keywords: Quartz Crystal Microbalance with Dissipation Monitoring, Surface Plasmon Resonance, Cellulose, Carboxymethyl Cellulose, Pectin and Mixed Linkage Glucans

Adsorption of Biomacromolecules onto Polysaccharide Surfaces

Xiao Zhang

ABSTRACT

Plant cell wall polysaccharides are abundant natural polymers making them potential sources for sustainable and biodegradable materials. Interfacial behavior, including adsorption and enzymatic degradation, of several plant cell wall polysaccharides and their derivatives were studied with a quartz crystal microbalance with dissipation monitoring (QCM-D), surface plasmon resonance (SPR) and atomic force microscopy (AFM). Xyloglucan adsorption isotherms were obtained to probe how cellulose-hemicellulose interactions were affected by the type of cellulose substrate and molar mass of xyloglucan. Xyloglucan as small as a heptasaccharide still adsorbed irreversibly onto cellulose. Carboxymethyl cellulose (CMC) adsorption onto cellulose and viscoelastic properties and water contents of the adsorbed CMC layers were obtained from a combination of QCM-D and SPR data. The CMC samples formed hydrated and viscoelastic layers compared to the relatively rigid xyloglucan layer. Pectin model surfaces were prepared by pectin adsorption from citric phosphate buffer onto gold substrates. These pectin model surfaces were used for subsequent interaction studies with xyloglucan and enzymatic degradation behavior. There is a strong correlation between the degree of esterification (DE) and film resistance to degradation with the high DE being the most susceptible to degradation. The adsorption of two mixed linkage glucans (MLG), barley and lichen MLG, onto regenerated cellulose (RC) surfaces in the absence and presence of other matrix polysaccharides was studied. Viscoelastic properties of the resulting layer were compared as a function of the proprotion of β-(1→3) linkages with lichen MLG forming softer gel-like layers on RC. The lichen MLG layers were further used for enzymatic degradation studies with respect to enzyme concentration, temperature, pH and ionic strength. These studies show that polymer adsorption is a promising strategy to modify material surfaces and provides fundamental understanding of interactions and biodegradation of cell wall polysaccharides at solid/liquid interfaces.

Dedicated to

My family, Changming Zhang and Dongmin Zhai, my grandfather Baotong Zhai and my grandmother Fanqin Meng, your love, support and encouragement through these years have made this and everything else possible.

Acknowledgements

My appreciation goes to all those involved in the research here at Virginia Tech. A special thanks to my advisor Prof. Alan R. Esker who played an important role during my study at Virginia Tech. I really appreciate him for providing me the opportunity to study under his auspices. As an advisor, he is strict, patient and enthusiastic, guiding me to realize the right directions to proceed. He also gave his technical insight and encouragement during my difficult times. Without him, I would have not made it this far. It is his high expectation and encouragement that drives me forward and keeps me improving. I also appreciate his trust in letting me take care of the lab, from which I have learned the importance of organizational skills as well as the beauty of teamwork. I also wish to acknowledge my advisory committee, Prof. Kevin J. Edgar, Prof. Louis A. Madsen, Prof. Hervé Marand and Prof. Maren Roman, who gave their expertise, support and encouragement over the years.

I would also like to acknowledge those not mentioned above who have played a critical role during my stay in Blacksburg. I am grateful to all my group members, Xiaosong Du, Aziz Kaya, Josh Kittle, Jianzhao Liu, Yang Liu, Zelin Liu, Suolong Ni, Ying Ni, Sumin Shen, Chao Wang, Qiongdan Xie and Wen Yin. In particular, I want to thank all the wonderful undergraduate students I have worked with during these years, Tarun Aggarwal, Jessica Chau, Travis DePriest, Shafile Rashid, Stephen Schmidt and Michael Whitacre. The undergraduate research experiences let me know the beauty and joy of teaching and mentoring.

Thanks to the Department of Chemistry at Virginia Tech for all the assistantships and fantastic research environment. I am also grateful to the Center for LignoCellulose

Structure and Formation (CLSF), an Energy Frontier Research Center funded by the U.S. Department of Energy, Office of Science, Office of Basic Energy Sciences under Award Number DE-SC0001090. Most of the projects were funded by CLSF. Special thanks to Prof. Daniel J. Cosgrove and Dr. Sarah N. Kiemle, from Penn State University, for their useful discussions and suggestions on a joint project.

I would like to acknowledge my family for their love, support and encouragement over the years. Special thanks to my mom and other family members for being so strong and supportive when dad was sick.

Table of Contents

List of Figures

Chapter 2

Chapter 3

Chapter 4

Chapter 5

Chapter 6

Chapter 7

Chapter 8

List of Tables

Chapter 2

Chapter 3

Chapter 4

Chapter 5

Chapter 6

Chapter 7

Chapter 1: Scope of Dissertation

Plant cell walls are natural composites composed of different cell wall polysaccharides having applications in many industrial sectors, such as food, pulp and paper, animal feed and biofuels.[1] A complete understanding of the interactions between these biomacromolecules is crucial for understanding cell wall assembly, deconstructing cell walls for biofuels and designing sustainable biomaterials. Lignocellulosic materials, containing cellulose, hemicelluloses, pectins and lignins, have gained more interest and attention due to their ability to produce products that meet the needs of people in a sustainable fashion. The overall goal of this dissertation is to prepare and characterize polysaccharide model surfaces for studying their interactions with other biomacromolecules, such as cell wall polysaccharides and enzymes. Understanding the interactions between cell wall polysaccharide and other biomacromolecules is of great fundamental importance for understanding the assembly of plant cell walls and designing new strategies for degrading lignocellulosic biomass.

While plant cell wall models continue to be refined with the advancement of different characterization techniques, little is known about the precise nature of interactions between cell wall components. Model polysaccharide surfaces have attracted increasing attention for studying interactions with other cell wall polysaccharides and are being used as substrates for enzymatic degradation. Over the past decade, surface techniques have addressed interactions between polysaccharides.[2] In this dissertation, several surface techniques have been applied, including a quartz crystal microbalance with dissipation monitoring (QCM-D), surface plasmon resonance (SPR) and atomic force microscopy (AFM). Especially for the cases of QCM-D and SPR, *in situ* measurements can provide rapid identification of interactions between cell wall polysaccharides and quantification of surface excess and water content of adsorbed layers.

Chapter 2 provides an overall introduction and literature review of the hierarchical structure of plants with three major cell wall polysaccharides, including cellulose, hemicelluloses and pectins, along with non-polysaccharide cell wall polymers, lignins. Corresponding model films are also discussed, specifically focusing on the assembly of plant cell walls and key interactions between cell wall polysaccharides. Biodegradation and bioconversion of lignocellulosic materials by various enzymes are introduced. Additionally, interfacial thermodynamics and polymer adsorption at solid/liquid interfaces are presented. Finally, a brief introduction to the key experimental techniques, including QCM-D, SPR and AFM, is provided.

Chapter 3 details the materials, substrate preparation and experimental procedures used in this dissertation. This information will not be repeated in subsequent chapters.

In Chapter 4, quantification of hemicellulose and cellulose derivative adsorption onto cellulose model surfaces is studied by QCM-D and SPR. Studying interactions between hemicelluloses and cellulose can provide a better understanding of the assembly of plant cell walls and is crucial to the development of advanced wood-based materials. Representative hemicelluloses, xyloglucan and its oligosaccharides, are used for studying cellulose-xyloglucan interactions and adsorption isotherms are determined and fit with Langmuir or Freundlich adsorption isotherms. Additionally, the adsorption of carboxymethyl cellulose (CMC), a representative cellulose derivative, onto cellulose is studied with respect to salt concentration, degree of substitution (DS) and degree of polymerization (DP). The discussion focuses on DS and DP effects on CMC adsorption onto cellulose and highlights the gel-like and viscoelastic properties of CMC layers compared to hemicellulose layers that adsorb flat onto cellulose.

In Chapter 5, the preparation and characterization of pectin model surfaces are introduced. Given previous studies on CMC and polygalacturonic acid adsorption,[3, 4] there was an excellent opportunity to prepare pectin model surfaces. This chapter highlights interaction studies between a xyloglucan and pectins by using pectin model surfaces and provides some insight into existing cell wall models. Better degradation and conversion strategies for lignocellulosic materials can be developed by knowing how plant cell walls assemble.

Chapter 6 presents an adsorption study of hemicelluloses from type II cell walls, mixed linkage glucans (MLG), onto cellulose. Two MLG samples, barley and lichen MLG, with different proportions of β-(1→3) linkages are studied. The influence of the proportion of β-(1→3) linkages on the final viscoelastic properties of the adsorbed MLG layers was examined. Additionally, MLG interactions with other cell wall matrix polysaccharides were investigated. This study shows that the viscoelastic properties of the adsorbed MLG layers are strongly dependent upon the molecular structure of the MLG and provides some insight into the deposition of cell wall polysaccharides.

Chapter 7 presents enzymatic degradation studies of different polysaccharide layers, including pectins and a lichen MLG, using QCM-D and AFM. Preparation of pectin and lichen MLG layers are described in Chapters 5 and 6, respectively. Pectin model surfaces were used as platforms for studying enzymatic degradation as a function of pectin molecular structure, especially degree of esterification (DE). Lichen MLG degradation by a lichenase with specific cleavage sites was investigated as a function of enzyme concentration, pH and temperature. A better understanding of plant cell wall polysaccharide degradation is helpful for the design of enzyme mixtures that can efficiently degrade crude biomass fractions.

The overall conclusions of this dissertation are provided in Chapter 8 as well as some suggestions for future work.

References:

(1) Beck, C. B., *An introduction to plant structure and development: Plant anatomy for the twenty-first century*. Cambridge University Press: 2010.

(2) Roman, M., *Model Cellulosic Surfaces*. American Chemical Society: 2009.

(3) Liu, Z.; Choi, H.; Gatenholm, P.; Esker, A. R., *Langmuir* **2011,** *27*, 8718-8728.

(4) de Kerchove, A. J.; Elimelech, M., *Biomacromolecules* **2006,** *8*, 113-121.

Chapter 2: Introduction and Literature Review

2.1 Introduction to Plant Cell Walls

Natural materials often exhibit unique properties that are not found in synthetic systems. Plants are biocomposites with unique properties conferred by their multilevel architectures as shown in Figure 2.1. The unique material properties and environmental tolerances of different plant species arise from their hierarchical structures over a wide range of length scales. Generally a tree is on the scale of meters, consisting of three basic substructures: roots, stems and leaves. Due to the multicellular origin of plants, each substructure is composed of different tissues and tissues are composed of different cell types. Each cell is surrounded by a multilayer cell wall within the range of micrometers. Cellulose microfibrils, in the scale of nanometers, are the major building blocks of the entire plant kingdom.

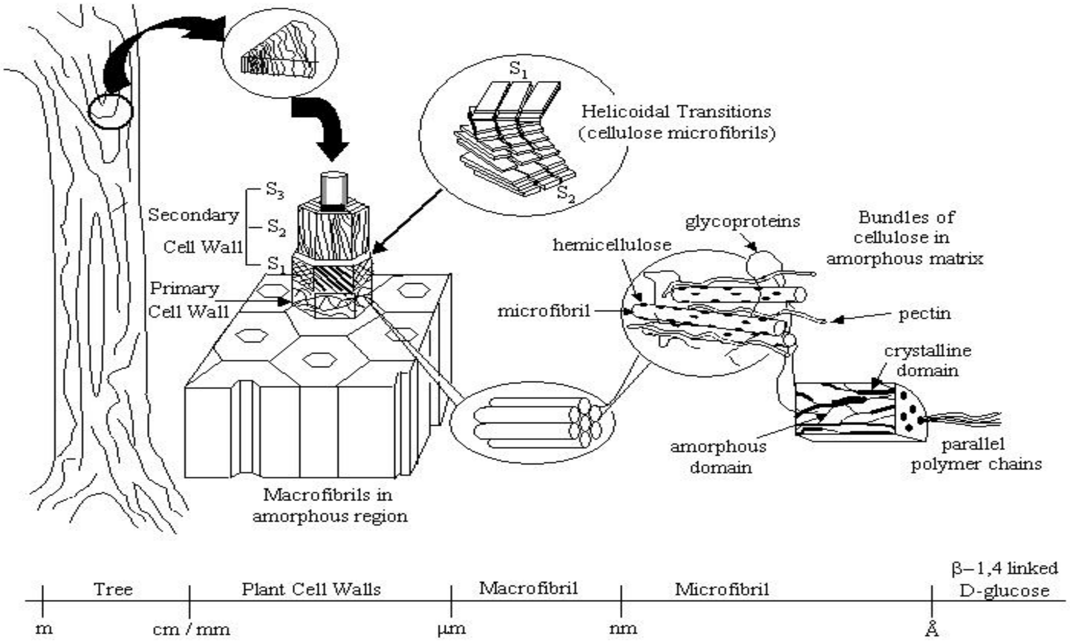

Figure 2.1 Hierarchical structure and complexity of wood: from tree to sugar unit. Adapted from Tirrell.[1]

Nearly all plant cells are characterized by an enclosing cell wall. Cell walls were first observed by Hooke in 1663 who regarded them as “dead” structures.[2] With the advancement of microscopic techniques, a clear demarcation between individual layers can be seen by the electron microscope. Recent studies have shown that the walls are dynamic structures and provide a pathway for molecular and mechanical signals between cells or between cells and the external environment.[2, 3] In addition to the communication role, cell walls also provide support and protective functions.[4]

Most cell walls are layered structures, consisting of a primary cell wall produced by the protoplast and a three-layer secondary cell wall deposited subsequently on the interior side of the primary cell wall. The primary and secondary cell walls differ in both composition and function. The primary cell wall, the first layer deposited during the development of a cell, is about 0.1 to 0.2 μm thick and contains randomly and loosely organized cellulose microfibrils, hemicelluloses, pectins and many proteins.[5] The polysaccharide composition of a primary cell wall can vary and is further designated as a type I or type II cell wall. Type I cell walls are most commonly found in dicots while type II cell walls are mainly observed in grasses and some lichen species. The secondary cell walls, with limited expandability, are responsible for the mechanical support of plants. They are composed of three distinct layers, including the S1, S2 and S3 layer with different orientations of the cellulose microfibrils (Figure 2.2). The outermost S1 layers with thicknesses of 0.1 to 0.3 μm and the innermost S3 layers with thicknesses of ~ 0.1 μm are characterized by shallow or flat helixes of cellulose microfibrils with large angles measured relative to the long axes of the cells. The S2 layers, with thicknesses of 1 to 5 μm, are typically the thickest layers of secondary cell walls, and are characterized by steep helices of cellulose microfibrils that are oriented almost parallel to the long axes of the cells. Changes in the orientation of cellulose microfibrils between the S1, S2 and S3 layers result from a helicoidal rotation of microfibrils between these layers.[6] Although different cell wall layers can be distinguished using an electron microscope, a direct isolation of various cell wall layers has not been achieved yet.[5]

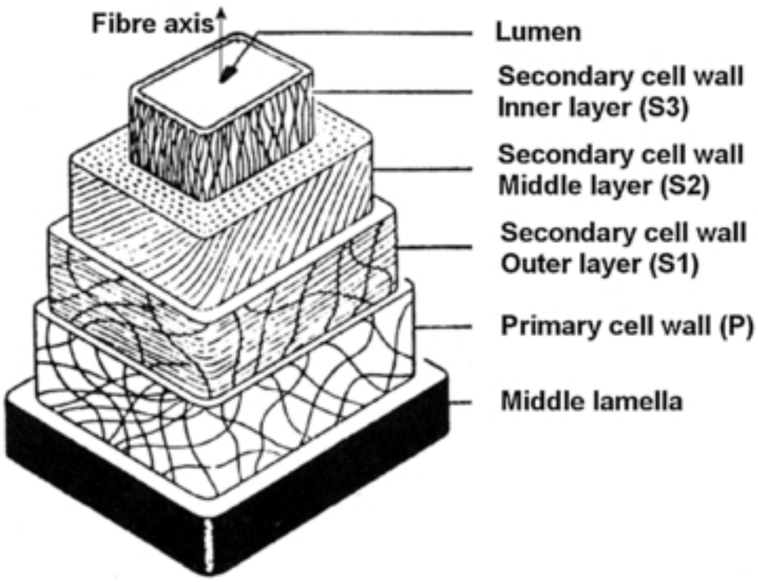

Figure 2.2 Simplified structure of the cell wall of a softwood tracheid or a hardwood fiber. Adapted from Timell.[5]

An increasing interest in environmentally benign and sustainable materials leads to a more extensive exploitation of the plant kingdom. With the advancement of various characterization techniques, several proposed models for primary cell walls were reviewed by Cosgrove (Figure 2.3).[7] Keegstra and coworkers (Figure 2.3A) have suggested that matrix polysaccharides are covalently linked together and anchor cellulose by hydrogen bonding to xyloglucan.[8] In a more recent model, as shown in Figure 2.3B, cellulose microfibrils are coated and tethered by xyloglucan as a network, while pectins form a coextensive but independent network filling the voids.[9, 10] A recently published model proposed hypothetical load-bearing junctions of xyloglucan located within limited regions of tight contact between microfibrils.[11] As is evident from Figures 2.3C and 2.3D, the multicoat model[12] and stratified model,[13] respectively, are based upon strong non-covalent interactions between matrix polysaccharides, especially xyloglucan and pectins. Recently, a new model proposed by Dick-Pérez and coworkers has suggested the central role of pectins in maintaining the structure and function of plant cell walls.[14] Although much has been learned about individual cell wall components over the past decade, a complete understanding on how they assemble into the structures that are cell walls remains a challenge.

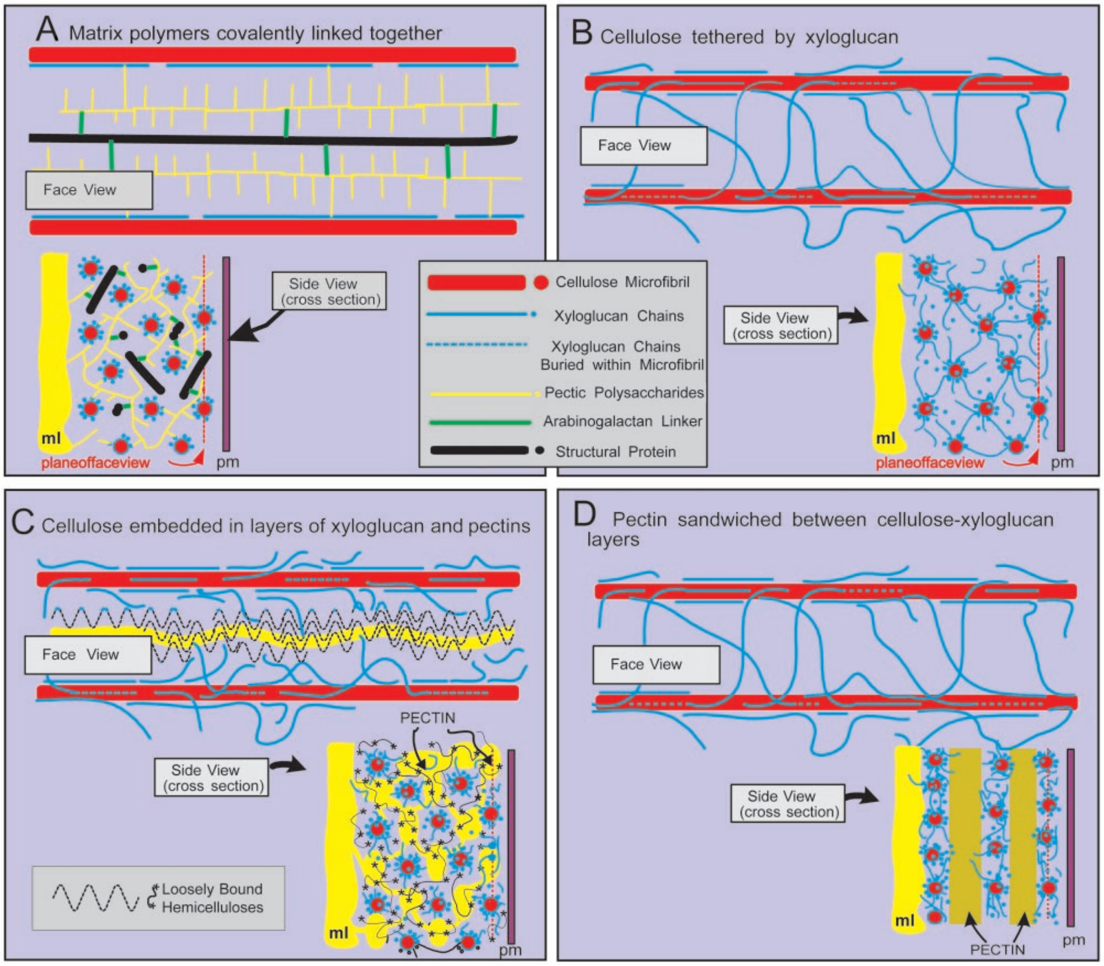

Figure 2.3 Various models for primary cell wall structure, including (A) covalently linked model, (B) tethered network model, (C) multicoat model and (D) stratified model.[7] "Reprinted from Plant Physiology, 125, Cosgrove, D. J. Wall structure and wall loosening. A look backwards and forwards, 131-134, Copyright (2001), with permission from American Society of Plant Biologists."

2.2 Major Cell Wall Polysaccharides

Cell wall polysaccharides are natural biomacromolecules with structural diversity and functional versatility.[15] In nature, cell wall polysaccharides have specific molecular structures and properties that allow them to fulfill their functions. The relative proportion of each cell wall polysaccharide depends upon the nature of the cell and its function. In dicots, the primary cell walls are called type I cell walls, consisting of approximately 30% cellulose, 30% hemicelluloses, 35% pectin and 1 to 5% structural proteins on a dry mass basis.[16] The walls of grasses and cereals differ dramatically from dicot species in terms of composition. These kinds of cell walls, also known as type II cell walls, are composed of cellulose microfibrils, glucuronoarabinoxylans and mixed linkage glucans, together with reduced amounts of xyloglucan and pectins.[17, 18]

2.2.1 Cellulose

Cellulose, the most abundant biomacromolecule in nature, is the major constituent of plant cell walls. The first identification of cellulose by Payne in 1838 is the onset of the modern history of cellulose chemistry.[19] Cellulose is highly abundant biopolymer representing about 1.5 trillion tons of the total annual biomass production.[20] Biosynthesis, physical and chemical aspects of cellulose have been widely studied and reviewed.[21, 22] Cellulose is expressed as fibrils from rosettes of cellulose synthesis complexes (CSCs) in plant cell membranes and elementary microfibrils aggregate into larger microfibrils.[23] These cellulose microfibrils are embedded in a polysaccharide matrix in both primary and secondary plant cell walls. Native cellulose always occurs as microfibrils and the cellulose chains are oriented along the direction of the microfibrils. Cellulose is the main load-bearing component of all plant cell walls and consists of anhydroglucose units (AGUs) linked together by β-(1→4) glycosidic bonds as shown in Figure 2.4A. The glucose dimer, cellobiose, is the structural repeating unit of cellulose and every other AGU is rotated 180° to achieve the thermodynamically favored acetal bond angle. Each cellulose chain has two different end groups, one is a reducing end with an aldehyde group and the other is a nonreducing end with a closed ring structure. Each glucose unit has three hydroxyl groups with different reactivity, including one primary hydroxyl group at the *C*6 position and two secondary hydroxyl groups at the *C*2 and *C*3 positions. As shown in Figure 2.4B, these hydroxyl groups participate in both intramolecular (*O*3−H···*O*5 and *O*2−H···*O*6) and intermolecular hydrogen bonding (*O*6−H···*O*3).[24]

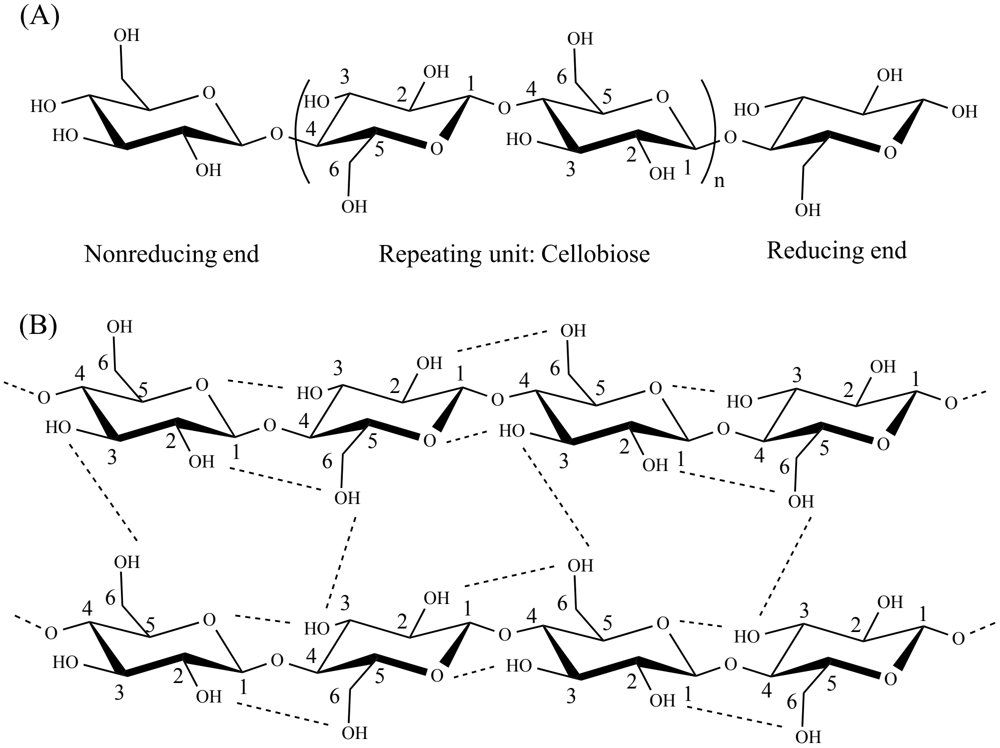

Figure 2.4 (A) A representative chemical structure of cellulose with cellobiose as the repeating unit. Two end groups, including a reducing and a nonreducing end, are labeled on the figure. (B) Depiction of the intermolecular (*O*6−H···*O*3) and intramolecular (*O*3−H···*O*5 and *O*2−H···*O*6) hydrogen bonding network within cellulose chains.

Six crystalline cellulose polymorphs, cellulose I (I_α and I_β), cellulose II, cellulose III_I, cellulose III_{II}, cellulose IV_I and cellulose IV_{II}, have been identified.[25] Interconversions between different cellulose polymorphs are summarized in Figure 2.5. Solid-state nuclear magnetic resonance (NMR) has shown that native cellulose consists of cellulose I_α (algae and bacteria) and I_β (plants).[26] Cellulose II is obtained by an irreversible conversion of cellulose I by either regeneration or mercerization. In contrast to cellulose I that has a parallel arrangement of individual cellulose chains in the unit cell of the crystal structure, cellulose II has an antiparallel arrangement of individual chains, yielding a more thermodynamically stable structure.[25] Cellulose III$_{\text{I}}$ and III$_{\text{II}}$ are obtained by treating cellulose I and II with ammonia, respectively. Cellulose IV$_{\text{I}}$ and IV$_{\text{II}}$ are obtained by heating cellulose III$_{\text{I}}$ and III$_{\text{II}}$ up to 260 °C in glycerol. Unlike irreversible conversion from cellulose I to II, interconversions among cellulose I, III and IV are reversible. The crystalline structure of cellulose can be determined by solid-state NMR, X-ray or neutron diffraction.[27-30] In nature, cellulose is considered to be partially crystalline, including both highly ordered crystalline and disordered amorphous regions. The relative amounts of crystalline and amorphous cellulose depend upon the origin of the sample and processing conditions used during isolation.

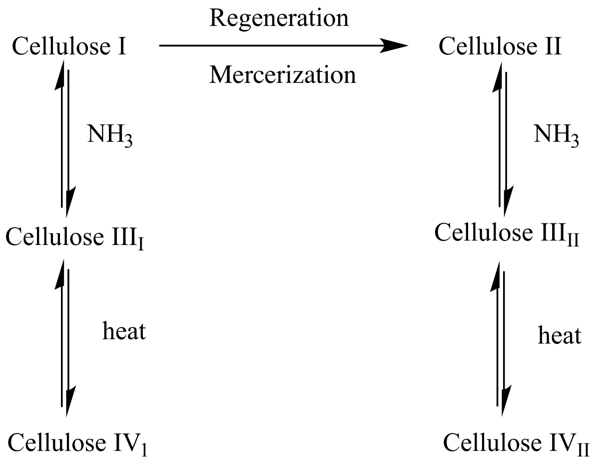

Figure 2.5 Interconversions between different cellulose polymorphs. Irreversible reactions are labeled with unidirectional arrows, while reversible reactions are labeled with bidirectional arrows.

Cellulose is insoluble in most solvents due to the presence of strong intermolecular and intramolecular hydrogen bonding. Several special solvent systems have been used for the dissolution of cellulose, including N,N-dimethylacetamide with lithium chloride (DMAc/LiCl), N-methylmorpholine-N-oxide (NMMO) monohydrate, or tri(ethylenediamine) cadmium hydroxide (Cadoxen).[22] Ionic liquids, known as “green solvents” also have the ability to dissolve cellulose. Various ionic liquids have been studied, such as 1-N-butyl-3-methylimidazolium ($[C4mim]^+$) with different anions, 3-methyl-N-butyl-pyridinium chloride and benzyldimethyl(tetradecyl)ammonium chloride (Figure 2.6).[31, 32]

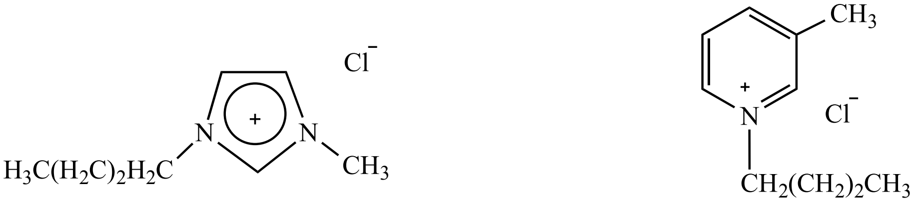

1-N-butyl-3-methylimidazolium chloride

3-methyl-N-butyl-pyridinium chloride

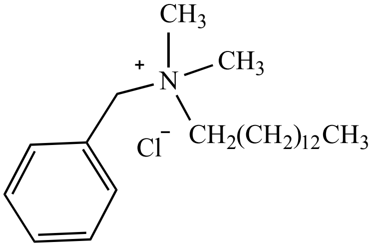

benzyldimethyl(tetradecyl)ammonium chloride

Figure 2.6 Representative molecular structures of ionic liquids used for cellulose dissolution and modification.

Unlike cellulose that is insoluble in most solvents, cellulose derivatives attract greater industrial interest because of their good solubility and processability compared to cellulose. Cellulose modification has been an active research area due to the three reactive hydroxyl groups per AGU. While each hydroxyl group shows somewhat different reactivity, regioselective esterification and etherification of cellulose via protecting group chemistry is highly desired especially for drug delivery applications.[33]

Representative cellulose derivatives include cellulose esters and cellulose ethers. For instance, cellulose nitrate, cellulose sulfate, cellulose phosphate and cellulose xanthate are important inorganic cellulose esters. Cellulose acetate is the most important organic cellulose ester and is widely used in coating and packaging applications.[34] Carboxymethyl cellulose (CMC), an important cellulose ether, is of prime significance in many industrial applications. For example, in papermaking, CMC has been used to introduce negative charges onto cellulose fiber surfaces,[35] while CMC has been used as an aqueous thickener and dispersion stabilizer in the food industry. Detergent applications are also important for CMC as it can coat the surfaces of clothing fibers and prevent redeposition of anionic dirt particles.[36]

2.2.2 Hemicelluloses

Unlike cellulose structure that is conserved throughout all plants, structures and amounts of hemicelluloses are strongly dependent upon the species, tissues and growth periods of plants. Hemicelluloses are non-crystalline, branched heteropolysaccharides that can be partially acetylated and even ionic. Several methods have been used to obtain hemicelluloses from plants, including extraction with alkali, dimethyl sulfoxide (DMSO), methanol/water, steam and microwave treatments.[15] Hemicelluloses are biosynthesized in the Golgi apparatus and are transported to the plasma membrane via Golgi vesicles. Hemicelluloses are chemically heterogeneous, consisting of glucose, galactose, mannose, xylose, arabinose, rhamnose and other sugar units (Figure 2.7). Hemicelluloses are categorized according to the main sugar in the backbone and four groups of hemicelluloses are defined: xyloglucans, xylans, β-glucans and mannans. As this dissertation focuses on the first three groups, they will be discussed in greater detail. The composition and distribution of hemicelluloses are strongly influenced by the botanical origin and the cytological localization. For instance, the composition of hemicelluloses varies notably between hardwoods and softwoods. Xylans are the most abundant hemicelluloses in hardwoods while glucomannans are the major hemicelluloses in softwoods. Hemicelluloses constitute the major part of plant biomass next to cellulose and are also excellent and sustainable alternatives to petroleum-based resources. In pulp and paper manufacturing from wood, the importance of hemicelluloses on the properties of the final paper has long been recognized. Hemicelluloses can be used as stabilizers in the thermomechanical pulping process to prevent extractive colloids from aggregating and accumulating on the fiber surfaces.[37]

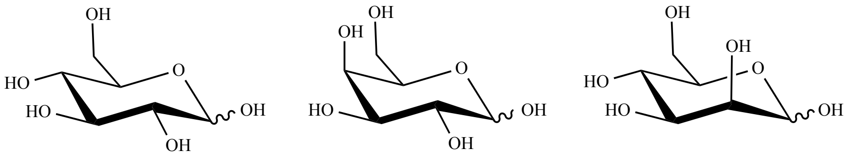

D-glucopyranose D-galactopyranose D-mannopyranose

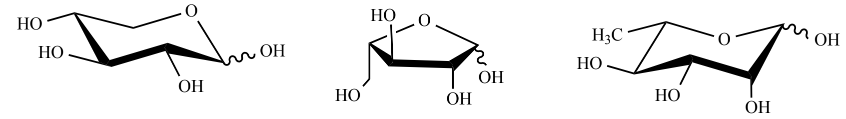

D-xylopyranose L-arabinofuranose L-rhamnopyranose

Figure 2.7 Representative sugars commonly found in hemicelluloses.

Xyloglucans (XG), the most abundant hemicelluloses in type I cell walls, have a cellulose-like backbone with xylose, galactose and fucose as side branches. They are the principal coating and crosslinking polysaccharides that are closely associated with cellulose through both surface adsorption and entrapment within the cellulose microfibrils. Cellulose-xyloglucan interactions are mainly through hydrogen bonding and hydrophobic interactions in primary cell walls.[9] In addition, a proportion of xyloglucans is covalently bonded to pectin.[38] It is also believed that xyloglucans perform an important role in the structural integrity of cell walls and the regulation of cell wall extension. In addition to their structural roles, xyloglucan oligosaccharides are related to the production of auxin, an important signaling molecule in plants.[39, 40] Xyloglucans also exist in secondary cell walls as storage polysaccharides.[41, 42] Considerable efforts have been devoted to the determination of the fine structure of xyloglucans and xyloglucan oligosaccharides by both chromatographic and spectroscopic techniques.[43-45] A single letter notation has been proposed to describe the complex structure of xyloglucan based upon the substitution pattern of glucose units in the backbone (Figure 2.8). An unsubstituted glucose is assigned "G", a glucose unit with a single unit of α-D-xylose substituent at *O*6 is assigned "X". As some of the xylose units are further substituted at *O*2 by β-D-galactose, they are assigned "L" and the "L" unit with an additional α-D-fucose substituent at *O*2 is assigned as "F". Two major types of xyloglucans with predominant structural units of XXXG or XXGG oligosaccharides have been identified (Figures 2.8A and 2.8B).[46] These structural units are biosynthesized by glucosyltransferase and xylosyltransferase in the Golgi apparatus.[47, 48] The backbones are further substituted by acetyl substituents and various sugar units, such as fucose and galactose. A representative structure of a xyloglucan segment is also provided in Figure 2.8C. Tamarind xyloglucan has been used as a model compound for cell wall xyloglucans due to its structural similarity.[42, 47] Xyloglucans have flexible random coil conformations and form viscous solutions at high concentrations due to polymer entanglements. Xyloglucans also have numerous practical applications as thickeners, stabilizers and gelling agents in the food industry.[42] Xyloglucans are also widely used as sizing agents for the pulp and textile industries.[49] Xyloglucans can bind to wood pulp fibers and enhance fiber crosslinking, thereby improving paper formation and strength. Xyloglucans also find application in drug delivery in controlled release formulations.[42, 50]

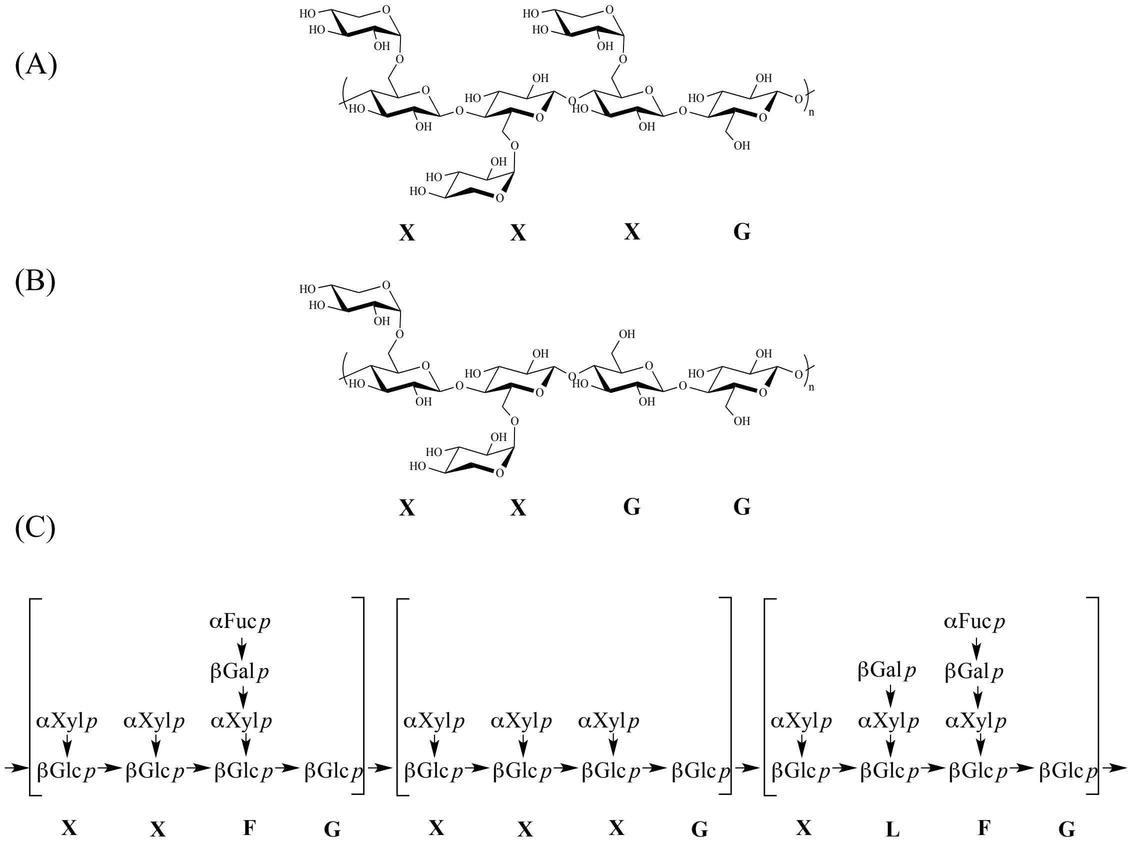

Figure 2.8 Structural units of (A) XXXG or (B) XXGG xyloglucan oligosaccharides and (C) a representative structure of a xyloglucan segment.

Partially acetylated, acidic xylans are the predominant hardwood hemicelluloses are, and about 70-80% of hardwood xylans can be isolated by aqueous potassium hydroxide.[5] Hardwood xylans are quite stable in alkaline solution at room temperature and the extraction products are quite similar to those from native xylans. The predominant softwood hemicelluloses are galactoglucomannans that cannot be directly extracted with alkali. Xylans are also the most abundant hemicelluloses in grass cell walls (type II). Xylans consist of a backbone of β-(1→4)-xylose that can be substituted by different side groups to form arabinoxylans and glucuronoarabinoxylans. An arabinoxylan consists of a xylan backbone that is partially glycosylated at the *O*2 or *O*3 positions with arabinose units. Arabinoxylans constitute 40% or more by mass of the primary cell walls of monocots.[51] In grass cell walls, glucuronoarabinoxylans take the place of xyloglucans, crosslinking cellulose microfibrils and constituting about 25% by dry mass of the primary cell walls. A glucuronoarabinoxylan consists of a xylan backbone with both neutral and acidic side chains. The neutral side chains are composed of arabinose units attached at the *O*3 positions on the xylose units and acidic side chains are glucuronic acid units at the *O*2 positions. These side chains not only provide surface charges to type II cell walls but also create spacing between cell wall components leading to porous cell wall structures.[18]

Mixed linkage glucans (MLGs) account for about 3 to 5% of the cell wall materials on a dry mass basis in the cell walls of Poales, cereals and some lichens (*Cetraria islandica*).[52] They are the major hemicelluloses in type II cell walls and are biosynthesized in the Golgi apparatus.[17] The primary structure of a MLG is an unbranched homopolymer of glucose with both β-(1→3) and β-(1→4) linkages as shown in Figure 2.9. The common ratio of β-(1→3) to β-(1→4) linkages in MLG molecules is about 2:1.[53] Typically, a MLG can be viewed as a β-(1→4) linked cellulosic backbone interrupted by single β-(1→3) linkages which introduce “kinks” into the backbone, giving rise to flexibility and MLG solubility in aqueous solutions.[54] Consecutive β-(1→3) linkages have not been found.[55] The conformation of a single MLG chain in aqueous solution is depicted as an extended random coil on the basis of both experimental results and theoretical models.[56, 57] Molecular structures of MLG are usually determined by quantitative analysis of the oligosaccharides obtained upon digestion of MLG with a lichenase.[58] As shown in Figure 2.9, most of the β-(1→4) linkages occur in randomly distributed cellotriosyl (x = 3) or cellotetraosyl (x = 4) units, while longer blocks of β-(1 →4) linkages (x = 5 to 11) are also present. The composition of the linkages is one of the most important characteristics of MLGs and varies on the basis of the origin and tissue type.[59] Some MLGs can also be found in high concentrations within the endosperms of some grains where they serve as storage carbohydrates.[60] They are associated with cellulose microfibrils during cell growth and are enzymatically hydrolyzed into small fragments when growth is complete. Turnover of MLGs during cell wall growth suggests that MLGs play an important role in the formation of plant cell walls.[17] Commercial interest in MLGs has increased due to their potential application in the treatment and prevention of several diseases, such as high cholesterol, obesity and heart disease.[60]

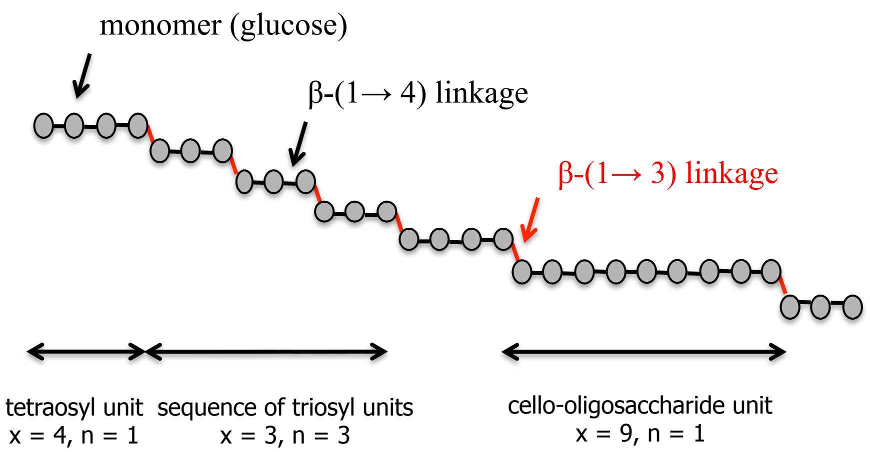

Figure 2.9 A representative molecular structure of a mixed linkage glucan (MLG). Bonds in black represent β-(1→4) linkages and bonds in red represent β-(1→3) linkages. Letter x is defined as the degree of polymerization in the cello-oligosaccharide unit and n is the number of sequential groups of the same cello-oligosaccharide unit.

2.2.3 Pectins

Pectins are less prominently present in most plant cell walls compared to cellulose and hemicelluloses. However, pectins contribute most of the negative charge carried by plant cell walls and can be found not only in primary cell walls but also in middle lamella. Pectins (Figure 2.10), are of the most complex classes of biomacromolecules, have domains of homogalacturonan (HG), rhamnogalacturonan I (RG I) and rhamnogalacturonan II (RG II). Polygalacturonic acid (PGA) is a pectin degradation product and commercial PGA is prepared from citrus pectin by partial depolymerization and demethylation. Greater than 60% of all pectins in the plant cell wall are HGs with the PGA backbone having varying degrees of methylation and acetylation.[61] The degrees of methylation and acetylation of PGA, as well as the distributions of methyl and acetyl groups, play important roles in interactions with other cell wall polysaccharides.[62, 63] Sequences designated as RG I have alternating galacturonic acid and rhamnose units as a backbone and are branched at approximately half of the rhamnose units with arabinan, galactan or arabinogalactan side chains as depicted in Figure 2.10. The structure of RG II sequences are even more complicated with four different complex side chains that can be crosslinked by diborate ester bonds.[64] The RG II sequences comprise about 10% of pectins and consist of approximately 30 monosaccharide units which also include some uncommon sugars, such as apiose, aceric acid, 2-*O*-methyl-L-fucose, 3-deoxy-lyxo-2-heptulosaric acid and 3-deoxy-D-manno-2-octulosonic acid.[65] Pectins can also be defined on the basis of their structures, including "smooth" regions with methylated or acetylated HG domains and "hairy" regions with RG I and RG II domains as depicted in Figure 2.11.

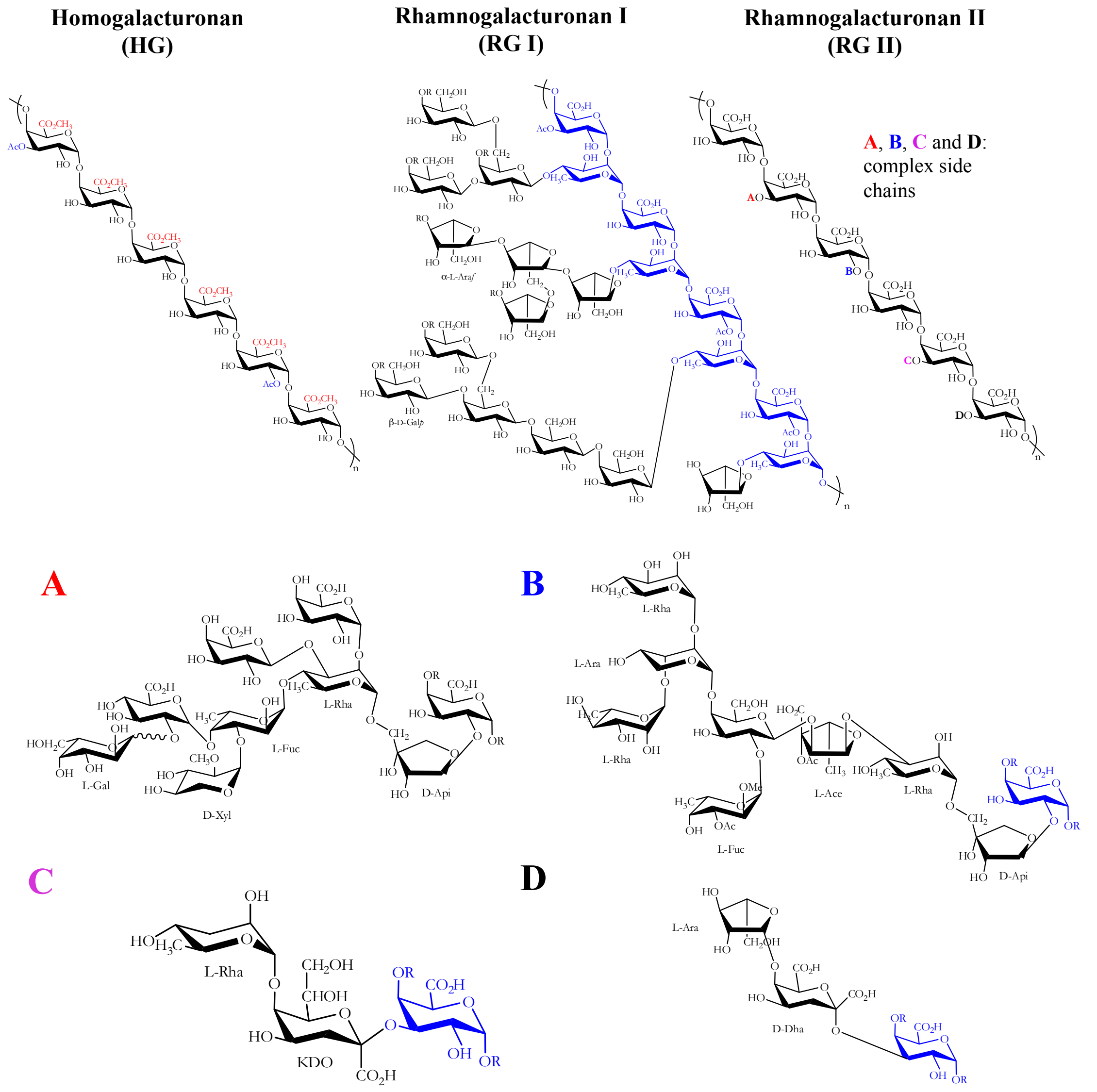

Figure 2.10 Detailed structure of three different domains of pectin, including homogalacturonan (HG), rhamnogalacturonan I (RG I) and rhamnogalacturonan II (RG II).

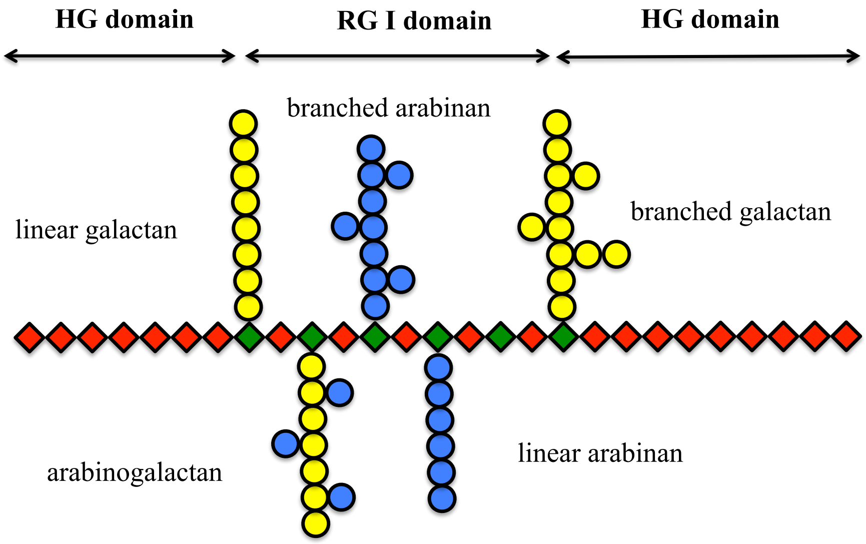

Figure 2.11 A simplified depiction of pectins like those in Figure 2.10 with different domains covalently linked together.

2.2.4 Lignins

Substantial amounts of lignin can be found in the secondary cell wall and middle lamella, providing rigidity and protective coating for the plant cell walls. Lignins are amorphous, crosslinked aromatic polymers. They are predominantly composed of three different monolignol monomers: p-coumaryl alcohol, coniferyl alcohol and sinapyl alcohol (Figure 2.12). The biosynthesis of lignin starts with the synthesis of monolignols in the cytoplasm and then the monomers are transported through the plasma membrane into the cell walls. Lignins are formed through the enzymatic dehydrogenation of monolignols that are further crosslinked by double bonds through radical coupling.[66, 67] Lignins can form two types of covalent crosslinks, including diferulic acid bridges and ester linkages, resulting in an increased rigidity of the cell wall that limits cell growth and reduces cell wall degradability.[46] Unlike cell wall polysaccharides that are hydrophilic in nature, lignins are hydrophobic and form waterproof channels in plants. The distribution of lignins has been studied with the aid of electron microscopy.[68, 69] Lignin content decreases in the order of softwoods > hardwoods > grasses. The exact structures of natural lignins are unknown due to their structural complexity as well as structural changes caused by harsh isolation conditions. Most commercially available lignins are obtained from the Kraft process, using sodium hydroxide and sodium sulfide to separate lignin from wood pulp. Lignins are the main source of color in mechanical pulps due to the presence of a variety of chromophores. The use of bleaching and optical brightening agents is necessary to improve the whiteness and brightness of paper products.[70] The presence of lignins in plants also prevents further processing and bioconversion of wood materials. Chemical pretreatments are required to degrade lignins into smaller fragments and improve biodegradability of biomass.

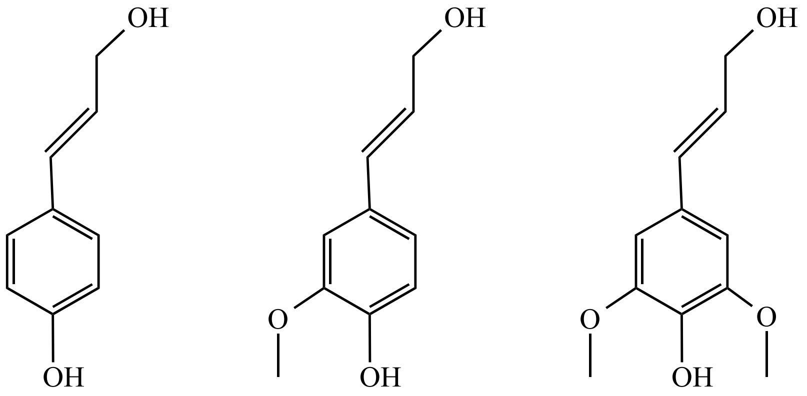

p-coumaryl alcohol coniferyl alcohol sinapyl alcohol

Figure 2.12 Molecular structures of three monolignol monomers for lignin.

2.3 Model Surfaces for Plant Cell Wall Polysaccharides

Due to their complex structures and undefined compositions, it is difficult for surface techniques to directly probe natural plant polysaccharides. Model surfaces prepared by depositing a small amount of chemically defined compounds onto a flat substrate are widely used in surface chemistry. There are two established techniques for the preparation of model surfaces: Langmuir-Blodgett (LB) deposition and spincoating. For LB-deposition, a Langmuir trough is required, while spincoating is a much simpler and easier way to prepare model surfaces.[71, 72] These model surfaces with well defined morphology and chemical characteristics are perfect platforms for studying interactions between different cell wall polysaccharides as well as interactions between cell wall polysaccharides and other biomacromolecules, such as enzymes.

Preparation of thin films of cellulose, using the LB-technique to deposit trimethylsilyl cellulose (TMSC) onto silicon wafers followed by subsequent acid vapor hydrolysis, was first reported in 1993.[73] The cellulose derivative, TMSC, can be prepared by dissolving cellulose in lithium chloride in dimethylacetamide (DMAc/LiCl) and reacting with hexamethyldisilazane (HMDS) as described elsewhere.[74] The bulky TMSC structure is converted into a compact, tightly hydrogen bonded cellulose structure upon the removal of the trimethylsilyl groups. The reactions involved in the preparation of TMSC and the regeneration of cellulose structure are given in Figure 2.13. The trimethylsilyl chloride is immediately hydrolyzed to trimethylsilanol and further condensed into volatile hexamethyldisiloxane.[75] Regenerated cellulose has long been studied and reviewed in the past[76, 77] and used as a model system for surface forces studies.[78] Kontturi and coworkers used an approach comparable to the LB-technique, spincoating, for the preparation of cellulose model surfaces from TMSC.[79] The regeneration of cellulose from TMSC converts the hydrophobic “as spincoated” surface into a hydrophilic surface as depicted in Figure 2.14. This method has motivated numerous studies involving the preparation of cellulose model surfaces in a similar fashion. It has been found that the source of cellulose and the method of film preparation influence the wetting properties of the substrates.[80] Regenerated cellulose (RC) surfaces obtained from spincoated TMSC films do not contain cellulose I domains. Previous studies of RC films via reflection absorption infrared spectroscopy[81] and grazing incidence X-ray diffraction[82] have determined that spincoated RC layers are largely amorphous.

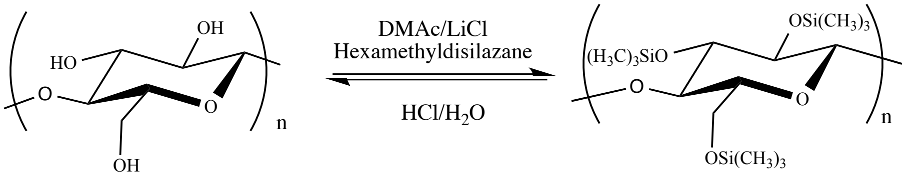

Figure 2.13 Reactions involved in the preparation of TMSC and regeneration of cellulose.

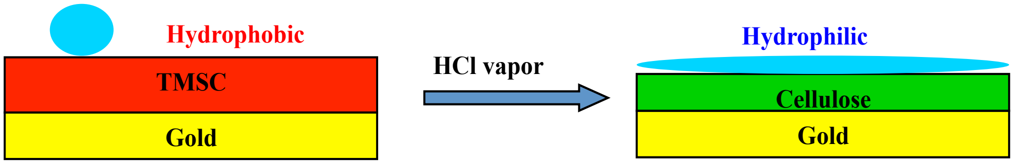

Figure 2.14 A schematic representation of the preparation of RC surfaces by spincoating, followed by regeneration in hydrochloric acid vapor. Water droplets (blue) bead on TMSC but undergo greater spreading on the RC surfaces.

Preparation and characterization of other cellulose model surfaces are summarized in Table 2.1. Besides RC surfaces, nanocrystalline cellulose (NC) surfaces have attracted interest for studying interactions between cell wall polysaccharides.[83] Preparation, modification and application of cellulose nanocrystals have been widely studied and reviewed.[25] In the 1950s, Ränby first reported the preparation of colloidal suspensions of cellulose by exposing native cellulose to mineral acids, such as H_2SO_4, for a limited period of time.[84] Partial degradation of the more accessible portions of the fibril occurred, leaving behind highly crystalline regions of cellulose I. Cellulose nanocrystals obtained by H_2SO_4 treatment often carry negative charges due to the presence of sulfate esters.[25] Jiang and coworkers recently showed that it was possible to desulfate nanocrystalline cellulose,[85] while other researchers have used HCl instead of H_2SO_4 to avoid the introduction of surface sulfate groups while retaining a cellulose I crystal structure.[86] The Avicel surface is another important and well-characterized cellulose model surface. These surfaces are prepared by spincoating Avicel-PH101 from NMMO/DMSO with subsequent precipitation with water.[76] The resulting film has a cellulose II crystal structure.[76]

Table 2.1 Selected properties of cellulose model surfaces.[a,b,c,d]

Model Surfaces	Preparation Method	Characterization Methods	Thickness /nm	Roughness /nm
Regenerated Cellulose (Amorphous)[79]	Spincoating from trimethylsilyl cellulose in toluene and subsequent regeneration via HCl vapor	XPS[a] ATR-IR[b] AFM[c] Ellipsometry	10	1
Nanocrystalline Cellulose (Type I)[83, 87]	Spincoating from aqueous suspensions of sulfated cellulose nanocrystals	XPS XRD[d] AFM Ellipsometry	9	2
Avicel Cellulose (Type II)[76]	Spincoating from Avicel-PH101 in NMMO/DMSO and subsequent precipitation	XPS AFM Ellipsometry	14	7

a. XPS = X-ray photoelectron spectroscopy
b. ATR-IR = Attenuated total reflectance infrared spectroscopy
c. AFM = Atomic force microscopy
d. XRD = X-ray diffraction

As hemicelluloses are polysaccharides with different side chain branches, the presence of branches affects not only the molecular structure but also the solution properties. The presence of side branches tends to disrupt the regularity and inhibit the close packing of the backbone, resulting in enhanced aqueous solubility for hemicelluloses. Enhanced solubility over cellulose makes the preparation of hemicellulose films extremely difficult, especially in a thin film situation. The resulting hemicellulose films are unstable and can be easily removed from the substrates with time in aqueous solutions. Bulk or surface chemical modification, such as esterification, etherification or grafting, is required to improve their stability. Sustainable films and coatings from hemicelluloses and modified hemicelluloses have been studied and used for food packaging and biomedical applications.[88]

Unlike cellulose model surfaces that have been widely studied, pectin model surfaces remain underdeveloped. Studies of pectin model surfaces are inhibited by the complex structure of pectin. A recent QCM-D study with an alginate and a polygalacturonic acid has shown that divalent Ca^{2+} can crosslink anionic polyelectrolytes and form stable coatings on SiO_2.[89] This approach provides an excellent opportunity to prepare pectin model surfaces.

Methods for preparing lignin model surfaces have been studied and reviewed. Lignin model surfaces can be prepared by solvent casting[90], LB deposition[91] and spincoating.[92] However, the lignin structure was altered from the native state due to the utilization of processed lignin. Preparation of model lignin surfaces using monolignols via the action of peroxidase has also been demonstrated.[93]

2.4 Biodegradation and Bioconversion of Lignocellulosic Materials

Current industrial practices have started to focus on sustainable technologies that produce safe materials with minimal hazardous by-products and waste generation as well as the ability to recycle or degrade the material at the end of use. All these foci make lignocellulosic materials perfect candidates for sustainable development. Lignocellulosic materials consist of three main polymers, cellulose, hemicelluloses and lignins. They are produced from carbon dioxide (CO_2) in the atmosphere during photosynthesis. Wood is the largest component of biomass in the US; about 700 million tons of lignocellulosic biomass accumulate annually.[94] Lignocellulosic biomass composed of renewable building blocks provides key materials for the sustainable production of renewable and environmentally friendly products to meet the needs of people in modern society. In addition, building functionality onto lignocellulosic surfaces at the nanoscale enables applications in pharmaceutical products, self-sterilizing surfaces and electronic lignocellulosic devices.[94, 95]

Various enzymes in plants participate in degradation and modification of lignocellulosic materials for the regulation of cell wall expansion and alteration.[4] In addition, enzymatic degradation of lignocellulosic materials has many industrial applications, especially for the sustainable production of fuels and chemicals. As a result, knowledge of different classes of enzymes involved in plant cell wall degradation is highly desirable. Enzymes involved in the degradation of lignocellulosic biomass have been reviewed with respect to their structural properties, specificity and degradation mechanisms.[4, 96] Four classes of enzymes are involved in the biodegradation of cellulose, including endoglucanases (EC 3.2.1.4), cellobiohydrolases (EC.3.2.1.91), β-glucosidases

(EC 3.2.1.21) and exoglucanases (EC 3.2.1.58). Although each enzyme shows specificity with respect to the cleavage site and degradation mechanism, they act synergistically to break down cellulose efficiently. The heterogeneous nature of hemicelluloses requires various enzymes for complete and efficient biodegradation. Some cellulose degrading enzymes can also be used for hemicellulose degradation. For instance, endoglucanases can cleave the backbone of xyloglucan and mixed linkage glucans (MLGs). Enzymes involved in pectin degradation are generally termed as pectinases and commercially available samples are usually a mixture of different enzymes. Pectinases are of great importance to the food industry as well as the pulp and paper industry. Although various enzymes are present in plants, efficient biodegradation of cell wall polysaccharides requires synergistic cooperation between different enzymes.

Another application of lignocellulosic materials is their conversion to liquid biofuels by fermentation, gasification or catalysis. For instance, glucose fermentation is an established technique of producing ethanol in large volumes. A schematic depiction of the bioconversion of lignocellulosic biomass to bioethanol is provided in Figure 2.15. The biodegradation of lignocellulosic materials is limited by several factors, such as cellulose crystallinity, lignin and hemicellulose content. These factors hinder the enzymatic digestion of lignocellulosic biomass and further affect the economics of the biochemical pathway to biofuels. Pretreatments, such as steam pretreatment, lime pretreatment, liquid hot water pretreatment, acid treatment and ammonia-based pretreatment, are necessary to alter or remove impediments and improve the rate of biodegradation and bioconversion.[97] Thermal, chemical and biological treatments are the principal techniques used for direct lignocellulosic biomass conversion. Thermal techniques include combustion, pyrolysis, gasification and liquefaction, for subsequent conversion to fuels and chemicals.[3] Technologies to produce liquid biofuels, including cellulosic ethanol, diesel and alcohol or alkane fuels, are being developed, especially biofuels from forest products via fermentation and gasification.[94]

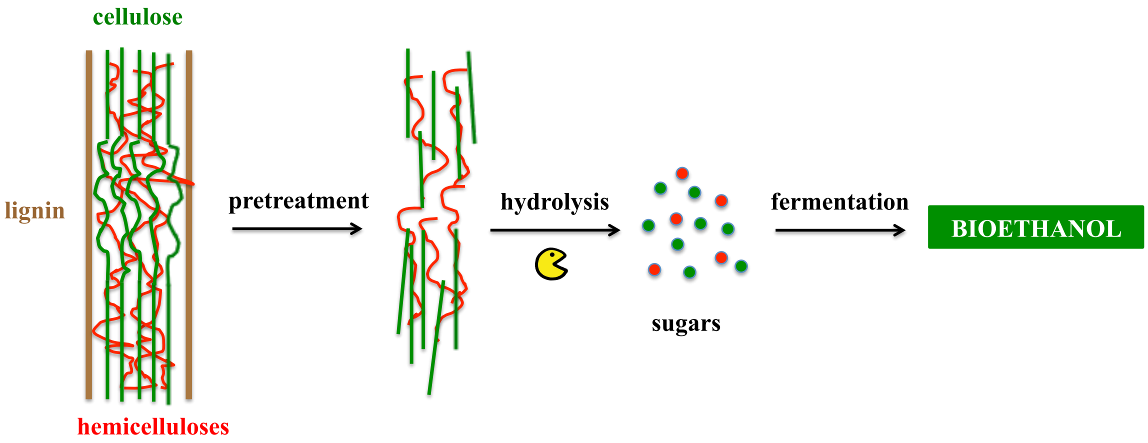

Figure 2.15 A schematic depiction of bioconversion of lignocellulosic biomass to bioethanol. Adapted from Moiser, Pingali and Dashtban *et al.* [97-99]

2.5 Polymer Adsorption at Solid/Liquid Interfaces

2.5.1 Interfacial Thermodynamics

An interface (σ) will be formed when two bulk phases (α and β) are in contact with each other as shown in Figure 2.16. The interface σ can be further categorized depending upon the types of phases in contact: liquid/liquid, liquid/solid, liquid/gas and solid/gas interfaces. According to the Gibbs convention, two phases are separated by an infinitesimal thin boundary layer, also known as the Gibbs ideal interface. An alternative model, for example, the Guggenheim model, places an extended interphase with a finite volume between the two bulk phases α and β. The Gibbs convention is usually more common, although the rise of nanofillers has expanded interest in interphases.[100]

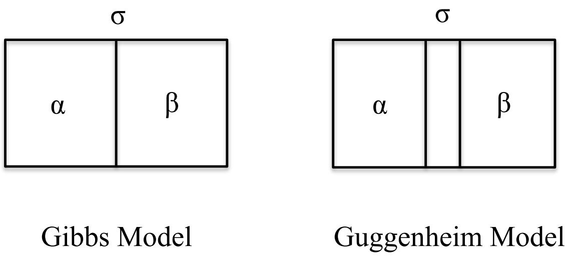

Figure 2.16 Depiction of a Gibbs ideal interface (σ) which is infinitely thin and a Guggenheim interface with a finite interfacial volume between two phases α and β.

For an open system, the Gibbs free energy G depends upon composition (n_i), temperature (T), pressure (p) and surface area (A),

$$dG = -SdT + Vdp + \gamma dA + \sum_{i=1}^{N} \mu_i dn_i \tag{2.1}$$

where S is entropy, V is volume, γ is surface tension and μ_i is the chemical potential for the ith component and N is number of components in the system. Increases in concentration for the ith component near the interface are characterized by a surface excess or surface concentration, defined as

$$\Gamma_i = \frac{n_i^{\sigma}}{A} \tag{2.2}$$

where A is surface area or interfacial area, n_i^{σ} is a number of molecules of type I in the interfacial layer and Γ_i is given as a number of molecules per unit area. Values of Γ_i can be either positive or negative by varying the position of the interface (Figure 2.17). For a two-component system ($N = 2$) in which solute is dissolved in a liquid solvent, the solute can increase or decrease in concentration near the interface. Both cases are characterized by a surface excess or surface concentration of solute (Γ_{solute}). The position of the interface σ is placed at z_0 where the surface excess of the solvent ($\Gamma_{solvent}$) is zero. Once the position of the interface σ is fixed at position z_0 under conditions of constant temperature and pressure, the surface excess of solute, Γ_{solute}, can be calculated from composition profiles like those in Figure 2.17 through

$$\Gamma_{solute} = -\frac{d\gamma}{d\mu_{solute}} \tag{2.3}$$

where γ is surface tension and μ_{solute} is the chemical potential of the solute. Gibbs also showed that for a binary system of solvent and solute,

$$\Gamma_{solute} = -\frac{a_{solute}}{RT}\left(\frac{d\gamma}{da_{solute}}\right) = -\frac{c_{solute}}{RT}\left(\frac{d\gamma}{dc_{solute}}\right) \tag{2.4}$$

where R is the gas constant and T is the absolute temperature. The second and third terms of Equation 2.4 convert μ_{solute} to an activity (a_{solute}) for non-ideal solutions or a molar concentration (c_{solute}) for ideal solutions.

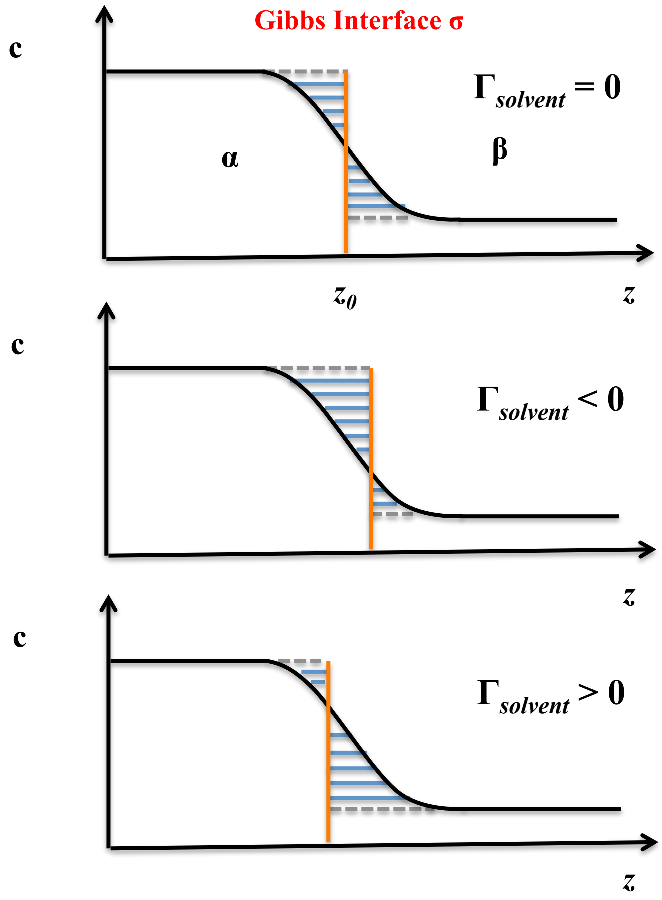

Figure 2.17 Dependence of the surface excess Γ upon the position of the Gibbs ideal interface (z_0) for a single component system. Adapted from Butt.[101]

Properties associated with the interface, for example, internal energy, Helmholtz energy, Gibbs free energy and molecular composition, are quite different from those of the bulk phases. The term adsorption means the accumulation of solute molecules at an interface, while desorption is the reverse process in which concentration of solute decreases. For an adsorption process, “adsorbent” refers to a material onto which adsorption occurred, “adsorbate” is the material that has already adsorbed and the bulk adsorbing species is called “adsorptive”. In general, there are two types of adsorption:

physisorption (physical interactions) and chemisorption (chemical reactions). Major differences between these two types of adsorption are summarized in Table 2.2.

Table 2.2 Comparison of physisorption and chemisorption.

Physisorption	**Chemisorption**
Weak, long range interactions	Strong, chemical bonding
Reversible process	Irreversible process
Unfavorable at high temperature	Favorable at high temperature
Adsorbate is mobile	Adsorbate is immobile
Not surface specific	Surface specific
Fast equilibrium	Slow equilibrium
No surface change	Surface reconstruction

2.5.2 Adsorption Isotherms

An adsorption isotherm is a fundamental concept in surface science and has been widely used to describe adsorption processes. It describes an equilibrium relationship between the adsorbed amount and the bulk concentration at a fixed temperature. A series of parameters, such as affinity, interaction parameters and maximum adsorbed amounts, can be deduced from adsorption isotherms.

For adsorption at solid/liquid interfaces, different isotherms have been proposed. The Langmuir adsorption isotherm was first proposed for the adsorption of gas molecules onto metal surfaces with maximal adsorbate surface coverages of monolayers. The key assumption of the Langmuir adsorption isotherm is a homogeneous substrate lacking preferential adsorption sites with non-interacting adsorbates under equilibrium conditions. As a result, the Langmuir isotherm predicts a finite capacity for the adsorbate where no further adsorption can occur. It is defined as

$$\Gamma = \frac{\Gamma_m K_L c}{1 + K_L c} \tag{2.5}$$

where Γ is surface excess, Γ_m is the maximum surface excess at monolayer coverage, K_L is the Langmuir constant and c is bulk concentration. For gases, pressure is commonly used instead of concentration. The Langmuir constant K_L and maximum surface excess Γ_m can be evaluated through nonlinear fitting methods or linearization of Equation 2.5. The Langmuir constant K_L is also the effective equilibrium constant, the ratio of the adsorption rate constant and the desorption rate constant, and is hence related to the standard Gibbs free energy of adsorption (ΔG^0_{ads}).

The Freundlich adsorption isotherm is often employed for heterogeneous systems. Heterogeneous systems are defined as systems with inequivalent binding sites. These can be inherently different binding sites on the substrates themselves, or inequivalencies that arise through interactions between adsorbed and adsorbing molecules. The adsorption initially occurs at high affinity regions and then at low affinity regions after the high affinity sites start filling. The Freundlich adsorption isotherm can be written as

$$\Gamma = K_F c^{\frac{1}{n_f}} \tag{2.6}$$

where Γ is the surface excess, K_F is the adsorbent capacity, c is the bulk concentration and $1/n_f$ is the adsorption affinity constant which is used to characterize the heterogeneity of the substrate. Both the adsorbent capacity K_F and the adsorption affinity constant $1/n_f$ can be deduced from a nonlinear fit or a linear form of Equation 2.6. The adsorbed amount of the material is the summation of adsorption onto all sites, thus adsorption in excess of a monolayer can occur. The Freundlich isotherm agrees well with the Langmuir adsorption isotherm over moderate concentration ranges, however, it is not restricted to the formation of a monolayer. The Freundlich adsorption isotherm works well for polymer systems which often involve irreversible adsorption and multilayer formation.

2.5.3 Polymer Adsorption

Unlike small molecules that can easily desorb, polymers frequently adsorb irreversibly onto a solid substrate if the interaction between the polymer and the substrate is more favorable than the interaction between the solvent and the substrate, resulting in the formation of adsorption layers (Figure 2.18).[102] Conversely, if the interaction between the substrate and the solvent is more favorable than the substrate interaction with the polymer, a depletion layer will be formed. Polymer adsorption kinetics have been studied and the layer formation involves three steps: (1) diffusion of molecules to the substrate, (2) adsorption onto the substrate and (3) rearrangement of adsorbed chains.

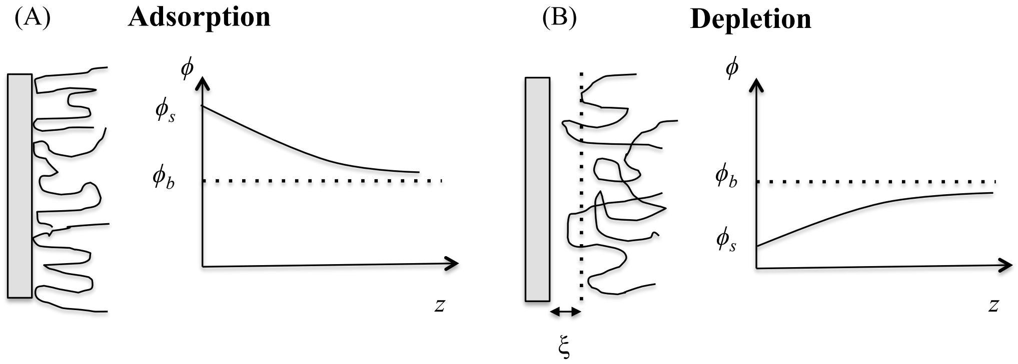

Figure 2.18 Polymer adsorption onto solid substrates with the formation of (A) an adsorption layer (i.e. substrate interactions with the polymer are preferential to interactions with the solvent) and (B) a depletion layer (i.e. substrate interactions with the solvent are preferential to interactions with the polymer). The parameter ϕ represents the segment density concentration profile and varies as a function of distance (z) from the substrate, where ϕ_s represents the segment density at the surface and ϕ_b represents the bulk segment density.

Polymers usually accumulate at the solid substrates and form a permanent layer due to their chain length and flexibility. Different chain segments adopt different conformations. A commonly accepted model for neutral polymer adsorption onto a solid substrate is depicted in Figure 2.19. Only a small number of consecutive chain segments of the polymer chain are directly in contact with the substrate. These segments are called "trains". Other segments protrude into the bulk phase as "loops" or "tails", for internal chain segments and chain ends, respectively. The distribution of different conformations (e.g. "train" vs. "loop") is dependent upon molecular weight, and segment-segment, segment-solvent, and segment-surface interactions.[103-105] These factors influence the physical properties of the adsorbed polymer layer, for instance, polymer concentration profiles and adsorbed amount.[103]

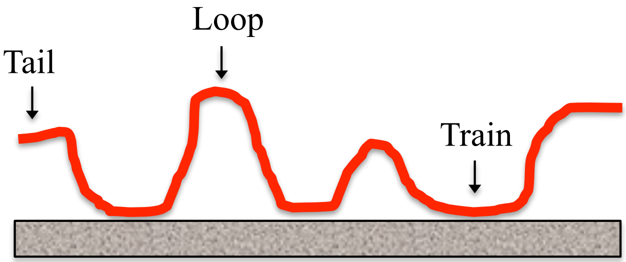

Figure 2.19 Illustration of neutral polymer adsorption onto a flat and homogeneous solid substrate. The "tail," "loop" and "train" conformations of the adsorbing chain are depicted.

Most polymer adsorption studies deal with ideal situations: smooth, flat and homogeneous substrates, long and linear homopolymer chains and simple interactions between monomer units and the substrate as well as between monomer units and the solvent.[106] Even under these simplified conditions, the underlying physical and mathematical considerations for understanding polymer adsorption are still complicated. However, Figure 2.19 serves as a good starting point for understanding more complex treatments of polymer adsorption.

Polymer adsorption has been intensively studied both theoretically and experimentally.[107] In particular, the adsorption of neutral polymers is more advanced and well understood compared to the adsorption of charged polymers (polyelectrolytes). In the past decade, several theoretical models have been proposed to describe neutral polymer adsorption at solid/liquid interfaces. Application of these models to experimental data has improved the overall understanding of polymer adsorption. These methods include not only conformational statistical methods, such as exact numeration, Monte Carlo simulations, and mean field approaches, but also scaling theory. Exact numeration uses a computer algorithm to generate a complete set of conformations for the estimation of various properties of the adsorbed polymer chain.[107] Deficiencies of this approach are limitations of single chain random walks with at least one segment in the surface plane and the absence of solvent effects. Monte Carlo calculations are based upon a sampling scheme, whereby a representative subset of the total number of possible conformations is generated.[108] Mean field approaches have been used to account for interactions of segments separated by great distances along the contour of the chain that still lie in close spatial proximity.[109] Scaling theory treats the interfacial layer in terms of a local concentration and concentration gradients and power laws have been derived for certain regions, including proximal, central and distal regions.[102]

Polymer adsorption from dilute solutions can be understood in terms of single chain adsorption onto the substrates and has been described by both Flory theory (mean-field) and scaling calculations.[110] It has become recognized that the mean field approach is not reliable for adsorbed layers that have fluctuations. For these cases, a completely different scheme, scaling theory, has been applied.[102] Scaling theory is not only precise but also provides improved insight into polymer adsorption. In order to gain adsorption energy, a chain should increase the number of monomers in contact with the surface by confining itself to a layer of thickness smaller than its unperturbed polymer size as depicted in Figure 2.20. The thickness of the adsorbed layer is defined as the adsorption blob size (ξ_{ads}) and can be expressed as

$$\xi_{ads} \approx \frac{b}{\delta} \quad \textit{ideal chain (theta solvent)} \tag{2.7}$$

$$\xi_{ads} \approx \frac{b}{\delta^{\frac{3}{2}}} \quad \textit{real chain (good solvent)} \tag{2.8}$$

where b is the freely-jointed effective bond length, also known as the Kuhn length. The blob size is strongly dependent upon surface attraction expressed as δ, where δ is the magnitude of the attractive interaction in units of kT, i.e. δkT. For the case of weak adsorption, where $0 < \delta < 1$, a weakly adsorbed and diffuse layer is expected.

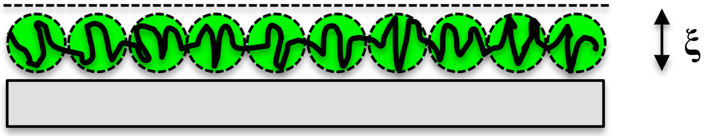

Figure 2.20 A schematic depiction of single chain adsorption where the polymer chain decorrelates into a number of blobs (shown as green circles) within which the chain executes an unperturbed random walk and the chain is confined to a layer on the solid substrate of thickness ξ.

Adsorption is treated as a competition between the attractive potential of the polymer and substrate (enthalpic) and unfavorable conformational restrictions on the adsorbed polymer (entropic).[106] Polymer adsorption onto solid substrates and the resulting chain conformations are closely related to solution conformations. There is also a strong correlation between polymer conformation and solvent quality as depicted in Figure 2.21. The strong dependence of polymer conformation on solvent conditions also suggests an important role for interactions. In a good solvent, polymer-solvent interactions are more favorable than polymer-polymer interactions, resulting in a more expanded conformation than what is expected in a vacuum. The theta state is a condition where polymer-solvent interactions are exactly balanced by the polymer-polymer interactions. In a poor solvent, polymer-solvent interactions are less favorable than polymer-polymer interactions, leading to a more compact and coiled conformation.

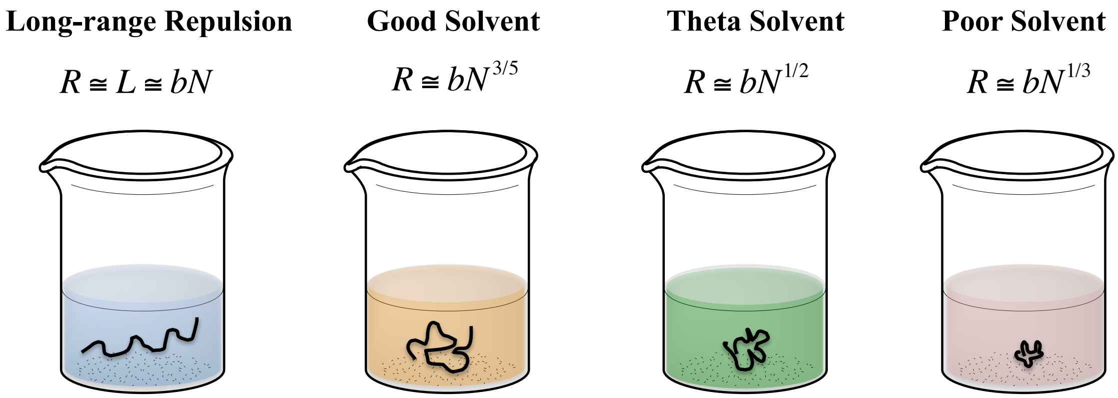

Figure 2.21 Dependence of polymer conformation on solvent quality. Equations provide a description of the polymer conformation in a specific solvent where R is defined as root-mean-square end-to-end distance, b is the Kuhn length, N is the number of monomers and L is the contour length.

In real cases, chains in solution are attracted to the substrate and try to maximize the number of contacts, leading to multichain adsorption onto the substrate. Only chains in the first layer gain adsorption energy due to direct contact with the substrate. On the basis of scaling theory, de Gennes has predicted that long, linear, flexible polymer chains strongly adsorb onto a solid substrate in a good solvent in the semi-dilute concentration regime to form a self-similar diffuse adsorbed layer, also known as the de Gennes self-similar carpet (Figure 2.22).[102, 110] The concentration profile of the adsorbed layer is divided into three distinct regions, including the proximal, central and distal regions as depicted in Figure 2.23. The segment density profile $\phi(z)$ changes with respect to distance z from the substrate. In the proximal region ($a < z < D$ in Figure 2.23), the short-range interactions between monomers and the substrate are important and segment density profiles $\phi(z)$ are assumed to vary slowly with z. In the central region ($D < z < \zeta^b$ in Figure 2.23), the density profile is universal and decays with a power law:

$$\phi(z) = (a/z)^{-4/3} \tag{2.9}$$

where a is the size of a monomer. In the distal regions ($z > \zeta^b$ in Figure 2.23), the excess polymer concentration decays exponentially to its bulk value,

$$\phi(z) - \phi_b \approx 4\phi_b \exp\left(-2z / \zeta^b\right) \tag{2.10}$$

where ϕ_b is the bulk polymer concentration, D is the adsorbed layer width and ζ^b is the bulk correlation length.

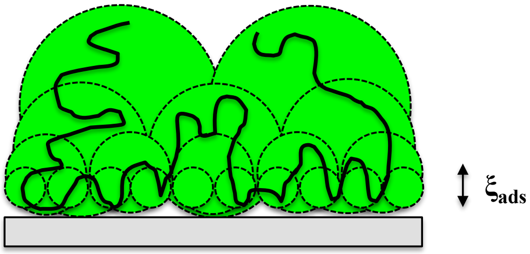

Figure 2.22 A depiction of the de Gennes self-similar carpet for an adsorbed polymer layer in a good solvent.

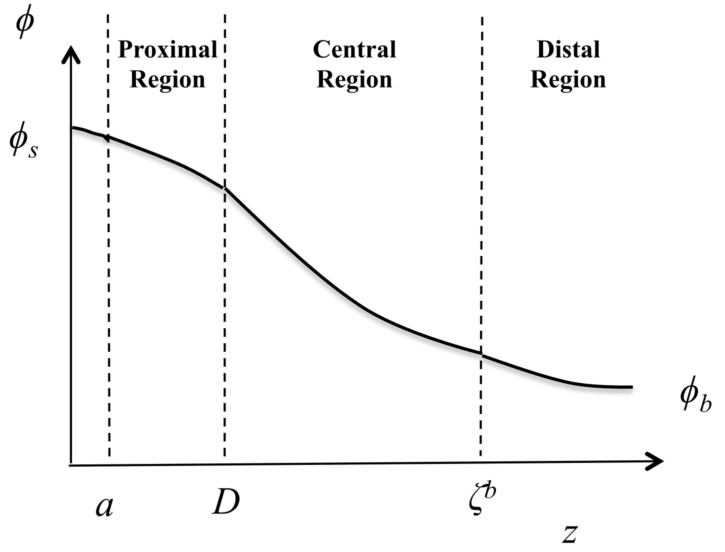

Figure 2.23 The schematic segment density profile $\phi(z)$ for the case of adsorption from a semi-dilute solution. A layer of molecular thickness $z \sim a$ is defined where $\phi(z)$ depends upon the details of the interactions between the substrate and monomer size. Three regions, including a proximal ($a < z < D$), central ($D < z < \zeta^b$) and distal region ($z > \zeta^b$), are labeled on the figure.

Charged polymers, also known as polyelectrolytes, are often used to tailor surface properties by adsorption. Polyelectrolytes are more interesting from the application point of view and have been used in a wide range of industrial and technical situations, such as the biomedical, mining, pharmaceuticals and paper making industries.[106] Polyelectrolytes are synthetic or natural polymers containing multiple charged groups. Representative polyelectrolytes include proteins, nucleic acids and some synthetic polymers, such as polystyrene sulfonate (PSS) and poly(acrylic acid) (PAA).

Polyelectrolyte adsorption onto charged surfaces is an active research area of polymer physics and has been an area of extensive theoretical and experimental studies.[111-113] For theoretical treatments of polyelectrolyte adsorption, four major parameters are considered, including the Flory-Huggins interaction parameter for polymers in solution (χ), adsorption energy parameter (χ_s), surface charge (σ_0) and charge of a polymer segment (q_m).[107] The adsorption of cationic polyelectrolytes onto anionic cellulose surfaces can be largely explained by Scheutjens-Fleer (SF) theory and is strongly dependent upon the charge density of the polyelectrolyte as well as the salt concentration.[114] This result also confirms that the adsorption behavior of the polyelectrolyte is most probably ascribed to a purely electrostatic interaction. Due to the ionic character of polyelectrolytes, their adsorption is strongly affected by salt concentration/ionic strength, charge density of the polyelectrolyte and surface charge density.[115] For low salt concentrations, the Debye length is typically larger than the chain length, resulting in electrostatic repulsion and thus an extended and flat conformation on an oppositely charged substrate. At the other extreme, the Debye length is reduced and the electrostatic repulsions are screened at high salt concentrations. As salt concentration/ionic strength increases, the salt screens the electrostatic interactions, resulting in contraction of an extended polyelectrolyte chain, leading to the formation of coiled structures and thicker adsorbed layers.[116] Besides electrostatic interactions, van der Waals interactions along the polyelectrolyte backbone can also affect polyelectrolyte adsorption.

A common property of polymer adsorption is weak or little desorption into a polymer-free solvent after adsorption has occurred. The reason for the mostly irreversible adsorption is that all chain segments in contact with the surface must be broken by solvent at the same time if desorption is to occur.[117] In a typical experiment, there is a small decrease in the adsorbed amount and the rate of desorption is dependent upon the change in concentration. For polymer adsorption at higher concentrations, desorption is more significant. The reason for this is that each single polymer chain had to compete with other chains for surface sites, thereby forming fewer monomer-surface interactions.

2.6 Surface Analysis Techniques

2.6.1 Quartz Crystal Microbalance with Dissipation Monitoring (QCM-D)

Quartz crystal microbalance with dissipation monitoring (QCM-D) experiments are relatively new and were not widely reported until 1999, even though quartz crystal microbalances (QCM) have existed for half a century.[118] A QCM-D is a surface-sensitive instrument that has been widely used for monitoring film deposition, antigen detection, binding kinetics, cell adhesion and adsorption of surfactants, proteins and polysaccharides at solid/liquid interfaces.[119-122] This technique enables *in situ* adsorption studies by simultaneously measuring changes in frequency and dissipation.[123] Measurements by QCM-D can provide both qualitative and quantitative information for adsorption processes at solid/liquid interfaces. The technique relies upon quartz crystals operating in a thickness shear mode of oscillation, where both surfaces move in parallel but opposite directions.[124] The QCM-D sensor consists of a thin disk shaped AT-cut quartz crystal sandwiched between two gold electrodes. As a result of the piezoelectric nature of the quartz crystal, application of an alternating electric field produces a shear deformation, resulting in oscillation of the crystal at its resonant frequency without any adsorbate. Upon deformation, acoustic waves are generated and propagate through the crystal in a direction that is perpendicular to the surface.[124] After adsorption, there is a decrease in the resonant frequency. When the power is switched off, the decay rate of the oscillation amplitude is monitored as depicted in Figure 2.24,

$$A = A_0 e^{\tau} \sin\left(2\pi f t + \varphi\right) \tag{2.11}$$

where A_0 is the amplitude of the waves, f is the number of cycles per unit time and the phase φ of the waves is the fraction of a wave cycle which has elapsed relative to an arbitrary point. Since the acquisition rate is very high, it is possible to record data from multiple overtones with good signal-to-noise ratios. The characteristic decay length δ is described as

$$\delta = \sqrt{\frac{\eta_l}{\pi f \rho_l}} \tag{2.12}$$

where η_l and ρ_l are the viscosity and density of the bulk liquid, respectively, and f is the number of cycles per time unit.

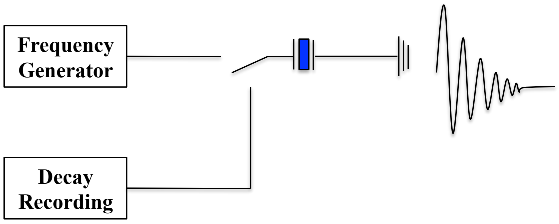

Figure 2.24 A schematic representation of QCM-D data acquisition.

Figure 2.25 shows two general cases frequently observed for QCM-D measurements. If the adsorbate is evenly distributed, rigidly attached, fully elastic and small compared to the mass of the crystal, the Sauerbrey equation can be used to quantify the adsorbed amount by the shift in resonant frequency,[125]

$$\Gamma_{QCM-D} = -C\left(\frac{\Delta f}{n}\right) \tag{2.13}$$

where $\Gamma_{QCM\text{-}D}$ is the adsorbed mass per unit area with units of mg•m^{-2}, C is a crystal specific constant with a value of 0.177 mg•m^{-2}•Hz^{-1} for the 5 MHz crystals used in this dissertation, Δf is the shift in resonant frequency and n is overtone number ($n = 1, 3, 5, 7, 9, 11$ and 13).

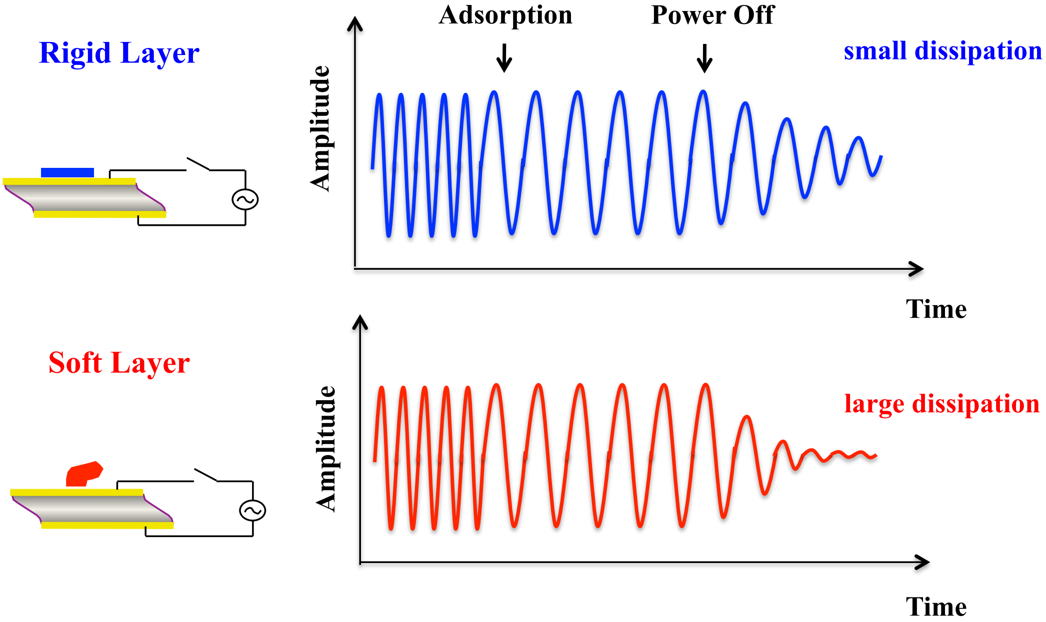

Figure 2.25 Representative depictions of signal decay for QCM-D measurements on a rigidly adsorbed surface layer with small dissipation and a soft, viscoelastic surface layer with large dissipation.

The resonant frequency of the crystal depends upon the total oscillating mass, including coupled water. In Figure 2.25, if the adsorbed layer is not fully elastic, frictional losses occur leading to a damping of the oscillation with a greater amplitude decay rate. The change in the dissipation factor, ΔD, is introduced. The dissipation factor (D) is defined as the ratio between the energy dissipated during one period of oscillation and the energy stored in one period of the oscillating system,[123]

$$D = \frac{E_{dissipated}}{2\pi E_{stored}} \tag{2.14}$$

where $E_{dissipated}$ and E_{stored} are the total energy dissipated and stored during one oscillation cycle, respectively. The energy dissipation factor provides a measure of the rigidity or viscoelasticity of the adsorbed layers.[123] For cases where soft and viscoelastic layers are attached onto the surface, the Sauerbrey equation is not valid and significant deviations from Equation 2.13 are expected. As a result, both frequency and dissipation data are required to obtain viscoelastic properties for the adsorbed layer.[126] The viscoelastic model is based upon the Kelvin-Voigt model and models the viscoelastic behavior as a spring (elastic element) and a dashpot (viscous element) combined in a parallel arrangement.[127] A complex shear modulus (G^*) is used for description of the viscoelastic properties and is defined as

$$G^* = G' + iG'' = \mu + i2\pi f\eta \tag{2.15}$$

where G' is the shear storage modulus, G'' is the shear loss modulus, μ is the elastic shear modulus, f is the oscillation frequency and η is the shear viscosity.

For soft and dissipative layers, quantitative information about the rheological properties and thicknesses can be extracted from the QCM-D response through a continuum Voigt-based viscoelastic model. A schematic depiction of the Voigt-based viscoelastic model is provided in Figure 2.26. The adsorbed viscoelastic layer is characterized by four parameters: density (ρ_f), thickness (h_f), shear viscosity (η_f) and elastic shear modulus (μ_f). The Voigt-based model describes the propagation and the damping of the acoustic waves in a homogeneous viscoelastic layer.

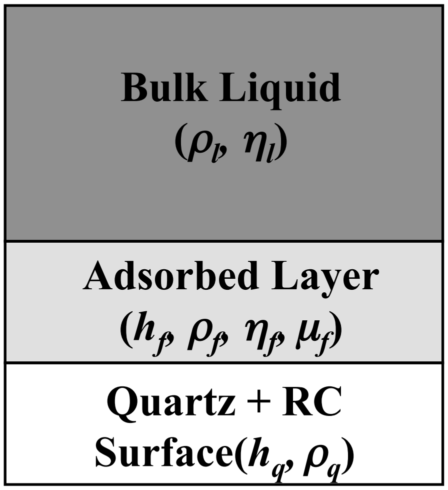

Figure 2.26 A schematic representation of the Voigt-based viscoelastic model for a crystal modified by a cellulose film regenerated from TMSC with a single adsorbed layer in a bulk liquid. The RC layer is treated as an extension of the quartz (larger h_q than the unmodified sensor), whereby all viscoelastic behavior is attributed to the layer adsorbed onto the RC.

Values of Δf and ΔD are dependent upon adsorbed layer parameters (ρ_f, h_f, η_f and μ_f) as well as parameters for quartz crystal (ρ_q and h_q), the bulk liquid (ρ_l and η_l) and overtone (n), and can be theoretically calculated from Equations 2.16 to 2.21.[126]

$$\Delta f = \mathrm{Im}\left(\frac{\beta}{2\pi\rho_q h_q}\right) \tag{2.16}$$

$$\Delta D = -\mathrm{Re}\left(\frac{\beta}{\pi\rho_q h_q}\right) \tag{2.17}$$

where

$$\beta = \xi_1\left(\frac{2\pi f\eta_f - i\mu_f}{2\pi f}\right)\left[\frac{1-\alpha\exp\left(2\xi_1 h_f\right)}{1+\alpha\exp\left(2\xi_1 h_f\right)}\right] \tag{2.18}$$

$$\alpha = \frac{\left(\frac{\xi_1}{\xi_2}\right)\left(\frac{2\pi f\eta_f - i\mu_f}{2\pi f\eta_l}\right)+1}{\left(\frac{\xi_1}{\xi_2}\right)\left(\frac{2\pi f\eta_f - i\mu_f}{2\pi f\eta_l}\right)-1} \tag{2.19}$$

$$\xi_1 = \sqrt{-\frac{\left(2\pi f\right)^2 \rho_f}{\mu_f + i2\pi f\eta_f}} \tag{2.20}$$

$$\xi_2 = \sqrt{i\left(\frac{2\pi f\rho_l}{\eta_l}\right)} \tag{2.21}$$

While many users of QCM-D are interested in the thickness of the adsorbed layer, care must be taken in order to obtain reasonable thickness values. Values of adsorbed layer h_f and ρ_f are not independent variables. In this dissertation, ρ_f was set to a value of 1050 kg□m^{-3} for the estimation of h_f throughout the dissertation. For simplicity, we assumed that ρ_f remained constant throughout the adsorption process and the resulting adsorbed layer was uniform in thickness. Even though h_f and ρ_f are not independent, their product, values of $\Gamma_{QCM\text{-}D}$ are independent of the choice of h_f and ρ_f for reasonable values of both quantities.[128]

2.6.2 Surface Plasmon Resonance (SPR)

Surface plasmon resonance (SPR) is an optical technique for characterizing film thicknesses and monitoring adsorption processes at solid/liquid interfaces. In biological systems, SPR is widely used to obtain real-time information about adsorption and desorption kinetics and thermodynamics.[129] In essence, an SPR instrument is nothing more than a refractometer. As a refractometer, the most fundamental underlying principle behind an SPR instrument is Snell's law. When light reaches a boundary between two media (Figure 2.27), reflection and refraction can occur. The relationship between the angles of incidence and refraction known as Snell's law is,

$$n_1 \sin\theta_1 = n_2 \sin\theta_2 \tag{2.22}$$

where n_1 and n_2 are the refractive indices of medium 1 and medium 2, respectively. Angle θ_1 and θ_2 are angles of incidence and refraction, respectively. When the light travels from an optically dense medium to a medium of lower optical density ($n_1 > n_2$), no transmission occurs and the light is completely reflected above a critical angle. The critical angle (θ_c) is the angle of incidence (θ_1) above which the refracted angle (θ_2) equals 90° and total internal reflection occurs,

$$\sin\theta_c = \frac{n_2}{n_1} \tag{2.23}$$

When one of the two media is a metal, there is also a possibility to excite a surface plasmon for $\theta_1 \geq \theta_c$. A surface plasmon is a charge-density oscillation that exists at the interface of two media with dielectric constants of opposite signs, for instance a metal/glass interface. The phenomenon of a surface plasmon requires the metal to exhibit free electron behavior. Metals capable of supporting a surface plasmon include silver, gold, copper and aluminum. Among all the metals, gold is the one most commonly used as a consequence of high chemical stability.[129]

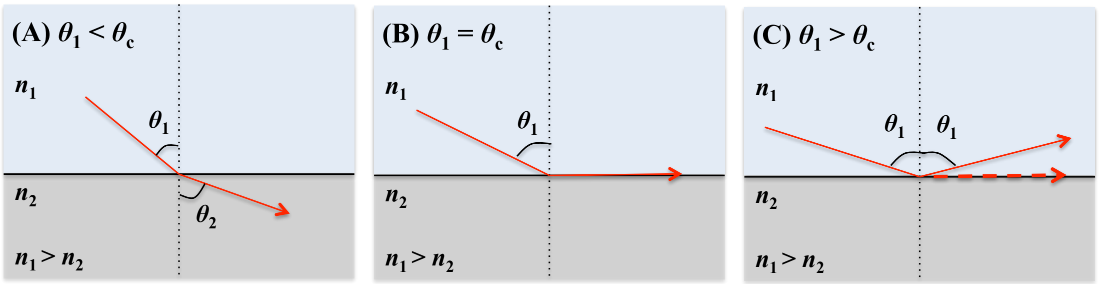

Figure 2.27 Depictions of the reflection and refraction of an incident light for three cases including (A) $\theta_1 < \theta_c$ (B) $\theta_1 = \theta_c$ and (C) $\theta_1 > \theta_c$, where light travels from an optically dense medium to a medium of lower optical density ($n_1 > n_2$). The dashed line in (C) depicts the evanescent wave.

In modern SPR instruments, there are options for the optical design. The Kretschmann prism configuration (Figure 2.28) based upon the principle of total internal reflection is commonly used for SPR measurements. When incident light from a *p*-polarized source travels through the glass slide towards the ambient medium (aqueous solution) at an angle above the critical angle (θ_c), most of the light is reflected to the detector. However, a component of the wave escapes the waveguide boundary and creates an evanescent field. The wave vector for the evanescent wave is given as

$$K_{ev} = \frac{2\pi}{\lambda}\sqrt{\varepsilon_g}\sin\theta \qquad (2.24)$$

where λ is the wavelength of light, ε_g is the dielectric permittivity of the glass prism and θ is the angle of the incident light. The evanescent field can penetrate the interface into the second medium. The wave vector for the surface plasmon is given as,

$$K_{sp} = \frac{2\pi}{\lambda}\sqrt{\frac{\varepsilon_m\varepsilon_a}{\varepsilon_m + \varepsilon_a}} \qquad (2.24)$$

where λ is the wavelength of the light, ε_m is the dielectric permittivity of the metal and ε_a is the dielectric permittivity of the ambient medium. When K_{ev} matches the value of K_{sp}, the light can couple with the oscillating electrons on the gold surface leading to the excitation of a plasmon. This condition occurs at a specific angle of incident light, also known as the SPR angle, which depends upon the refractive index of the ambient conditions. At optical frequencies, the refractive index $n = \sqrt{\varepsilon}$. If the ambient medium is transparent whereby no absorption of light occurs, Equations 2.24 and 2.25 can be rewritten as a function of refractive index,

$$K_{ev} = \frac{2\pi}{\lambda}\sqrt{\frac{n_m^2 n_a^2}{n_m^2 + n_a^2}} \tag{2.26}$$

$$K_{sp} = \frac{2\pi}{\lambda} n_g \sin\theta_{sp} \tag{2.27}$$

where n_m, n_a and n_g refer to the refractive indices of the metal, the surrounding ambient medium and glass, respectively. The SPR angle, where the incident beam is coupled to the surface plasmon, is obtained by equating Equations 2.26 and 2.27.

$$\theta_{sp} = \sin^{-1}\left(\frac{1}{n_g}\sqrt{\frac{n_m^2 n_a^2}{n_m^2 + n_a^2}}\right) \tag{2.28}$$

As resonance occurs at the SPR angle, a minimum in the reflected intensity will be observed. During an adsorption process as depicted in Figure 2.29, solvent molecules (e.g. water, n = 1.33) are replaced with adsorbate molecules with a higher refractive index (e.g. polymer, n = 1.45) leading to an increase in the average refractive index of the ambient medium (n_a). According to Equation 2.28, as the refractive index of the ambient medium increases during adsorption, the SPR angle, where the minimum in the reflected intensity is observed, also increases. In practice, the change in the SPR angle ($\Delta\theta$) was monitored as a function of time (Figure 2.29), and further used for the calculation of the adsorbed amount (Γ_{SPR}). The total change in SPR angle ($\Delta\theta_{tot}$) corresponds to the observed changes in the resonance angle caused by reversible adsorption ($\Delta\theta_{rev}$), irreversible adsorption ($\Delta\theta_{irr}$) and the bulk effect ($\Delta\theta_{bulk}$). On the basis of the equation of de Feijter *et al.*, the change in resonant angle can be used to determine Γ_{SPR},[130]

$$\Gamma_{SPR} = \frac{L\left(n_f - n_s\right)}{dn/dc} = \frac{\Delta\theta_a}{d\theta/dL}\frac{\left(n_f - n_s\right)}{dn/dc} \tag{2.29}$$

where L is the thickness of the adsorbed layer, n_f is the refractive index of the film (or substrate), n_s is the refractive index of the solvent, $\Delta\theta_a$ is the change in the resonant angle caused by the change in refractive index of the ambient medium, $d\theta/dL$ is the change in resonant angle with respect to layer thickness which can be calculated from Fresnel simulations and dn/dc is the refractive index increment measured by a differential refractometer. In this dissertation, irreversible adsorption is measured and $\Delta\theta_a$ is the same as $\Delta\theta_{irr}$. Furthermore, the combination of QCM-D and SPR data and the assumption of an ideal solution have facilitated the determination of water contents of adsorbed layers,

$$\%H_2O = \left(1 - \frac{\Gamma_{SPR}}{\Gamma_{QCM-D}}\right) \times 100\% \tag{2.30}$$

where Γ_{SPR} and Γ_{QCM-D} are surface concentrations obtained from SPR and QCM-D measurements, respectively. Typically, values of Γ_{SPR} and Γ_{QCM-D} are different. The difference represents the fact that the “optical mass” or “dry mass” deduced from SPR is based upon refractive index differences (only sees the polymer), whereas the “acoustic mass” or “wet mass” from QCM-D includes both polymer and coupled water. These measurements allow us to directly correlate chemical structure with water uptake in adsorbed polysaccharide films.

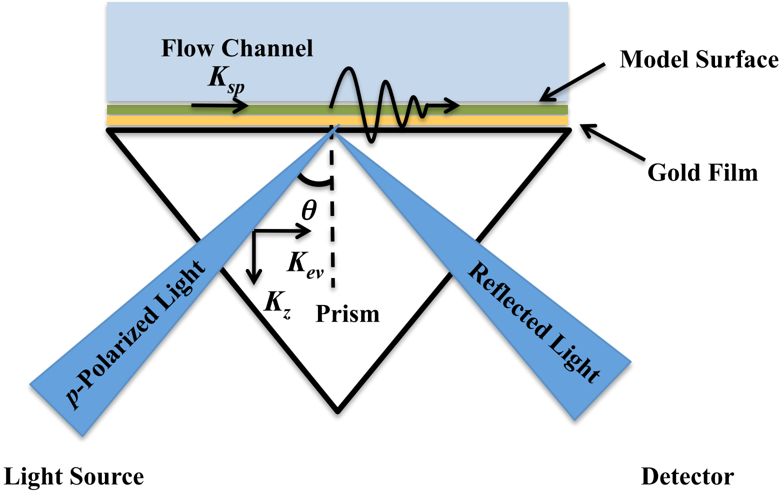

Figure 2.28 A schematic representation of the Kretschmann prism configuration for $\theta_1 \geq \theta_c$.

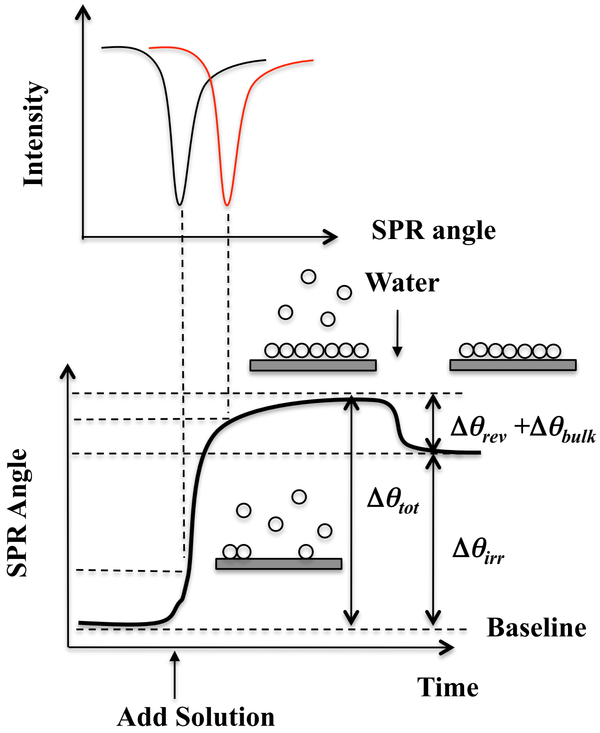

Figure 2.29 A schematic representation of adsorption profiles measured by SPR.

2.6.3 Atomic Force Microscopy (AFM)

Working from an understanding of scanning tunneling microscopy (STM), Binnig and coworkers introduced atomic force microscopy (AFM) for surface imaging through mechanical forces.[131] As an imaging technique, AFM is sensitive and in principle non-destructive with atomic scale resolution. In AFM, the sample is mounted on a piezoelectric scanner that ensures 3D positioning with high resolution. Images obtained from AFM are generated by recording the force changes as a sharp tip scans across the sample surface. The tips are typically mounted on a cantilever made of silicon or silicon nitride by microfabrication techniques. When the tip is brought near a surface, forces existing between tip atoms and surface atoms, typically in the range of 10^{-2} to 10^{-6} N, will cause a deflection of the cantilever as depicted in Figure 2.30. The greater the cantilever deflection, the higher the force experienced by the tip. The deflection is most commonly measured by an optical method in modern instruments. For instance, a laser beam focused on the free end of the cantilever can be used for the measurement. The position of the reflected laser beam (Figure 2.31) is detected with a position-sensitive detector (photodiode array). The photodiode is segmented into four quadrants and a voltage is generated from each quadrant that is proportional to the amount of light hitting it. The deflection signal is defined as the difference between the voltages generated in the top and bottom halves of the detector,

$$Deflection = V_{top} - V_{bottom} = \left(V_A + V_B\right) - \left(V_C + V_D\right) \tag{2.31}$$

where V_A, V_B , V_C and V_D represent voltages generated in each quadrant. Typically, the light source is aligned so the spot hits the center of the photodiode when the cantilever is undeflected (Figure 2.31, gray line). When the cantilever experiences an overall repulsive force, it deflects upward and the spot moves up on the detector (Figure 2.31, blue line). More light hits the top half than the bottom half of the photodiode, so $V_{top} > V_{bottom}$ and the deflection is positive. When the cantilever experiences an overall attractive force, it deflects downward and the spot moves down on the detector (Figure 2.31, orange line). More light hits the bottom than top, so $V_{top} < V_{bottom}$ and the deflection is negative.

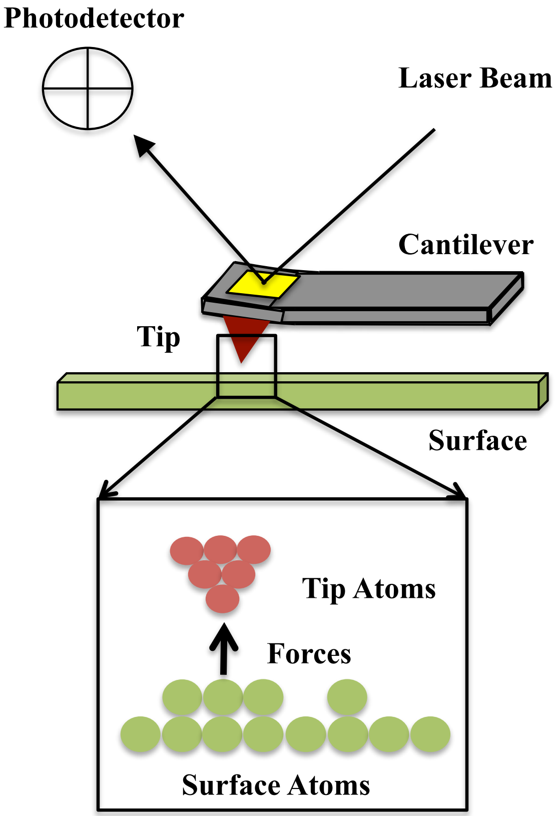

Figure 2.30 A schematic depiction of the key features necessary for AFM imaging.

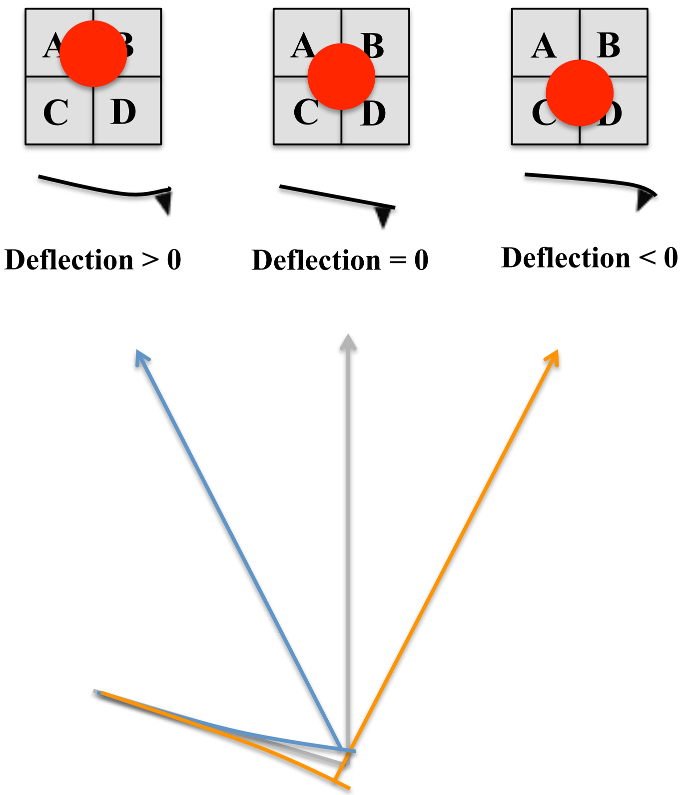

Figure 2.31 A schematic depiction of cantilever deflections as the tip scans across a surface and corresponding spot positions detected on the photodiode. Blue, gray and orange lines represent deflection > 0, deflection = 0 and deflection < 0, respectively.

The AFM can be operated in a number of modes, including tapping mode and contact mode. In tapping mode, the cantilever is driven to oscillate up and down near the resonant frequency and the amplitude and the phase of the cantilever are monitored. The oscillating tip intermittently contacts the sample surface. The intermittent contacts minimize destruction of sample, making tapping mode the most widely used mode for studying polysaccharides and other biomacromolecules.[132] For contact mode, the force between the tip and the surface is held constant during scanning by maintaining a constant deflection. It is also known as constant deflection mode or constant force mode. During scanning, the sample height is adjusted to maintain constant deflection of the cantilever. The surface morphology information can be obtained from the measurement of the tip. Surface morphologies are obtained through the correlation of the height (z) with position (x-y) on the sample.

2.7 References

(1) Tirrell, D. A.; Aksay, I.; Baer, E.; Calvert, P. D.; Cappello, J.; Dimarzio, E. A.; Evans, E. A.; Fessler, J., *National Academy of Sciences, Washington DC* **1994**.

(2) Beck, C. B., *An introduction to plant structure and development: Plant anatomy for the twenty-first century*. Cambridge University Press: 2010.

(3) Fengel, D.; Wegener, G., *Wood: Chemistry, ultrastructure, reactions*. Walter de Gruyter: 1983.

(4) Minic, Z.; Jouanin, L., *Plant Physiology and Biochemistry* **2006,** *44*, 435-449.

(5) Timell, T., *Wood Science and Technology* **1967,** *1*, 45-70.

(6) Emons, A. M. C., *Canadian Journal of Botany* **1989,** *67*, 2401-2408.

(7) Cosgrove, D. J., *Plant Physiology* **2001,** *125*, 131-134.

(8) Keegstra, K.; Talmadge, K. W.; Bauer, W. D.; Albersheim, P., *Plant Physiology* **1973,** *51*, 188-197.

(9) Hayashi, T.; Marsden, M. P. F.; Delmer, D. P., *Plant Physiology* **1987,** *83*, 384-389.

(10) Fry, S. C., *Physiologia Plantarum* **1989,** *75*, 532-536.

(11) Park, Y. B.; Cosgrove, D. J., *Plant Physiology* **2012,** *158*, 1933-1943.

(12) Talbott, L. D.; Ray, P. M., *Plant Physiology* **1992,** *98*, 357-368.

(13) Ha, M. A.; Apperley, D. C.; Jarvis, M. C., *Plant Physiology* **1997,** *115*, 593-598.

(14) Dick-Pérez, M.; Zhang, Y.; Hayes, J.; Salazar, A.; Zabotina, O. A.; Hong, M., *Biochemistry* **2011,** *50*, 989-1000.

(15) Dumitriu, S., *Polysaccharides: Structural diversity and functional versatility*. CRC Press: 2012.

(16) Vorwerk, S.; Somerville, S.; Somerville, C., *Trends in Plant Science* **2004,** *9*, 203-209.

(17) Buckeridge, M. S.; Rayon, C.; Urbanowicz, B.; Tiné, M. A. S.; Carpita, N. C., *Cereal Chemistry* **2004,** *81*, 115-127.

(18) Carpita, N. C.; Defernez, M.; Findlay, K.; Wells, B.; Shoue, D. A.; Catchpole, G.; Wilson, R. H.; McCann, M. C., *Plant Physiology* **2001,** *127*, 551-565.

(19) Payen, A., *Comptes rendus* **1838,** *7*, 1052-1056.

(20) Wegner, T. H.; Jones, E. P., *The nanoscience and technology of renewable biomaterials* **2009,** *1*, 1-41.

(21) Arioli, T.; Peng, L.; Betzner, A. S.; Burn, J.; Wittke, W.; Herth, W.; Camilleri, C.; Höfte, H.; Plazinski, J.; Birch, R.; Cork, A.; Glover, J.; Redmond, J.; Williamson, R. E., *Science* **1998,** *279*, 717-720.

(22) Klemm, D.; Heublein, B.; Fink, H. P.; Bohn, A., *Angew Chem Int Edit* **2005,** *44*, 3358-3393.

(23) Haigler, C. H.; Brown, R. M., Jr., *Protoplasma* **1986,** *134*, 111-120.

(24) Gardner, K. H.; Blackwell, J., *Biopolymers* **1974,** *13*, 1975-2001.

(25) Habibi, Y.; Lucia, L. A.; Rojas, O. J., *Chemical Reviews* **2010,** *110*, 3479-3500.

(26) Atalla, R. H.; Vanderhart, D. L., *Science* **1984,** *223*, 283-285.

(27) Wada, M.; Nishiyama, Y.; Langan, P., *Macromolecules* **2006,** *39*, 2947-2952.

(28) Wada, M.; Okano, T.; Sugiyama, J., *Cellulose* **1997,** *4*, 221-232.

(29) Nishiyama, Y.; Langan, P.; Chanzy, H., *Journal of the American Chemical Society* **2002,** *124*, 9074-9082.

(30) Nishiyama, Y.; Sugiyama, J.; Chanzy, H.; Langan, P., *Journal of the American Chemical Society* **2003,** *125*, 14300-14306.

(31) Heinze, T.; Schwikal, K.; Barthel, S., *Macromolecular bioscience* **2005,** *5*, 520-525.

(32) Zhu, S.; Wu, Y.; Chen, Q.; Yu, Z.; Wang, C.; Jin, S.; Ding, Y.; Wu, G., *Green Chemistry* **2006,** *8*, 325-327.

(33) Fox, S. C.; Li, B.; Xu, D.; Edgar, K. J., *Biomacromolecules* **2011,** *12*, 1956-1972.

(34) Appendini, P.; Hotchkiss, J. H., *Innovative Food Science & Emerging Technologies* **2002,** *3*, 113-126.

(35) Taggart, T. E.; Schellhamer, A. J.; Schuster, M. A. Papermaking using cationic starch and carboxymethyl cellulose or its additionally substituted derivatives. 1991.

(36) Black, H., *Analytical Chemistry* **1951,** *23*, 1792-1795.

(37) Tammelin, T.; Paananen, A.; Österberg, M., *The nanoscience and technology of renewable biomaterials* Wiley Publishing Inc: 2009.

(38) Thompson, J. E.; Fry, S. C., *Planta* **2000,** *211*, 275-286.

(39) Lopez, M.; Bizot, H.; Chambat, G.; Marais, M.-F.; Zykwinska, A.; Ralet, M.-C.; Driguez, H.; Buléon, A., *Biomacromolecules* **2010,** *11*, 1417-1428.

(40) McDougall, G. J.; Fry, S. C., *Plant Physiology* **1989,** *89*, 883-887.

(41) Lima, D. U.; Loh, W.; Buckeridge, M. S., *Plant Physiology and Biochemistry* **2004,** *42*, 389-394.

(42) Zhou, Q.; Rutland, M.; Teeri, T.; Brumer, H., *Cellulose* **2007,** *14*, 625-641.

(43) Hantus, S.; Pauly, M.; Darvill, A. G.; Albersheim, P.; York, W. S., *Carbohydrate Research* **1997,** *304*, 11-20.

(44) York, W. S.; Harvey, L. K.; Guillen, R.; Alberhseim, P.; Darvill, A. G., *Carbohydrate Research* **1993,** *248*, 285-301.

(45) Picard, C.; Gruza, J.; Derouet, C.; Renard, C. M. G. C.; Mazeau, K.; Koca, J.; Imberty, A.; Hervé du Penhoat, C., *Biopolymers* **2000,** *54*, 11-26.

(46) de Vries, R. P.; Visser, J., *Microbiology and Molecular Biology Reviews* **2001,** *65*, 497-522.

(47) Marry, M.; Cavalier, D. M.; Schnurr, J. K.; Netland, J.; Yang, Z.; Pezeshk, V.; York, W. S.; Pauly, M.; White, A. R., *Carbohyd Polym* **2003,** *51*, 347-356.

(48) Vincken, J. P.; de Keizer, A.; Beldman, G.; Voragen, A., *Plant Physiology* **1995,** *108*, 1579-1585.

(49) Shankaracharya, N. B., *Journal of food science and technology* **1998,** *35*, 193-208.

(50) Coviello, T.; Matricardi, P.; Marianecci, C.; Alhaique, F., *Journal of Controlled Release* **2007,** *119*, 5-24.

(51) Burke, D.; Kaufman, P.; McNeil, M.; Albersheim, P., *Plant Physiology* **1974,** *54*, 109-115.

(52) Wood, P. J., *Trends in Food Science & Technology* **2004,** *15*, 313-320.

(53) Hu, G.; Burton, C., *Cereal Chemistry* **2008,** *85*, 648-653.

(54) Bacic, A.; Harris, P. J.; Stone, B. A., *The biochemistry of plants* **1988,** *14*, 297-371.

(55) Lazaridou, A.; Biliaderis, C.; Micha-Screttas, M.; Steele, B., *Food Hydrocolloids* **2004,** *18*, 837-855.

(56) Gómez, C.; Navarro, A.; Manzanares, P.; Horta, A.; Carbonell, J. V., *Carbohyd Polym* **1997,** *32*, 17-22.

(57) Roubroeks, J. P.; Mastromauro, D. I.; Andersson, R.; Christensen, B. E.; Åman, P., *Biomacromolecules* **2000,** *1*, 584-591.

(58) Carpita, N. C., *Annual Review of Plant Biology* **1996,** *47*, 445-476.

(59) Izydorczyk, M. S.; Dexter, J. E., *Food Research International* **2008,** *41*, 850-868.

(60) Vogel, J., *Current Opinion in Plant Biology* **2008,** *11*, 301-307.

(61) Caffall, K. H.; Mohnen, D., *Carbohydrate Research* **2009,** *344*, 1879-1900.

(62) Thibault, J. F.; Rinaudo, M., *Biopolymers* **1986,** *25*, 455-468.

(63) Ralet, M. C.; Crépeau, M. J.; Buchholt, H. C.; Thibault, J. F., *Biochemical Engineering Journal* **2003,** *16*, 191-201.

(64) Abdel-Massih, R. M.; Baydoun, E. A. H.; Brett, C. T., *Planta* **2003,** *216*, 502-511.

(65) de Vries, J. A.; Rombouts, F. M.; Voragen, A. G. J.; Pilnik, W., *Carbohyd Polym* **1982,** *2*, 25-33.

(66) Boerjan, W.; Ralph, J.; Baucher, M., *Annual Review of Plant Biology* **2003,** *54*, 519-546.

(67) Ralph, J.; Lundquist, K.; Brunow, G.; Lu, F.; Kim, H.; Schatz, P.; Marita, J.; Hatfield, R.; Ralph, S.; Christensen, J.; Boerjan, W., *Phytochemistry Reviews* **2004,** *3*, 29-60.

(68) Fergus, B. J.; Procter, A. R.; Scott, J. A. N.; Goring, D. A. I., *Wood Science and Technology* **1969,** *3*, 117-138.

(69) Müsel, G.; Schindler, T.; Bergfeld, R.; Ruel, K.; Jacquet, G.; Lapierre, C.; Speth, V.; Schopfer, P., *Planta* **1997,** *201*, 146-159.

(70) Kringstad, K. P.; Lindström, K., *Environmental Science & Technology* **1984,** *18*, 236-248.

(71) Tammelin, T.; Saarinen, T.; Österberg, M.; Laine, J., *Cellulose* **2006,** *13*, 519-535.

(72) Roman, M., *Model Cellulosic Surfaces*. American Chemical Society: 2009.

(73) Schaub, M.; Wenz, G.; Wegner, G.; Stein, A.; Klemm, D., *Advanced Materials* **1993,** *5*, 919-922.

(74) Heinze, T.; Liebert, T., *Prog Polym Sci* **2001,** *26*, 1689-1762.

(75) Greber, G.; Paschinger, O., *Papier* **1981,** *35*, 547-554.

(76) Gunnars, S.; Wågberg, L.; Stuart, M. A. C., *Cellulose* **2002,** *9*, 239-249.

(77) Kontturi, E.; Tammelin, T.; Österberg, M., *Chem Soc Rev* **2006,** *35*, 1287-1304.

(78) Rutland, M. W.; Carambassis, A.; Willing, G. A.; Neuman, R. D., *Colloids and Surfaces A: Physicochemical and Engineering Aspects* **1997,** *123–124*, 369-374.

(79) Kontturi, E.; Thüne, P. C.; Niemantsverdriet, J. W., *Langmuir* **2003,** *19*, 5735-5741.

(80) Luner, P.; Sandell, M., *Journal of Polymer Science Part C: Polymer Symposia* **1969,** *28*, 115-142.

(81) Kaya, A.; Du, X. S.; Liu, Z. L.; Lu, J. W.; Morris, J. R.; Glasser, W. G.; Heinze, T.; Esker, A. R., *Biomacromolecules* **2009,** *10*, 2451-2459.

(82) Kontturi, E.; Suchy, M.; Penttilä, P.; Jean, B.; Pirkkalainen, K.; Torkkeli, M.; Serimaa, R., *Biomacromolecules* **2011,** *12*, 770-777.

(83) Aulin, C.; Ahola, S.; Josefsson, P.; Nishino, T.; Hirose, Y.; Österberg, M.; Wågberg, L., *Langmuir* **2009,** *25*, 7675-7685.

(84) Ränby, B., *Discussions of the Faraday Society* **1951,** *11*, 158-164.

(85) Jiang, F.; Esker, A. R.; Roman, M., *Langmuir* **2010,** *26*, 17919-17925.

(86) Araki, J.; Wada, M.; Kuga, S.; Okano, T., *Colloids and Surfaces A: Physicochemical and Engineering Aspects* **1998,** *142*, 75-82.

(87) Edgar, C. D.; Gray, D. G., *Cellulose* **2003,** *10*, 299-306.

(88) Hansen, N.; Plackett, D., *Biomacromolecules* **2008,** *9*, 1493-1505.

(89) de Kerchove, A. J.; Elimelech, M., *Biomacromolecules* **2006,** *8*, 113-121.

(90) Micic, M.; Radotic, K.; Benitez, I.; Ruano, M.; Jeremic, M.; Moy, V.; Mabrouki, M.; Leblanc, R. M., *Biophysical Chemistry* **2001,** *94*, 257-263.

(91) Constantino, C. J. L.; Juliani, L. P.; Botaro, V. R.; Balogh, D. T.; Pereira, M. R.; Ticianelli, E. A.; Curvelo, A. A. S.; Oliveira Jr, O. N., *Thin Solid Films* **1996,** *284-285*, 191-194.

(92) Notley, S. M.; Norgren, M., *Biomacromolecules* **2008,** *9*, 2081-2086.

(93) Wang, C.; Qian, C.; Roman, M.; Glasser, W. G.; Esker, A. R., *Biomacromolecules* **2013,** *14*, 3964-3972.

(94) Wegner, T.; Skog, K. E.; Ince, P. J.; Michler, C. J., *Journal of Forestry* **2010,** *108*, 165-173.

(95) Atalla, R.; Beecher, J.; Caron, R.; Catchmark, J.; Deng, Y.; Glasser, W.; Gray, D.; Haigler, C.; Jones, P.; Joyce, M., Nanotechnology for the forest products industry: Vision and technology roadmap. In USDA Forest Service: 2005.

(96) Stone, B. A.; Svensson, B.; Collins, M. E.; Rastall, R. A., Polysaccharide degradation. In *Glycoscience*, Springer Berlin Heidelberg: 2008.

(97) Mosier, N.; Wyman, C.; Dale, B.; Elander, R.; Lee, Y. Y.; Holtzapple, M.; Ladisch, M., *Bioresource Technology* **2005,** *96*, 673-686.

(98) Pingali, S. V.; Urban, V. S.; Heller, W. T.; McGaughey, J.; O'Neill, H.; Foston, M.; Myles, D. A.; Ragauskas, A.; Evans, B. R., *Biomacromolecules* **2010,** *11*, 2329-2335.

(99) Dashtban, M.; Schraft, H.; Qin, W., *International Journal of Biological Sciences* **2009,** *5*, 578-595.

(100) Reynaud, E.; Jouen, T.; Gauthier, C.; Vigier, G.; Varlet, J., *Polymer* **2001,** *42*, 8759-8768.

(101) Butt, H.-J.; Graf, K.; Kappl, M., *Physics and chemistry of interfaces*. John Wiley & Sons: 2006.

(102) de Gennes, P. G., *Macromolecules* **1981,** *14*, 1637-1644.

(103) de Gennes, P. G., *Advances in Colloid and Interface Science* **1987,** *27*, 189-209.

(104) Stuart, M. A. C.; Fleer, G. J.; Lyklema, J.; Norde, W.; Scheutjens, J. M. H. M., *Advances in Colloid and Interface Science* **1991,** *34*, 477-535.

(105) Scheutjens, J. M. H. M.; Fleer, G. J., *The Journal of Physical Chemistry* **1980,** *84*, 178-190.

(106) Netz, R. R.; Andelman, D., *Physics Reports* **2003,** *380*, 1-95.

(107) Fleer, G. J.; Cohen Stuart, M. A. S.; M., J. M. H.; Cosgrove, T. V.; Vincent, B., *Polymers at interfaces*. Chapman & Hall, London: 1993.

(108) Eisenriegler, E.; Kremer, K.; Binder, K., *The Journal of Chemical Physics* **1982,** *77*, 6296-6320.

(109) Scheutjens, J. M. H. M.; Fleer, G. J., *The Journal of Physical Chemistry* **1979,** *83*, 1619-1635.

(110) Rubinstein, M.; Colby, R. H., *Polymer physics*. OUP Oxford: 2003.

(111) Decher, G.; Hong, J. D.; Schmitt, J., *Thin Solid Films* **1992,** *210–211, Part 2*, 831-835.

(112) Muthukumar, M., *The Journal of Chemical Physics* **1987,** *86*, 7230-7235.

(113) Dobrynin, A. V.; Deshkovski, A.; Rubinstein, M., *Physical Review Letters* **2000,** *84*, 3101-3104.

(114) Wågberg, L., *Nordic Pulp and Paper Research Journal* **2000,** *15*, 586-597.

(115) Shubin, V., *J Colloid Interf Sci* **1997,** *191*, 372-377.

(116) Volk, N.; Vollmer, D.; Schmidt, M.; Oppermann, W.; Huber, K., Conformation and phase diagrams of flexible polyelectrolytes. In *Polyelectrolytes with Defined Molecular Architecture II*, Schmidt, M., Ed. Springer Berlin Heidelberg: 2004; Vol. 166, pp 29-65.

(117) Andrade, J. D., *Surface and interfacial aspects of biomedical polymers*. Plenum Press New York: 1985; Vol. 2.

(118) O'Sullivan, C. K.; Guilbault, G. G., *Biosensors and Bioelectronics* **1999,** *14*, 663-670.

(119) Etchenique, R.; Brudny, V. L., *Langmuir* **2000,** *16*, 5064-5071.

(120) Ayela, C.; Roquet, F.; Valera, L.; Granier, C.; Nicu, L.; Pugnière, M., *Biosensors and Bioelectronics* **2007,** *22*, 3113-3119.

(121) Richter, R.; Mukhopadhyay, A.; Brisson, A., *Biophysical journal* **2003,** *85*, 3035-3047.

(122) Cooper, M. A.; Singleton, V. T., *Journal of Molecular Recognition* **2007,** *20*, 154-184.

(123) Rodahl, M.; Kasemo, B., *Rev Sci Instrum* **1996,** *67*, 3238-3241.

(124) Ferreira, G. N. M.; da-Silva, A.-C.; Tomé, B., *Trends in Biotechnology* **2009,** *27*, 689-697.

(125) Sauerbrey, G., *Z. Phys* **1959,** *155*, 206-222.

(126) Voinova, M.; Rodahl, M.; Jonson, M.; Kasemo, B., *Physica Scripta* **1999,** *59*, 391-396.

(127) Malkin, A. Y.; Isayev, A. I., *Rheology - Concepts, Methods, and Applications*. ChemTec Publishing: 2006.

(128) Malmström, J.; Agheli, H.; Kingshott, P.; Sutherland, D. S., *Langmuir* **2007,** *23*, 9760-9768.

(129) Green, R. J.; Frazier, R. A.; Shakesheff, K. M.; Davies, M. C.; Roberts, C. J.; Tendler, S. J. B., *Biomaterials* **2000,** *21*, 1823-1835.

(130) de Feijter, J. A.; Benjamins, J.; Veer, F. A., *Biopolymers* **1978,** *17*, 1759-1772.

(131) Binnig, G.; Quate, C. F.; Gerber, C., *Phys Rev Lett* **1986,** *56*, 930-933.

(132) Wu, J.; Deng, X.; Zhang, Y.; Wang, L.; Tian, B.-q.; Xie, B.-j., *Agricultural Sciences in China* **2009,** *8*, 1458-1465.

Chapter 3: Materials and Experimental Techniques

3.1 Materials

3.1.1 Trimethylsilyl Cellulose (TMSC) and Nanocrystalline Cellulose (NC)

Trimethylsilyl cellulose (TMSC, degree of substitution = 2.71) was synthesized homogenously by reacting microcrystalline cellulose (Acivel pH101) with hexamethyldisilazane, using chlorotrimethylsilane as a catalyst for 24 h at 100 °C as previously described.[1] Cellulose nanocrystals was prepared by sulfuric acid hydrolysis of dissolving grade softwood pulp (Temalfa 93-A-A, Tembec Inc.).[2] The charge density of the NC was 0.340 mequiv•g^{-1} as determined by conductometric titration.

3.1.2 Carboxymethyl Cellulose (CMC)

Sodium salts of carboxymethyl cellulose (CMC) were purchased from Sigma-Aldrich and used without further purification. The four sodium CMC samples used in Chapter 4 were denoted as CMC-x-y, where x represented the degree of substitution (DS) and y represented the weight average degree of polymerization (DP). Specific samples were CMC-1.2-965 (419281, weight average molar mass M_w = 250 kDa), CMC-0.9-1064 (419303, M_w = 250 kDa), CMC-0.7-1143 (419311, M_w = 250 kDa) and CMC-0.7-412 (419273, M_w = 90 kDa). Weight average molar masses were determined by size exclusion chromatography (SEC). The DS values were determined by conductometric titration.[3] The first three samples were used for studying DS effects on CMC adsorption and the last two samples were used for studying DP effects on CMC adsorption.

3.1.3 Pectins and Polygalacturonic Acid (PGA)

The polygalacturonic acid (PGA) sample (P-PGACT, galacturonic acid content ≥ 95.0%) prepared from citrus pectin by partial depolymerization and demethylation, was purchased from Megazyme Inc. and used as received. Pectin samples extracted from citrus fruits were purchased from Sigma-Aldrich, including pectin (P9135, galacturonic acid content ≥ 74.0%), low DE pectin (P9311, degree of esterification 20-34%) and high DE pectin (P9436, degree of esterification 55-70%). Weight average molar masses were determined by SEC.

3.1.4 Mixed Linkage Glucans (MLGs)

Mixed linkage glucans (MLGs) from barley (P-BGBM) and lichen (P-LICHN) were purchased from Megazyme, Ireland. According to the supplier, lichen MLG showed a higher proportion of β-(1→3) to β-(1→4) linkages compared to that of barley MLG, and the ratio of β-(1→4) to β-(1→3) linkages was approximately 2:1. Weight average molar masses were determined by SEC.

3.1.5 Other Hemicelluloses

Xyloglucan (Megazyme, P-XYGLN) was extracted from tamarind seeds and had a molar mass of 202 kDa. High degree of polymerization (DP) xyloglucan oligosaccharide (Megazyme, O-XGHDP) with a molar mass of 3 to 4 kDa was produced by exhaustive hydrolysis of tamarind seed xyloglucan with *endo*-cellulase followed by β-galactosidase. Xyloglucan heptasaccharide (Megazyme, O-X3G4) with a molar mass of 1063 Da was prepared by controlled enzymatic hydrolysis of xyloglucan. Glucuronoarabinoxylan (GAX) from spruce was a generous gift from Prof. Paul Gatenholm from Chalmers University of Technology in Sweden.[4] Arabinoxylan (P-WAXYL) extracted from wheat flour with low viscosity and arabinan (P-ARAB) from sugar beet were also purchased from Megazyme. Weight average molar masses were determined by SEC.

3.1.6 Enzymes: Pectinase and Lichenase

Pectinase from *Aspergillus niger* was purchased from Sigma-Aldrich (P4716) as an aqueous glycerol solution with 20 $U \bullet mg^{-1}$ protein. One unit (1 U) is defined to liberate 1.0 μmol of galacturonic acid from polygalacturonic acid per min at pH 4.0 at 25 °C. Lichenase from *Bacillus subtilis* (E-LICHN) in a 3.2 M ammonium sulfate solution was purchased from Megazyme with a concentration of 273 $U \bullet mg^{-1}$. One unit (1 U) of enzyme activity is defined as the enzyme that releases 1 $\mu mol \bullet mL^{-1} \bullet min^{-1}$ glucose under standard assay conditions (pH = 6.5 and 40 °C).

3.1.7 Other Materials

Calcium chloride dihydrate was purchased from Sigma-Aldrich (223506, ACS reagent, ≥ 99%) and used as received. Citric phosphate buffer was prepared using sodium phosphate dibasic (Sigma-Aldrich, S9390, ACS reagent, 98.0%-102.0%) and citric acid (Sigma-Aldrich, 251275, ACS reagent, ≥ 99.5%). The final concentration of the buffer was 50 mM and the pH was adjusted to 5.0 using sodium hydroxide (Spectrum, S1295, ACS reagent, ≥ 97%). Sodium acetate buffer was prepared using sodium acetate trihydrate (Sigma-Aldrich, S8625, ACS reagent, ≥ 99%) and acetic acid (EMD, AX0073-6, ACS reagent, 99.7%, LOT# 45067). The final concentration and pH were adjusted accordingly. Sodium phosphate buffer was prepared using sodium phosphate dibasic heptahydrate and sodium phosphate monobasic monohydrate (Sigma-Aldrich, S9638, ACS reagent, 98.0-102.0%). The final concentration and pH were adjusted accordingly. Sulfuric acid (98%) and ammonium hydroxide (30% w/w) were purchased from Fisher Scientific. Toluene (HPLC-grade) was purchased from EMD. Hydrogen peroxide (30% w/w) was purchased from EM Science. Amine-terminated self-assembled monolayers

(SAMs) were prepared from 11-amino-1-undecanethiol (SAM-NH_2) purchased from VWR International. Ultrapure water (Milli-Q Gradient A-10, Milli-Q, 18.2 MΩ•cm, < 5 ppb organic impurities) was used in all experiments. Nitrogen with ultrahigh purity (NI-UHP300, Airgas) was used for the cleaning and drying of the substrate. Gold sensors (QSX-301) were purchased from Q-sense. The gold sensors were 14 mm in diameter with a 0.3 mm quartz thickness. The quartz was plated with a chromium layer (~ 2 nm), followed by a gold layer (~ 100 nm). Gold SPR slides (13206060) were purchased from Reichert. The slides were 12 mm × 12 mm glass substrates (~ 1 mm) coated with a chromium layer (~ 2 nm), followed by a gold layer (~ 50 nm). All glassware was cleaned by immersion into a 5 L base bath (4:1 isopropanol to water, 300 g KOH) for at least 24 hours and then rinsed with deionized water, followed by a rinse with ultrapure water and overnight oven drying at 110 °C.

3.2 Preparation of Cellulose Model Surfaces

3.2.1 Substrate Cleaning

Substrates were first cleaned with a UV/ozone ProCleaner (Bioforce Nanoscience Inc.) for 20 min and boiled in a mixture of ammonium hydroxide, hydrogen peroxide and water (1:1:5 v/v/v) for 20 min. Substrates for SPR measurements were further cleaned by immersion into a piranha solution which consisted of a mixture of hydrogen peroxide:sulfuric acid (3:7 v/v) for 20 min. Both QCM-D and SPR substrates were rinsed exhaustively with ultrapure water and dried with ultrapure nitrogen prior to spincoating.

3.2.2 Self-Assembled Monolayers (SAMs)

Self-assembled monolayers were prepared by immersing cleaned gold substrates into a 1 mM solution of 11-amino-1-undecanethiol in ethanol for 24 h. Then the substrates were rinsed with ethanol twice and dried with ultrapure nitrogen.

3.2.3 Regenerated Cellulose (RC) Surfaces

Regenerated cellulose (RC) surfaces were prepared on QCM-D and SPR sensors. Solutions of TMSC (10 $g \bullet L^{-1}$ in toluene) were spincoated onto cleaned sensors at 2000 rpm for 1 min. The TMSC solutions were prepared by dissolution of 0.1 g of TMSC powder in 10 mL of toluene and subsequent filtering with a PTFE filter (pore size = 0.45 μm). Trimethylsilyl groups were removed by exposure of the coated surfaces to the vapor of a 10% (w/w) aqueous solution of hydrochloric acid for 5 min, yielding a smooth RC film with nominal thicknesses of ~10 nm and root-mean-square (RMS) roughnesses of ~ 1 nm. Previous studies of RC films via attenuated total reflectance infrared spectroscopy[5] and grazing incidence X-ray diffraction[6] showed spincoated RC layers were largely amorphous.

3.2.4 Nanocrystalline Cellulose (NC) Surfaces

Gold substrates with amine-terminated SAMs were prepared as described in Chapter 3.2.2. Nanocrystalline cellulose (NC) surfaces were prepared by spincoating 1% (w/w) aqueous suspensions of cellulose nanocrystals at 4000 rpm for 1 min. Films were subsequently placed in an oven at 70 °C overnight. Previous studies via powder X-ray diffraction and small incident angle X-ray diffraction confirmed that the cellulose in NC films had a cellulose I crystal structure.[7, 8]

3.2.5 Avicel Cellulose Surfaces

Microcrystalline cellulose (Avicel-pH101) was first dissolved in a binary solvent system, consisting of N-methylmorpholine-N-oxide (NMMO) and dimethyl sulfoxide (DMSO).[9] Then the solution was spincoated onto pretreated silicon wafers, followed by regeneration via ultrapure water. Previous studies of Avicel surfaces based upon X-ray diffraction and atomic force microscopy determined that Avicel cellulose surfaces have a cellulose II crystal structure.[8, 9]

3.3 Experimental Techniques

3.3.1 Ellipsometry

Ellipsometry measurements were conducted with an ellipsometer (Picometer Ellipsometer, Beaglehole Instruments, New Zealand) equipped with a laser light source with a single wavelength of 633 nm. The film thickness was modeled with TFCompanion software (Semiconsoft) assuming a refractive index of 1.51 for cellulose model surfaces.[5] Three different spots on the same substrate were measured before the adsorption measurements by QCM-D and SPR and reported thickness values indicate an average film thickness ± one standard deviation.

3.3.2 Differential Refractometer

Refractive index increments *dn/dc* of sample solutions were determined by a differential refractometer (Optilab rEX, Wyatt technology Corp.). The experiments were carried out at λ = 780 nm over the desired concentration ranges. Values of *dn/dc* for specific sample solutions were determined through the instrumental software from the slope of a plot of refractive index versus concentration.

3.3.3 Atomic Force Microscopy (AFM)

Surfaces to be examined were dried in a vacuum oven overnight before being imaged with an Asylum Research AFM (MFP-3D-BIO, Asylum Research). The microscope collected height images in tapping mode with a silicon tip (OMCL-AC160TS, Olympus Corp.) under ambient conditions. The reported RMS roughnesses were determined from 2 μm x 2 μm scan areas.

3.3.4 Quartz Crystal Microbalance with Dissipation Monitoring (QCM-D)

An E4 system (Q-Sense AB) was used for all the QCM-D measurements. For adsorption studies, gold or RC-coated QCM-D sensors were placed in the flow cells and mounted on the working station. Ultrapure water was introduced into the flow cells for equilibration at a flow rate of 0.200 $mL{\bullet}min^{-1}$ for at least 20 min. Once stable baselines were established for water or a specific solution condition, sample solution was flowed over the substrate and changes in scaled frequency ($\Delta f/n$) and dissipation (ΔD) from different overtones (n) were monitored simultaneously. After a plateau or a saturation of the substrate was obtained, ultrapure water was pumped through the system for the removal of reversibly bound molecules. All measurements were performed under a continuous flow rate of 0.200 $mL{\bullet}min^{-1}$ in triplicate and the averages ± one standard deviation were calculated. For QCM-D data analysis, the change in mass per unit area, $\Gamma_{QCM\text{-}D}$, also known as surface concentration or surface excess, was calculated through the Sauerbrey equation[10] or Voigt-based viscoelastic modeling[11] (Figure 3.1) depending upon the viscoelastic character of the adsorbed layers.

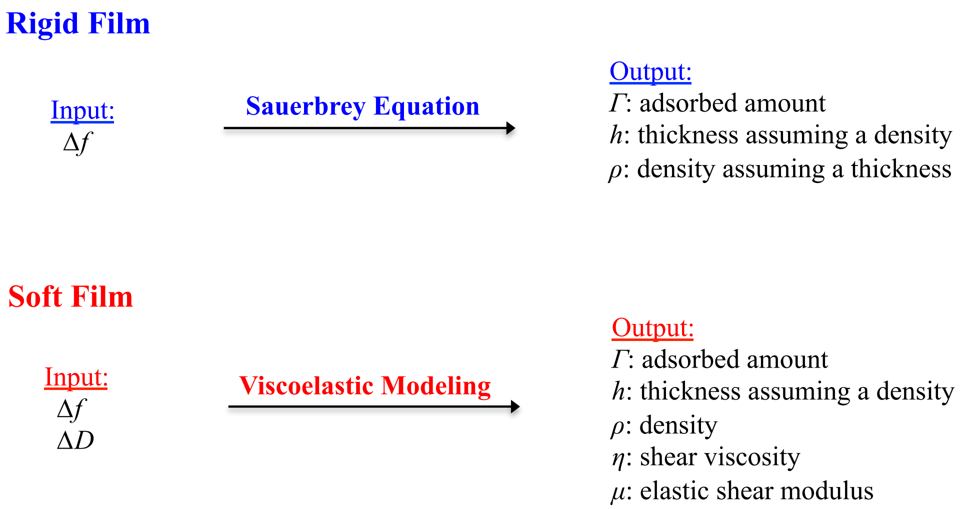

Figure 3.1 Methods used for the quantification of QCM-D raw data for rigid and soft films.

For degradation studies, surface layers were first prepared following the adsorption procedures of this section followed by exposure to a specific buffer solution based upon enzyme activity. Then fresh enzyme solution was introduced into the flow cell at the same temperature and flow rate as the buffer solution. Specific degradation modes (batch mode or continuous flow) were chosen based upon the enzyme-substrate interactions. After an appropriate degradation time, buffer solution was pumped through the system for the removal of reversibly bound molecules and degradation products from the substrate. Values of $\Delta f/n$ and ΔD from different overtones were monitored simultaneously. All measurements were performed in triplicate and averages ± one standard deviation were calculated.

Analysis of QCM-D Data

When the adsorbed layer was evenly distributed, rigidly attached, fully elastic and small compared to the mass of the crystal, the Sauerbrey equation could be used to quantify the adsorbed amount through $\Delta f/n$,[10]

$$\Gamma_{QCM-D} = -C\left(\frac{\Delta f}{n}\right) \tag{3.1}$$

where Γ_{QCM-D}, the adsorbed amount per unit area had units of mg•m^{-2} and C was a crystal specific constant with a value of 0.177 mg•m^{-2}•Hz^{-1} for the 5 MHz crystals used in this dissertation. Values of $\Delta f/n$ and ΔD for n = 1, 3, 5, 7, 9, 11 and 13 were measured simultaneously. Typically, data from the fifth overtone were chosen as representative data for adsorption profiles provided in this dissertation as well as the calculation of the adsorbed amounts using Equation 3.1.

If the adsorbed layer was not fully elastic, frictional losses occurred that led to additional damping of the oscillation amplitude. For cases where soft and viscoelastic layers were attached onto the surface, the Sauerbrey equation was not valid and significant deviations from Equation 3.1 were expected. As a result, both frequency and dissipation data were required to obtain viscoelastic parameters for the adsorbed layers.[11] For soft and dissipative layers, quantitative information about the rheological properties and thicknesses were extracted from the QCM-D response through a continuum Voigt-based viscoelastic model. The Voigt-based model described the propagation and the damping of the acoustic waves in a homogeneous viscoelastic layer. As shown in Figure 3.2, the Voigt-based viscoelastic model assumed that the RC layer was an extension of the purely elastic quartz crystal and the surrounding solution was a purely viscous, semi-infinite Newtonian fluid. The adsorbed layer was treated as a viscoelastic layer that was in contact with the quartz crystal plus RC surface and the bulk liquid under no-slip boundary conditions.[12]

The quartz crystal plus the RC film were assumed to be purely elastic (density ρ_q = 2650 kg•m^{-3} and h_q = 3 ×10^{-4} m) and the surrounding bulk liquid was assumed to be purely viscous. The density (ρ_l) and viscosity (η_l) of the liquid were 998 kg•m^{-3} and 1.00 ×10^{-3} N•s•m^{-2}, respectively, at 20.0 °C.[13] The adsorbed viscoelastic layer was characterized by four parameters: density (ρ_f), thickness (h_f), shear viscosity (η_f) and elastic shear modulus (μ_f). Constraints on the viscoelastic parameters for the modeling are summarized in Table 3.1. Values of h_f and ρ_f of the adsorbed layer were not independent variables and ρ_f was set to 1050 kg•m^{-3} for the estimation of h_f throughout the dissertation. For simplicity, we assumed that ρ_f remained constant throughout the adsorption process and the resulting adsorbed layer was uniform in thickness. However, the adsorbed amount $\Gamma_{QCM\text{-}D}$ was conserved for different solutions over the relevant density interval.[14]

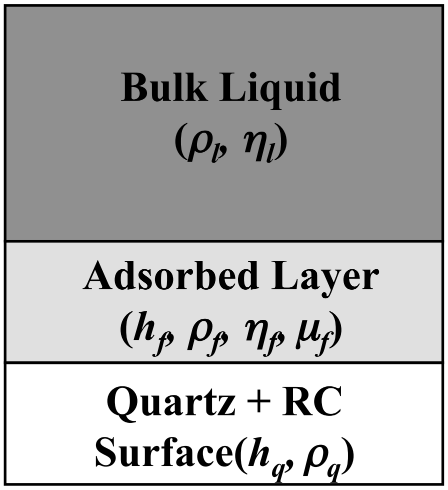

Figure 3.2 A schematic representation of the Voigt-based viscoelastic model. The RC layer was treated as an extension of the purely elastic quartz crystal and the adsorbed layer was treated as a viscoelastic layer that was sandwiched between the RC coated quartz crystal and the bulk liquid.

Table 3.1 Constraints for the viscoelastic parameters used in the Voigt-based modeling.

	Minimum Value	**Maximum Value**
η_f /N•s•m^{-2}	5×10^{-4}	1×10^{-2}
μ_f /N•m^{-2}	1×10^{4}	1×10^{6}
h_f /m	1×10^{-10}	1×10^{-5}

Adsorption curves for the viscoelastic layer from n = 3, 5, 7, 9, 11 and 13 were fit with a Voigt-based viscoelastic model for the estimation h_f, η_f and μ_f using the software package QTools 3.0.5 (Q-Sense) as outlined in Figure 3.3. Values of ρ_l, η_l and ρ_f were fixed and then initial estimate for fitting h_f, η_f and μ_f were provided. As values of $\Delta f/n$ and ΔD depend upon these parameters, the software varied values of ρ_f, h_f, η_f and μ_f to calculate f/n and D for different n. The calculated values were compared to the experimental values until a best fit was obtained. The goodness of fit criterion was a χ^2 value defined as

$$\chi^2 = \sum_i \left(\frac{Y_{theory,i} - Y_{meas,i}}{\sigma_i} \right)^2 \tag{3.2}$$

$Y_{theory,i}$ was the calculated value based upon the viscoelastic modeling, $Y_{meas,i}$ was the experimental value from QCM-D and σ_i was the standard deviation for each data point. Typically the best fit had the lowest χ^2 value which was around 10^5-10^6.[15] Surface concentrations (Γ_{QCM-D}), including the mass of biomacromolecules and coupled water, were obtained from

$$\Gamma_{QCM-D} = h_f \rho_f \tag{3.3}$$

Different overtone combinations were used to find the best fits and to examine how values of h_f, η_f and μ_f depended upon the frequency range used for the modeling. Better fitting was usually obtained when more overtones were included.

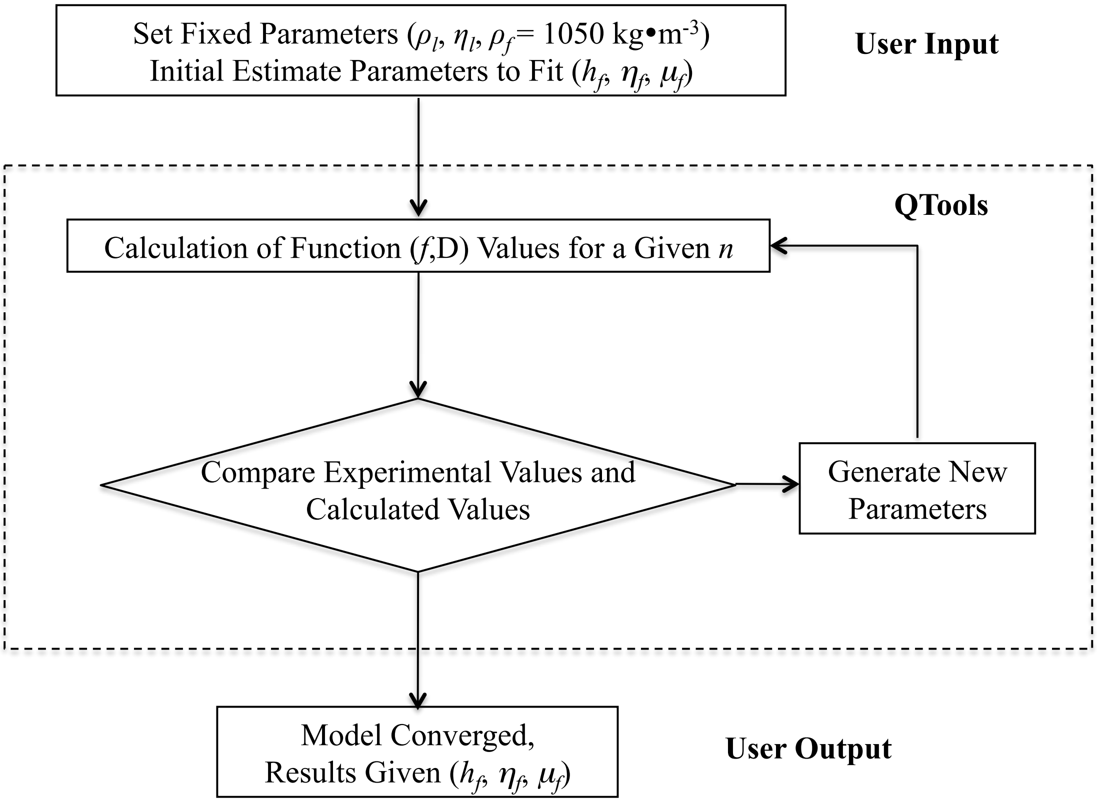

Figure 3.3 A flow chart representation of the Voigt-based viscoelastic modeling.

3.3.5 Surface Plasmon Resonance (SPR)

The gold or RC-coated SPR sensors were placed on the prism and refractive index-matched to the prism of the refractometer with immersion oil (n_D = 1.5150). The flow cell body was equipped with a Viton gasket (DuPont Dow Elastomers, LLC) and mounted on top of the sensor slide. All of the aqueous solutions were degassed before use to avoid the introduction of air bubbles into the system. First water was flowed over the sensor at a flow rate of 0.20 mL•min^{-1} for at least 1 hour via a cartridge pump

(Masterflex). The pump was linked to a switch valve that allowed switching between sample solutions. After a stable water baseline (initial water baseline) was obtained, sample solution was introduced into the system via the switch valve until a plateau was observed. The adsorption time was the same as the QCM-D measurements. The adsorption step was then followed by a rinse with ultrapure water for the removal of reversibly adsorbed molecules until a constant value was obtained. Each SPR experiment was performed in triplicate and values provided in this thesis are average values ± one standard deviation. In practice, changes in the SPR angle ($\Delta\theta$) were monitored as a function of time, and used for the subsequent calculation of the adsorbed mass per unit area (Γ_{SPR}).

Analysis of SPR Data

In practice, refractive index changes in the vicinity of the gold substrate were detected through $\Delta\theta$. A schematic depiction of SPR data is provided in Figure 3.4. The SPR angle corresponds to the incident angle at which reflected light intensity is at a minimum and was further used for the calculation of the adsorbed mass. The total change in SPR angle ($\Delta\theta_{tot}$) corresponded to the observed changes in the resonance angle caused by reversible adsorption ($\Delta\theta_{rev}$), irreversible adsorption ($\Delta\theta_{irr}$) and the bulk effect ($\Delta\theta_{bulk}$). The adsorbed amount obtained by SPR, Γ_{SPR}, was calculated from different values of $\Delta\theta$ with the equation of de Feijter *et al.*[16]

$$\Gamma_{SPR} = \frac{L\left(n_f - n_s\right)}{dn/dc} = \frac{\Delta\theta}{d\theta/dL}\frac{\left(n_f - n_s\right)}{dn/dc} \tag{3.4}$$

where L was the thickness of the film, n_f was the refractive index of the film, n_s was the refractive index of solvent and *dn/dc* was the refractive index increment of sample solution determined independently as described in Chapter 3.3.2. Values of Γ_{SPR} were calculated from $\Delta\theta_{irr}$, which also depended upon the thickness of the adsorbed film through $d\theta/dL$. Values of $d\theta/dL$ were deduced from theoretical Fresnel calculations with a computer simulation program.[17] Values for each parameter used in the de Feijter equation are summarized in Table 3.2. For the data in this dissertation, values of Γ_{SPR} were calculated from $\Delta\theta_{irr}$, which corresponds to the difference between the initial water base line and the final value in water.

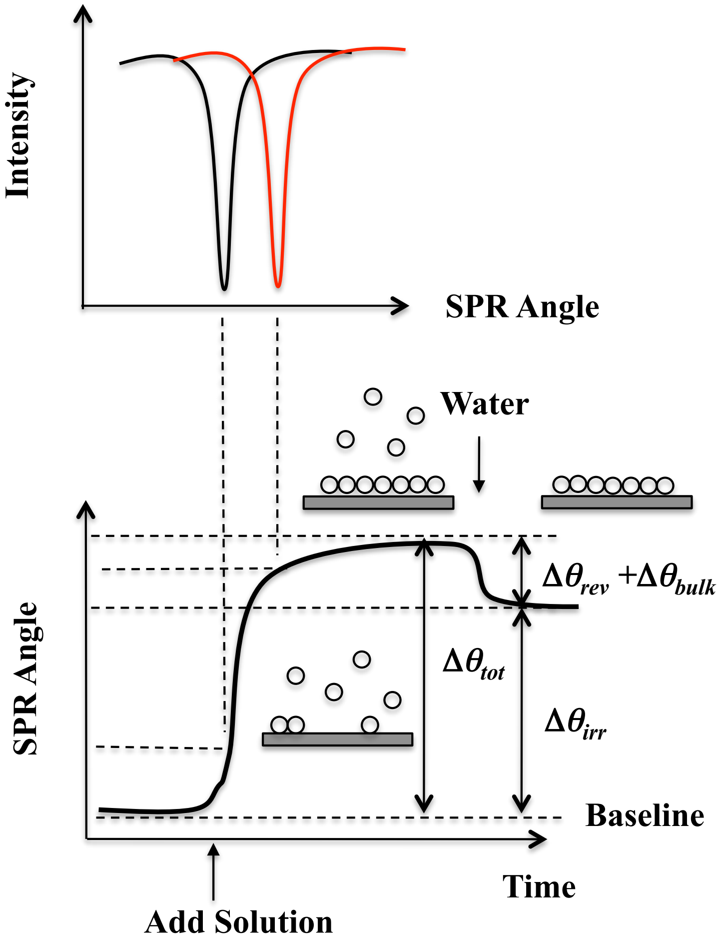

Figure 3.4 A schematic depiction of SPR data for the case where water was used to establish a baseline.

Table 3.2 Values for the parameters used in the equation of de Feijter *et al.* to convert measured SPR data into Γ_{SPR}.

Parameter	**Value**
$d\theta/dL$	4.3×10^{-3} deg•Å^{-1} (cellulose)^{5} and 4.3×10^{-3} deg•Å^{-1} (Au)^{5}
n_f	1.45^{5}
n_s	1.33 (water)^{18}
dn/dc	determined by differential refractometer

3.4 References

(1) Heinze, T.; Liebert, T., *Prog Polym Sci* **2001,** *26*, 1689-1762.

(2) Jiang, F.; Esker, A. R.; Roman, M., *Langmuir* **2010,** *26*, 17919-17925.

(3) Eyler, R. W.; Klug, E. D.; Diephuis, F., *Analytical Chemistry* **1947,** *19*, 24-27.

(4) Escalante, A.; Goncalves, A.; Bodin, A.; Stepan, A.; Sandstrom, C.; Toriz, G.; Gatenholm, P., *Carbohyd Polym* **2012,** *87*, 2381-2387.

(5) Kaya, A.; Du, X. S.; Liu, Z. L.; Lu, J. W.; Morris, J. R.; Glasser, W. G.; Heinze, T.; Esker, A. R., *Biomacromolecules* **2009,** *10*, 2451-2459.

(6) Kontturi, E.; Suchy, M.; Penttilä, P.; Jean, B.; Pirkkalainen, K.; Torkkeli, M.; Serimaa, R., *Biomacromolecules* **2011,** *12*, 770-777.

(7) Edgar, C. D.; Gray, D. G., *Cellulose* **2003,** *10*, 299-306.

(8) Aulin, C.; Ahola, S.; Josefsson, P.; Nishino, T.; Hirose, Y.; Österberg, M.; Wågberg, L., *Langmuir* **2009,** *25*, 7675-7685.

(9) Gunnars, S.; Wågberg, L.; Stuart, M. A. C., *Cellulose* **2002,** *9*, 239-249.

(10) Sauerbrey, G., *Z. Phys* **1959,** *155*, 206-222.

(11) Voinova, M.; Rodahl, M.; Jonson, M.; Kasemo, B., *Physica Scripta* **1999,** *59*, 391-396.

(12) Liu, Z.; Choi, H.; Gatenholm, P.; Esker, A. R., *Langmuir* **2011,** *27*, 8718-8728.

(13) Keslin, J., *J. Phys. Chem. Ref. Data* **1978,** *7*, 941-948.

(14) Malmström, J.; Agheli, H.; Kingshott, P.; Sutherland, D. S., *Langmuir* **2007,** *23*, 9760-9768.

(15) Eisele, N. B.; Andersson, F. I.; Frey, S.; Richter, R. P., *Biomacromolecules* **2012,** *13*, 2322-2332.

(16) de Feijter, J. A.; Benjamins, J.; Veer, F. A., *Biopolymers* **1978,** *17*, 1759-1772.

(17) Tulpar, A.; Ducker, W. A., *The Journal of Physical Chemistry B* **2004,** *108*, 1667-1676.

(18) Harvey, A. H.; Gallagher, J. S.; Levelt Sengers, J., *Journal of Physical and Chemical Reference Data* **1998,** *27*, 761-774.

Chapter 4: Adsorption of Hemicelluloses and Carboxymethyl Cellulose onto Cellulose Surfaces

4.1 Abstract

Hemicelluloses, the second most abundant plant materials after cellulose, play an important role in the food and paper industries. Elucidating the interactions between cellulose and hemicelluloses is of great technological significance and importance for understanding plant cell wall assembly. The adsorption of a xyloglucan, a major type of hemicellulose in dicot plants, onto different cellulose surfaces was studied by a quartz crystal microbalance with dissipation monitoring (QCM-D) and surface plasmon resonance (SPR). Three different cellulose surfaces, including nanocrystalline cellulose (NC), Avicel cellulose and cellulose regenerated (RC) from trimethylsilyl cellulose (TMSC), were used in this study. One of the key findings was that the adsorbed amounts of xyloglucan correlated with the morphology and the surface area of the cellulose substrates and increased in the order of RC < NC < Avicel. Xyloglucan oligosaccharide and heptasaccharide adsorption onto cellulose were also studied. Even the structural unit of xyloglucan, xyloglucan heptasaccharide (XXXG), showed affinity towards RC surfaces, confirming the existence of strong cellulose-xyloglucan interactions. This study highlighted that the binding capacity of cellulose for xyloglucan increased with increasing xyloglucan molar mass. Interfacial behavior of a representative cellulose derivative, carboxymethyl cellulose (CMC), was also examined using QCM-D and SPR. Unlike xyloglucan that adsorbed onto RC surfaces with relatively rigid conformation, CMC formed a hydrated and dissipative layer with a water content > 90%. A Voigt-based viscoelastic model was used for the estimation of thicknesses and adsorbed amounts of

the adsorbed CMC layer. The introduction of Ca^{2+} significantly promoted adsorption as well as the stability of CMC on RC surfaces. Effects of ionic strength, degree of substitution (DS) and degree of polymerization (DP) on CMC adsorption were investigated. The adsorbed amount increased with increasing ionic strength, decreasing DS and increasing DP.

4.2 Introduction

Hemicelluloses are the second most abundant plant materials after cellulose, representing about 20 to 30% of the dry mass of the plant.[1] Understanding interactions between hemicelluloses and cellulose is essential for understanding plant cell wall assembly, and designing sustainable composites from these materials.

Xyloglucans are most abundant in the primary cell walls of dicots and are composed of β-(1→4)-glucose backbones with side branches of xylose at the *C*6 positions that may further be substituted with galactose and fucose units. A major structural unit of a xyloglucan is a heptasaccharide (XXXG) consisting of seven sugar units as shown in Figure 4.1. Unlike cellulose chains that can self-associate to form microfibrils, self-association of xyloglucan is hindered by the presence of side branches. Xyloglucans are known to interact with cellulose via hydrogen bonding and prevent cellulose aggregation into even larger complexes, thereby enabling the formation of a strong but flexible network.[2] Although interactions between xyloglucans and cellulose have been extensively studied, the binding of xyloglucan oligosaccharides onto cellulose is not fully understood. The effect of molar mass on cellulose-xyloglucan interactions has been an active subject in several *in vitro* studies. The existence and size of a minimum backbone length for xyloglucan binding to cellulose have long been controversial topics.

Valent and coworkers demonstrated that xyloglucan oligosaccharides did not bind to cellulose from aqueous solutions using radiolabeled xyloglucan oligosaccharides for equilibrium binding studies.[3] Previous studies by Hayashi using binding assays showed that at least five consecutive glucose units were required for binding onto cellulose, while Lopez and coworkers using isothermal titration calorimetry (ITC) determined that a minimum of 12 glucose residues was required.[4, 5] On the basis of previous results, cellulose-xyloglucan interactions included both hydrogen bonding and hydrophobic interactions.[5, 6] The nature of the binding was clearly demonstrated by the presence of exothermic (hydrogen bonding) and endothermic (hydrophobic interactions) processes measured by ITC.[5] Despite numerous studies on cellulose-xyloglucan interactions, the real mechanism involved in xyloglucan binding remains unclear and a challenge that needs to be addressed. Binding of xyloglucan oligosaccharides onto cellulose is of great help for a complete understanding on the binding of xyloglucan to cellulose.

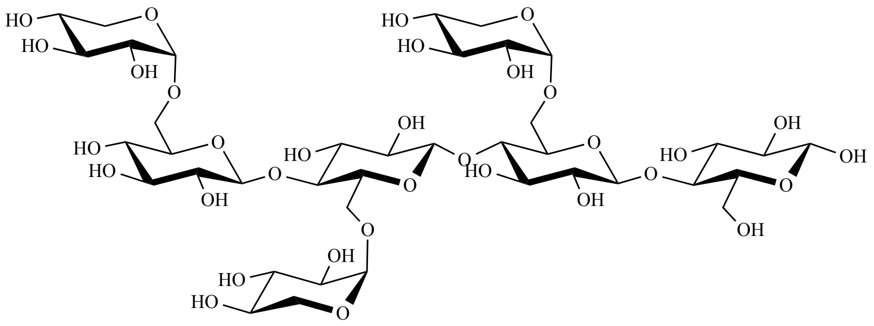

Figure 4.1 Molecular structure of xyloglucan heptasaccharide (XXXG) as a structural unit of xyloglucan. Xyloglucan heptasaccharide consists of 4 glucose and 3 xylose units.

Carboxymethyl cellulose (CMC, Figure 4.2) is a cellulose derivative of significant industrial importance and has been widely used in food, textile, mining, pulp and paper applications.[7] As a material, CMC is one of the world's largest produced polymers and can be prepared in a homogeneous reaction by treating alkali cellulose with sodium monochloroacetate ($ClCH_2COONa$) in a nitrogen atmosphere.[8] The carboxymethyl groups at the *C*6 positions of CMC make this polysaccharide anionic at appropriate pH. The degrees of substitution (DS) and polymerization (DP) are the most important characteristics of CMC. The DS is defined as the average number of carboxymethyl groups per anhydroglucose unit (AGU). Theoretically, the maximum DS value is 3 with all three hydroxyl groups substituted by carboxymethyl groups. However, reactions at the *C*6 and *C*2 positions are preferred. For commercially available CMC, DS values normally range from 0.5 to 1.5.[9] Samples of CMC with different DS can be obtained by varying the amount of sodium monochloroacetate added to the cellulose. The DS of CMC influences aqueous solubility as well as adsorption at solid/liquid interfaces. Higher DS affords better aqueous CMC solubility. The DP of CMC is commonly controlled by adding different amounts of hydrogen peroxide to a CMC sample. The hydrogen peroxide leads to random cleavage of the cellulose backbone.

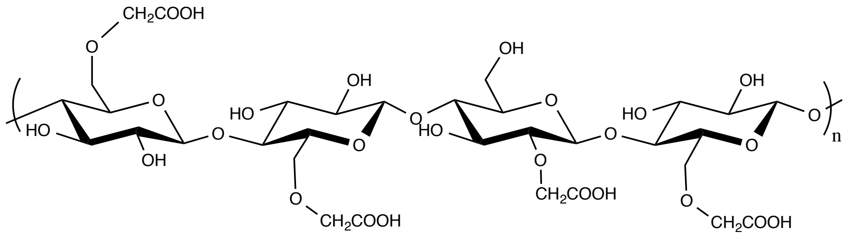

Figure 4.2 Representative molecular structure of CMC. For the specific structure shown here, the DS is 1.0 and the DP is 4n.

For solid/liquid interfaces, CMC adsorption has been widely studied using electrophoretic mobility measurements, Fourier transform infrared (FTIR) spectroscopy, fluorescence spectroscopy, atomic force microscopy (AFM), molecular modeling and electron paramagnetic resonance (EPR).[7, 10, 11] As a cellulose derivative, CMC is water-soluble and behaves like a polyelectrolyte. CMC is negatively charged in aqueous solution due to the presence of carboxymethyl groups (pK_a = 4.5). Adsorption of CMC onto inorganic and organic surfaces has been studied systematically.[12] Several mechanisms have been proposed for CMC adsorption, including a combination of electrostatic interactions and hydrogen bonding[10] and a chemical complexation mechanism[7] via the carboxyl groups. On the basis of previous studies, adsorption behavior of CMC onto slightly anionic surfaces can largely be explained by the screening of electrostatic repulsions.[13] As a result, CMC adsorption behavior is highly dependent upon ionic strength. Changes in ionic strength will alter the intra- and intermolecular interactions, leading to different adsorption behavior. As CMC adsorption behavior at solid/liquid interfaces has many industrial applications, it is still an active area of research.

In this chapter, interactions between xyloglucan and different cellulose surfaces were studied using QCM-D and SPR. Xyloglucan oligosaccharide adsorption onto RC substrates was studied for a better understanding of molar mass effects on cellulose-xyloglucan interactions and for the elucidation of the underlying mechanism of xyloglucan adsorption onto cellulose. The adsorption behavior and layer properties of CMC were quantified by QCM-D and SPR. Systematic studies on the effects of DS, DP and ionic strength on CMC adsorption onto RC surfaces were performed and quantified through a Voigt-based viscoelastic model.

4.3 Experimental

4.3.1 Materials

Preparation of different cellulose surfaces, including NC, Avicel and RC surfaces, were outlined in Chapter 3.2. Ellipsometry and atomic force microscopy (AFM) were used for the characterization of cellulose surfaces as described in Chapters 3.3.1 and 3.3.3, respectively. Hemicelluloses used in this study are commercially available and summarized in Table 4.1. Hemicellulose solutions were prepared by dissolving the materials in ultrapure water with a concentration of 500 mg•L^{-1}.

Table 4.1 Summary of xyloglucan, xyloglucan oligosaccharide and xyloglucan heptasaccharide samples used in this study.[a]

	Supplier	**Source**	**[a]Molar Mass /kDa**
Xyloglucan	Megazyme	Tamarind Seeds	202
Xyloglucan Oligosaccharide	Megazyme	Tamarind Seeds	3 to 4
Xyloglucan Heptasaccharide	Megazyme	Tamarind Seeds	1.063

a.Weight average molar mass.

Four commercially available CMC samples with different DS and DP were used in this chapter and are summarized in Table 4.2. The CMC samples used without further purification, were denoted as CMC-x-y, where x is the DS and y is the weight average DP. Solutions of CMC were prepared by dissolving in ultrapure water or aqueous $CaCl_2$ solutions (5 mM or 10 mM) with an initial concentration of 500 mg•L^{-1}.

Table 4.2 Four commercially available CMC samples from Sigma-Aldrich.[a]

	CMC-1.2-965	**CMC-0.9-1064**	**CMC-0.7-1143**	**CMC-0.7-412**
Supplier	Sigma-Aldrich	Sigma-Aldrich	Sigma-Aldrich	Sigma-Aldrich
[a]Molar Mass	250 kDa	250 kDa	250 kDa	90 kDa
DS	1.15-1.45	0.80-0.95	0.65-0.90	0.65-0.90
DP	965	1064	1143	412

a.Weight average molar mass.

4.3.2 QCM-D Measurements

Cellulose-coated sensor crystals were used as substrates for all QCM-D measurements in this chapter. The adsorption of xyloglucan onto NC, Avicel and RC surfaces was studied by adsorbing xyloglucan with a concentration of 500 mg•L^{-1} from water. The adsorption process proceeded until a plateau in the adsorption profile was obtained. Dynamic adsorption isotherms were obtained in a sequential fashion with a series of concentrations: 10, 25, 50, 100, 250, 500 and 1000 mg•L^{-1}. Adsorption times of 20 min were used for each concentration. Detailed procedures for QCM-D measurements are provided in Chapter 3.3.4. Procedures for CMC adsorption from $CaCl_2$ solution were slightly different from the one used for xyloglucan or CMC adsorption from water. Water was first introduced into the flow cells for at least 1 h until a flat baseline (initial water baseline) was obtained. Then $CaCl_2$ solution was introduced into the flow cells, and subsequently CMC sample dissolved in $CaCl_2$ with the same ionic strength was introduced. Finally, $CaCl_2$ and water were sequentially pumped through the flow cells to establish a final water baseline. Adsorption times of 30 min were used for all CMC experiments. All measurements were performed on triplicate under a continuous flow rate of 0.200 mL•min^{-1} at 20.0 °C in triplicate and averages ± one standard deviation were calculated.

Details for viscoelastic modeling are provided in Chapter 3.3.4. Adsorption profiles for CMC adsorption from multiple overtones were fit using a Voigt-based viscoelastic model employing the software package QTools 3.0.5 (Q-Sense). According to the Voigt-based viscoelastic model, the cellulose layer was treated as an extension of the quartz and the CMC layer was in contact with the bulk liquid under no-slip boundary conditions. Values of density (ρ_f) of the adsorbed CMC layer were set to 1050 kg•m^{-3} for the estimation of thickness (h_f). For simplicity, we assumed that ρ_f remained constant throughout the adsorption process and that the resulting adsorbed layer was uniform in thickness.

4.3.3 SPR Measurements

Detailed procedures for SPR measurements were outlined in Chapter 3.3.5. Water was introduced into the SPR flow cell at a rate of 0.20 mL•min^{-1} at 20.0 °C for at least 1 h until a stable baseline was obtained. After a 10 min water baseline (initial water baseline), sample solution (xyloglucan, xyloglucan oligosaccharide, xyloglucan heptasaccharide or CMC) was introduced into the flow cell at the same flow rate and temperature as water. Adsorption was allowed to proceed for the same amount of time as QCM-D measurements. Finally, water was introduced into the flow cell in order to allow desorption of reversibly adsorbed molecules until a final water baseline was obtained. Adsorption isotherms were performed in a sequential fashion using the same concentrations and same adsorption times as QCM-D measurements. All measurements were performed under a continuous flow rate of 0.20 mL•min^{-1} at 20.0 °C in triplicate and the averages ± one standard deviation were calculated. Refractive index increments were determined by a differential refractometer as described in Chapter 3.3.2 and summarized in Table 4.3.

Table 4.3 Refractive index increments (*dn/dc*) of all xyloglucan and CMC samples used in this study.

Sample	Solution Condition	*dn/dc* /mL•g^{-1}
Xyloglucan Heptasaccharide	H_2O	0.1357 ± 0.0003
Xyloglucan Oligosaccharide	H_2O	0.1422 ± 0.0006
Xyloglucan	H_2O	0.1391 ± 0.0003
CMC-1.2-965	5 mM $CaCl_2$	0.145 ± 0.003
	10 mM $CaCl_2$	0.142 ± 0.006
CMC-0.9-1064	5 mM $CaCl_2$	0.147 ± 0.002
	10 mM $CaCl_2$	0.137 ± 0.003
CMC-0.7-1143	5 mM $CaCl_2$	0.148 ± 0.003
	10 mM $CaCl_2$	0.143 ± 0.002
CMC-0.7-412	5 mM $CaCl_2$	0.144 ± 0.006
	10 mM $CaCl_2$	0.142 ± 0.004

4.4 Results and Discussion

4.4.1 Xyloglucan Adsorption onto Cellulose Surfaces

Xyloglucan adsorption from aqueous solutions onto different cellulose surfaces, including NC, Avicel and RC, was investigated by QCM-D and SPR. On the basis of previous studies, the adsorption process should be sensitive to surface characteristics.[14] The use of NC, Avicel and RC surfaces provided three types of cellulose substrate: almost fully crystalline and porous cellulose I, crystalline cellulose II and a non-porous almost completely amorphous cellulose, respectively. Characterization of cellulose surfaces was performed using ellipsometry and AFM as described in Chapters 3.3.1 and 3.3.3, respectively. Height images from AFM along with thicknesses and root-mean-square (RMS) roughnesses are presented in Figure 4.3. These three cellulose surfaces had similar thicknesses of ~10 nm. The NC and RC surfaces were quite smooth with low RMS roughnesses, however, the Avicel cellulose surface was considerably rougher.

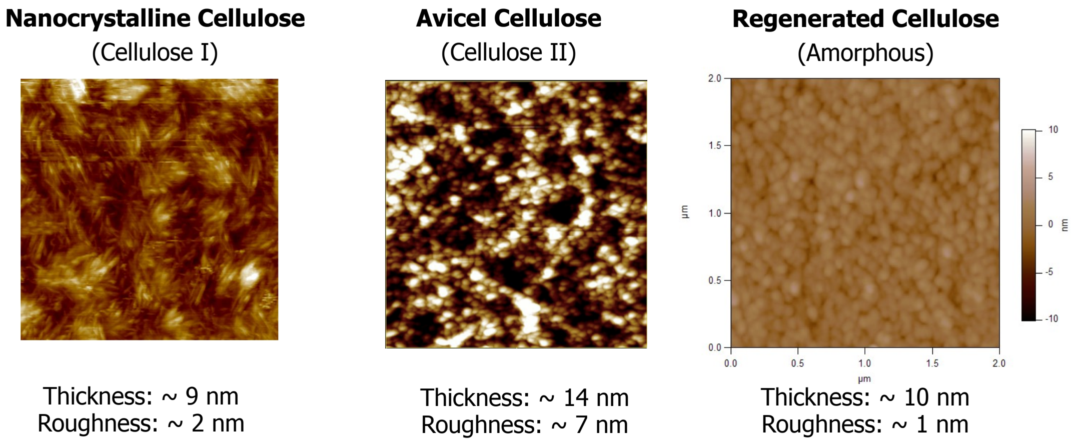

Figure 4.3 Representative AFM height images of three different cellulose surfaces, including NC, Avicel and RC surfaces. The RMS roughnesses were obtained from 2 µm × 2 µm scan areas and the z range was 20 nm. Film thicknesses were measured by ellipsometry as described in Chapter 3.3.1.

A summary of QCM-D and SPR results is provided in Table 4.4. Details for the analysis of QCM-D and SPR raw data are provided in Chapters 3.3.4 and 3.3.5, respectively. In brief, the Sauerbrey equation[15] and the equation of de Feijter *et al.*[16] were used for the calculation of adsorbed amount $\Gamma_{QCM\text{-}D}$ and Γ_{SPR}, respectively. Both QCM-D and SPR results showed that the 202 kDa xyloglucan sample irreversibly adsorbed onto the three cellulose surfaces. However, the amount of xyloglucan that adsorbed and the hydration state of the adsorbed layer strongly varied for different cellulose surfaces. As is seen in Table 4.4, $\Gamma_{QCM\text{-}D}$ and Γ_{SPR} increased in the order of RC < NC < Avicel. This trend was consistent with previously published results for cellulase adsorption onto RC and NC surfaces where the porosity of the NC film afforded greater accessible surface area for adsorption.[17] This finding was also in agreement with the *in vitro* and *in vivo* study that confirmed strong interactions between xyloglucan and cellulose.[2] Furthermore, it was also believed that xyloglucan not only bound to the cellulose surface, but also tethered the cellulose microfibrils. However, QCM-D and SPR, as surface techniques, can only confirm the surface attachment rather than the tethering effect. The main driving force proposed for xyloglucan adsorption is nonelectrostatic interactions, presumably through hydrogen bonding.[2] When xyloglucan comes close to cellulose, the formation of hydrogen bonds between xyloglucan and cellulose becomes more favorable than the formation of hydrogen bonds between cellulose and water. It has long been suggested that the xyloglucan-cellulose interactions involve the alignment of polysaccharide chains due to the structural similarity between xyloglucan and cellulose.[18, 19] Furthermore, some simulation results showed that van der Waals interactions made a significant contribution to xyloglucan adsorption onto cellulose under aqueous conditions.[20]

Table 4.4 Values of $\Gamma_{QCM\text{-}D}$ and Γ_{SPR} for 202 kDa xyloglucan adsorption onto different cellulose surfaces from 500 mg•L^{-1} aqueous solutions at 20.0 °C.[a,b,c]

	Regenerated Cellulose (Amorphous)	**Nanocrystalline Cellulose (Cellulose I)**	**Avicel Cellulose (Cellulose II)**
$^a\Gamma_{QCM\text{-}D}$ /mg•m^{-2}	4.64 ± 0.71	5.13 ± 0.14	5.23 ± 0.35
$^b\Gamma_{SPR}$ /mg•m^{-2}	1.02 ± 0.35	1.72 ± 0.15	2.78 ± 0.84
^{c}%H_2O	78 ± 8	64 ± 1	47 ± 14

a. Calculated from Equation 3.1 for the fifth overtone.
b. Calculated from Equation 3.4.
c. Degree of hydration by mass calculated from Equation 2.30.

A complementary use of SPR to QCM-D allowed for the estimation of water contents or degrees of hydration of the adsorbed xyloglucan layers. As is evident in Table 4.4, $\Gamma_{QCM\text{-}D}$ was greater than Γ_{SPR}. This was expected, as QCM-D measured not only the adsorbed polymer but also coupled water, whereas SPR was only sensitive to the adsorbed polymer. The average water content of adsorbed xyloglucan layers on different cellulose surfaces increased in the order of Avicel (47 ± 14%) < NC (64 ± 1%) < RC (78

± 8%). This observation is also consistent with a previous study that showed that the adsorption of tamarind seed xyloglucan onto cellulose led to the formation of a lubricating layer.[21] This trend was also similar to previous results where cellulase penetrated into porous NC films but not into RC films (non-porous).[17] Unlike RC surfaces, penetration of xyloglucan into NC and Avicel films allowed the displacement of water already coupled to the films leading to smaller apparent water contents.

4.4.2 Xyloglucan Oligosaccharide Adsorption onto Cellulose Surfaces

Dynamic adsorption isotherms for xyloglucan, xyloglucan oligosaccharide and xyloglucan heptasaccharide from water onto RC surfaces were studied by QCM-D. Each adsorption isotherm was collected in a sequential fashion by pumping sample solutions from low to high concentration. Representative adsorption profiles for xyloglucan heptasaccharide, xyloglucan oligosaccharide and xyloglucan are provided in Figure 4.4. For xyloglucan heptasaccharide and xyloglucan oligosaccharide, changes in scaled frequency ($\Delta f/n$) and dissipation (ΔD) comparable to the detection limit of the instrument ($\Delta f/n < \sim 1$ Hz and $\Delta D < \sim 0.2 \times 10^{-6}$) were observed. It was impossible to extract useful information from QCM-D raw data for these two oligosaccharides. In contrast, for xyloglucan greater changes in $\Delta f/n$ and ΔD were observed with increasing concentration. Values of $\Delta f/n$ for each concentration were converted to $\Gamma_{QCM\text{-}D}$ using the Sauerbrey equation as described in Chapter 3.3.4 and results are summarized in Table 4.5. The QCM-D data showed that the adsorption equilibrium shifted towards more bound materials (greater $\Gamma_{QCM\text{-}D}$) with increasing concentration for the high molar mass xyloglucan. As is evident in Figure 4.4, molar mass had a significant influence on xyloglucan adsorption. This conclusion is in agreement with previous results from xyloglucan-cellulose binding assays and ITC measurements, suggesting that the molar mass of xyloglucan has a marked effect on binding.[22]

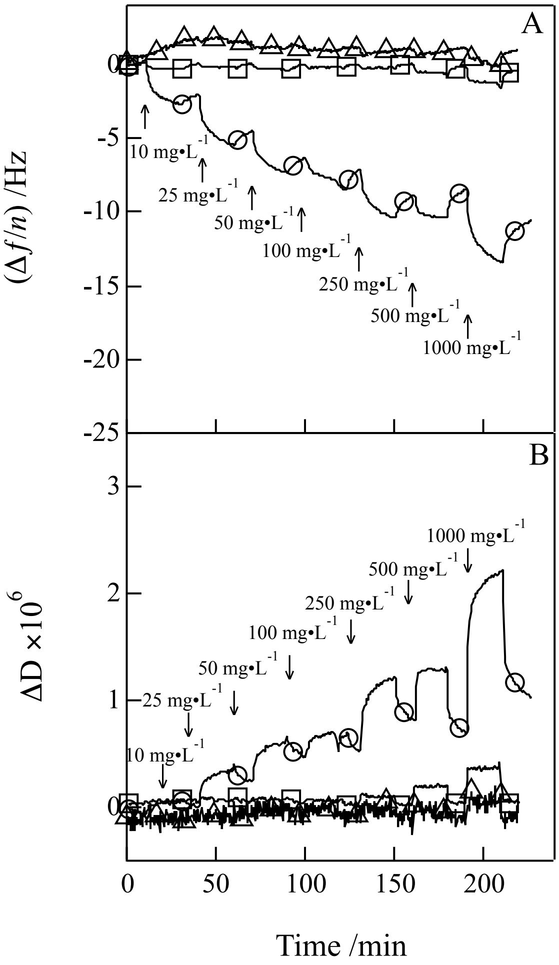

Figure 4.4 Representative dynamic adsorption isotherms for (O) xyloglucan, (☐) xyloglucan oligosaccharide and (**Δ**) xyloglucan heptasaccharide aqueous solutions adsorbed onto RC surfaces at 20.0 °C. Arrows indicate where solutions were switched. Each adsorption isotherm was collected in a sequential fashion from low to high concentration. Data correspond to the fifth overtone and arrows indicate where solutions were switched.

Table 4.5 Irreversible $\Delta f/n$, ΔD and $\Gamma_{QCM\text{-}D}$ for 202 kDa xyloglucan adsorption onto RC surfaces from water at 20.0 °C.[a]

Concentration /mg•L^{-1}	**$\Delta f/n$ /Hz**	**ΔD × 10^{6}**	**[a]$\Gamma_{QCM\text{-}D}$ /mg•m^{-2}**
10	-2.14 ± 0.11	0.10 ± 0.02	0.38 ± 0.02
25	-4.55 ± 0.20	0.34 ± 0.05	0.81 ± 0.03
50	-6.33 ± 0.24	0.57 ± 0.07	1.12 ± 0.04
100	-7.06 ± 0.26	0.63 ± 0.11	1.25 ± 0.04
250	-8.74 ± 0.35	0.92 ± 0.13	1.55 ± 0.06
500	-8.30 ± 0.42	0.83 ± 0.11	1.47 ± 0.07
1000	-10.25 ± 0.47	1.14 ± 0.12	1.81 ± 0.08

a. Calculated from Equation 3.1 for the fifth overtone.

Dynamic adsorption isotherms for xyloglucan, xyloglucan oligosaccharide and xyloglucan heptasaccharide adsorption onto RC were also obtained in a sequential fashion using SPR. Adsorption times were the same as those used for the corresponding QCM-D measurements. Representative SPR adsorption profiles are provided in Figure 4.5. As seen in Figure 4.5, changes in SPR angle (θ_{sp}) increased with increasing concentration and molar mass. Irreversible changes in SPR angle ($\Delta\theta_{irr}$) and adsorbed amounts (Γ_{SPR}) for xyloglucan heptasaccharide, xyloglucan oligosaccharide and xyloglucan adsorption onto RC surfaces are summarized in Table 4.6. Conversion from $\Delta\theta_{irr}$ to Γ_{SPR} followed the procedures in Chapter 3.3.5. Unlike QCM-D results, where significant xyloglucan heptasaccharide and xyloglucan oligosaccharide adsorption could not be detected, SPR data clearly demonstrated irreversible $\Delta\theta_{irr}$ upon exposure of the cellulose surfaces to xyloglucan oligosaccharide and xyloglucan heptasaccharide solutions.

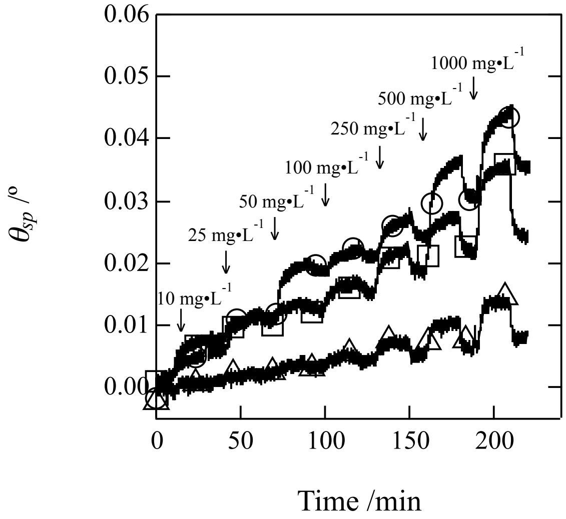

Figure 4.5 Representative θ_{sp} versus time for RC surfaces exposed to (O) xyloglucan, (☐) xyloglucan oligosaccharide and (**Δ**) xyloglucan heptasaccharide aqueous solutions at 20.0 °C. Arrows indicate where solutions were switched. Each adsorption isotherm was collected in a sequential fashion from low to high concentration with an intervening rinsing step.

Table 4.6 Summary of $\Delta\theta_{irr}$ and Γ_{SPR} for xyloglucan heptasaccharide, xyloglucan oligosaccharide and xyloglucan aqueous solutions adsorbed onto RC surfaces at 20.0 °C.[a,b]

Conc. /mg•L^{-1}	**Xyloglucan**		**Xyloglucan**		**Xyloglucan**	
	$\Delta\theta_{irr}$ /°	**$^{a}\Gamma_{SPR}$ /mg•m^{-2}**	**$\Delta\theta_{irr}$ /°**	**$^{a}\Gamma_{SPR}$ /mg•m^{-2}**	**$\Delta\theta_{irr}$ /°**	**$^{a}\Gamma_{SPR}$ /mg•m^{-2}**
10	0.0014(4)	0.030(9)	0.0058(1)	0.118(2)	0.0055(1)	0.115(2)
25	0.0031(5)	0.066(11)	0.0088(1)	0.180(2)	0.0099(8)	0.207(17)
50	0.0041(5)	0.088(11)	0.0118(5)	0.241(10)	0.0164(18)	0.342(37)
100	0.0058(8)	0.124(17)	0.0146(4)	0.298(8)	0.0192(16)	0.400(33)
250	0.0071(13)	0.152(28)	0.0170(5)	0.347(10)	0.0221(23)	0.461(48)
500	0.0081(13)	0.173(28)	0.0206(8)	0.420(16)	0.0282(29)	0.588(60)
1000	0.0094(16)	0.201(34)	0.0242(10)	0.494(20)	0.0324(30)	0.676(63)

a. Calculated from Equation 3.4.
b. Number in parenthesis represents one standard deviation of the last one or two digits.

Dynamic adsorption isotherms for xyloglucan, xyloglucan oligosaccharide and xyloglucan heptasaccharide adsorption onto RC surfaces are provided in Figure 4.6. Values of Γ_{SPR} increased with increasing sample concentration between 10 and 1000 mg•L^{-1}. Initially, there was a steep change in Γ_{SPR} in the low concentration region and a more gradual change in the high concentration region. The dramatic increases in the low concentration region emphasized the high affinity nature of both xyloglucan and its oligosaccharides towards cellulose. Only the xyloglucan heptasaccharide exhibited a plateau in the high concentration region, indicating surface saturation with xyloglucan heptasaccharide. The lack of plateaus for both xyloglucan oligosaccharide and xyloglucan may reflect inadequate adsorption times or polydispersity in the samples. As a polymeric material, 202 kDa xyloglucan is expected to form a de Gennes self-similar carpet structure with a tightly bound layer and a more diffuse layer, especially for high sample concentrations.[23, 24] As a consequence, “loop” and “tail” conformations make a greater contribution to the adsorbed amount of xyloglucan with high molar mass. The existence of a diffuse layer for high molar mass xyloglucan is consistent with the higher observed ΔD values summarized in Table 4.5, i.e. the formation of more dissipative layers. However, these values are still well below the typical threshold ($\Delta D < 5 \times 10^{-6}$) where the Sauerbrey equation (Equation 3.1) is no longer valid.

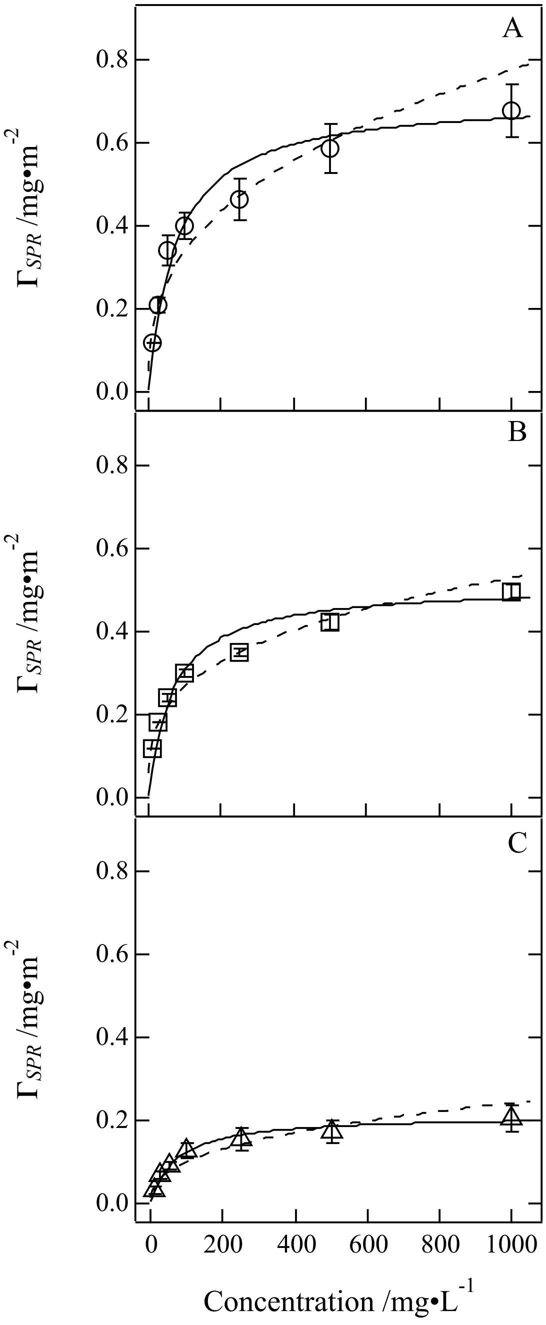

Figure 4.6 Dynamic adsorption isotherms for (O) xyloglucan, (☐) xyloglucan oligosaccharide and (**Δ**) xyloglucan heptasaccharide adsorbed onto RC surfaces from water at 20.0 °C. Error bars represent one standard deviation. The solid lines represent Langmuir fits (Equation 2.5) and the dashed lines represent Freundlich fits (Equation 2.6).

Values of Γ_{SPR} for xyloglucan, xyloglucan oligosaccharide and xyloglucan heptasaccharide adsorption were also fit with Langmuir (Equation 2.5) and Freundlich (Equation 2.6) adsorption isotherms, represented by solid and dashed lines in Figure 4.6, respectively. For 202 kDa xyloglucan (Figure 4.6A) and xyloglucan oligosaccharide (Figure 4.6B), Freundlich adsorption isotherm appeared to be a better fit. For xyloglucan heptasaccharide (Figure 4.6C), the adsorption isotherm was better described by a Langmuir fit. While neither isotherm is strictly valid for polymer adsorption, Freundlich adsorption isotherms frequently give better semi-empirical fits for polymeric systems. For xyloglucan heptasaccharide, even though the fit to Langmuir equation was good, the isotherm could only be considered as pseudo-Langmuirian since polymer adsorption failed to satisfy all the criteria required for Langmuir adsorption.[25] The pseudo-Langmuirian behavior has also been found for other polysaccharides, for example, guar gum adsorption onto talc.[26] Adsorption isotherm parameters for xyloglucan heptasaccharide, xyloglucan oligosaccharide and xyloglucan aqueous solutions adsorbed onto RC surfaces are summarized in Table 4.7. A LB monolayer of cellulose has a surface concentration of ~ 0.45 mg•m^{-2} based on previous study.[27] As xyloglucans have cellulose-like backbones with only slightly smaller side branches, similar surface concentrations for a xyloglucan monolayer are expected. On the basis of adsorption isotherm parameters, especially maximum surface excess (Γ_m), xyloglucan oligosaccharide layer (Γ_m = 0.51 mg•m^{-2}) is considered to be within the range of a monolayer, while the xyloglucan heptasaccharide layer (Γ_m = 0.21 mg•m^{-2}) represents a partial monolayer and 202 kDa xyloglucan layer (Γ_m = 0.71 mg•m^{-2}) must have multilayer features. From the Langmuir fitting results, all three samples, xyloglucan heptasaccharide, xyloglucan oligosaccharide and xyloglucan, had the same Langmuir constant (K_L) of 0.014 L•mg^{-1}, indicating there was no strong molar mass effect on the affinity of xyloglucan for RC. However, adsorbent capacity (K_F) obtained from Freundlich fits, which was analogous to Γ_m obtained from Langmuir fits, increased with increasing molar mass of xyloglucan. The adsorption affinity constant ($1/n_f$) measures preferential adsorption of one adsorbate over others.[28] Similar values of $1/n_f$ also confirmed the absence of a molar mass dependence for the inherent affinity of xyloglucan for RC surfaces.

Table 4.7 Adsorption isotherm parameters from SPR experiments for xyloglucan heptasaccharide, xyloglucan oligosaccharide and 202 kDa xyloglucan adsorbed onto RC surfaces from aqueous solutions at 20.0 °C.[a,b]

	Langmuir Fits		**Freundlich Fits**	
	$^a\Gamma_m$ /mg•m^{-2}	**^aK_L /L•mg^{-1}**	**^bK_F**	**$^b1/n_f$**
Xyloglucan Heptasaccharide	0.211 ± 0.006	0.0137 ± 0.0001	0.017 ± 0.004	0.384 ± 0.052
Xyloglucan Oligosaccharide	0.51 ± 0.02	0.015 ± 0.004	0.068 ± 0.008	0.297 ± 0.024
Xyloglucan	0.71 ± 0.03	0.013 ± 0.003	0.064 ± 0.015	0.361 ± 0.047

a. Determined by nonlinear fits to Equation 2.5.
b. Determined by nonlinear fits to Equation 2.6.

As it was not possible to extract statistically significant information from QCM-D raw data for xyloglucan heptasaccharide and oligosaccharide, only QCM-D data for xyloglucan was used together with SPR data for estimating the water content associated with the xyloglucan layers adsorbed onto RC surfaces (Figure 4.7A). As shown in Figure 4.7B, an average water content of ~ 65% was obtained for all of the concentrations investigated in the dynamic adsorption isotherm experiments. This value is comparable to the water content obtained for the equilibrium estimates of the surface morphology studies (78 ± 8%, Table 4.4). A slightly lower water content value is attributed to the shorter adsorption time (20 min vs. 2 h) whereby less time is allowed for a diffuse layer to fully form.

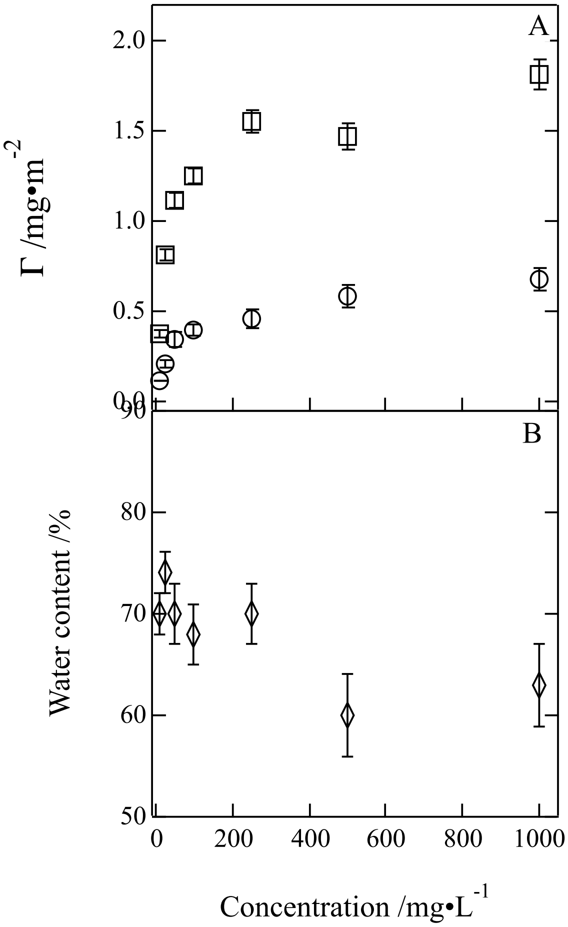

Figure 4.7 (A) Adsorption isotherms from (O) SPR and (☐) QCM-D and (B) water contents (%H_2O, ◊) for dynamic adsorption of xyloglucan onto RC surfaces from aqueous solutions at 20.0 °C. Error bars represent one standard deviation.

The study of xyloglucan oligosaccharide adsorption onto cellulose provided additional insight into the underlying mechanism of xyloglucan adsorption onto cellulose. Both QCM-D and SPR results confirmed strong interactions between cellulose and xyloglucan, and in SPR experiments even for the structural unit of xyloglucan (XXXG).

The observation of both XXXG and polymeric xyloglucan binding to cellulose suggests that xyloglucan shows strong affinity towards cellulose. Schematic representations of xyloglucan heptasaccharide, xyloglucan oligosaccharide and xyloglucan interactions with RC surfaces are provided in Figure 4.8. As depicted in Figure 4.8A, even the XXXG (a single circle in the figure) interacts with the cellulose surface, confirming the presence of strong cellulose-xyloglucan interactions. As no preferential adsorption exists for all three xyloglucan samples, both single structural unit and consecutive structural units can interact with cellulose surfaces. As XXXG adsorption is consistent with submonolayer surface coverage (Figure 4.8A), incomplete coating of cellulose is expected. As xyloglucan oligosaccharide adsorption is consistent with monolayer coverage (Figure 4.8B), it fits depicted as forming a complete coating on cellulose. For 202 kDa xyloglucan (Figure 4.8C), a fraction of segments form “loops” and “tails” sticking out into solution, leading to the formation of multilayer. This depiction is consistent with the de Gennes self-similar carpet with the formation of a diffuse adsorbed layer for xyloglucan with high molar mass.[23, 24]

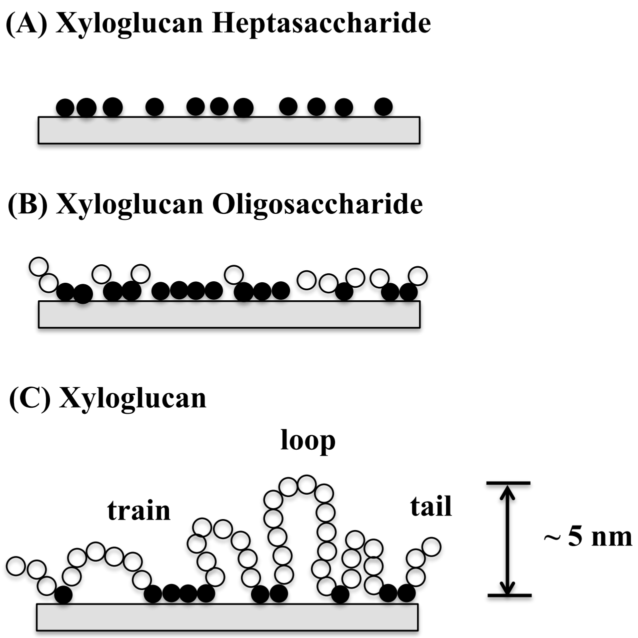

(A) Xyloglucan Heptasaccharide

(B) Xyloglucan Oligosaccharide

(C) Xyloglucan

Figure 4.8 Schematic representations of (A) xyloglucan heptasaccharide, (B) xyloglucan oligosaccharide and (C) xyloglucan interactions with RC surfaces. Each circle represents a major structural unit (XXXG). Filled circles represent building blocks that directly interact with cellulose, also known as "trains".

4.4.3 Carboxymethyl Cellulose Adsorption onto Cellulose Surfaces

The adsorption of CMC from water and salt solutions onto RC surfaces and the properties of the resulting adsorbed layers were examined using QCM-D and SPR. Four sodium salts of CMC samples were used in this study as summarized in Table 4.2. For the case of adsorption from water, there were no significant changes in $\Delta f/n$ or ΔD between the final and initial water baselines. Hence, any CMC adsorption that occurred from water was reversible. This observation was similar to some previous studies and was attributed to the electrostatic repulsions between negatively charged CMC molecules and slightly anionic cellulose surfaces (surface potential = -2 mV).[29, 30] Changes in $\Delta f/n$ and ΔD during adsorption most likely reflected changes in viscosity and density of the solution rather than reversible adsorption. All four CMC samples used in this chapter failed to irreversibly adsorb onto RC surfaces from water. Based upon previous studies, the addition of salt can reduce the electrostatic repulsions and facilitate polysaccharide adsorption.[31, 32] Representative adsorption profiles for CMC adsorption onto RC surfaces from 5 mM $CaCl_2$ are provided in Figure 4.9 and values of $\Delta f/n$ and ΔD deduced from multiple adsorption experiments are summarized in Table 4.8. Unlike the case of reversible CMC adsorption from water, the observed non-zero changes in both $\Delta f/n$ and ΔD after $CaCl_2$ solution and water were reintroduced into the flow cells indicated an irreversible adsorption of CMC from $CaCl_2$. This enhancement could be explained by crosslinks formed between CMC molecules via Ca^{2+} as well as the interaction with regard to charge neutralization along the CMC backbones.[9] There was also a significant increase in ΔD upon switching back to water at the end of the adsorption experiment. Liu *et al.* attributed this to the softening and swelling of CMC/Ca^{2+} complex layers by water.[30] As is evident in Figure 4.9, there was an initial rapid decrease in $\Delta f/n$ attributed to CMC adsorption from $CaCl_2$ followed by the uptake of additional CMC at a lower rate. Approximately 80% of the adsorption occurred within 10 min of RC exposure to the CMC solutions containing 5 mM $CaCl_2$. The observation of at least two stages for CMC adsorption, including diffusion-controlled adsorption (initial rapid uptake) and rearrangement of CMC molecules, is consistent with the literature.[12]

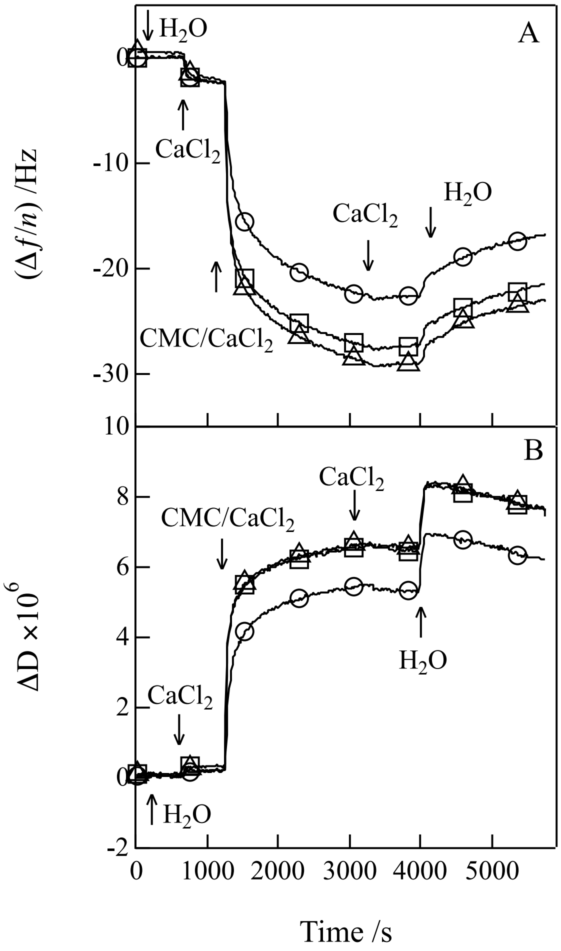

Figure 4.9 Representative time dependent (A) Δ*f*/*n* and (B) ΔD profiles for CMC adsorption onto RC from 500 mg•L^{-1} solutions containing 5 mM $CaCl_2$ at 20.0 °C. Different symbols correspond to CMC samples with similar DP but different DS: (O) 1.2, (□) 0.9 and (**Δ**) 0.7. Data correspond to the fifth overtone and arrows indicate where solutions were switched.

Table 4.8 Irreversible $\Delta f/n$ and ΔD for CMC samples adsorption onto RC surfaces from 500 mg•L^{-1} solutions containing 5 mM and 10 mM CaCl$_2$ solution at 20.0 °C.

		$\Delta f/n$ /Hz	**ΔD ×10^6**
5 mM CaCl$_2$	**CMC-1.2-965**	-16.72 ± 0.55	6.28 ± 0.10
	CMC-0.9-1064	-22.06 ± 0.35	7.58 ± 0.01
	CMC-0.7-1143	-23.60 ± 0.45	7.78 ± 0.34
	CMC-0.7-412	-24.8 ± 2.1	6.85 ± 0.14
10 mM CaCl$_2$	**CMC-1.2-965**	-20.4 ± 1.7	7.44 ± 0.22
	CMC-0.9-1064	-28.0 ± 2.8	9.00 ± 0.52
	CMC-0.7-1143	-26.66 ± 0.52	9.28 ± 0.26
	CMC-0.7-412	-23.10 ± 0.70	6.84 ± 0.42

Unlike the hemicellulose xyloglucan that adsorbed onto cellulose with flatter and more rigid conformations, CMC formed soft and viscoelastic layers on RC surfaces with $\Delta D \geq 5 \times 10^{-6}$. For such dissipative layers, a Voigt-based viscoelastic model was used for the quantification of the adsorbed CMC layers.[33] Detailed procedures for Voigt-based viscoelastic modeling are provided in Chapter 3.3.4. The density and viscosity of water, ρ_0 = 1000 kg•m^{-3} and $\eta_0 = 1 \times 10^{-3}$ N•s•m^{-2}, respectively, were used for all of the bulk liquids due to negligible effects of dissolved electrolytes and CMC on the values of density and viscosity.[30] Fitting data from different overtone combinations are summarized in Table 4.9. The fitting results showed that greater $\Gamma_{QCM\text{-}D}$ were obtained from the lower overtone combination (n = 3, 5, and 7) compared to the higher overtone combination (n = 9, 11, and 13). As the film density was held constant, ρ_f = 1050 kg•m^{-3}, values of h_f necessarily showed the same trend. These differences were attributed to a decrease in the penetration depth of the acoustic waves through the film and into the surrounding media with increasing frequency (larger n).[34, 35] The acoustic waves generated by higher overtones can only sample the region of the adsorbed layer closest to the quartz crystal due to a smaller penetration depth. The acoustic waves generated by lower overtones can penetrate deeper into the bulk liquid and sample flexible "loops" and "tails" dangling into the bulk liquid. The viscosity and elastic shear moduli of CMC layers adsorbed from $CaCl_2$ solution were on the order of 10^{-3} N•s•m^{-2} and 10^{5} N•m^{-2}, respectively. These values are consistent with a previously published study on the viscoelastic properties of CMC layers adsorbed from $CaCl_2$ solution onto cellulose.[30]

Table 4.9 Summary of h_f and $\Gamma_{QCM\text{-}D}$ using different overtone combinations for CMC layers adsorbed onto RC surfaces from 500 mg•L^{-1} solutions containing 5 mM and 10 mM $CaCl_2$ solutions at 20.0 °C.[a,b]

Sample	[Ca^{2+}] /mM	$^a h_f$ /nm (n = 3, 5, 7)	$^a h_f$ /nm (n = 9, 11, 13)	$^b\Gamma_{QCM\text{-}D}$ /mg•m^{-2} (n = 3, 5, 7)	$^b\Gamma_{QCM\text{-}D}$ /mg•m^{-2} (n = 9, 11, 13)
CMC -1.2-965	5	8.15 ± 0.21	4.87 ± 0.66	8.97 ± 0.23	5.36 ± 0.73
	10	8.95 ± 1.05	5.29 ± 0.78	9.85 ± 1.15	5.82 ± 0.86
CMC -0.9-1064	5	9.45 ± 0.78	5.43 ± 1.11	10.40 ± 0.86	5.97 ± 1.22
	10	10.56 ± 0.36	7.93 ± 0.53	11.62 ± 0.40	8.72 ± 0.58
CMC -0.7-1143	5	10.58 ± 0.93	6.51 ± 1.02	11.64 ± 1.02	7.16 ± 1.12
	10	11.67 ± 0.48	7.20 ± 1.28	12.84 ± 0.53	7.92 ± 1.41
CMC -0.7-412	5	9.68 ± 0.24	6.76 ± 0.49	10.65 ± 0.26	7.44 ± 0.54
	10	8.40 ± 0.11	5.87 ± 0.32	9.24 ± 0.12	6.46 ± 0.35

a. Assumes ρ_f = 1050 kg•m^{-3}.
b. Calculated from Equation 3.3.

In order to probe ionic strength effects on CMC adsorption, 5 mM and 10 mM $CaCl_2$ solution were used for QCM-D measurements. An analogous plot to Figure 4.9 for the case of 10 mM $CaCl_2$ is provided as Figure 4.10. As seen in Figure 4.10, there are no qualitative differences from the 5 mM $CaCl_2$ case presented in Figure 4.9. Nonetheless, there are some small quantitative differences with respect to $\Delta f/n$ and ΔD that are summarized in Table 4.8. At high salt concentrations, slight differences in the adsorption profiles in Figure 4.9 for CMC-0.9-1064 and CMC-0.7-1143 disappeared as seen in Figure 4.10, even though CMC-1.2-965 still showed a significant difference from low DS samples. Although the increase in ionic strength yielded an increase in CMC adsorption, equilibrium adsorption occurred over comparable time scales. Fitting data for CMC adsorption from different salt concentrations is summarized in Table 4.9. In general, greater h_f and $\Gamma_{QCM\text{-}D}$ were obtained with increasing [Ca^{2+}]. This result could be explained by a decrease in the range of the double-layer force with increasing ionic strength. Anionic CMC came closer to the anionic cellulose surface and other short-range attractive forces, such as van der Waals forces, became more important.[36] This result is similar to the case of negatively charged hemicellulose adsorption onto cellulose, where the short-range forces play an important role in the adsorption process.[19] In addition, the lower solubility of CMC at higher ionic strength also provides a strong driving force for CMC adsorption. As CMC-1.2-965 has the highest DS, it may have a significantly lower driving force for adsorption due to the greater electrostatic repulsions as well as better aqueous solubility.

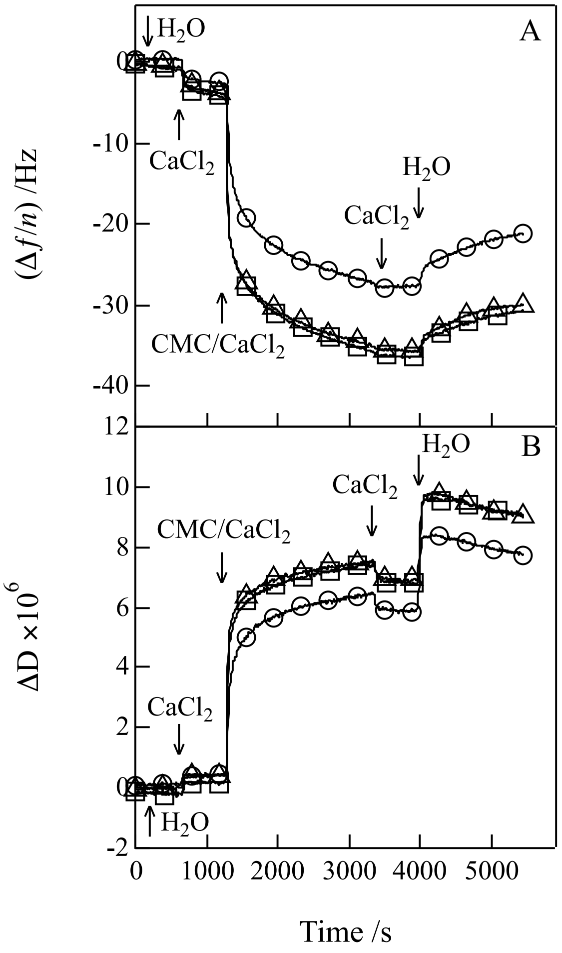

Figure 4.10 Representative time dependent (A) $\Delta f/n$ and (B) ΔD profiles for CMC adsorption onto RC surfaces from 500 mg•L^{-1} solutions containing 10 mM CaCl$_2$ onto RC surfaces at 20.0 °C. Different symbols correspond to CMC samples with similar DP but different DS: (O) 1.2, (□) 0.9 and (**Δ**) 0.7. Data correspond to the fifth overtone and arrows indicate where solutions were switched.

In order to study the effect of DS on CMC adsorption onto RC surfaces, three samples with DS ranging from 0.7 to 1.2, were used in this study. As is evident in Table 4.9, values of h_f and $\Gamma_{QCM\text{-}D}$ increased with decreasing DS. This behavior is consistent with previous studies that demonstrated increased CMC adsorption with decreasing charge density, i.e. decreasing DS.[37] One possible explanation is that decreasing charge density can reduce the electrostatic repulsions and enhance the adsorption of CMC. This result can also be explained as CMC samples with higher DS having a greater fraction of chain segments interacting with RC surface through Ca^{2+}, leading to more compact conformations. In contrast, CMC samples with lower DS have a lower fraction of chain segments directly interacting with RC while other chain segments form “loop” and “tail” conformations. More extended conformations would also be consistent with larger ΔD observed for low DS films (Table 4.8). Moreover, there is a small difference in adsorption kinetics with respect to DS for CMC. By comparing the initial adsorption rate which is measured by the slope of the $\Delta f/n$ versus time curves at an early stage of adsorption (Figures 4.9 and 4.10), the adsorption of CMC with higher DS (CMC-1.2-965) onto RC was slightly slower than CMC-0.9-1064 and CMC-0.7-1143. Slower adsorption was probably attributed to the stronger electrostatic repulsions between the more highly charged CMC chains in solution as well as between CMC chains in solution and those already adsorbed onto the RC surfaces.

In order to investigate the effect of DP on CMC adsorption, QCM-D measurements were performed on CMC samples of the same DS (DS = 0.7) but different DP. Representative time dependent adsorption profiles for CMC adsorption onto RC surfaces from 5 mM $CaCl_2$ and 10 mM $CaCl_2$ are provided in Figures 4.11 and 4.12, respectively. As seen in Figures 4.11 and 4.12, greater changes in $\Delta f/n$ and ΔD were observed for CMC samples with high DP (CMC-0.7-1143). On the basis of viscoelastic modeling data summarized in Table 4.9, greater h_f and $\Gamma_{QCM\text{-}D}$ were obtained for the CMC sample with the higher DP for DS = 0.7. Similar results were obtained for CMC adsorption onto talc surfaces where the adsorbed amounts increased with increasing DP.[9]

At low salt concentrations (5 mM $CaCl_2$), DP had a smaller effect on CMC adsorption onto RC surfaces. One possible reason is electrostatic repulsions between adsorbed CMC and CMC molecules in solution at lower salt concentration hinder additional adsorption.[9] A more significant DP effect was observed at higher salt concentration (10 mM $CaCl_2$) as seen in Figure 4.12 and Table 4.9. Previous results also confirmed that the electrostatic repulsions between high DP CMC molecules were more significantly reduced by high ionic strength.[38] This observation could also be explained by the fact that an increase in ionic strength caused the negatively charged CMC molecules to take on coil conformations. Therefore, CMC molecules with higher DP occupied more space than CMC molecules with lower DP, leading to greater adsorbed amounts per unit area. Molar mass of the polymer was also expected to affect the dynamics of polyelectrolyte adsorption.[39] However, there were no significant differences in the adsorption dynamics for the two CMC samples with different DP at the concentration investigated.

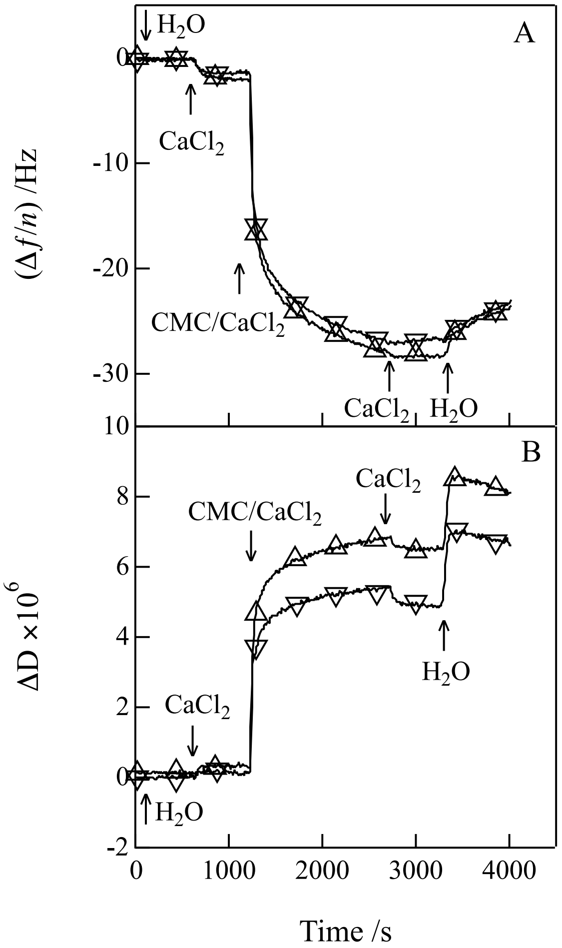

Figure 4.11 Representative time dependent (A) $\Delta f/n$ and (B) ΔD profiles for CMC adsorption onto RC from 500 mg•L^{-1} solutions containing 5 mM $CaCl_2$ at 20.0 °C. Different symbols correspond to CMC samples with the same DS of 0.7 but different DP: (**Δ**) 1143 and (∇) 412. Data correspond to the fifth overtone and arrows indicate where solutions were switched.

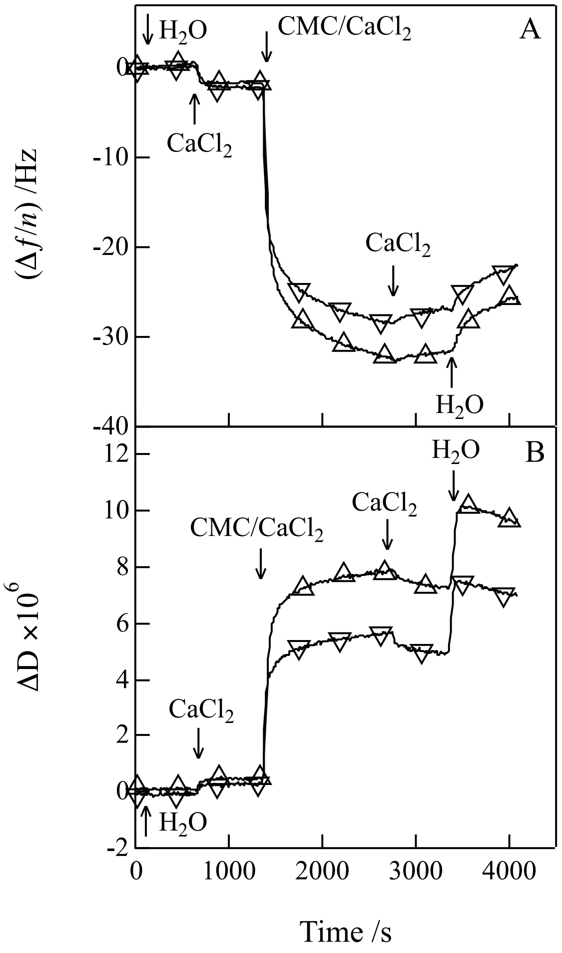

Figure 4.12 Representative time dependent (A) $\Delta f/n$ and (B) ΔD profiles for CMC adsorption onto RC surfaces from 500 mg•L^{-1} solutions containing 10 mM CaCl$_2$ at 20.0 °C. Different symbols correspond to CMC samples with the same DS of 0.7 but different DP: (**Δ**) 1143 and (∇) 412. Data correspond to the fifth overtone and arrows indicate where solutions were switched.

Adsorption of CMC onto RC surfaces was also studied by SPR and $\Delta\theta_{irr}$ and calculated Γ_{SPR} are summarized in Table 4.10. The SPR angle only increased by 0.005° for CMC adsorption from water and returned to the initial water baseline after a water rinse, indicating reversible adsorption. This was consistent with the QCM-D results that no irreversible adsorption of CMC onto cellulose occurred from water. Changes in SPR angle during the adsorption was attributed to the higher refractive index of the CMC solutions compared to water. Greater $\Delta\theta_{irr}$ were observed for CMC adsorption from $CaCl_2$ solutions. This observation was in agreement with the QCM-D data that showed the addition of salt enhanced CMC adsorption onto RC surfaces. Comparable $\Delta\theta_{irr}$ and Γ_{SPR} values were obtained for all CMC samples except the one with the highest DS (CMC-1.2-965). For CMC-0.7-1143 and CMC-0.7-412, similar $\Delta\theta_{irr}$ and Γ_{SPR} values were obtained, indicating no significant DP effect on CMC adsorption onto RC. Surprisingly, $\Delta\theta_{irr}$ and Γ_{SPR} measured by SPR decreased with increasing salt concentration, especially for CMC samples with high DS (CMC-1.2-965).

Table 4.10 Summary of $\Delta\theta_{irr}$ and Γ_{SPR} for CMC adsorption onto RC surfaces from 500 mg•L^{-1} solutions containing 5 mM and 10 mM $CaCl_2$ at 20.0 °C.[a]

	[CaCl$_2$] /mM	**$\Delta\theta_{irr}$ /°**	**$^{a}\Gamma_{SPR}$ /mg• m^{-2}**
CMC-1.2-965	5	0.0185 ± 0.0007	0.37 ± 0.02
	10	0.015 ± 0.001	0.31 ± 0.02
CMC-0.9-1064	5	0.026 ± 0.001	0.51 ± 0.02
	10	0.024 ± 0.001	0.51 ± 0.02
CMC-0.7-1143	5	0.0266 ± 0.0007	0.52 ± 0.02
	10	0.025 ± 0.003	0.51 ± 0.06
CMC-0.7-412	5	0.026 ± 0.004	0.52 ± 0.08
	10	0.025 ± 0.003	0.51 ± 0.06

a. Calculated from Equation 3.4.

Adsorbed amounts measured by QCM-D and SPR as well as water contents associated with CMC layers are summarized in Table 4.11. All CMC samples showed similar Γ_{SPR} values except for the one with the highest DS (CMC-1.2-965). However, $\Gamma_{QCM\text{-}D}$ was significantly higher than Γ_{SPR} and varied with respect to DS and DP. The differences in $\Gamma_{QCM\text{-}D}$ could be attributed to different amounts of water associated with adsorbed CMC layers. As all of the CMC samples formed soft and viscoelastic layers on

RC surfaces with relatively high water contents (> 90%), no significant differences in water contents were observed. These values were consistent with previously published results for CMC layers on cellulose substrates.[30] Water contents obtained from the lower overtone combination were slightly higher than those from the higher overtone combination. These differences were attributed to the greater penetration depth of the acoustic waves into the surrounding medium.

Table 4.11 Summary of $\Gamma_{QCM\text{-}D}$, Γ_{SPR} and $\%H_2O$ for CMC layers adsorbed onto RC surfaces from 500 mg•L^{-1} solutions containing 5 mM and 10 mM $CaCl_2$ at 20.0 °C.[a,b,c]

Sample	**[Ca^{2+}] /mM**	**$^{a}\Gamma_{QCM\text{-}D}$ /mg•m^{-2} (n = 3, 5, 7)**	**$^{a}\Gamma_{QCM\text{-}D}$ /mg•m^{-2} (n = 9, 11, 13)**	**$^{b}\Gamma_{SPR}$ /mg•m^{-2}**	**$^{c}\%H_2O$ (n = 3, 5, 7)**	**$^{c}\%H_2O$ (n = 9, 11, 13)**
CMC -1.2-965	5	8.97 ± 0.23	5.36 ± 0.73	0.37 ± 0.02	96 ± 1	93 ± 1
	10	9.85 ± 1.15	5.82 ± 0.86	0.31 ± 0.02	97 ± 1	95 ± 1
CMC -0.9-1064	5	10.40 ± 0.86	5.97 ± 1.22	0.51 ± 0.02	95 ± 1	92 ± 2
	10	11.62 ± 0.40	8.72 ± 0.58	0.51 ± 0.02	96 ± 1	94 ± 1
CMC -0.7-1143	5	11.64 ± 1.02	7.16 ± 1.12	0.52 ± 0.02	96 ± 1	93 ± 1
	10	12.84 ± 0.53	7.92 ± 1.41	0.51 ± 0.06	96 ± 1	94 ± 1
CMC -0.7-412	5	10.65 ± 0.26	7.44 ± 0.54	0.52 ± 0.08	95 ± 1	93 ± 1
	10	9.24 ± 0.12	6.46 ± 0.35	0.51 ± 0.06	94 ± 1	92 ± 1

a. Calculated from Equation 3.3.
b. Calculated from Equation 3.4.
c. Degree of hydration by mass calculated from Equation 2.30.

Negatively charged CMC did not adsorb onto RC surfaces from water. While the addition of Ca^{2+} led to the formation of CMC/Ca^{2+} complex layers with greater stability after flowing water over the surface. First, the presence of Ca^{2+} in solution provided strong bridges between CMC and RC surfaces. Moreover, the carboxyl groups at the *C*6 positions could form inter- and intramolecular crosslinks through Ca^{2+}. Similar effects of Ca^{2+} on the adsorption of CMC onto talc surfaces have been demonstrated by Parolis and coworkers.[40] A schematic depiction of CMC adsorption onto RC surfaces is provided in Figure 4.13. Compared to CMC adsorption onto mineral surfaces that formed rather flat conformations to make more contacts with the surface,[13] adsorption of CMC led to the formation soft and viscoelastic layers which are consistent with the greater changes in ΔD. For CMC samples with higher DS, lower values of ΔD and smaller h_f indicate a more compact and flatter conformation with a greater fraction of the segments in "train" conformations. For CMC samples with lower DS, a high degree of "loop" and "tail" conformations were formed as a consequence of the preferential adsorption of the charged segments. This interpretation is also consistent with the relatively higher ΔD and larger h_f values. For CMC samples with the same DS (DS = 0.7) but different DP, the longer chains formed larger loops. This interpretation is consistent with the greater ΔD and h_f values observed for CMC samples with higher DP. In summary, both "tail" and long "loop" conformations have significant contributions to greater adsorbed amounts of CMC samples with lower DS and higher DP adsorbed onto RC surfaces. This interpretation is consistent with previous studies on polymer adsorption that "tail" and "loop" conformations contribute most to the adsorbed amounts at solid/liquid interfaces.[41]

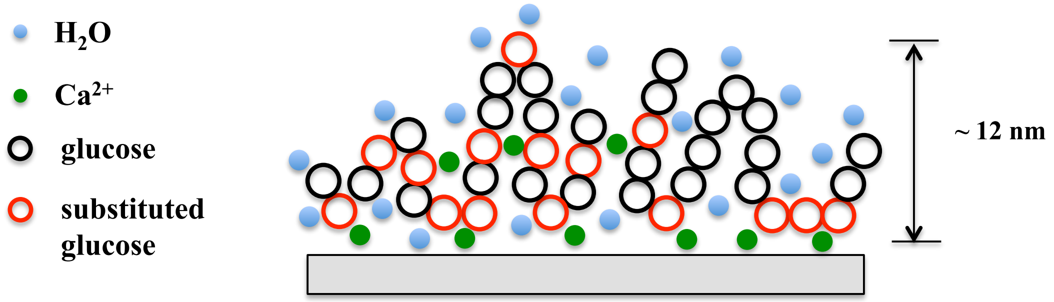

Figure 4.13 A schematic representation of CMC adsorption onto RC surfaces. Black circles represent unsubstituted glucose units and red circles represent glucose units with carboxymethyl substitution.

4.5 Conclusions

One major hemicellulose from dicot plants, xyloglucan, showed irreversible adsorption onto three different cellulose surfaces. Adsorbed amounts strongly correlated with increasing porosity and roughness of the substrates and increased in the order of RC < NC < Avicel. Dynamic adsorption isotherms were studied for 202 kDa xyloglucan and oligosaccharides. For xyloglucan heptasaccharide, a Langmuir adsorption isotherm fit the experimental data well, whereas for xyloglucan oligosaccharide and xyloglucan, Freundlich adsorption isotherms provided better fits. On the basis of adsorption isotherm parameters, there was no significant molar mass dependence for the affinity of xyloglucan for RC surfaces. Xyloglucan interacts with cellulose through different building blocks like xyloglucan heptasaccharide and xyloglucan oligosaccharide. Compared to hemicelluloses, CMC adsorption from $CaCl_2$ formed soft and hydrated layers on RC that can not be directly quantified by the Sauerbrey equation. Viscoelastic modeling and the combination of QCM-D and SPR data confirmed the formation of soft and dissipative CMC/Ca^{2+} layers on RC with average water contents > 90%. This study also demonstrated the adsorption of CMC onto RC was strongly affected by the addition of $CaCl_2$ as well as the salt concentration. The adsorbed amounts increased with increasing [Ca^{2+}]. The DS and DP played important roles in CMC adsorption onto RC surfaces with greater adsorption for low DS and high DP CMC samples.

4.6 References

(1) Fengel, D.; Wegener, G., *Wood: Chemistry, ultrastructure, reactions*. Walter de Gruyter: 1983.

(2) Hayashi, T.; Marsden, M. P. F.; Delmer, D. P., *Plant Physiology* **1987,** *83*, 384-389.

(3) Valent, B. S.; Albersheim, P., *Plant Physiology* **1974,** *54*, 105-108.

(4) Hayashi, T.; Takeda, T.; Ogawa, K.; Mitsuishi, Y., *Plant and Cell Physiology* **1994,** *35*, 893-899.

(5) Lopez, M.; Bizot, H.; Chambat, G.; Marais, M.-F.; Zykwinska, A.; Ralet, M.-C.; Driguez, H.; Buléon, A., *Biomacromolecules* **2010,** *11*, 1417-1428.

(6) Morris, S.; Hanna, S.; Miles, M. J., *Nanotechnology* **2004,** *15*, 1296-1301.

(7) Cuba-Chiem, L. T.; Huynh, L.; Ralston, J.; Beattie, D. A., *Langmuir* **2008,** *24*, 8036-8044.

(8) Heinze, T.; Koschella, A., *Macromolecular Symposia* **2005,** *223*, 13-40.

(9) Khraisheh, M.; Holland, C.; Creany, C.; Harris, P.; Parolis, L., *International Journal of Mineral Processing* **2005,** *75*, 197-206.

(10) Wang, J.; Somasundaran, P., *J Colloid Interf Sci* **2005,** *291*, 75-83.

(11) Arêas, E. P. G.; Galembeck, F., *J Colloid Interf Sci* **1991,** *147*, 370-377.

(12) Fujimoto, J.; Petri, D. F. S., *Langmuir* **2000,** *17*, 56-60.

(13) Hoogendam, C. W.; de Keizer, A.; Cohen Stuart, M. A.; Bijsterbosch, B. H.; Batelaan, J. G.; van der Horst, P. M., *Langmuir* **1998,** *14*, 3825-3839.

(14) Netz, R. R.; Andelman, D., *Physics Reports* **2003,** *380*, 1-95.

(15) Sauerbrey, G., *Z. Phys* **1959,** *155*, 206-222.

(16) de Feijter, J. A.; Benjamins, J.; Veer, F. A., *Biopolymers* **1978,** *17*, 1759-1772.

(17) Kittle, J. D.; Du, X.; Jiang, F.; Qian, C.; Heinze, T.; Roman, M.; Esker, A. R., *Biomacromolecules* **2011,** *12*, 2881-2887.

(18) Taylor, I. E. P.; Atkins, E. D. T., *FEBS Letters* **1985,** *181*, 300-302.

(19) Tammelin, T.; Paananen, A.; Österberg, M., *The nanoscience and technology of renewable biomaterials* Wiley Publishing Inc: 2009.

(20) Zhang, Q.; Brumer, H.; Ågren, H.; Tu, Y., *Carbohydrate Research* **2011,** *346*, 2595-2602.

(21) Stiernstedt, J.; Brumer, H.; Zhou, Q.; Teeri, T. T.; Rutland, M. W., *Biomacromolecules* **2006,** *7*, 2147-2153.

(22) Lima, D. U.; Loh, W.; Buckeridge, M. S., *Plant Physiology and Biochemistry* **2004,** *42*, 389-394.

(23) Vincken, J. P.; de Keizer, A.; Beldman, G.; Voragen, A., *Plant Physiology* **1995,** *108*, 1579-1585.

(24) de Gennes, P. G., *Macromolecules* **1981,** *14*, 1637-1644.

(25) Hollander, A. F.; Somasundaran, P.; Gryte, C. C., Adsorption of polyacrylamide and pulfonated polyacrylamide on Na-Kaolinite. In *Adsorption From Aqueous Solutions*, Tewari, P. H., Ed. Springer US: 1981; pp 143-162.

(26) Jenkins, P.; Ralston, J., *Colloids and Surfaces A: Physicochemical and Engineering Aspects* **1998,** *139*, 27-40.

(27) Kawaguchi, T.; Nakahara, H.; Fukuda, K., *Thin Solid Films* **1985,** *133*, 29-38.

(28) Desta, M. B., *Journal of Thermodynamics* **2013,** *2013*, 6-11.

(29) Österberg, M., *J Colloid Interf Sci* **2000,** *229*, 620-627.

(30) Liu, Z.; Choi, H.; Gatenholm, P.; Esker, A. R., *Langmuir* **2011,** *27*, 8718-8728.

(31) Mohammed, Z. H.; Haque, A.; Richardson, R. K.; Morris, E. R., *Carbohyd Polym* **2007,** *70*, 38-45.

(32) de Kerchove, A. J.; Elimelech, M., *Biomacromolecules* **2006,** *8*, 113-121.

(33) Voinova, M.; Rodahl, M.; Jonson, M.; Kasemo, B., *Physica Scripta* **1999,** *59*, 391-396.

(34) Vogt, B. D.; Lin, E. K.; Wu, W. L.; White, C. C., *J Phys Chem B* **2004,** *108*, 12685-12690.

(35) Patel, A. R.; Kanazawa, K. K.; Frank, C. W., *Analytical chemistry* **2009,** *81*, 6021-6029.

(36) Israelichvili, J., *Intermolecular and surface forces*. Academic Press, New York: 1991.

(37) Williams, P. A.; Harrop, R.; Phillips, G. O.; Pass, G.; Robb, I. D., *Journal of the Chemical Society, Faraday Transactions 1: Physical Chemistry in Condensed Phases* **1982,** *78*, 1733-1740.

(38) Shortridge, P. G.; Harris, P. J.; Bradshaw, D. J., *Polymers in Mineral Processing, JS Laskowski, Met Soc, Quebec* **1999**, 155-170.

(39) Dobrynin, A. V.; Deshkovski, A.; Rubinstein, M., *Physical Review Letters* **2000,** *84*, 3101-3104.

(40) Parolis, L. A. S.; van der Merwe, R.; Groenmeyer, G. V.; Harris, P. J., *Colloids and Surfaces A: Physicochemical and Engineering Aspects* **2008,** *317*, 109-115.

(41) Fleer, G. J.; Cohen Stuart, M. A. S.; M., J. M. H.; Cosgrove, T. V.; Vincent, B., *Polymers at interfaces*. Chapman & Hall, London: 1993.

Chapter 5: Pectin and Polygalacturonic Acid: Their Model Surfaces and Interactions with Cellulose and Xyloglucan

5.1 Abstract

Xyloglucans and pectins are two major classes of primary plant cell wall polymers and studies of their interactions with each other, as well as cellulose, can enhance the understanding of the assembly of primary plant cell walls. The adsorption of pectin and polygalacturonic acid (PGA) onto different substrates, including regenerated cellulose (RC) and gold was studied via a quartz crystal microbalance with dissipation monitoring (QCM-D). The best coatings were for pectin and PGA adsorbed from a pH = 5.0 citric phosphate buffer. On the gold substrates, pectin and PGA formed better coatings than on RC surfaces as irreversible xyloglucan adsorption was completely inhibited on pectin/PGA-coated gold but not on pectin/PGA-coated RC. For RC surfaces, initial treatment of the RC with xyloglucan completely inhibited the subsequent adsorption of pectin. These results indicated that there were no significant or negligible interactions between xyloglucan and pectins with high galacturonic acid content for the solution condition study.

5.2 Introduction

Primary plant cell walls are interesting, “naturally engineered” structures that combine mechanical strength, protection against pathogen intrusion, tissue cohesion and matter transport.[1] In dicotyledonous plants, primary cell walls consist of approximately 30% cellulose, 30% hemicelluloses, 35% pectins and 1 to 5% structural proteins on a dry mass basis.[2] Cellulose is the most abundant biomacromolecule on earth and is comprised of β-(1→4)-linked glucose in linear chains which further associate into cellulose microfibrils. Xyloglucans, major hemicelluloses in primary cell walls, have a cellulose-like backbone with xylose, galactose and arabinose as side branches. Pectins, possibly the most complex class of biomacromolecules, have domains of homogalacturonan (HG), rhamnogalacturonan I (RG I) and rhamnogalacturonan II (RG II). Pectins are essentially branched heteropolysaccharides with side chains consisting mainly of galactose and arabinose, as well as some less common sugars. The side chains are mainly grafted onto rhamnose units in RGI domains and are widely distributed along the pectin backbone.[3] Polygalacturonic acid (PGA) is a pectin degradation product and commercial PGA is prepared from citrus pectin by partial depolymerization and demethylation. The chains of PGA may be crosslinked by Ca^{2+}, hydrogen bonds and hydrophobic interactions. Greater than 60% of all pectins in the plant cell walls are HG segments with the PGA backbones having varying degrees of methylation and acetylation.[4] The degrees of methylation and acetylation of PGA, as well as the distribution of methyl and acetyl groups, play important roles in these interactions.[5, 6] Typical RG I has alternating galacturonic acid and rhamnose units as a backbone with branching at approximately half of the rhamnose residues. The side chain branches are usually arabinan, galactan and arabinogalactan.[4] The rhamnose units serve as "kinks" along the backbone, giving rise to irregularity that enables the flexibility of pectin molecules.[3] The structure of RG II is even more complicated with four different complex side chains that can be crosslinked by borate ester bonds.[7]

The structures of individual cell wall components are usually well known, however, their specific arrangement and interactions with other cell wall polymers are usually not fully understood. Many studies have focused on the interactions between cellulose and xyloglucan, but the interactions between pectins and other cell wall components, such as cellulose and especially xyloglucan remain under-explored. Spurred by advances in different characterization techniques, several primary cell wall models have emerged and continue to evolve. Keegstra and coworkers proposed that cell wall components are covalently linked together to form giant networks[8] and a recent study confirms the existence of such pectin-xyloglucan complexes via covalent bonding.[9] However, the two polysaccharides within the complex are polydisperse and there is still a possibility that they may only be linked together non-covalently through intermolecular forces.[9] The currently prevailing model, proposed by Hayashi and Fry, states that cellulose microfibrils are coated and tethered by xyloglucan as a network mainly through hydrogen bonding.[10, 11] In this model, pectins form co-extensive but independent networks that physically interact with the cellulose-xyloglucan network. Indeed, pectins are thought to fill the interstices within the cellulose-xyloglucan network. Recently, a new model has been proposed that may alter the existing paradigm of cell wall structure. Dick-Pérez and coworkers suggested a central role of pectin in maintaining the structure and function of plant cell walls.[1] They proved that pectin interacts extensively with both cellulose and hemicelluloses in a single network using 2D and 3D magic-angle-spinning solid-state NMR. As incomplete somewhat contradictory information is available about the interactions between pectin and xyloglucan, the structure of the primary cell wall is still under debate.

The preparation of pectin films dates back several decades, and most of the studies focused upon cast films formed from aqueous solutions of pectin with the introduction of Ca^{2+} or other additives.[12-14] It was recently reported that smooth PGA and xyloglucan films could be prepared by directly spincoating PGA or xyloglucan aqueous solution onto a freshly cleaved mica substrate with subsequent vacuum oven drying.[15] The resulting films were on the order of 100 to 200 nm thick and their roughnesses were ~ 0.3 nm. However, these films had poor resistance to water because of their hydrophilic nature (water contact angles on xyloglucan and PGA films were 25 ± 1° and 13 ± 1°, respectively).[15] When placed in quartz crystal microbalance with dissipation monitoring (QCM-D) or surface plasmon resonance (SPR) modules, these films dissolved into aqueous solutions. A recent study investigated the structural growth of two polysaccharide layers, PGA and sodium alginate, on poly-L-lysine coated SiO_2 substrates. The impacts of Ca^{2+} complexation and variation in ionic strengths were studied by combining results from QCM-D and atomic force microscopy (AFM).[16] Recently Orelma et al. proposed a generic method for the modification of cellulose films by preadsorption of carboxymethyl cellulose (CMC) and chitosan in order to achieve controlled attachment of biomolecules on the modified cellulose surfaces.[17]

In this work, we describe the preparation of pectin and PGA model surfaces in order to study their interactions with cellulose and xyloglucan via QCM-D and SPR. The adsorption of pectin and PGA onto regenerated cellulose (RC) and gold substrates from different solution conditions were studied and compared to the well-known adsorption of xyloglucan. Preparation of pectin and PGA model surfaces can be achieved via their adsorption from citric phosphate buffer onto gold substrates. The resulting model surfaces were used to study interactions between pectin or PGA and xyloglucan, in order to establish a better understanding of potential interactions that may exist in primary plant cell walls.

5.3 Experimental

5.3.1 QCM-D Measurements

Gold and RC-coated QCM-D sensors prepared as in Chapter 3.2.3 were used in this chapter. Detailed procedures for QCM-D measurements are provided in Chapter 3.3.4. Once a water baseline was established, three solution conditions were investigated: water, 1 mM $CaCl_2$ and a citric phosphate buffer (50 mM, pH = 5.0). All measurements were performed under a continuous flow rate of 0.200 $mL \bullet min^{-1}$ at 20.0 °C in triplicate and the averages ± one standard deviation for each condition were calculated.

5.3.2 SPR Measurements

Gold SPR sensors were used for all SPR measurements in this chapter. Detailed procedures for SPR measurements were provided in Chapter 3.3.5. All of the aqueous solutions were degassed before use for the avoidance of the introduction of air bubbles into the system. Each SPR experiment was performed at 20.0 °C in triplicate and the average values ± one standard deviation were calculated.

5.3.3 AFM Measurements

Detailed procedures for AFM measurements were provided in Chapter 3.3.3. Pectin and PGA layers for interaction studies with xyloglucan were dried in a vacuum oven at 45 °C for 5 h and then imaged with an MFP-3D-Bio atomic force microscope (MFP-3D-BIO, Asylum Research) in tapping mode. The AFM images were collected under ambient conditions using a silicon tip (OMCL-AC 160TS, Olympus Corp.). The reported roughnesses are root-mean-square (RMS) values determined from 2 µm × 2 µm scan areas.

5.4 Results and Discussion

5.4.1 Adsorption of Pectin and PGA onto Cellulose

Pectin and PGA adsorption onto cellulose surfaces was investigated by QCM-D. Prior to the introduction of pectin or PGA solutions, water and the appropriate solvent (water, $CaCl_2$ or citric phosphate buffer) were sequentially flowed through the QCM-D modules. Figure 5.1 shows scaled frequency changes ($\Delta f/n$) and dissipation changes (ΔD) as a function of time for pectin adsorption onto RC surfaces. The first observed small change arose from viscosity and density changes associated with the switch from water to the solvent ($CaCl_2$ or citric phosphate buffer) and returned to zero upon a switch back to water in control experiments. Immediately after the injection of pectin from a given solvent, there was a significant $\Delta f/n$ decrease and a ΔD increase, followed by a much more gradual change of $\Delta f/n$ and ΔD. After 30 min of adsorption time, the same solvent and finally water were introduced for the removal of reversibly bound molecules. For the case where water was used as a solvent, shifts in $\Delta f/n$ and ΔD were small and comparable to the detection limit of the instrument. This observation is quite different from xyloglucan adsorption onto RC surfaces under identical conditions (Figure 5.3, diamonds), suggesting a weaker interaction between cellulose and pectin compared to the well-known cellulose-xyloglucan interactions. Weaker pectin adsorption may arise from the negative charges carried on the pectin and residual negative charges on cellulose (surface potential = -2 mV) introduced by the pulping process. This behavior is similar to the case of carboxymethyl cellulose (CMC) adsorption onto cellulose surfaces.[18] Romanowski and coworkers found that the adsorption of plasmid DNA onto mineral surfaces was promoted by the introduction of divalent cations as well as solution conditions with high ionic strength,[19] thus the effects of Ca^{2+} and a citric phosphate buffer with high ionic strength (50 mM, pH = 5.0) were investigated in this study. Greater changes in both $\Delta f/n$ and ΔD between the final and initial water baselines were obtained for adsorption from 1 mM $CaCl_2$ and the citric phosphate buffer (50 mM, pH = 5.0), an indication of greater irreversible adsorption onto the cellulose surfaces from these solution conditions. The value of 1 mM for the $CaCl_2$ represented the maximum value that could be used with retention of PGA solubility. The adsorbed amount, Γ_{QCM-D}, was calculated from the Sauerbrey equation, as the change in ΔD was relatively small ($< 4 \times 10^{-6}$). With the introduction of divalent Ca^{2+} ions, crosslinks that enhanced pectin adsorption onto cellulose surfaces formed. This behavior is similar to the case of CMC where the presence of divalent Ca^{2+} promoted CMC adsorption onto cellulose and the formation of a hydrated layer on the substrate.[17, 18] For the case of citric phosphate buffer condition, most of all the carboxyl groups along the pectin backbones were ionized (negatively charged) at a pH of 5.0. The hindrance to adsorption by electrostatic repulsions between an adsorbate and a surface can be counteracted by high ionic strength solutions. With sufficiently high electrolyte concentrations, adsorption can occur even when the polymer and substrate are both anionic, as in the current study using pectin and RC surfaces. Similar QCM-D adsorption profiles were obtained for PGA adsorbed from water, 1 mM $CaCl_2$ and a citric phosphate buffer (50 mM, pH = 5.0) onto RC surfaces as provided in Figure 5.2. Changes in $\Delta f/n$, ΔD and adsorbed amount Γ_{QCM-D} are summarized in Table 5.1. The Γ_{QCM-D} of PGA were greater than pectin for all solution conditions tested. Greater PGA adsorption was attributed to the regular structure of PGA molecules and higher galacturonic acid content that allowed better packing on the substrate compared to pectin molecules with pendant side chains. It was also recently demonstrated through enzymatic and alkali degradation procedures that there are non-covalent interactions between pectin and cellulose, mediated by the arabinan and pectic galactan side chains.[20] From the QCM-D data, even at low ionic strength, Ca^{2+} was efficient enough to improve pectin or PGA adsorption onto RC surfaces with Γ_{QCM-D} comparable to citric phosphate buffer with high ionic strength (Table 5.1). The main driving force for pectin or PGA adsorption onto RC surfaces is electrostatic interactions, as both the introduction of Ca^{2+} and citric phosphate buffer solution with high ionic strength promotes the adsorbed amounts by neutralizing and/or screening the anionic groups on pectin/PGA and cellulose.

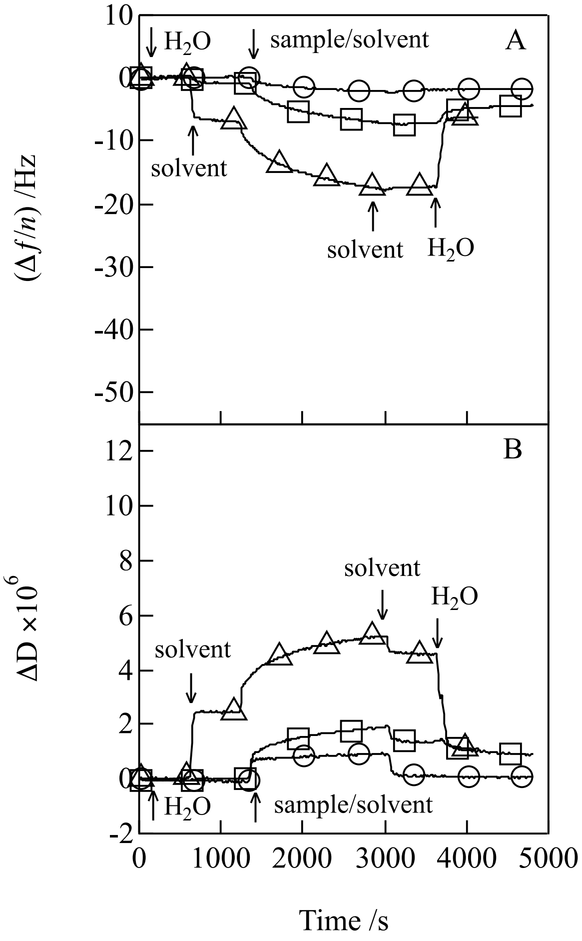

Figure 5.1 Representative time dependent (A) $\Delta f/n$ and (B) ΔD profiles for pectin (500 mg•L^{-1}) adsorption onto RC surfaces from (O) water, (☐) 1 mM $CaCl_2$ and (Δ) citric phosphate buffer (50 mM, pH = 5.0) at 20.0 °C. Data correspond to the fifth overtone and arrows indicate where solutions were switched.

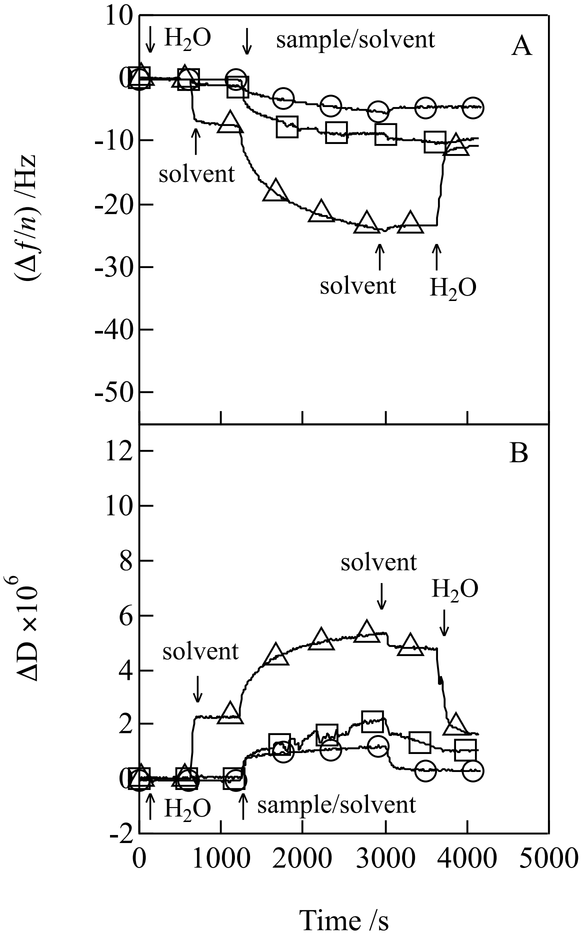

Figure 5.2 Representative time dependent (A) $\Delta f/n$ and (B) ΔD profiles for PGA (500 mg•L^{-1}) adsorption onto RC surfaces from (O) water, (☐) 1mM $CaCl_2$ and (Δ) citric phosphate buffer (50 mM, pH = 5.0) at 20.0 °C. Data correspond to the fifth overtone and arrows indicate where solutions were switched.

Table 5.1 Irreversible $\Gamma_{QCM\text{-}D}$ for pectin and PGA adsorption onto different substrates from 500 mg•L^{-1} solutions at 20.0 °C.[a,b]

	$^a\Gamma_{QCM\text{-}D,\ pectin}$ /mg•m^{-2}			$^a\Gamma_{QCM\text{-}D,\ PGA}$ /mg•m^{-2}	
	RC	**Gold**		**RC**	**Gold**
H_2O	0.27 ± 0.11	1.52 ± 0.08	**H_2O**	0.73 ± 0.14	2.23 ± 0.04
$CaCl_2$[b]	0.94 ± 0.14	3.27 ± 0.21	**$CaCl_2$**[b]	1.56 ± 0.14	3.36 ± 0.71
buffer[c]	1.17 ± 0.09	4.57 ± 0.02	**buffer**[c]	1.88 ± 0.09	2.65 ± 0.27

a. Calculated from Equation 3.1 for the fifth overtone.
b. 1 mM $CaCl_2$
c. A citric phosphate buffer (50 mM, pH = 5.0)

5.4.2 Adsorption of Xyloglucan onto Cellulose, and Pectin- and PGA-coated Cellulose

Xyloglucan is known to interact with cellulose, presumably through hydrogen bonds.[10] Furthermore, it is believed that xyloglucan can bind to the surface and tether the cellulose microfibrils. Data from QCM-D in Figure 5.1 showed slight irreversible pectin adsorption from water onto cellulose surfaces with $\Delta f/n$ = -1.5 Hz, a value that corresponds to $\Gamma_{QCM\text{-}D}$ = 0.3 mg•m^{-2} on the basis of Sauerbrey equation (Equation 3.1). Irreversible pectin adsorption from water onto cellulose is much smaller than xyloglucan adsorption onto cellulose ($\Gamma_{QCM\text{-}D}$ = 3.4 mg•m^{-2}) under the same conditions (Figure 5.2, diamonds). The differences in irreversible adsorption indicate much stronger xyloglucan-cellulose interactions than the pectin-cellulose interactions.

After the preadsorption of pectin or PGA onto RC surfaces, the subsequent adsorption of xyloglucan onto pectin-coated cellulose surfaces was studied. As seen in Figure 5.3, Δf/n values after rinsing off reversibly bound xyloglucan are nearly identical for xyloglucan irreversibly bound onto virgin cellulose and cellulose with different preadsorbed pectin coatings. This result indicated the presence of pectin did not substantially decrease the amount of xyloglucan bound to cellulose. On the basis of previous studies, polymer adsorption tends to form a de Gennes self-similar carpet layer.[21, 22] This layer consists of a dense layer comparable to the size of the adsorption blob and a more diffuse layer. The dense layer has a high fraction of “train” segments, whereas the diffuse layer is comprised of “loops” and “tails”. The inability of pectin to substantially inhibit xyloglucan adsorption likely reflects incomplete blockage of surface sites that still allows xyloglucan to bind to cellulose and form a self-similar layer. The same experiments were carried out for PGA-coated cellulose surfaces as provided in Figure 5.4, and there were no significant differences in xyloglucan adsorption onto pectin- or PGA-coated RC surfaces. This result is also in agreement with the conclusion of Zykwinska and coworkers from *in vitro* binding assays of ternary pectin/xyloglucan/cellulose systems.[23]

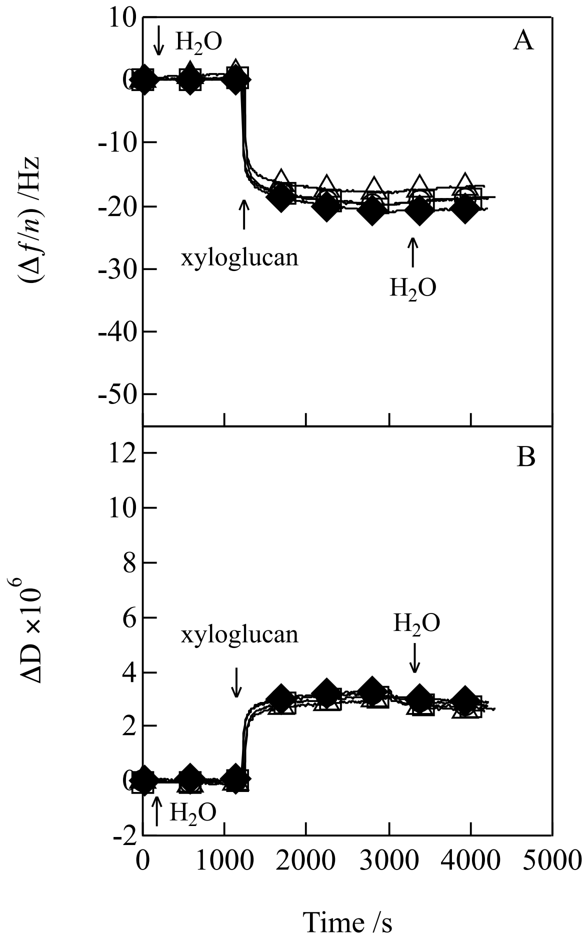

Figure 5.3 Representative time dependent (A) Δ*f*/*n* and (B) ΔD profiles for xyloglucan (500 mg•L^{-1}) adsorption onto (◆) RC and pectin-coated RC surfaces obtained from different solution conditions: (O) water, (☐) 1 mM $CaCl_2$ and (Δ) citric phosphate buffer (50 mM, pH = 5.0) at 20.0 °C. Data correspond to the fifth overtone and arrows indicate where solutions were switched.

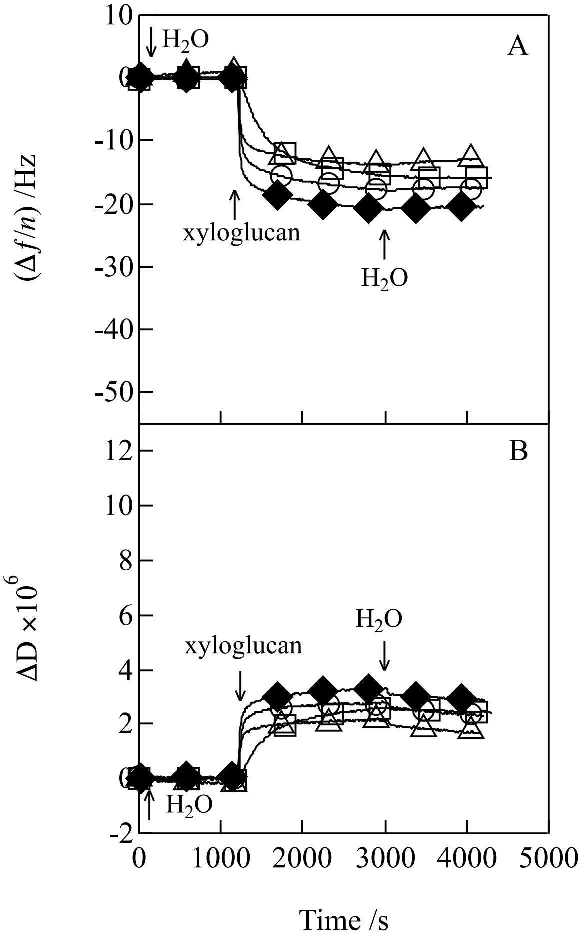

Figure 5.4 Representative time dependent (A) Δ*f*/*n* and (B) ΔD profiles for xyloglucan (500 mg•L^{-1}) adsorption onto (◆) RC and PGA-coated RC surfaces obtained from different solution conditions: (O) water, (☐) 1 mM $CaCl_2$ and (Δ) citric phosphate buffer (50 mM, pH = 5.0) at 20.0 °C. Data correspond to the fifth overtone and arrows indicate where solutions were switched.

5.4.3 Adsorption of Pectin and PGA onto Gold Substrates

The adsorption of pectin and PGA onto gold substrates was quite different from their adsorption onto RC surfaces from citric phosphate buffer (50 mM, pH = 5.0) as shown in Figures 5.5 and 5.6, respectively. Changes in Δ*f*/*n* and ΔD were much larger for pectin and PGA adsorption onto gold than onto RC surfaces. These observations were true both prior to and after rinsing, indicating greater amounts of reversibly and irreversibly adsorbed pectin or PGA, respectively, onto the gold substrates. The adsorption kinetics were faster for gold than RC substrates, an indication of greater pectin and PGA affinity towards the gold substrates than cellulose. As polyelectrolytes, pectin and PGA adsorption can be affected by a series of parameters: such as solvent conditions, charge density, molecular weight, hydrophobicity of the polymer as well as substrate properties.[24] The gold substrate (water contact angle of 62 ± 2°)[25] is more hydrophobic than the RC substrate (water contact angle of 27 ± 1°).[26] Stronger pectin adsorption onto gold relative to PGA under the same conditions would be attributed to more methyl esters along the pectin backbones that contribute to hydrophobic characters compared to PGA backbones with carboxyl groups at the *C*6 positions. The stronger attraction and greater affinity towards gold substrates for pectin molecules are attributed to stronger van der Waals interactions between pectin and RC substrates. In addition, it was also recently found that cellulose derivatives irreversibly adsorbed onto a flat gold substrate with greater adsorbed amounts from a citrate buffer.[27] Previous studies have also shown strong affinity of citrate ions towards gold substrates leading to the formation of a citrate layer on gold substrates.[27] The adsorption enhancement could be attributed to the negatively charged citrate layer on gold that enhances electrostatic interactions between adsorbate and the gold substrate by activating more adsorption sites.[27, 28] The enhanced electrostatic interactions also contributed to greater adsorption of pectin compared to PGA onto gold substrates. Moreover, when Ca^{2+} or citric phosphate buffer solution with high ionic strength was introduced, adsorption of pectin/PGA onto gold substrate was also enhanced. As a result, both van der Waals interactions and electrostatic interactions play important roles in pectin and PGA adsorption onto gold substrates.

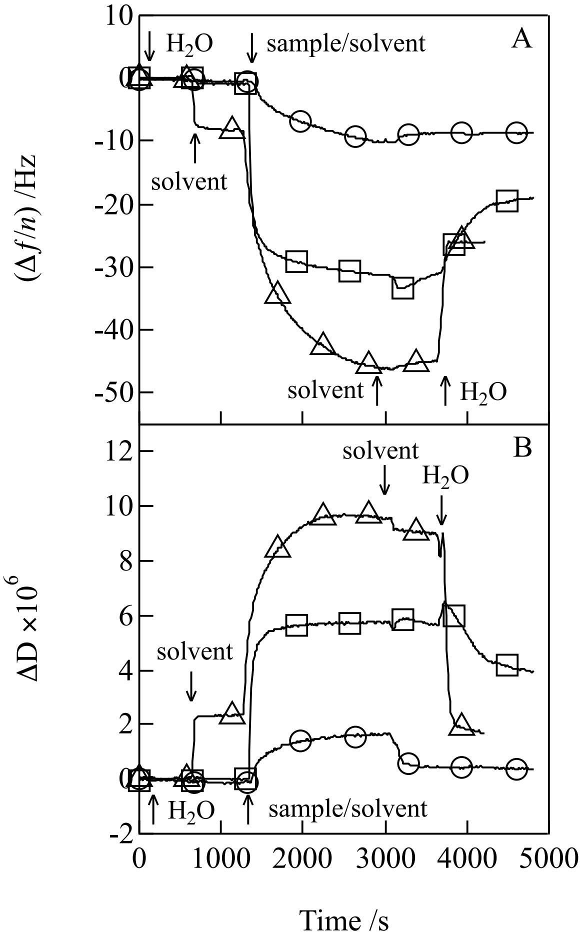

Figure 5.5 Representative time dependent (A) Δ*f*/*n* and (B) ΔD profiles for pectin (500 mg•L^{-1}) adsorption onto gold substrates from (O) water, (☐) 1 mM $CaCl_2$ and (Δ) citric phosphate buffer (50 mM, pH = 5.0) at 20.0 °C. Data correspond to the fifth overtone and arrows indicate where solutions were switched.

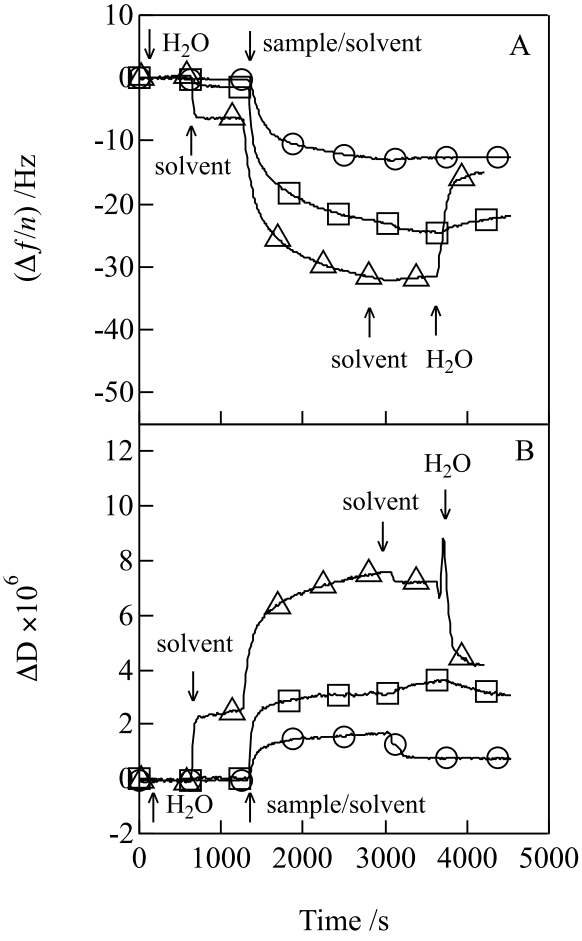

Figure 5.6 Representative time dependent (A) Δ*f*/*n* and (B) ΔD profiles for PGA (500 mg•L^{-1}) adsorption onto gold substrates from (O) water, (□) 1 mM $CaCl_2$ and (Δ) citric phosphate buffer (50 mM, pH = 5.0) at 20.0 °C. Data correspond to the fifth overtone and arrows indicate where solutions were switched.

After the preadsorption of pectin and PGA onto gold substrates, the resulting pectin- and PGA-coated gold substrates were dried at 45 °C for 5 h in a vacuum oven prior to AFM measurements. Representative AFM images of the gold substrates modified by pectin or PGA adsorbed from citric phosphate buffer (50 mM, pH = 5.0) with concentrations of 500 mg•L^{-1} and 1000 mg•L^{-1} are provided in Figures 5.7 and 5.8, respectively. Pectin appeared as aggregates on the gold substrate with a small overall

RMS roughness (< 2 nm). For PGA, solutions with higher concentrations (1000 mg•L^{-1}) yielded pinhole-free and smooth layers with RMS roughnesses of ~ 1.4 nm that were comparable to pectin layers obtained under the same conditions (Figure 5.6C). At lower PGA concentrations, voids in the film were easily identified from the AFM images (Figure 5.6B), and the resulting films had larger RMS roughnesses (~ 3.4 nm). Pectin formed better coatings than PGA on gold substrates when lower concentrations were used, while pinhole-free films with similar morphology were formed for both pectin and PGA on gold substrates when using higher concentrations. Better quality pectin films at lower concentrations relative to PGA were reflected in greater $\Gamma_{QCM\text{-}D}$ for pectin layers. This result can be explained by both the presence of methyl esters along pectin backbones that enhances van der Waals interactions between pectin and gold substrate as well as the side chains of pectin which are known to hold more water molecules within the adsorbed pectin layer.[3, 29] In addition, previous studies showed there is a noticeable increase in the flexibility of pectins due to the presence of rhamnose units within pectin backbones.[30] Pectin chains with greater flexibility also contribute to the stronger pectin adsorption onto gold substrates compared to more rigid PGA backbones due to stronger electrostatic repulsions between PGA chains. Pectin molecules can easily undergo conformational rearrangements and cover all the accessible gold substrates. This result is similar to previous studies on equilibrium and dynamic properties of adsorbed polymer as a function of polymer chain flexibility.[31] Flexible chains showed a greater fraction of "loop" and "tail" conformations as well as shorter integration times, denoted as the time for adsorbed polymers to become fully integrated into the adsorbed layer, compared to rigid chains.[31]

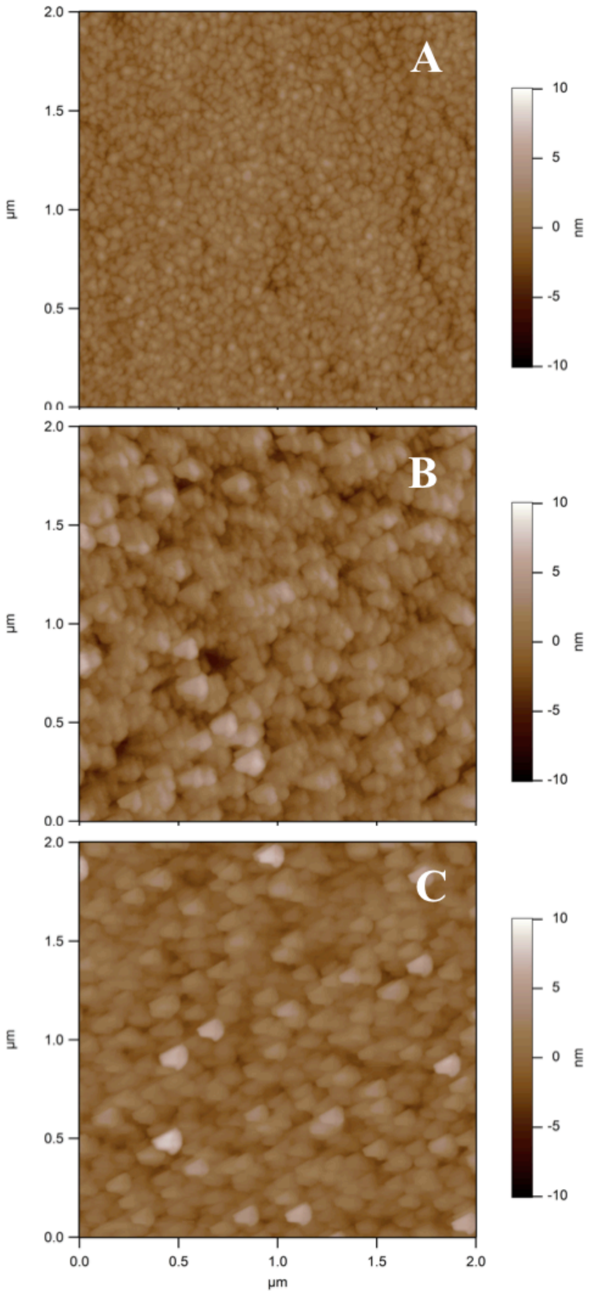

Figure 5.7 Representative AFM height images of (A) a gold substrate and gold substrates after the adsorption of pectin from citric phosphate buffer (50 mM, pH = 5.0) with pectin concentrations of (B) 500 mg•L^{-1} and (C) 1000 mg•L^{-1} at 20.0 °C. The RMS roughnesses of (A) 1.0 nm, (B) 1.8 nm and (C) 1.5 nm were obtained from the entire 2 µm × 2 µm scan areas and the z range was 20 nm.

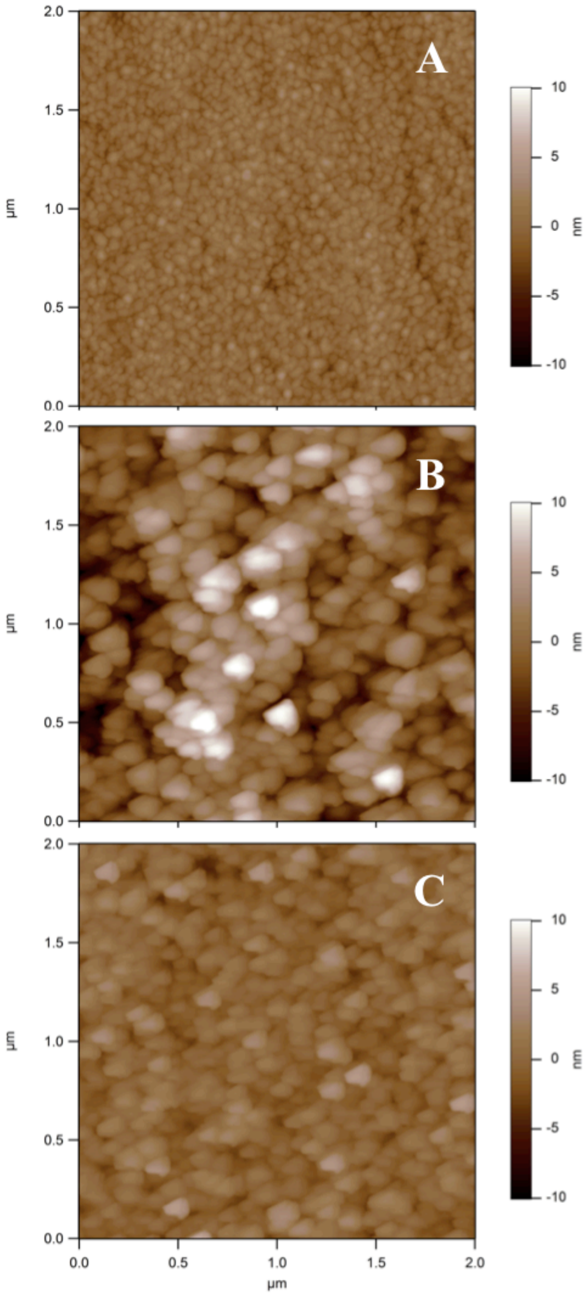

Figure 5.8 Representative AFM height images of (A) a gold substrate and gold substrates after the adsorption of PGA from citric phosphate buffer (50 mM, pH = 5.0) with a PGA concentration of (B) 500 mg•L^{-1} and (C) 1000 mg•L^{-1} at 20.0 °C. The RMS roughnesses of (A) 1.0 nm, (B) 3.4 nm and (C) 1.4 nm were obtained from the entire 2 µm × 2 µm scan areas and the z range was 20 nm.

The water contents associated with the pectin or PGA layers prepared by adsorption from citric phosphate buffer (50 mM, pH = 5.0) onto the gold substrates were also investigated. Assuming ideal solution behavior, the water contents can be calculated from the different Γ determined by QCM-D and SPR through Equation 2.30 (Figure 5.9). For films prepared from the citric phosphate buffer (50 mM, pH = 5.0), the water contents of the adsorbed pectin and PGA layers were 58 ± 2% and 39 ± 2%, respectively. This difference is attributed to a more highly charged PGA with a more extended chain conformation. As a consequence, PGA adsorbed with a flatter conformation and less coupled water in accord with theoretical work carried out by Rubinstein *et al.* and Fleer *et al.*[22, 32] This result is also similar to CMC adsorption onto cellulose where CMC samples with higher degree of substitution (DS) tend to form flatter conformations due to the electrostatic repulsions between CMC molecules.

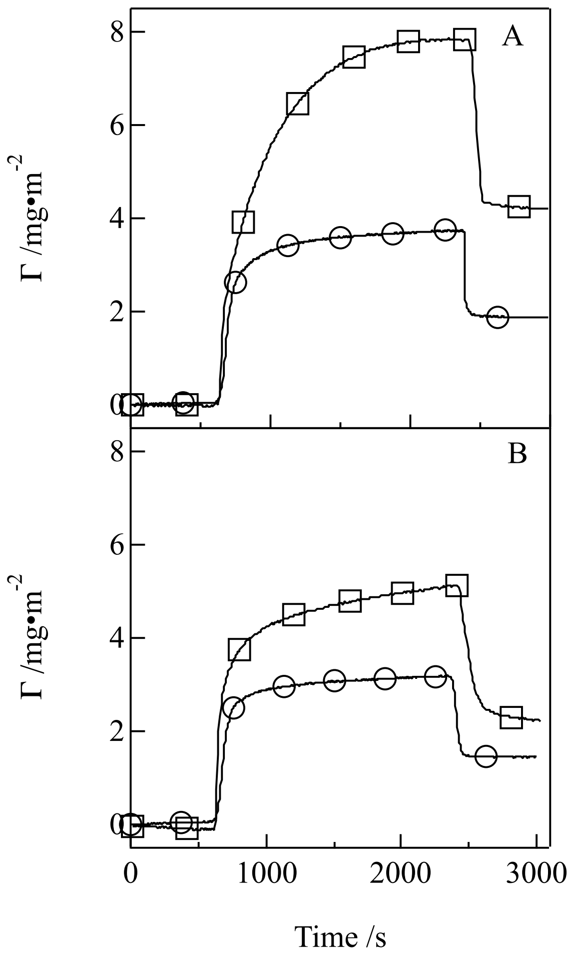

Figure 5.9 Representative adsorption profiles obtained from (☐) QCM-D and (O) SPR measurements for (A) pectin and (B) PGA adsorbed onto gold from 500 mg•L^{-1} solutions in citric phosphate buffer (50 mM, pH = 5.0) at 20.0 °C.

Dynamic adsorption isotherms were obtained for pectin and PGA adsorbed from citric phosphate buffer (50 mM, pH = 5.0) onto gold substrates (Figure 5.10). In Figure 5.10, the $\Gamma_{QCM\text{-}D}$ values are plotted against the concentration of the bulk solution. Adsorption isotherms were obtained by two different methods: individual and sequential adsorption experiments. For the range of concentrations from 5 mg•L^{-1} to 1000 mg•L^{-1}, both pectin and PGA irreversibly adsorbed onto gold. In both cases, the adsorption time was fixed at 20 min. Under these conditions, $\Gamma_{QCM\text{-}D}$ increased with increasing bulk concentration. It was also observed that the adsorbed amounts obtained from adsorption experiments for a single concentration were lower than those obtained from sequential adsorption. For sequential adsorption, pectin molecules that adsorbed onto gold at lower concentrations remained on the surface. Additional pectin was able to adsorb onto the partially covered gold substrates leading to higher adsorbed amounts compared to the individual adsorption experiments. These differences may reflect initially flatter binding conformations for pectin and PGA adsorbed at lower concentrations, followed by the adsorption of the three-dimensional chains on top of the flat underlayer in the sequential adsorption experiments. In contrast, single-shot adsorption at high concentrations occurred rapidly with likely retention of a three-dimensional conformation that yielded a film which lacked a flat underlayer. This observation is also consistent with experimental[33] and theoretical studies[21] on polymer adsorption at solid/liquid interfaces leading to the formation of a tightly adsorbed underlayer and a loosely bound outer layer.

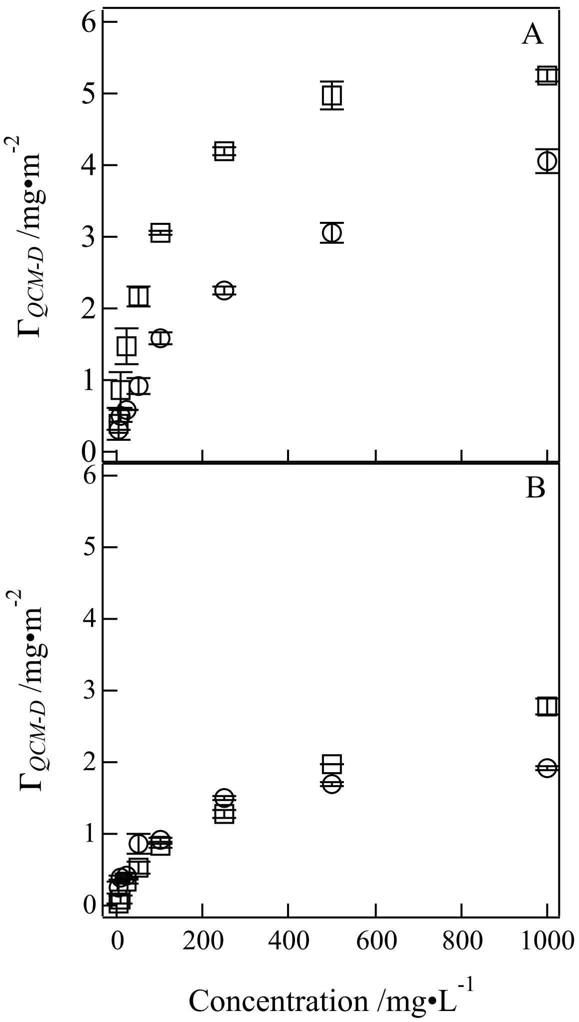

Figure 5.10 Dynamic QCM-D adsorption isotherms for (A) pectin and (B) PGA adsorbed onto gold from citric phosphate buffer (50 mM, pH = 5.0) by (O) individual and (□) sequential adsorption at 20.0 °C. The data are average values ± one standard deviation error bars. The adsorption time for each solution was fixed at 20 min.

The dynamics of pectin adsorption from citric phosphate buffer onto gold were also studied via QCM-D (Figure 5.11). The adsorption process proceeded until equilibrium occurred. Equilibrium was operationally defined as the point where values of $\Delta f/n$ and ΔD were constant for more than 10 minutes. Both $\Delta f/n$ values for pectin prior to rinsing (~ -45 Hz) and after rinsing with water (~ -28 Hz) were independent of concentration. The values of the equilibrium, irreversibly adsorbed $\Gamma_{QCM\text{-}D}$ calculated from the Sauerbrey equation (Equation 3.1) for six concentrations ranging from 25 to 1000 mg•L^{-1} were nearly the same ($\Gamma_{QCM\text{-}D} \sim 5.0$ mg•m^{-2}). This result can be explained as complete saturation of the exposed gold substrate. Given sufficient time, the pectin adsorbed and occupied the entire gold substrate and formed a stable hydrated layer. The overall adsorbed amount most closely corresponded to the result from sequential adsorption experiments presented in Figure 5.10A. The adsorption from different concentrations exhibited different adsorption kinetics at early stages of adsorption and the initial adsorption rate increased with increasing concentration (Figure 5.11B). As seen in Figure 5.11B, 20 min was adequate for surface saturation for samples with pectin concentrations of 500 or 1000 mg•L^{-1}. Since the ultimate goal of this work was the preparation of smooth and homogeneous pectin/PGA layers, this observation is the reason why 20 min adsorption times were used for Figure 5.10.

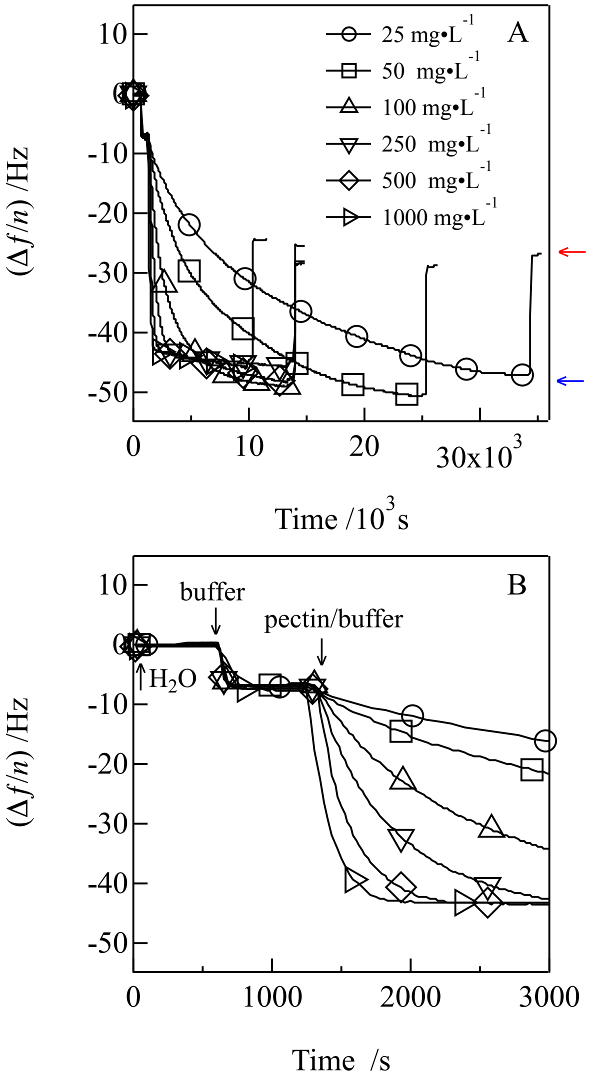

Figure 5.11 Kinetic studies for pectin adsorption onto gold from citric phosphate buffer (50 mM, pH = 5.0) with different pectin concentrations as indicated in the legend at 20.0 °C. The adsorption process proceeded until equilibrium occurred. (A) Adsorption all the way through desorption after rinsing the surface with buffer and then water. The blue and red arrows next to graph (A) represent $(\Delta f/n)_{\mathrm{minimum}}$ prior to and after rinsing with water, respectively. (B) The same data as (A) for the first 3000 sec to highlight the effect of concentration on the adsorption kinetics. Data correspond to the fifth overtone and arrows indicate where solutions were switched.

5.4.4 Adsorption of Xyloglucan onto Gold, and Pectin- and PGA-coated Gold

Representative data for the adsorption of xyloglucan from 500 mg•L^{-1} aqueous solutions onto bare gold and gold substrates covered with preadsorbed pectin layers are provided in Figure 5.10. Xyloglucan irreversibly adsorbed onto gold substrates with greater changes in $\Delta f/n$ and ΔD than pectin or PGA under the same conditions. Xyloglucan has a stronger affinity towards gold substrates and the $\Gamma_{QCM\text{-}D}$ (Figure 5.12, diamonds) after rinsing with water corresponded to an irreversibly adsorbed $\Gamma_{QCM\text{-}D}$ = 5.8 ± 0.2 mg•m^{-2}. For gold substrates with preadsorbed pectin layers formed from solutions of different concentrations, the subsequent binding of xyloglucan was significantly diminished. For the case where pectin layers were prepared from citric phosphate buffer (50 mM, pH = 5.0) with a pectin concentration of 500 mg•L^{-1}, $\Delta f/n$ and ΔD returned to the baseline after the switch back to water. This result showed that irreversible adsorption of xyloglucan was completely inhibited by the preadsorbed pectin layer. This result led to a systematic study of the best conditions for the formation of pectin and PGA layers from citric phosphate buffer (50 mM, pH = 5.0). Figure 5.13 shows the dependence of the surface concentration of irreversibly adsorbed xyloglucan ($\Gamma_{QCM\text{-}D,\, xyloglucan}$) on the surface concentration of the preadsorbed pectin layer ($\Gamma_{QCM\text{-}D,\, pectin}$). Bulk solution concentrations used for the control of $\Gamma_{QCM\text{-}D,\, pectin}$ are summarized in Table 5.2. As seen in Figure 5.13, incomplete coverage of the gold substrate by the pectin layer allowed subsequent adsorption of some xyloglucan onto the surface. For $\Gamma_{QCM\text{-}D,\, pectin} > 2.1$ mg•m^{-2}, the pectin layer completely coated the gold substrate and completely inhibited xyloglucan adsorption. Similar results were obtained for xyloglucan adsorption onto PGA-coated gold substrates (Figure 5.14). The bulk solution concentrations used to achieve different values of $\Gamma_{QCM\text{-}D,\ PGA}$ in Figure 5.14 are also summarized in Table 5.2. In contrast to pectin, complete PGA coverage of the gold was not achieved until the concentration of the PGA solution was increased to 1000 mg•L^{-1} in citric phosphate buffer (50 mM, pH = 5.0). This result was consistent with AFM images obtained for preadsorbed pectin and PGA layers. For the case of pectin adsorption from both 500 and 1000 mg•L^{-1} solutions in citric phosphate buffer (50 mM, pH = 5.0), gold substrates were completely covered by pectin layers with small RMS roughnesses (Figure 5.7). In contrast, voids were identified in AFM images for PGA layers on gold formed from PGA solutions with concentrations below 1000 mg•L^{-1} (Figure 5.8).

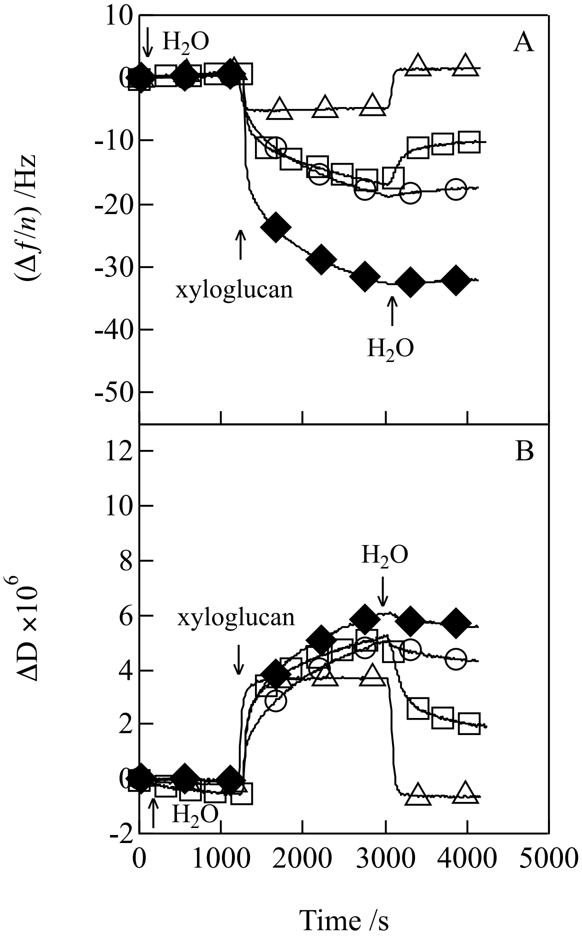

Figure 5.12 Representative time dependent (A) $\Delta f/n$ and (B) ΔD profiles for xyloglucan (500 mg•L^{-1}) adsorption onto (◆) gold and pectin-coated gold substrates obtained from solutions with pectin concentrations of 500 mg•L^{-1} in (O) water, (□) 1 mM $CaCl_2$ and (Δ) citric phosphate buffer (50 mM, pH = 5.0) at 20.0 °C. Data correspond to the fifth overtone and arrows indicate where solutions were switched.

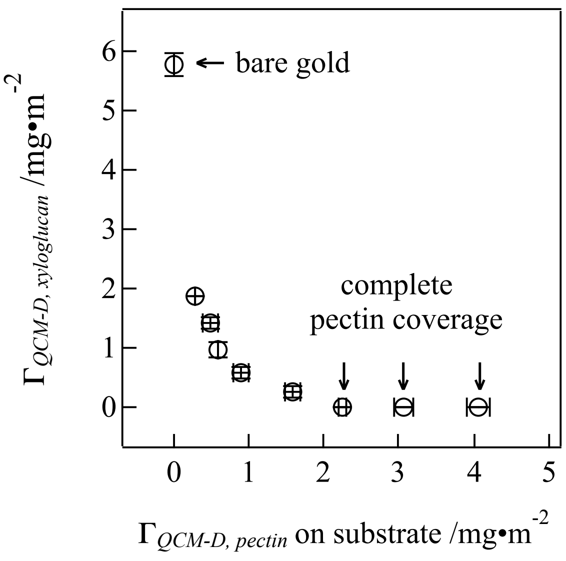

Figure 5.13 Xyloglucan adsorption onto gold and pectin-coated gold substrates from 500 mg•L^{-1} aqueous solutions at 20.0 °C. Gold substrates with different values of $\Gamma_{QCM\text{-}D,\,pectin}$ were obtained by the adsorption of pectin onto gold from citric phosphate buffer solutions (50 mM, pH = 5.0) with different bulk concentrations. The adsorption time was fixed at 20 min for each concentration. Specific solution conditions used to produce different $\Gamma_{QCM\text{-}D,\,pectin}$ are summarized in Table 5.2. Error bars represent one standard deviation.

Table 5.2 Irreversible $\Gamma_{QCM\text{-}D}$ for pectin or PGA adsorption onto gold substrates from different bulk concentrations in citric phosphate buffer (50 mM, pH = 5.0) at 20.0 °C.[a]

Concentration /mg• L^{-1}	**[a]$\Gamma_{QCM\text{-}D,\,pectin}$ /mg• m^{-2}**	**[a]$\Gamma_{QCM\text{-}D,\,PGA}$ /mg• m^{-2}**
5	0.30 ± 0.01	0.24 ± 0.07
10	0.50 ± 0.09	0.40 ± 0.04
25	0.59 ± 0.01	0.41 ± 0.02
50	0.91 ± 0.11	0.87 ± 0.13
100	1.59 ± 0.10	0.92 ± 0.02
250	2.24 ± 0.05	1.50 ± 0.02
500	3.06 ± 0.14	1.70 ± 0.02
1000	4.06 ± 0.16	1.91 ± 0.02

a. Calculated from Equation 3.1 for the fifth overtone.

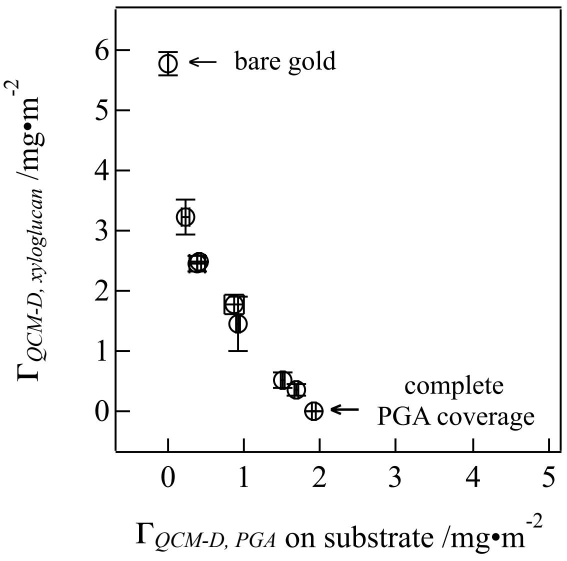

Figure 5.14 Xyloglucan adsorption onto gold and PGA-coated gold substrates from 500 mg•L^{-1} aqueous solutions at 20.0 °C. Gold substrates with different values of $\Gamma_{QCM\text{-}D,\ PGA}$ were obtained by the adsorption of PGA onto gold from citric phosphate buffer solutions (50 mM, pH = 5.0) with different bulk concentrations. The adsorption time was fixed at 20 min for each concentration. Specific solution conditions used to produce different $\Gamma_{QCM\text{-}D,\ PGA}$ are summarized in Table 5.2. Error bars represent one standard deviation.

The results of Figures 5.13 and 5.14 can be interpreted as xyloglucan only adsorbed onto exposed gold substrates and not onto the regions covered by pectin or PGA. As more pectin or PGA adsorbed, less gold substrate was available for subsequent xyloglucan adsorption. This interpretation is presented schematically in Figure 5.15, where complete inhibition of xyloglucan adsorption did not occur until pectin completely coated the gold substrate. The results for the gold substrates are similar to studies by Zykwinska *et al.* that concluded xyloglucan and pectin are most likely in competition to form associations with cellulose.[23]

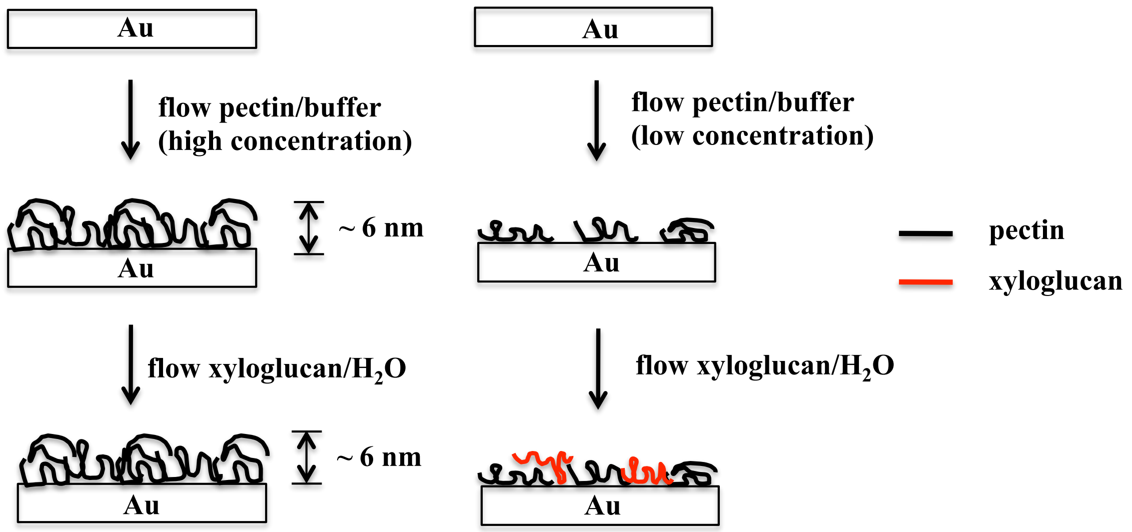

Figure 5.15 Schematic representations of the preadsorption of pectin from citric phosphate buffer (50 mM, pH = 5.0) onto gold substrates and subsequent adsorption of xyloglucan onto gold substrates completely or partially coated by pectin. Thickness values were calculated on the basis of results from Voigt-based viscoelastic modeling as described in Chapter 3.3.4.

5.4.5 Interactions between Pectin and Xyloglucan

Although non-specific interactions between pectin and xyloglucan have been hypothesized,[34] significant non-specific interactions between these two entities were not observed in the present study. It was observed that when pectin or PGA fully coated the gold substrate, xyloglucan adsorption was completely inhibited. This observation meant there were no significant interactions between xyloglucan and pectin with high galacturonic acid content for the solution condition study. Moreover, xyloglucan-coated RC surfaces completely inhibited pectin adsorption for all solution conditions (Figure 5.16). As shown in Figure 5.1 (triangles), pectin can irreversibly adsorb onto RC surfaces from citric phosphate buffer (50 mM, pH = 5.0); however, pectin adsorption onto xyloglucan-coated RC surfaces had $\Delta f/n$ and ΔD values that returned to the baseline after rinsing. As expected, solution conditions that led to weaker pectin adsorption onto RC surfaces (water or $CaCl_2$) were also inhibited by a preadsorbed xyloglucan layer. This result suggests that there is no significant or negligible interaction between xyloglucan and pectin with high galacturonic acid content for the solution condition study. However, our results cannot rule out the possibility that there are covalent bonds between xyloglucan and pectin, leading to pectin-xyloglucan complexes. Evidence for pectin-xyloglucan complexes have been reported by several researchers for inseparable fractions of polysaccharides co-extracted from the cell walls.[7-9, 29]

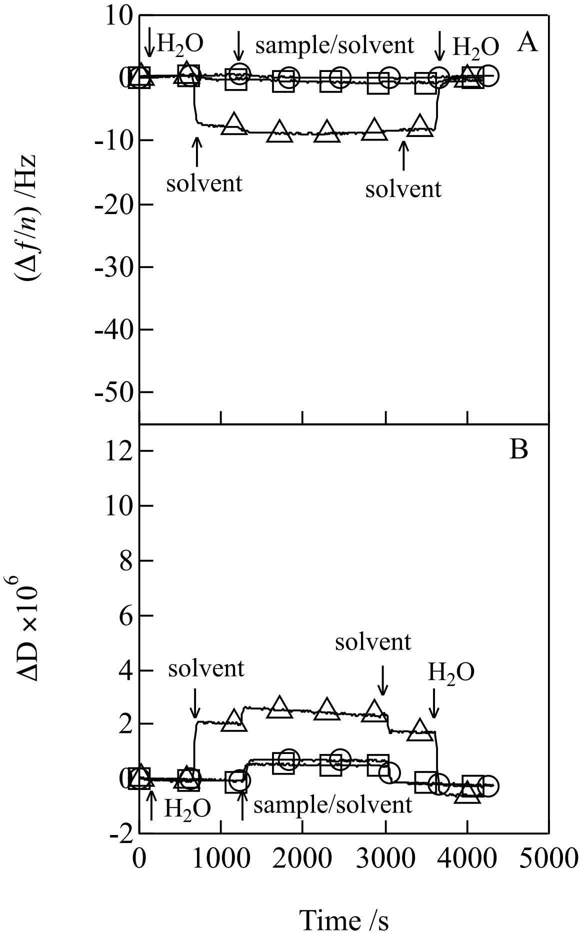

Figure 5.16 Representative time dependent (A) Δ*f*/*n* and (B) ΔD profiles for pectin (500 mg•L^{-1}) adsorption onto xyloglucan-coated RC surfaces from (O) water, (☐) 1 mM $CaCl_2$ and (Δ) citric phosphate buffer (50 mM, pH = 5.0) at 20.0 °C. Data correspond to the fifth overtone and arrows indicate where solutions were switched.

5.5 Conclusions

In the present study, both pectin and PGA adsorbed onto cellulose as well as gold with greater adsorption from solutions containing calcium ions or citric phosphate buffered to pH = 5.0. These films were stable upon switching to water and were used as platforms for evaluating pectin and PGA interactions with xyloglucan. Complete coverage of the gold substrates by pectin or PGA inhibited xyloglucan adsorption.

Likewise, xyloglucan adsorption onto regenerated cellulose surfaces completely inhibited pectin adsorption. These results indicate that there is no significant or negligible physical interaction between xyloglucan and pectins with high galacturonic acid content for the solution condition study.

5.6 References

(1) Dick-Pérez, M.; Zhang, Y.; Hayes, J.; Salazar, A.; Zabotina, O. A.; Hong, M., *Biochemistry* **2011,** *50*, 989-1000.

(2) Vorwerk, S.; Somerville, S.; Somerville, C., *Trends in Plant Science* **2004,** *9*, 203-209.

(3) Hwang, J.; Pyun, Y. R.; Kokini, J. L., *Food Hydrocolloids* **1993,** *7*, 39-53.

(4) Caffall, K. H.; Mohnen, D., *Carbohydrate Research* **2009,** *344*, 1879-1900.

(5) Thibault, J. F.; Rinaudo, M., *Biopolymers* **1986,** *25*, 455-468.

(6) Ralet, M.-C.; Crépeau, M.-J.; Buchholt, H.-C.; Thibault, J.-F., *Biochemical Engineering Journal* **2003,** *16*, 191-201.

(7) Abdel-Massih, R. M.; Baydoun, E. A. H.; Brett, C. T., *Planta* **2003,** *216*, 502-511.

(8) Keegstra, K.; Talmadge, K. W.; Bauer, W. D.; Albersheim, P., *Plant Physiology* **1973,** *51*, 188-197.

(9) Thompson, J. E.; Fry, S. C., *Planta* **2000,** *211*, 275-286.

(10) Hayashi, T.; Marsden, M. P. F.; Delmer, D. P., *Plant Physiology* **1987,** *83*, 384-389.

(11) Cosgrove, D. J., *Plant Physiology* **2001,** *125*, 131-134.

(12) Schultz, T. H.; Owens, H. S.; Maclay, W. D., *Journal of Colloid Science* **1948,** *3*, 53-62.

(13) Schultz, T. H.; Miers, J. C.; Owens, H. S.; Maclay, W. D., *The Journal of Physical and Colloid Chemistry* **1949,** *53*, 1320-1330.

(14) Pavlath, A. E.; Voisin, A.; Robertson, G. H., *Macromolecular Symposia* **1999,** *140*, 107-113.

(15) Raj, G.; Balnois, E.; Helias, M.-A.; Baley, C.; Grohens, Y., *Journal of Materials Science* **2011,** *47*, 1-7.

(16) de Kerchove, A. J.; Elimelech, M., *Biomacromolecules* **2006,** *8*, 113-121.

(17) Orelma, H.; Filpponen, I.; Johansson, L.-S.; Laine, J.; Rojas, O. J., *Biomacromolecules* **2011,** *12*, 4311-4318.

(18) Liu, Z.; Choi, H.; Gatenholm, P.; Esker, A. R., *Langmuir* **2011,** *27*, 8718-8728.

(19) Romanowski, G.; Lorenz, M. G.; Wackernagel, W., *Applied and Environmental Microbiology* **1991,** *57*, 1057-1061.

(20) Zykwinska, A.; Thibault, J.-F.; Ralet, M.-C., *Journal of Experimental Botany* **2007,** *58*, 1795-1802.

(21) de Gennes, P. G., *Macromolecules* **1981,** *14*, 1637-1644.

(22) Rubinstein, M.; Colby, R. H., *Polymer physics*. OUP Oxford: 2003.

(23) Zykwinska, A.; Thibault, J.-F.; Ralet, M.-C., *Carbohyd Polym* **2008,** *74*, 957-961.

(24) Wang, J.; Somasundaran, P., *J Colloid Interf Sci* **2005,** *291*, 75-83.

(25) Mattiuzzi, A.; Jabin, I.; Mangeney, C.; Roux, C.; Reinaud, O.; Santos, L.; Bergamini, J.-F.; Hapiot, P.; Lagrost, C., *Nat Commun* **2012,** *3*, 1130.

(26) Kontturi, E.; Suchy, M.; Penttilä, P.; Jean, B.; Pirkkalainen, K.; Torkkeli, M.; Serimaa, R., *Biomacromolecules* **2011,** *12*, 770-777.

(27) Amirkhani, M.; Volden, S.; Zhu, K.; Glomm, W. R.; Nyström, B., *J Colloid Interf Sci* **2008,** *328*, 20-28.

(28) Turkevich, J.; Stevenson, P. C.; Hillier, J., *A General Discussion of the Faraday Society* **1951,** *11*, 55-75.

(29) Selvendran, R. R., *Journal of Cell Science. Supplement* **1985,** *2*, 51-88.

(30) Axelos, M. A. V.; Thibault, J. F., *International Journal of Biological Macromolecules* **1991,** *13*, 77-82.

(31) Linse, P.; Källrot, N., *Macromolecules* **2010,** *43*, 2054-2068.

(32) Fleer, G. J.; Cohen Stuart, M. A. S.; M., J. M. H.; Cosgrove, T. V.; Vincent, B., *Polymers at interfaces*. Chapman & Hall, London: 1993.

(33) Huang, Y.; Santore, M. M., *Langmuir* **2002,** *18*, 2158-2165.

(34) Talbott, L. D.; Ray, P. M., *Plant Physiology* **1992,** *98*, 357-368.

Chapter 6: Mixed Linkage Glucan Adsorption onto Regenerated Cellulose and Modified Regenerated Cellulose Surfaces

6.1 Abstract

β-(1→3, 1→4) glucans, also known as mixed linkage glucans (MLGs), are unique to Poales, including economically important grasses and cereals, as well as a few other organisms such as Icelandic moss (*Cetraria islandica*). Quartz crystal microbalance with dissipation monitoring (QCM-D) was utilized to investigate the adsorption of two MLG samples, barley and lichen MLG, onto regenerated cellulose (RC) surfaces in the absence and presence of other matrix polysaccharides, including hemicelluloses and pectins. Both MLGs irreversibly adsorbed onto RC surfaces and a Voigt-based viscoelastic model was used to fit the time-dependent adsorption profiles. Thicker MLG layers with comparable viscoelastic properties were obtained with increasing concentration of MLG solutions. Lichen MLG formed softer layers with smaller elastic shear moduli (0.3×10^5 N•m^{-2}) than barley MLG layers (1.4×10^5 N•m^{-2}) obtained under identical conditions. The formation of softer lichen MLG layers was attributed to a higher proportion of β-(1→3) linkages for lichen MLG, leading to more flexible lichen MLG chains. With increasing temperature, thinner and more rigid lichen MLG layers were obtained due to dehydration of the surface layers. Preadsorption of matrix polysaccharides onto RC surfaces partially inhibited the subsequent adsorption of viscoelastic MLG layers onto cellulose. The interaction studies also shed light on how different matrix polysaccharides may assemble in the primary plant cell walls.

6.2 Introduction

Primary cell walls of plants are complex structures that provide mechanical support, defensive barriers against pathogens, tissue cohesion and matter transport.[1] Primary cell walls of flowering plants can be divided into two categories. In dicot plants, the primary cell walls are known as type I cell walls, consisting of approximately 30% cellulose, 30% hemicelluloses, 35% pectins and 1 to 5% structural proteins on a dry mass basis.[2] The walls of grasses and cereals differ dramatically from dicot species in composition. Grass and cereal cell walls, also known as type II cell walls, are composed of cellulose microfibrils, glucuronoarabinoxylans (GAXs), and mixed linkage glucans (MLGs), together with reduced amounts of xyloglucan and pectins.[3, 4] Grass cell walls are major sources of dietary fiber and have wide ranging applications in brewing, human nutrition and animal feeds.[3]

Cellulose is the main load-bearing component in cell walls and is composed of β-(1→4)-glucose linear chains which are further associated into cellulose microfibrils by hydrogen bonding. The linear structures of cellulose are conserved throughout all plants, while the structures and amounts of other cell wall polysaccharides strongly depend upon the species, tissue and growth period of a plant. Xyloglucans (XG), the most abundant type of hemicellulose in type I cell walls, have a cellulose-like backbone with xylose, galactose and arabinose as side branches. Xyloglucans are the principal crosslinking polysaccharides that interact with cellulose through hydrogen bonding and hydrophobic interactions.[5] In contrast, the most abundant hemicelluloses in type II cell walls are xylans, consisting of a backbone of β-(1→4)-xylose that can be branched to form arabinoxylan (AX) and glucuronoarabinoxylan (GAX). The xylan backbone of AX is partially glycosylated at the *O*2 and/or *O*3 position(s) with arabinose units and AXs constitute 40% or more by dry mass of the material in the primary cell walls of monocots.[6] In grass cell walls, GAXs take the place of xyloglucans, crosslinking cellulose microfibrils and represent about 25% by dry mass of all material present in the primary cell walls. The xylan backbones of GAXs have both neutral and acidic side chains. The neutral side chains are composed of arabinose units attached at the *O*3 positions of the xylose units and acidic side chains are glucuronic acid units at the *O*2 positions. These side chains not only provide surface charges to the type II cell walls but also create spacing among cell wall components leading to porous cell wall structures.[4]

Accounting for about 3% to 5% of the material in the primary cell walls of grass species on a dry mass basis,[7] MLGs are unique to Poales, cereals and some lichens (*Cetraria islandica*). The primary structure of an MLG is an unbranched homopolymer of glucose with both β-(1→3) and β-(1→4) linkages. The most common ratio of β-(1→3) to β-(1→4) linkages in MLG molecules is about 1 to 2.[8] Typically MLG can be viewed as a β-(1→4) linked cellulosic backbone interrupted by single β-(1→3) linkages which introduce "kinks" within the molecules, giving rise to greater flexibility and solubility of MLGs in aqueous solutions compared to cellulose.[9, 10] Consecutive β-(1→3) linkages have not been found.[11] The conformation of a single MLG chain in aqueous solution is depicted as an extended random coil on the basis of both experimental results and theoretical models.[12, 13] Most of the β-(1→4) linkages occur in randomly distributed cellotriosyl (x = 3) or cellotetraosyl (x = 4) units, while longer blocks of β-(1→4) linkages (x = 5 to 11) are also present (Figure 6.1). The composition of the linkages is one of the most important characteristics of MLGs and varies on the basis of the origin and tissue type.[14] The two MLG samples used in this study were a β-glucan from barley (barley MLG) and lichen MLG from Icelandic moss (*Cetraria islandica*). Barley is one of the major grains with high β-glucan content (2.5% to 11.3%) and is widely used as a cereal.[14] Lichen MLG is structurally similar to barley MLG, consisting of β-(1→3) linked cellotriosyl (78%), cellotetraosyl (4%) and longer cello-oligosaccharide units (18%).[11] A recent study showed that lichen MLG exhibited potential antiviral and antitumor properties.[15] High concentrations of MLGs are found in the endosperm of some grains where they serve as storage carbohydrates.[16] They are also associated with cellulose microfibrils during cell growth, and are enzymatically hydrolyzed into small fragments when growth is complete.[3] Turnover of MLGs during cell wall growth suggests that MLGs play an important role in the formation of plant cell walls. A recent study showed that the localization of MLGs from *Equisetum arvense* was independent of the cell growth and occurred in both young and old regions of the plant.[17] Commercial interest in MLGs has increased due to their potential applications in the treatment and prevention of several diseases, such as high cholesterol, obesity and heart disease.[16]

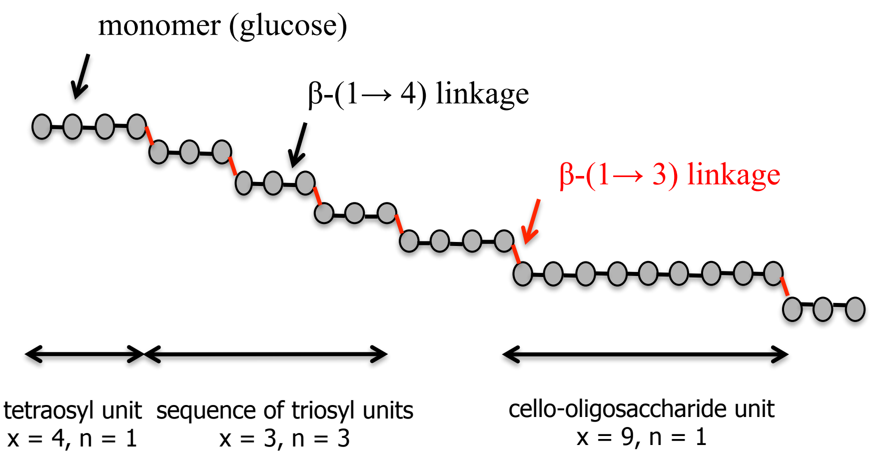

Figure 6.1 A representative chemical structure of a MLG where x is defined as the degree of polymerization in the cello-oligosaccharide unit and n is the number of sequential groups of the same cello-oligosaccharide unit. Adapted from Tosh *et al.*[18]

Because of the complexity of plant cell walls and the difficulty of extracting unmodified cell wall components, model cellulose systems are often used for the investigation of interactions between cellulose and other cell wall components. In this study, cellulose was regenerated from spincoated thin films of trimethylsilyl cellulose (TMSC) in a process that yields a dense and amorphous cellulose layer.[19] The roles of XGs in dicot primary cell walls (type I cell walls) have been widely studied, while the roles of MLGs as well as their interactions with other matrix polysaccharides in type II cell walls have yet to be determined. The aim of this chapter was to investigate the interactions between MLGs and cellulose as well as other cell wall matrix polysaccharides using a quartz crystal microbalance with dissipation monitoring (QCM-D). This technique also provides a direct comparison of two MLG samples with respect to their viscoelastic properties. Atomic force microscopy (AFM) measurements also enabled the imaging of the structures adopted by MLGs and other matrix polysaccharides on the model cellulose surfaces.

6.3 Experimental

6.3.1 Materials

The polysaccharides used in this study are summarized in Table 6.1 and were used without further purification. Other materials were detailed in Chapter 3. The preparation of regenerated cellulose surfaces was outlined in Chapter 3.2.3. For Barley and lichen MLG, the polydispersity indices (PDI), are 2.00 and 2.03, respectively, as determined by size exclusion chromatography.

Table 6.1 Summary of the polysaccharide samples used in this chapter.[a,b]

Sample	Supplier	Source	[b]Molar Mass /kDa
Barley MLG	Megazyme	Barley	229
Lichen MLG	Megazyme	Icelandic Moss	99
Xyloglucan (XG)	Megazyme	Tamarind Seed	202
Glucuronoarabinoxylan (GAX)	[a]Gift from Prof. Paul Gatenholm	Spruce	13
Arabinoxylan (AX)	Megazyme	Wheat	-
Arabinan	Megazyme	Sugar Beet	15
Pectin	Sigma-Aldrich	Citrus Fruit	23 to 71

a. Chalmers University of Technology, Sweden.
b. Weight average molar mass.

6.3.2 QCM-D Measurements

Sensors coated with regenerated cellulose (RC) were used in this study. Detailed procedures for QCM-D measurements were provided in Chapter 3.3.4. All measurements were performed under a continuous flow rate of 0.200 mL•min^{-1} at 50.0 °C in triplicate and the averages ± one standard deviation for each measurement were calculated. Detailed viscoelastic modeling procedures were covered in Chapter 3.3.4.

6.3.3 SPR Measurements

Sensors coated with RC were used in this study. Detailed procedures for SPR measurements were provided in Chapter 3.3.5. Adsorption times were the same as QCM-

D measurements. Each SPR experiment was performed in triplicate and the average values ± one standard deviation were calculated. Details for the calculation can be found in Chapter 3.3.5. The combination of QCM-D and SPR allowed for the determination of film water contents (%H_2O), also known as the degree of hydration of the adsorbed layers (Equation 2.30). A refractive index increment (*dn/dc*) of 0.146 ± 0.001mL•g^{-1} for lichen MLG solution was determined with a differential refractometer and used for the calculation of surface excess from SPR (Γ_{SPR}).

6.3.4 AFM Measurements

Detailed procedures for AFM measurements were provided in Chapter 3.3.3. Barley and lichen MLG layers were dried in a vacuum oven at 50.0 °C overnight and then imaged with an MFP-3D-Bio atomic force microscope (MFP-3D-BIO, Asylum Research) in tapping mode. The AFM images were collected under ambient conditions using a silicon tip (OMCL-AC 160TS, Olympus Corp.). The reported roughnesses are root-mean-square (RMS) values determined from 2 μm × 2 μm scan areas.

6.4 Results and Discussion

6.4.1 Adsorption of Barley MLG onto RC Surfaces

Sensors coated with RC films were placed into the QCM-D flow cells and time-dependent adsorption profiles for the scaled frequency changes ($\Delta f/n$) and dissipation changes (ΔD) were collected. Representative time dependent $\Delta f/n$ and ΔD profiles are provided in Figure 6.2. First, water was introduced into the flow cell at a rate of 0.200 mL•min^{-1} at 50.0 °C for several hours until a stable baseline was obtained. Barley MLG from sodium acetate buffer (20 mM, pH = 5.5) was then introduced into the flow cell at the same rate and temperature and the changes in $\Delta f/n$ and ΔD were recorded.

Immediately after the injection of barley MLG in sodium acetate buffer (20 mM, pH = 5.5), a significant initial $\Delta f/n$ decrease and a ΔD increase occurred, followed by much more gradual changes of $\Delta f/n$ and ΔD at later times. The adsorption time for barley MLG was 1 hour as this was long enough to observe plateaus in $\Delta f/n$ and ΔD profiles. Finally, water was introduced into the flow cells for the removal of the reversibly bound molecules. Values of $\Delta f/n$ and ΔD did not return to the baseline, indicating irreversible adsorption of barley MLG onto RC surfaces. Greater changes in $\Delta f/n$ and ΔD values were observed for adsorption from barley MLG solutions with higher concentrations. Each experiment was performed at 50.0 °C in triplicate and the average values ± one standard deviation were calculated (Table 6.2). The temperature of 50.0 °C used in this study was chosen as associations between β-glucan chains are enhanced at elevated temperature.[20] The differences in adsorption kinetics at early stages of adsorption (from 500 to 900 seconds) are highlighted in Figure 6.3. The initial rates of adsorption increased with increasing concentration. After barley MLG adsorption, RC-coated quartz crystal sensors with barley MLG toplayers were dried in a vacuum oven at 50.0 °C overnight and then imaged with an atomic force microscope in tapping mode. AFM has been successfully applied for the visualization of different polysaccharides, including xyloglucan, curdlan, pectin and alginate.[21] Representative AFM images are provided in Figure 6.4 and a smooth, homogeneous barley MLG layer with a RMS roughness of 1.1 nm was formed on the RC-coated substrate (Figure 6.4B). The original particle-like morphology of the RC substrate (Figure 6.4A) was replaced by a more continuous network-like morphology (Figure 6.4B). Previous studies showed that the MLG tended to from small round particles on mica surfaces after vacuum drying due to the existence of slight interactions between the MLG chains themselves as well as between the MLG chains and the mica surface.[22] As the AFM images in this study were taken after the substrates were vacuum-dried, the continuous network morphology in the absence of water suggested a strong interaction between MLG and the RC substrates.

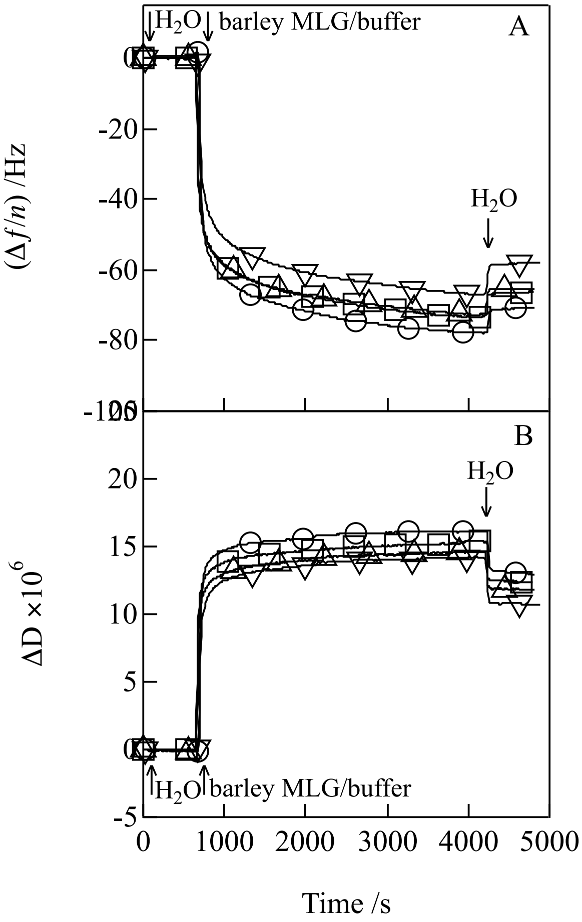

Figure 6.2 Representative time dependent (A) $\Delta f/n$ and (B) ΔD profiles for barley MLG adsorption onto RC surfaces from MLG solutions in SA buffer (20 mM, pH = 5.5) with concentrations (w/w) of (O) 0.1%, (☐) 0.05%, (Δ) 0.025% and (∇) 0.01% at 50.0 °C. Data correspond to the fifth overtone and arrows indicate where solutions were switched.

Table 6.2 Irreversible $\Delta f/n$ and ΔD for barley and lichen MLG adsorption from SA buffer (20 mM, pH = 5.5) onto RC surfaces at 50.0 °C.

Sample	$\Delta f/n$ /Hz	ΔD $\times 10^6$	Sample	$\Delta f/n$ /Hz	ΔD $\times 10^6$
Barley-0.1%	-71.9 ± 0.2	13.4 ± 0.4	**Lichen-0.1%**	-58 ± 2	7.1 ± 0.5
Barley-0.05%	-69 ± 1	12.5 ± 0.2	**Lichen-0.05%**	-55 ± 1	6.9 ± 0.2
Barley-0.025%	-66 ± 2	12.3 ± 0.4	**Lichen-0.025%**	-50 ± 1	7.1 ± 0.3
Barley-0.01%	-60 ± 1	10.9 ± 0.1	**Lichen-0.01%**	-48 ± 2	6.4 ± 0.4

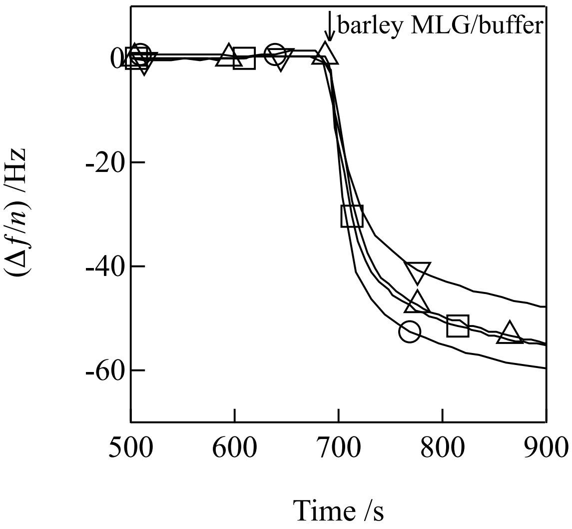

Figure 6.3 Representative kinetic data for barley MLG adsorption onto RC surfaces from solutions in SA buffer (20 mM, pH = 5.5) with different concentrations at 50.0 °C. The data is the same as the data in Figure 6.2 between 500 and 900 seconds. Symbols correspond to barley MLG solutions with concentrations (w/w) of (O) 0.1%, (□) 0.05%, (Δ) 0.025% and (∇) 0.01%. Data correspond to the fifth overtone and arrows indicate where solutions were switched.

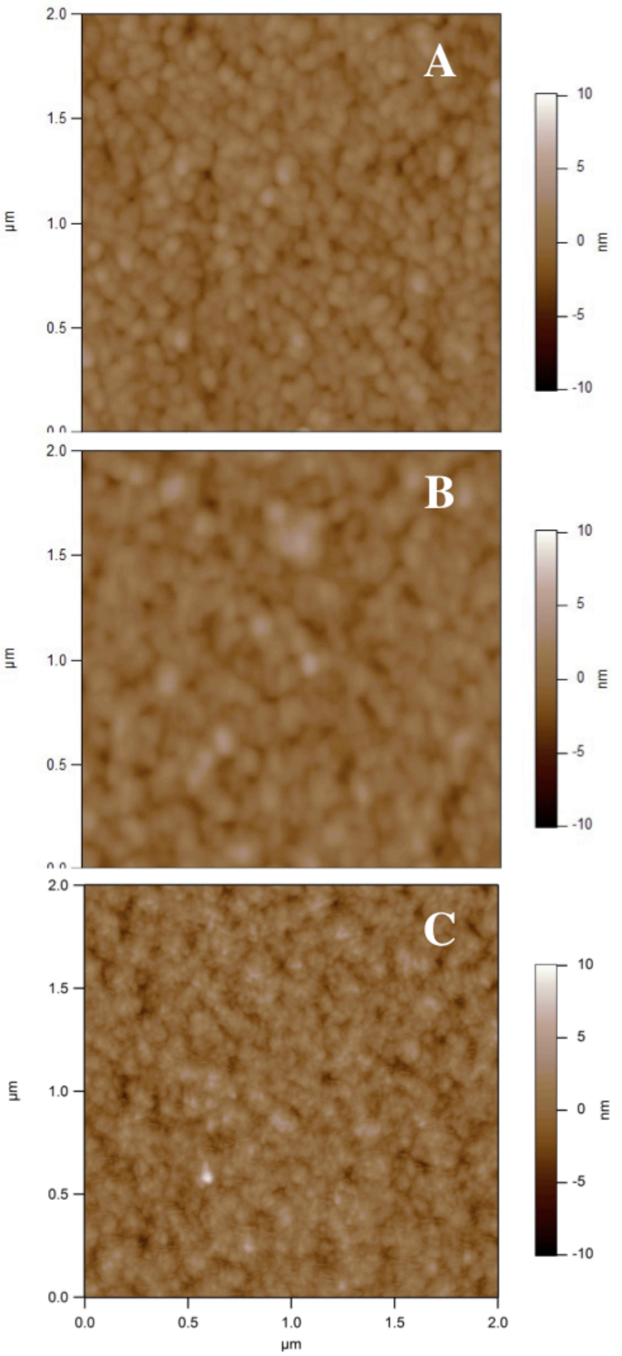

Figure 6.4 Representative AFM height images of (A) a bare RC-coated substrate and RC-coated substrates after the adsorption of (B) barley and (C) lichen MLG from 0.05% (w/w) solutions in SA buffer (20 mM, pH = 5.5) at 50.0 °C. The RMS roughnesses were (A) 1.0 nm, (B) 1.1 nm and (C) 1.3 nm and were obtained from the entire 2 µm × 2 µm scan areas and the z range was 20 nm.

6.4.2 Viscoelastic Modeling of Barley MLG Adsorption onto RC Surfaces

Adsorption of barley MLG from solutions in SA buffer (20 mM, pH = 5.5) led to the formation of soft and dissipative layers on RC substrates ($\Delta D > 5 \times 10^{-6}$). This observation is also similar to the cholesterol-lowering effect of β-glucan that has been explained by the formation of a viscous layer in the small intestine that inhibits intestinal uptake of dietary cholesterol.[23] For such gel-like layers, the Sauerbrey equation (Equation 3.1) is invalid for the calculation of the adsorbed amount from QCM-D experiments (Γ_{QCM-D}). The mechanical properties of the adsorbed viscoelastic layer lie between those of a purely elastic solid and a viscous liquid. Thus the adsorption data from different overtones (n = 7, 9, 11 and 13) were fit with a Voigt-based viscoelastic model for the estimation of the thickness (h_f) and two other viscoelastic parameters (shear viscosity η_f and elastic shear modulus μ_f) using the software package QTools 3.0.5. Detailed fitting procedures are provided in Chapter 3.3.4. The adsorbed MLG layer was treated as a homogeneous layer that is in contact with the RC-coated quartz crystal and a semi-infinite Newtonian liquid (water or buffer) under no-slip boundary conditions. The density and viscosity of water were used for all of the bulk liquids, as the dissolved electrolytes and biomacromolecules had little effects on the values of density and viscosity.[24] Density of the adsorbed layer (ρ_f) was set to 1050 kg•m^{-3} and assumed to be constant throughout the adsorption process. This assumption was made because ρ_f and h_f are coupled parameters whereas their product Γ_{QCM-D} is unique. Hence, any differences in Γ_{QCM-D} are being expressed as changes in h_f. Representative experimental data for barley MLG adsorption from 0.05% (w/w) solutions in SA buffer (20 mM, pH = 5.5) onto RC substrate and the best fits from Voigt-based viscoelastic model are provided in Figure

6.5. Values of h_f, $\Gamma_{QCM\text{-}D}$, μ_f and η_f obtained from viscoelastic modeling are summarized in Table 6.3 using n = 7 to 13. The results showed that thicker layers were obtained for barley MLG solutions with higher concentrations, while μ_f values were quite similar (~ 1.4×10^5 N•m^{-2}). The shear viscosity was comparable to the viscosity of water, indicating a hydrogel-like state for the adsorbed layer.

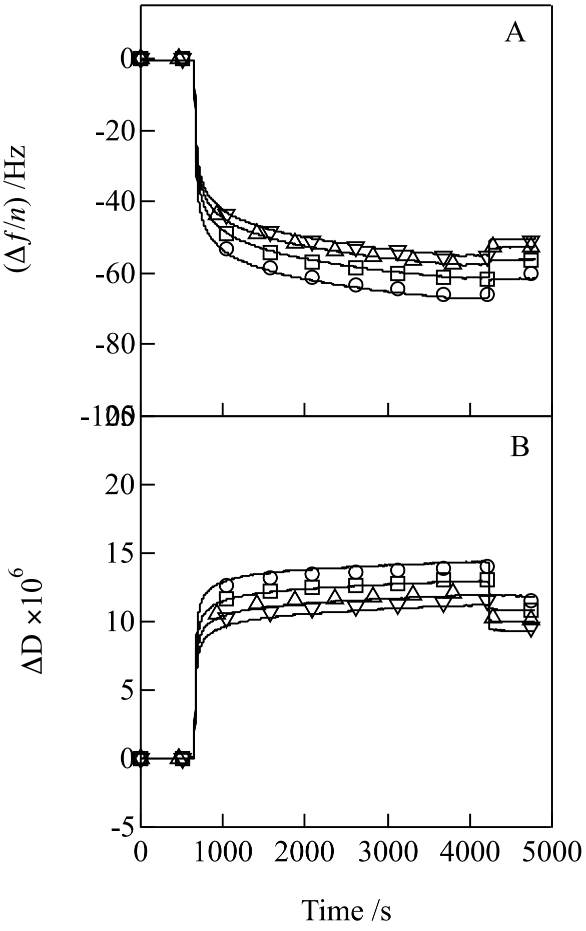

Figure 6.5 Representative time dependent (A) Δ*f*/*n* and (B) ΔD adsorption curves with fits obtained from Voigt-based viscoelastic modeling for barley MLG adsorption onto RC substrates from 0.05% (w/w) solutions in SA buffer (20 mM, pH = 5.5) at 50.0 °C. For both graphs, isolated symbols represent a subset of smooth experimental data from *n* = (O) 7, (□) 9, (Δ) 11 and (∇) 13 and solid lines represent fits of the entire data set.

Table 6.3 Summary of bulk concentration effects on h_f, $\Gamma_{QCM\text{-}D}$, μ_f and η_f obtained from Voigt-based viscoelastic modeling of QCM-D data using n = 7 to 13 for barley MLG layers adsorbed onto RC surfaces from solutions in SA buffer (20 mM, pH = 5.5) at 50.0 °C.[a]

Concentration	**$^{a}h_f$ /nm**	**$\Gamma_{QCM\text{-}D}$ /mg•m^{-2}**	**$\mu_f \times 10^{-5}$ /N•m^{-2}**	**$\eta_f \times 10^{3}$ /N•s•m^{-2}**
0.1%	18 ± 2	19 ± 2	1.5 ± 0.3	1.08 ± 0.03
0.05%	16.7 ± 0.1	17.5 ± 0.1	1.42 ± 0.06	1.11 ± 0.01
0.025%	17 ± 1	18 ± 1	1.4 ± 0.2	1.08 ± 0.02
0.01%	15 ± 1	16 ± 1	1.4 ± 0.2	1.05 ± 0.01

a. Assumes ρ_f = 1050 kg•m^{-3}.

The adsorbed barley MLG layers were also analyzed using different overtone combinations. Figure 6.6 and Table 6.4 provide results obtained from all of the overtones (n = 3, 5, 7, 9, 11 and 13). The fundamental overtone (n = 1) was omitted due to insufficient energy trapping.[25] In Figure 6.6, data from n = 3 to 5 appeared to be noisy and there were small discrepancies between the fitting and the experimental data for these two overtones, while fits of n = 7 to 13 were better. Fits and fitting parameters using only n = 9, 11 and 13 are summarized in Figure 6.7 and Table 6.5, respectively. The results showed $\Gamma_{QCM\text{-}D}$ and by extension h_f obtained from n = 3 to 13 were greater than those obtained from only n = 9, 11 and 13, whereas the elastic shear moduli were smaller. These differences were attributed to a decrease in the penetration depth of the acoustic waves generated by higher overtones.[26, 27] The acoustic waves generated by higher overtones can only sample part of the adsorbed layer that is closest to the quartz crystal due to smaller penetration depths, while acoustic waves generated by lower overtones can penetrate deeper into the bulk liquid and sample the flexible and dangling chain ends extending into the bulk liquid. Differences in penetration depth for different n can also explain the smaller μ_f values obtained from multiple overtones. As a result, we choose to model the experimental data using n = 7 to 13 with excellent agreement between the experimental data and the fits. The selected density only had a slight effect on the fitting parameter values and the Γ_{QCM-D} remained constant when the density of the adsorbed layer was varied.[24, 28] Thus, a density of 1050 kg•m^{-3} was assumed for the adsorbed layer for all computations.

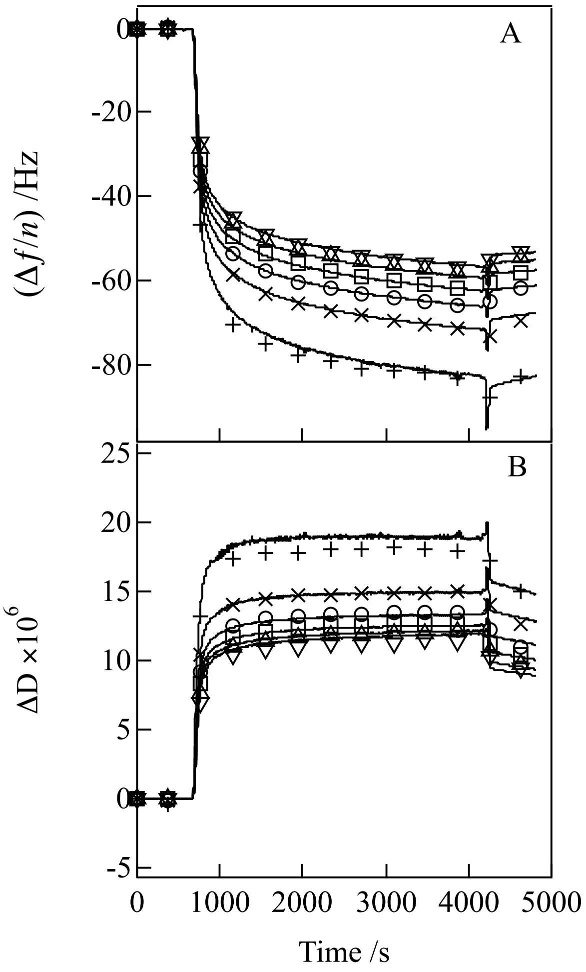

Figure 6.6 Representative time dependent (A) Δ*f*/*n* and (B) ΔD adsorption curves with fits obtained from Voigt-based viscoelastic modeling for barley MLG adsorption onto RC substrates from 0.05% (w/w) solutions in SA buffer (20 mM, pH = 5.5) at 50.0 °C. For both graphs, isolated symbols represent a sub set of smooth experimental data from *n* = (+) 3, (×) 5, (O) 7, (☐) 9, (Δ) 11 and (∇) 13 and solid lines represent fits of the entire data set.

Table 6.4 Summary of bulk concentration effects on h_f, $\Gamma_{QCM\text{-}D}$, μ_f and η_f obtained from Voigt-based viscoelastic modeling using n = 3 to 13 for barley MLG layers adsorbed onto RC surfaces from solutions in SA buffer (20 mM, pH = 5.5) at 50.0 °C.[a]

Concentration	**[a]h_f /nm**	**$\Gamma_{QCM\text{-}D}$ /mg•m^{-2}**	**$\mu_f \times 10^{-5}$ /N•m^{-2}**	**$\eta_f \times 10^{3}$ /N•s•m^{-2}**
0.1%	21 ± 2	22 ± 2	0.8 ± 0.2	1.04 ± 0.02
0.05%	19.8 ± 0.5	20.8 ± 0.5	0.8 ± 0.1	1.05 ± 0.02
0.025%	19 ± 2	20 ± 2	1.0 ± 0.2	1.04 ± 0.03
0.01%	16.0 ± 0.6	16.8 ± 0.6	1.08 ± 0.03	1.03 ± 0.02

a. Assumes ρ_f = 1050 kg•m^{-3}.

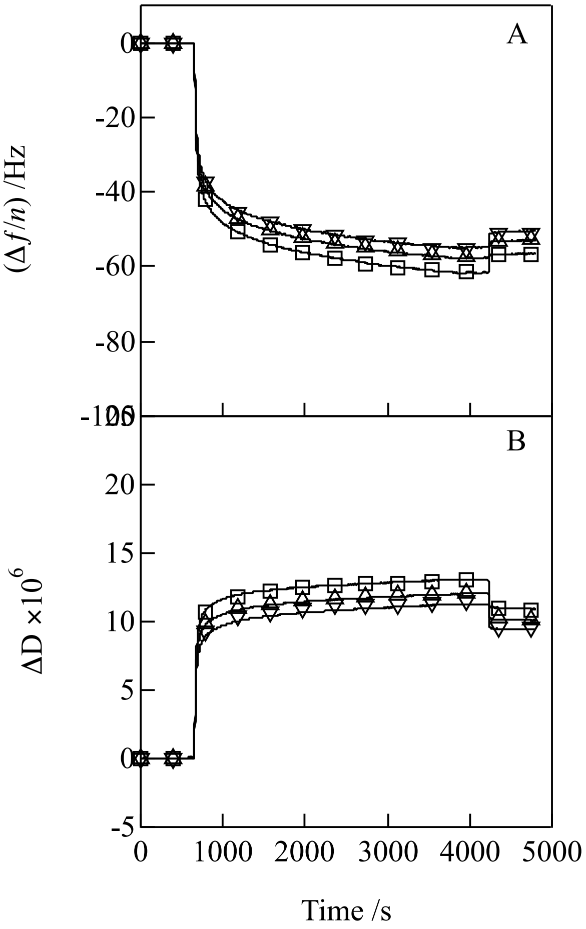

Figure 6.7 Representative time dependent (A) Δ*f*/*n* and (B) ΔD adsorption curves with fits obtained from Voigt-based viscoelastic modeling for barley MLG adsorption onto RC substrates from 0.05% (w/w) solutions in SA buffer (20 mM, pH = 5.5) at 50.0 °C. For both graphs, isolated symbols represent a subset of smooth experimental data from *n* = (☐) 9, (Δ) 11 and (∇) 13 and solid lines represent fits of the entire data set.

Table 6.5 Summary of bulk concentration effects on h_f, $\Gamma_{QCM\text{-}D}$, μ_f and η_f obtained from Voigt-based viscoelastic modeling using n = 9 to 13 for barley MLG layers adsorption onto RC surfaces from solutions in SA buffer (20 mM, pH = 5.5) at 50.0 °C.[a]

Concentration	$^{a}h_f$ /nm	$\Gamma_{QCM\text{-}D}$ /mg•m^{-2}	$\mu_f \times 10^{-5}$ /N•m^{-2}	$\eta_f \times 10^{3}$ /N•s•m^{-2}
0.1%	17.0 ± 0.4	17.9 ± 0.4	1.6 ± 0.1	1.12 ± 0.01
0.05%	17 ± 1	18 ± 1	1.3 ± 0.3	1.10 ± 0.02
0.025%	16 ± 2	17 ± 2	1.8 ± 0.4	1.08 ± 0.02
0.01%	16 ± 1	17 ± 1	1.1 ± 0.1	1.02 ± 0.01

a. Assumes ρ_f = 1050 kg•m^{-3}.

6.4.3 Adsorption of Lichen MLG onto RC Surfaces

Lichen MLG adsorption onto RC surfaces was investigated following the same procedure used for barley MLG. Figure 6.8 shows representative $\Delta f/n$ and ΔD profiles for lichen MLG adsorption onto RC surfaces. Values of $\Delta f/n$ and ΔD did not return to the baseline, indicating irreversible adsorption of lichen MLG onto RC surfaces. Changes in $\Delta f/n$ and ΔD values, as well as the initial rate of adsorption, increased with increasing concentration (Figure 6.9 and Table 6.2). After lichen MLG adsorption, RC-coated quartz crystal sensors with lichen MLG toplayers were dried in a vacuum oven at 50.0 °C overnight and imaged with an atomic force microscope in tapping mode. A representative AFM height image showed that a smooth lichen MLG layer formed on the RC substrate with a RMS roughness of ~ 1.3 nm from a 2 μm × 2 μm scan area and a more continuous network-like morphology (Figure 6.4C) that was quite similar to the barley MLG layer (Figure 6.4B). The more obvious network structure for the adsorbed lichen MLG layer was probably due to its relatively smaller molar mass which diffuses more easily and more readily to form gels. This observation is also in agreement with the conclusion that the gel-like behavior is a characteristic of MLG, especially MLG with low molar mass.[29]

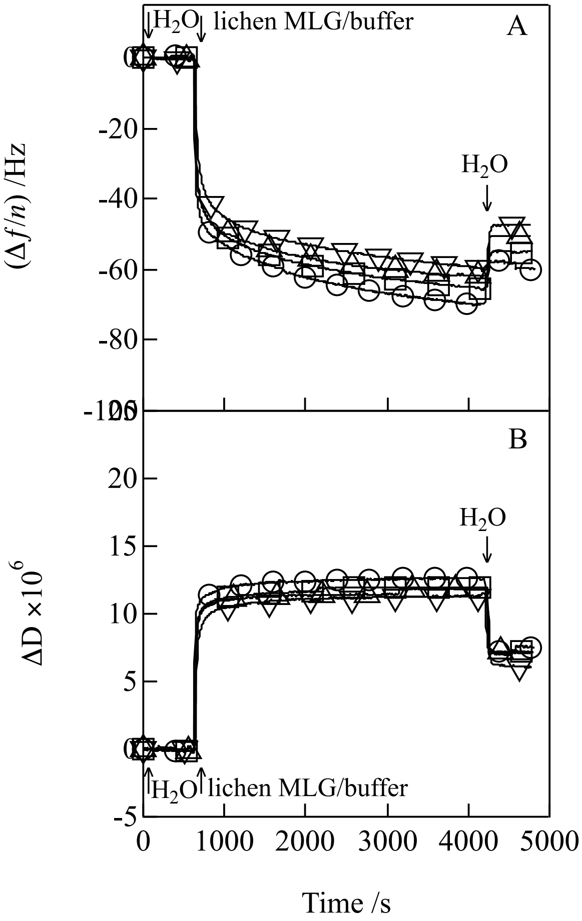

Figure 6.8 Representative time dependent (A) Δ*f*/*n* and (B) ΔD profiles for lichen MLG adsorption onto RC surfaces from solutions in SA buffer (20 mM, pH = 5.5) with lichen MLG concentrations (w/w) of (O) 0.1%, (□) 0.05%, (Δ) 0.025% and (∇) 0.01% at 50.0 °C. Data correspond to the fifth overtone and arrows indicate where solutions were switched.

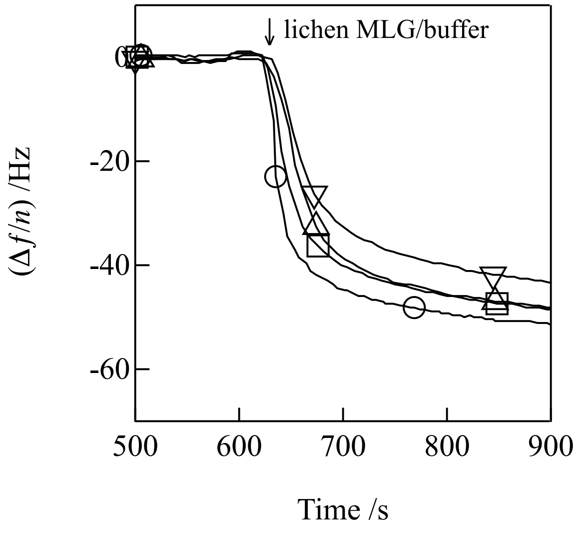

Figure 6.9 Representative kinetic data for lichen MLG adsorption onto RC surfaces from solutions in SA buffer (20 mM, pH = 5.5) with different concentrations. The data is the same as the data in Figure 6.8 from 500 to 900 seconds. Symbols correspond to lichen MLG solutions with concentrations (w/w) of (O) 0.1%, (☐) 0.05%, (Δ) 0.025% and (∇) 0.01%. Data correspond to the fifth overtone and arrows indicate where solutions were switched.

In addition to the effect of concentration on lichen MLG adsorption, the effect of temperature was also investigated using QCM-D. A range of temperatures from 15.0 °C to 50.0 °C were investigated and representative adsorption profiles are provided in Figure 6.10. Irreversible $\Delta f/n$ and ΔD for lichen MLG adsorbed onto RC surfaces from 0.05% (w/w) solutions in SA buffer (20 mM, pH = 5.5) at different temperatures was summarized in Table 6.6. Magnitudes of $\Delta f/n$ increased with increasing temperature, while changes in ΔD were quite similar for all the investigated temperatures. Differences in ΔD during the adsorption, from 600 to 4200 seconds, were attributed to the different rigidities of the adsorbed layers as well as different solution viscosities.

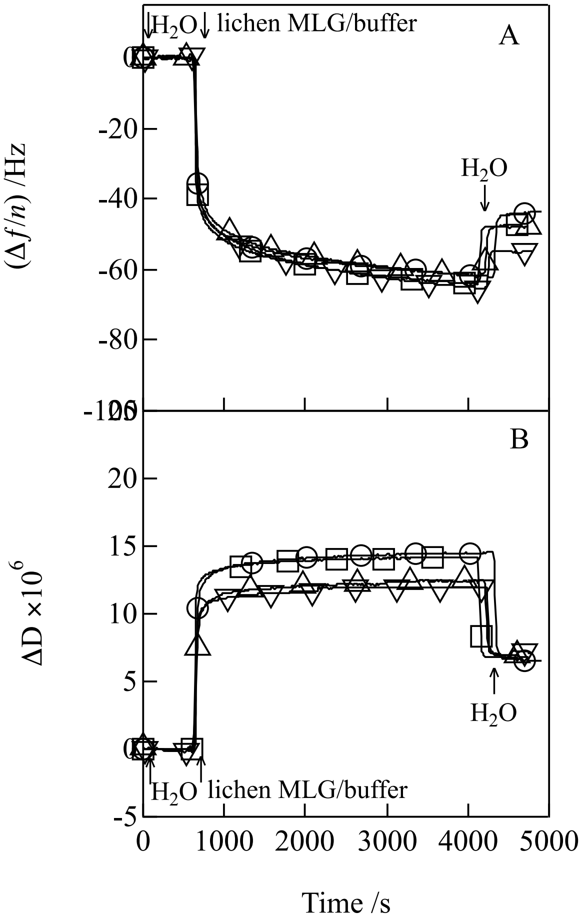

Figure 6.10 Representative time dependent (A) Δ*f*/*n* and (B) ΔD profiles for lichen MLG adsorption onto RC surfaces from 0.05% (w/w) solutions in SA buffer (20 mM, pH = 5.5) at temperatures of (O) 15.0 °C, (□) 30.0 °C, (Δ) 40.0 °C and (∇) 50.0 °C. Data correspond to the fifth overtone and arrows indicate where solutions were switched.

Table 6.6 Irreversible $\Delta f/n$ and ΔD for lichen MLG adsorbed onto RC surfaces from 0.05% (w/w) solutions in SA buffer (20 mM, pH = 5.5) at different temperatures.

Temperature /°C	$\Delta f/n$ /Hz	$\Delta D \times 10^6$
15.0	-45 ± 1	6.7 ± 0.1
30.0	-48 ± 1	6.9 ± 0.2
40.0	-49 ± 1	6.7 ± 0.2
50.0	-55 ± 1	6.9 ± 0.2

6.4.4 Viscoelastic Modeling of Lichen MLG Adsorption onto RC Surfaces

The same procedure used for modeling the viscoelastic behavior of barley MLG was used for lichen MLG layers adsorbed onto RC surfaces. Adsorption curves from multiple overtones were used for the estimation of h_f, $\Gamma_{QCM\text{-}D}$, μ_f and η_f using the software package QTools 3.0.5. Representative fits of adsorption profiles for lichen MLG adsorption onto RC surfaces from 0.05% (w/w) solutions in SA buffer (20 mM, pH = 5.5) are provided in Figure 6.11 and h_f, $\Gamma_{QCM\text{-}D}$, μ_f and η_f obtained from viscoelastic modeling are summarized in Table 6.7 using n = 7 to 13. The viscoelastic properties for barley and lichen MLG did not vary significantly with concentrations, however, there were variations that depended upon the source of the MLG. According to the supplier, lichen MLG has a much higher proportion of β-(1→3) to β-(1→4) linkages than barley MLG, indicating more "kinks" along the backbone. The irregular spacing of β-(1→3) linkages in the backbone of lichen MLG is responsible for greater flexibility and solubility. The results of Voigt-based viscoelastic modeling of the lichen MLG films were consistent with softer layers relative to barley MLG layers adsorbed onto RC surfaces under the same conditions. This result was in agreement with the conclusions of Böhm that the gelation occurs more readily with lichen MLG than barley MLG due to the increasing proportion of β-(1→3) linkages.[30] The differences in elastic shear moduli for two MLG samples were mainly attributed to the different β-(1→3) linkage proportions rather than the different molar mass. The polysaccharides had relatively high molar masses (Table 6.1), which are greater than the entanglement molecular weight (M_c) of linear glucans. For example, the values of M_c for cellulose and curdlan are 3.5 kDa and 12 kDa, respectively, on the basis of dynamic rheology measurements.[31] As the molar mass surpasses the value of M_c, the elastic shear modulus shows no dependence upon the molar mass.[31] Based upon previous studies, lower molar mass did improve the gelation rate of MLG due to the higher mobility of shorter chains.[7, 29] However, the higher proportion of β-(1→3) linkages of lichen MLG was the main contributor to the formation of softer lichen MLG layers compared to barley MLG. Two mechanisms have been proposed for MLG gelation: one is the aggregation of the longer blocks of contiguous β-(1→4) linkages associated with cellulose-like hydrogen bonding[32] and the other is the association of consecutive cellotriosyl units, involving both β-(1→3) and β-(1→4) linkages that form extended junction zones.[30] According to a previous study, Lazaridou and coworkers determined that there was a probability that both proposed gelation mechanisms exist for the case of lichen MLG from both dynamic rheometry and differential scanning calorimetry measurements.[11]

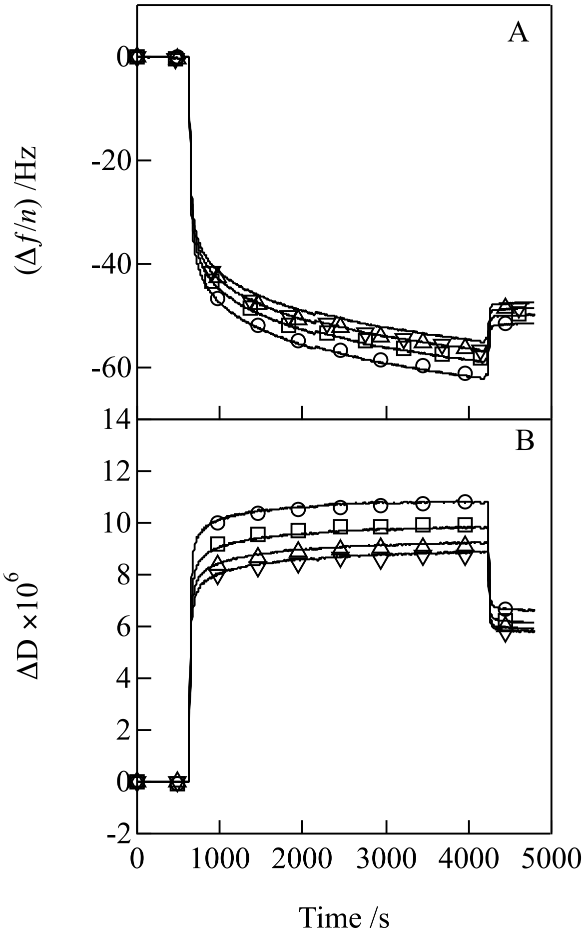

Figure 6.11 Representative time dependent (A) $\Delta f/n$ and (B) ΔD adsorption curves with fits obtained from Voigt-based viscoelastic modeling for lichen MLG adsorption onto RC substrates from 0.05% (w/w) solutions in SA buffer (20 mM, pH = 5.5) at 50.0 °C. For both graphs, isolated symbols represent a subset of smooth experimental data from n = (O) 7, (□) 9, (Δ) 11 and (∇) 13 and solid lines represent fits of the entire data set.

Table 6.7 Summary of bulk concentration effects on h_f, $\Gamma_{QCM\text{-}D}$, μ_f and η_f obtained from Voigt-based viscoelastic modeling using $n = 7$ to 13 for lichen MLG layers adsorbed onto RC surfaces from solutions in SA buffer (20 mM, pH = 5.5) at 50.0 °C.[a]

Concentration	$^a h_f$ /nm	$\Gamma_{QCM\text{-}D}$ /mg•m^{-2}	$\mu_f \times 10^{-5}$ /N•m^{-2}	$\eta_f \times 10^{3}$ /N•s•m^{-2}
0.1%	20 ± 2	21 ± 2	0.7 ± 0.2	1.0 ± 0.1
0.05%	19.3 ± 0.7	20.3 ± 0.8	0.32 ± 0.04	0.98 ± 0.03
0.025%	18 ± 1	19 ± 1	0.3 ± 0.1	0.9 ± 0.1
0.01%	12.4 ± 0.7	13.0 ± 0.8	0.6 ± 0.2	1.1 ± 0.1

a. Assumes $\rho_f = 1050$ kg•m^{-3}.

A range of temperatures from 15.0 to 50.0 °C were used for the investigation of temperature effects on lichen MLG adsorption onto RC surfaces. The resulting lichen MLG layers were dissipative and the viscoelastic modeling was performed using $n = 7$ to 13. A summary of h_f, $\Gamma_{QCM\text{-}D}$, μ_f and η_f values are provided in Table 6.8. At higher temperatures, adsorbed lichen MLG layers have higher elastic shear moduli and smaller thicknesses. These results indicated the formation of more rigid and compact layers at higher temperatures. This result was attributed to dehydration of lichen MLG layers. This result was also confirmed by SPR experiments performed under the same experimental conditions for lichen MLG adsorption onto RC surfaces. Irreversible changes in SPR angle ($\Delta\theta_{irr}$), adsorbed amounts (Γ_{SPR} and $\Gamma_{QCM\text{-}D}$) and water contents (%H_2O) are summarized in Table 6.9. For all the investigated temperatures, there was only a slight increase in dry mass Γ_{SPR} obtained by SPR. This results indicated similar amounts of lichen MLG molecules adsorbed onto RC surfaces, while the differences in wet masses $\Gamma_{QCM\text{-}D}$, including both the lichen MLG and the associated water, from different temperatures were attributed to the different water contents of the adsorbed lichen MLG layers. The water contents were calculated from Equation 2.30 assuming ideal mixing and decreased from 96% to 92% with increasing temperatures. This result is also consistent with fitting results from Voigt-based viscoelastic modeling and further confirmed the dehydration of lichen MLG layers at high temperatures.

Table 6.8 Summary of the temperature effects on h_f, $\Gamma_{QCM\text{-}D}$, μ_f and η_f obtained from Voigt-based viscoelastic modeling using n = 7 to 13 for lichen MLG layers adsorbed onto RC surfaces from 0.05% (w/w) solutions in SA buffer (20 mM, pH = 5.5) at 50.0 °C.[a]

Temperature /°C	**$^a h_f$ /nm**	**$\Gamma_{QCM\text{-}D}$ /mg•m^{-2}**	**$\mu_f \times 10^{-5}$ /N•m^{-2}**	**$\eta_f \times 10^{3}$ /N•s•m^{-2}**
15.0	33 ± 3	35 ± 3	0.14 ± 0.06	1.56 ± 0.12
30.0	25 ± 3	26 ± 3	0.18 ± 0.06	1.13 ± 0.03
40.0	17.4 ± 0.8	18.3 ± 0.9	0.40 ± 0.08	1.12 ± 0.05
50.0	19.3 ± 0.7	20.3 ± 0.8	0.32 ± 0.04	0.98 ± 0.03

a. Assumes ρ_f = 1050 kg•m^{-3}.

Table 6.9 Summary of $\Delta\theta_{irr}$, Γ_{SPR}, $\Gamma_{QCM\text{-}D}$ and %H_2O for lichen MLG adsorbed onto RC surfaces from 0.05% (w/w) solutions in SA buffer (20 mM, pH = 5.5) at different temperatures.[a,b,c]

Temperature /°C	**$\Delta\theta_{irr}$ /°**	**$^a\Gamma_{SPR}$ /mg•m^{-2}**	**$^b\Gamma_{QCM\text{-}D}$ /mg•m^{-2}**	**^{c}%H_2O**
15.0	0.0787 ± 0.0008	1.56 ± 0.02	35 ± 3	96 ± 1
30.0	0.0792 ± 0.0021	1.57 ± 0.04	26 ± 3	94 ± 1
40.0	0.0787 ± 0.0006	1.56 ± 0.02	18.3 ± 0.9	92 ± 1
50.0	0.0781 ± 0.0011	1.55 ± 0.02	20.3 ± 0.8	92 ± 1

a. Calculated from Equation 3.4.
b. Fitting results from Voigt-based viscoelastic modeling using n = 7 to 13.
c. Degree of hydration by mass calculated from Equation 2.30.

6.4.5 Adsorption of Lichen MLG onto Modified RC Surfaces

Modified RC surfaces were prepared by preadsorbing specific matrix polysaccharides, xyloglucan (XG), glucuronoarabinoxylan (GAX), arabinoxylan (AX), arabinan and pectin onto RC surfaces prior to exposure to lichen MLG. The solutions used for these experiments were 0.05% (w/w) matrix polysaccharide solutions in SA buffer (20 mM, pH = 5.5). The preadsorption was monitored by QCM-D and the adsorption time was fixed at 30 min for the saturation of the RC surfaces with each matrix polysaccharide followed by a rinse with water for the removal of reversibly adsorbed matrix polysaccharide. The RC-coated sensors were placed into the QCM-D flow cells and the preadsorption profiles were collected. Irreversible $\Delta f/n$ and ΔD for matrix polysaccharide adsorbed onto RC surfaces are summarized in Table 6.10. The resulting modified RC surfaces were used for AFM measurements and the subsequent adsorption of lichen MLG. These modified RC surfaces carrying a specific matrix polysaccharide layer, are referred to hereafter as XG-, GAX-, AX-, arabinan- and pectin-coated RC surfaces.

Table 6.10 Irreversible $\Delta f/n$, ΔD and $\Gamma_{QCM\text{-}D}$ for different matrix polysaccharides adsorbed onto RC surfaces from 0.05% (w/w) solutions in SA buffer (20 mM, pH = 5.5) at 50.0 °C.[a]

Sample	$\Delta f/n$ /Hz	ΔD ×10^6	[a]$\Gamma_{QCM\text{-}D}$ /mg•m^{-2}
Xyloglucan (XG)	-24 ± 1	4.45 ± 0.36	4.22 ± 0.25
Glucuronoarabinoxylan (GAX)	-12 ± 2	1.55 ± 0.19	2.08 ± 0.28
Arabinoxylan (AX)	-12.4 ± 0.6	2.16 ± 0.15	2.19 ± 0.11
Arabinan	-5.7 ± 0.8	0.76 ± 0.05	1.02 ± 0.14
Pectin	-4.75 ± 0.07	0.33 ± 0.06	0.84 ± 0.01

a. Calculated from Equation 3.1 for the fifth overtone.

The modified RC surfaces were used for subsequent studies of lichen MLG adsorption from 0.05% (w/w) solutions in SA buffer (20 mM, pH = 5.5) to investigate how the presence of specific matrix polysaccharides on RC surfaces affected the lichen MLG-cellulose interaction. Representative adsorption profiles and a summary of irreversible $\Delta f/n$ and ΔD for lichen MLG adsorption onto bare and modified RC surfaces are provided in Figure 6.12 and Table 6.11, respectively. Adsorption of lichen MLG onto bare RC surfaces yielded irreversible $\Delta f/n$ = -55 Hz. As is evident in Table 6.11, the data showed that the preadsorption of matrix polysaccharide onto RC surfaces reduced subsequent adsorption of lichen MLG. This reduction is particularly strong for the case of XG, where $\Gamma_{QCM\text{-}D}$ = 4.22 mg•m^{-2} for XG preadsorbed onto RC surfaces, caused a decrease in $\Delta f/n$ values from -55 Hz (bare RC) to -27 Hz (XG-coated RC) for lichen MLG adsorption. As XG is known to strongly interact with cellulose via hydrogen bonding in primary cell walls of dicots, strong *in vitro* adsorption was expected. Based upon results from Chapter 5, XG can completely cover a RC surface and inhibit subsequent pectin adsorption. Hence, most of the lichen MLG that adsorbed was likely interacting with XG rather than cellulose through interactions with the β-glucan backbone of XG. Preadsorbed xylans, including GAX and AX, also reduced lichen MLG adsorption onto cellulose, although the effect was smaller than XG (Table 6.11). For these two materials, preadsorbed $\Gamma_{QCM\text{-}D}$ indicate substantial coverage of the cellulose occurred. As such, the $\Gamma_{QCM\text{-}D}$ values for lichen MLG adsorption onto GAX and AX treated RC likely reflect interactions between lichen MLG and GAX and AX. Recent studies showed that there were strong intermolecular interactions between the unsubstituted regions of xylan and the cellulose-like regions from the backbone of MLG.[11, 33] This result is also consistent with the type II cell wall model proposed by Carpita *et al.* for grass and cereal cell walls.[34] For instance, in the alleurone cells of barley, xylans and MLG coexist through both non-covalent interactions and covalent crosslinks to form a coextensive network that coats cellulose microfibrils.[35] As both of the interactions depend upon the molecular structures of the polysaccharide, the structural characteristics govern the overall interactions. For GAX with higher degrees of substitution relative to AX, weakened interactions between cell wall polymers are expected. The fact that GAX had a slightly stronger inhibitory effect than less branched AX is consistent with expectations. For pectin and side chain arabinan incomplete coverage of RC surfaces occurred. Hence, the reduction in $\Delta f/n$ is most likely attributed to blockage of some adsorption sites on RC surfaces. This result is also consistent with similar ΔD values obtained for lichen MLG layer on bare and arabinan- or pectin-coated RC surfaces. Representative AFM measurements were performed before and after lichen MLG adsorption onto matrix polysaccharide modified RC surfaces. Figures 6.13 and 6.14 showed the changes in morphology before and after lichen MLG adsorption onto matrix polysaccharide modified RC surfaces. Similar smoothening effects with a reduction in RMS roughnesses before and after lichen MLG adsorption were observed for all the investigated matrix polysaccharides.

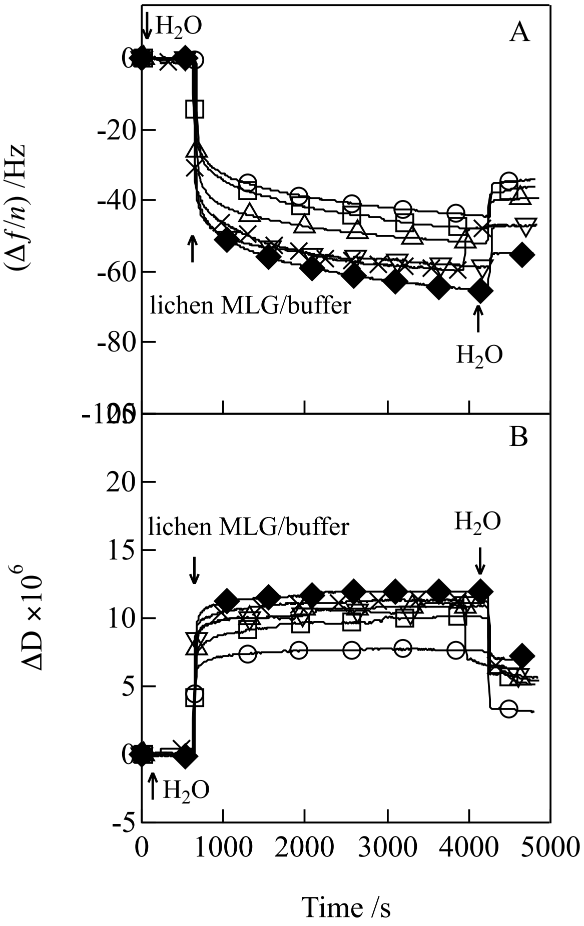

Figure 6.12 Representative time dependent (A) Δ*f*/*n* and (B) ΔD profiles for the adsorption of lichen MLG adsorption onto (O) XG-, (□) GAX-, (Δ) AX-, (∇) arabinan-, (×) pectin-coated RC surfaces and (◆) RC surfaces from 0.05% (w/w) solutions in SA buffer (20 mM, pH =5.5) at 50.0 °C. Data correspond to the fifth overtone and arrows indicate where solutions were switched.

Table 6.11 Irreversible $\Delta f/n$ and ΔD for lichen MLG adsorbed onto bare and matrix polysaccharide modified RC surfaces from 0.05% (w/w) solutions in SA buffer (20 mM, pH = 5.5) at 50.0 °C.

Substrate	**$\Delta f/n$ /Hz**	**$\Delta D \times 10^6$**
XG-coated RC	-27 ± 2	3.9 ± 0.3
arabinan-coated RC	-47.5 ± 0.5	6.8 ± 0.5
pectin-coated RC	-46.5 ± 0.6	6.5 ± 0.3
GAX-coated RC	-38 ± 2	5.7 ± 0.6
AX-coated RC	-38.9 ± 0.3	5.2 ± 0.4
bare RC	-55 ± 1	6.9 ± 0.2

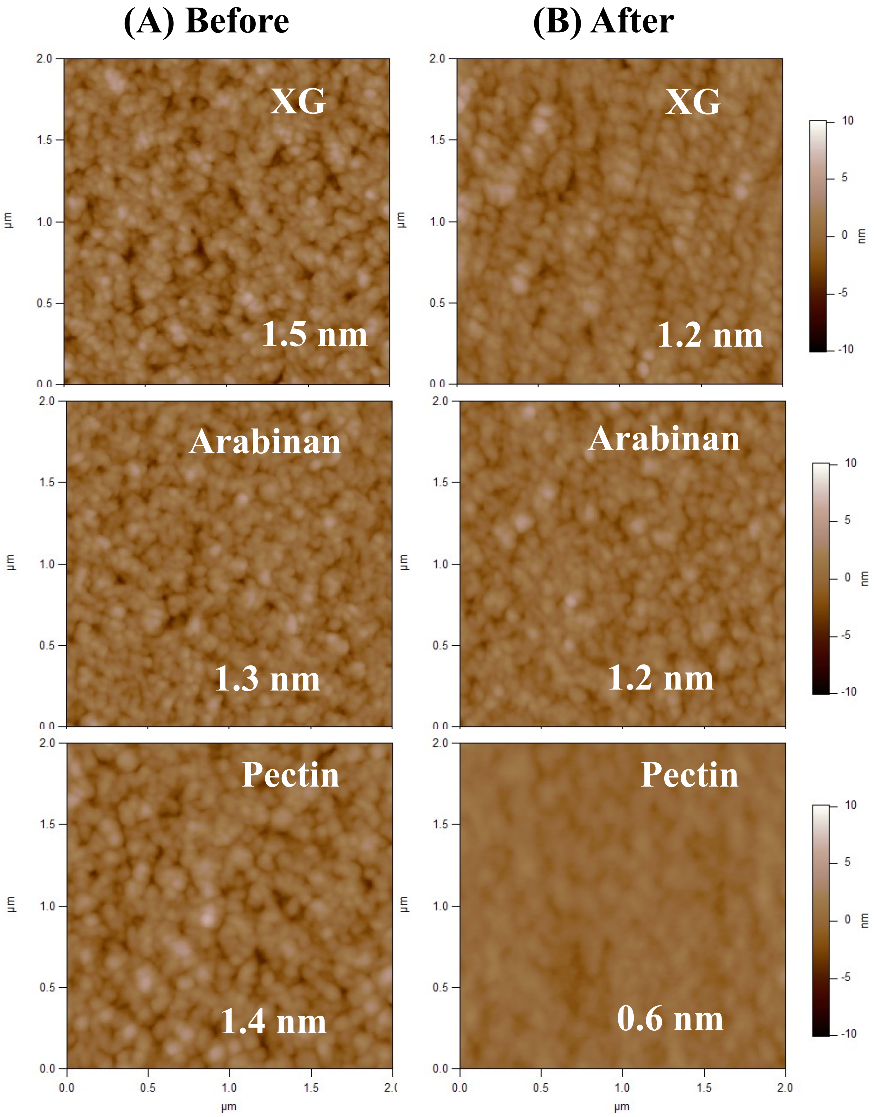

Figure 6.13 Representative AFM height images for bare and modified RC surfaces obtained (A) before and (B) after the adsorption of lichen MLG onto XG-, arabinan- and pectin-coated RC from 0.05% (w/w) solutions in SA buffer (20 mM, pH = 5.5) at 50.0 °C. The matrix polysaccharide is indicated in white letters on each image. The RMS roughnesses (white numbers on images) were obtained from the entire 2 μm × 2 μm scan areas and the z range was 20 nm.

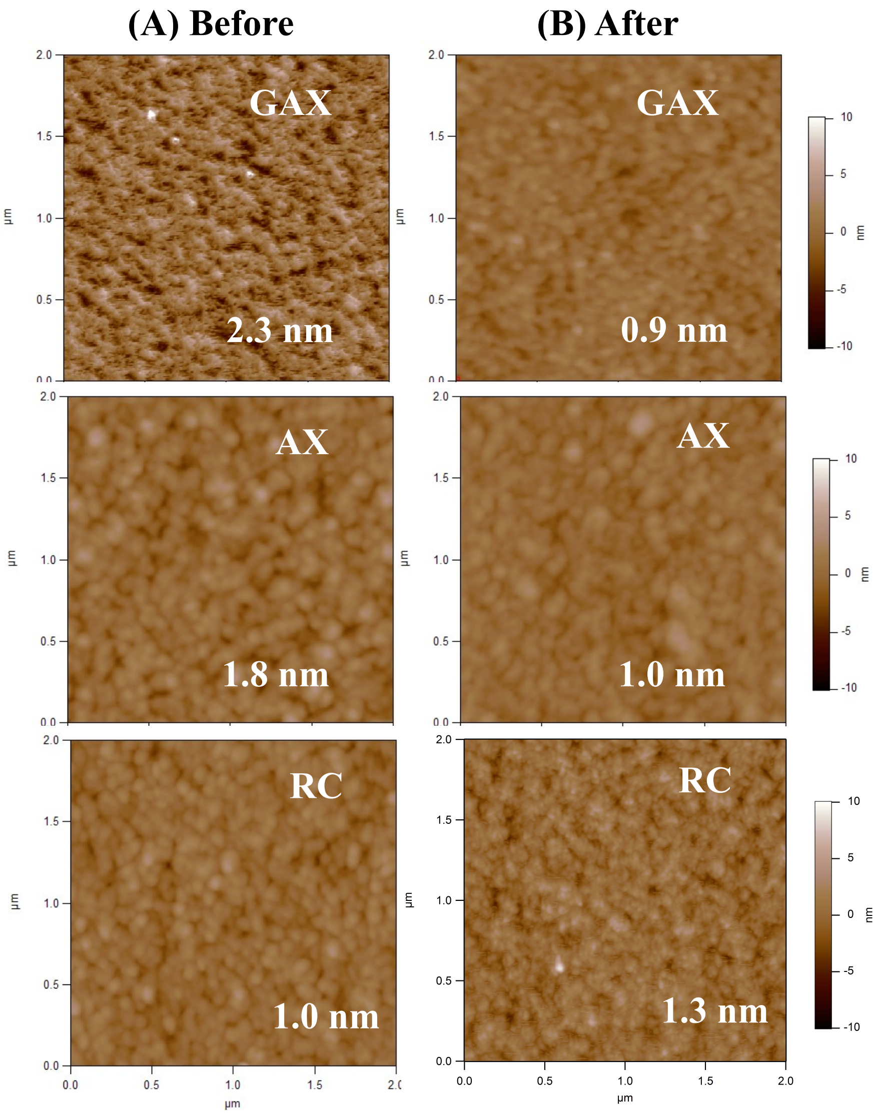

Figure 6.14 Representative AFM height images for bare and modified RC surfaces obtained (A) before and (B) after the adsorption of lichen MLG onto GAX- and AX-coated and untreated bare RC surfaces from 0.05% (w/w) solutions in SA buffer (20 mM, pH = 5.5) at 50.0 °C. The matrix polysaccharide is indicated in white letters on each image. The RMS roughnesses (white numbers on images) were obtained from the entire 2 µm × 2 µm scan areas and the z range was 20 nm.

Adsorption of lichen MLG onto modified RC surfaces also led to the formation of dissipative layers ($\Delta D > 5 \times 10^{-6}$), thus curves from multiple overtones (n = 7, 9, 11 and

13) were fit with a Voigt-based viscoelastic model. The same procedures were used as described in Chapter 3.3.4. Representative fitting of adsorption profiles for lichen MLG adsorption onto XG-coated RC surfaces from 0.05% (w/w) solutions in SA buffer (20 mM, pH = 5.5) are provided in Figure 6.15. Thicknesses, adsorbed amounts and viscoelastic parameters obtained from a Voigt-based model for lichen MLG layers adsorbed onto modified RC surfaces, including GAX-, AX-, arabinan- and pectin-coated RC surfaces, are summarized in Table 6.12. Lichen MLG adsorption onto XG-coated RC surfaces led to the formation of relatively thin layers with thicknesses of ~ 5.1 nm and relatively rigid layers with larger elastic shear moduli (~ 3.13×10^5 N•m^{-2}), compared to lichen MLG layers adsorbed onto RC surfaces modified with other matrix polysaccharides. From the fitting parameters, the presence of GAX or AX on RC surfaces only slightly changed the thicknesses and the viscoelastic properties of the adsorbed lichen MLG layers. However, the presence of XG had a more significant effect on the thickness and the viscoelastic properties of the adsorbed lichen MLG layer. The results indicated that lichen MLG adsorbed onto GAX or AX in a manner similar to bare RC surfaces. While for arabinan- or pectin-coated RC, the thicknesses of adsorbed lichen MLG layers were about half of the value for bare RC surfaces. The modeling results suggested an inhibitory role for pectins to lichen MLG adsorption onto RC. These conclusions are also in agreement with a study on the sequence of deposition of individual cell wall polysaccharides in developing barley endoperm.[36] That study showed that the deposition of MLG onto cellulose microfibrils occurred before other matrix polysaccharides, such as mannans and arabinoxylans. The MLG had to be deposited first for the development of maximal interactions with cellulose.

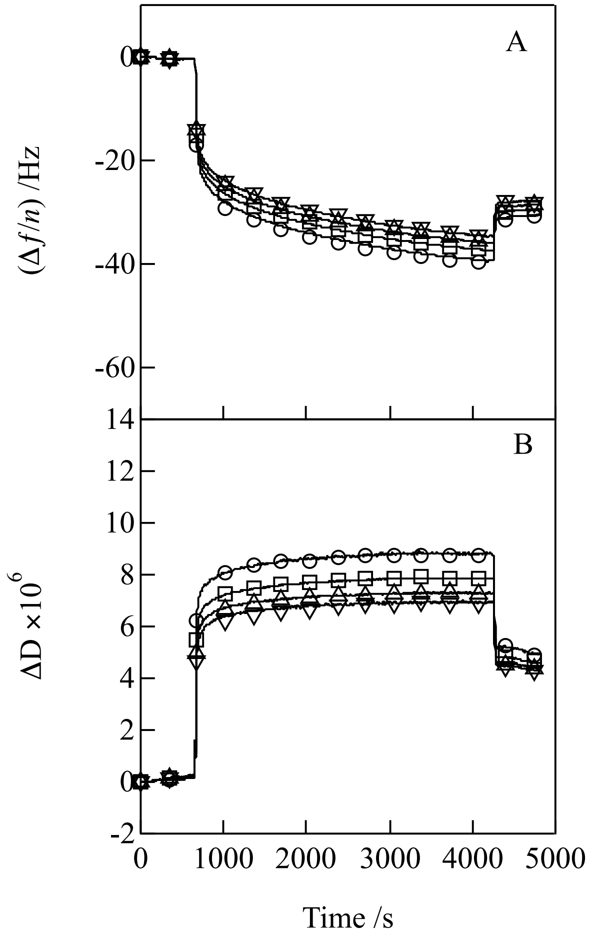

Figure 6.15 Representative time dependent (A) Δ*f*/*n* and (B) ΔD adsorption curves with fits obtained from Voigt-based viscoelastic modeling for lichen MLG adsorption onto XG-coated RC surface from 0.05% (w/w) solutions in SA buffer (20 mM, pH = 5.5) at 50.0 °C. For both graphs, isolated symbols represent a subset of smooth experimental data from *n* = (O) 7, (□) 9, (Δ) 11 and (∇) 13 and solid lines represent fits of the entire data set.

Table 6.12 Summary of h_f, $\Gamma_{QCM\text{-}D}$, μ_f and η_f obtained from a Voigt-based model for lichen MLG layers adsorbed onto bare and matrix polysaccharide modified RC surfaces from 0.05% (w/w) solutions in SA buffer (20 mM, pH = 5.5) at 50.0 °C.[a]

Substrate	$^{a}h_f$ /nm	$\Gamma_{QCM\text{-}D}$ /mg•m^{-2}	$\mu_f \times 10^{-5}$ /N•m^{-2}	$\eta_f \times 10^{3}$ /N•s•m^{-2}
XG-coated RC	5.1 ± 0.3	5.3 ± 0.3	3.13 ± 0.25	1.44 ± 0.08
arabinan-coated	11.0 ± 0.9	11.6 ± 1.0	2.00 ± 0.52	1.25 ± 0.02
pectin-coated RC	11.9 ± 1.3	12.5 ± 1.4	1.58 ± 0.38	1.23 ± 0.03
GAX-coated RC	15.7 ± 0.1	16.4 ± 0.2	0.30 ± 0.01	0.88 ± 0.01
AX-coated RC	15.8 ± 0.8	16.6 ± 0.9	0.28 ± 0.02	0.93 ± 0.04
bare RC	19.3 ± 0.7	21.2 ± 0.8	0.32 ± 0.04	0.98 ± 0.03

a. Assumes $\rho_f = 1050$ kg•m^{-3}.

6.5 Conclusions

In this work, a generic method for the preparation MLG surface layers using QCM-D and AFM was developed. The resulting MLG layers are gel-like and the viscoelastic properties were obtained from a Voigt-based viscoelastic model. The combination of QCM-D and SPR data also confirmed the formation of highly hydrated surface layers, while AFM results showed the formation of smooth homogeneous layers with small RMS roughnesses. Two MLG samples, barley and lichen MLG, were used for the investigation of molecular structure effects on adsorption. Both experimental and modeling data suggested that lichen MLG formed softer layers compared to barley MLG. This observation was attributed to the higher proportion of β-(1→3) linkages in lichen MLG. We also probed the interactions between lichen MLG and other matrix polysaccharides to obtain a better understanding of the assembly of primary cell walls. For XG-, GAX- and AX-coated RC, most of the lichen MLG that adsorbed was likely interacting with preadsorbed polysaccharides rather than cellulose through intermolecular interactions. However, for pectin and arabinan, the reduction of subsequent lichen MLG adsorption is most likely attributed to the blockage of some adsorption sites on RC surfaces.

6.6 References

(1) Dick-Pérez, M.; Zhang, Y.; Hayes, J.; Salazar, A.; Zabotina, O. A.; Hong, M., *Biochemistry* **2011,** *50*, 989-1000.

(2) Vorwerk, S.; Somerville, S.; Somerville, C., *Trends in Plant Science* **2004,** *9*, 203-209.

(3) Buckeridge, M. S.; Rayon, C.; Urbanowicz, B.; Tiné, M. A. S.; Carpita, N. C., *Cereal Chemistry* **2004,** *81*, 115-127.

(4) Carpita, N. C.; Defernez, M.; Findlay, K.; Wells, B.; Shoue, D. A.; Catchpole, G.; Wilson, R. H.; McCann, M. C., *Plant Physiology* **2001,** *127*, 551-565.

(5) Hayashi, T.; Marsden, M. P. F.; Delmer, D. P., *Plant Physiology* **1987,** *83*, 384-389.

(6) Burke, D.; Kaufman, P.; McNeil, M.; Albersheim, P., *Plant Physiology* **1974,** *54*, 109-115.

(7) Wood, P. J., *Trends in Food Science & Technology* **2004,** *15*, 313-320.

(8) Hu, G.; Burton, C., *Cereal Chemistry* **2008,** *85*, 648-653.

(9) Bacic, A.; Harris, P. J.; Stone, B. A., *The biochemistry of plants* **1988,** *14*, 297-371.

(10) Buliga, G. S.; Brant, D. A.; Fincher, G. B., *Carbohydrate Research* **1986,** *157*, 139-156.

(11) Lazaridou, A.; Biliaderis, C.; Micha-Screttas, M.; Steele, B., *Food Hydrocolloids* **2004,** *18*, 837-855.

(12) Gómez, C.; Navarro, A.; Manzanares, P.; Horta, A.; Carbonell, J. V., *Carbohyd Polym* **1997,** *32*, 7-15.

(13) Roubroeks, J. P.; Mastromauro, D. I.; Andersson, R.; Christensen, B. E.; Åman, P., *Biomacromolecules* **2000,** *1*, 584-591.

(14) Izydorczyk, M. S.; Dexter, J. E., *Food Research International* **2008,** *41*, 850-868.

(15) Stübler, D.; Buchenauer, H., *Journal of Phytopathology* **1996,** *144*, 37-43.

(16) Vogel, J., *Current Opinion in Plant Biology* **2008,** *11*, 301-307.

(17) Sørensen, I.; Pettolino, F. A.; Wilson, S. M.; Doblin, M. S.; Johansen, B.; Bacic, A.; Willats, W. G. T., *The Plant Journal* **2008,** *54*, 510-521.

(18) Tosh, S. M.; Brummer, Y.; Wood, P. J.; Wang, Q.; Weisz, J., *Carbohyd Polym* **2004,** *57*, 249-259.

(19) Kontturi, E.; Thüne, P. C.; Niemantsverdriet, J. W., *Langmuir* **2003,** *19*, 5735-5741.

(20) Gómez, C.; Navarro, A.; Gamier, C.; Horta, A.; Carbonell, J. V., *Carbohyd Polym* **1997,** *34*, 141-148.

(21) Wu, J.; Zhang, Y.; Wang, L.; Xie, B.; Wang, H.; Deng, S., *Journal of Agricultural and Food Chemistry* **2006,** *54*, 925-934.

(22) Morgan, K. R.; Roberts, C. J.; Tendler, S. J. B.; Davies, M. C.; Williams, P. M., *Carbohydrate Research* **1999,** *315*, 169-179.

(23) Othman, R. A.; Moghadasian, M. H.; Jones, P. J. H., *Nutrition Reviews* **2011,** *69*, 299-309.

(24) Liu, Z.; Choi, H.; Gatenholm, P.; Esker, A. R., *Langmuir* **2011,** *27*, 8718-8728.

(25) Bottom, V. E., *Introduction to quartz crystal unit design*. Van Nostrand Reinhold New York: 1982.

(26) Vogt, B. D.; Lin, E. K.; Wu, W. L.; White, C. C., *J Phys Chem B* **2004,** *108*, 12685-12690.

(27) Patel, A. R.; Kanazawa, K. K.; Frank, C. W., *Analytical chemistry* **2009,** *81*, 6021-6029.

(28) Gurdak, E.; Dupont-Gillain, C. C.; Booth, J.; Roberts, C. J.; Rouxhet, P. G., *Langmuir* **2005,** *21*, 10684-10692.

(29) Doublier, J. L.; Wood, P. J., *Cereal Chemistry* **1995,** *72*, 335-340.

(30) Böhm, N.; Kulicke, W.-M., *Carbohydrate Research* **1999,** *315*, 302-311.

(31) Horinaka, J.-i.; Okuda, A.; Yasuda, R.; Takigawa, T., *Colloid Polym Sci* **2012,** *290*, 1793-1797.

(32) Fincher, G.; Stone, B., *Advances in cereal science and technology* **1986,** *8*, 207-295.

(33) Izydorczyk, M. S.; MacGregor, A. W., *Carbohyd Polym* **2000,** *41*, 417-420.

(34) Carpita, N. C., *Annual Review of Plant Biology* **1996,** *47*, 445-476.

(35) Bacic, A.; Stone, B. A., *Functional Plant Biology* **1981,** *8*, 475-495.

(36) Wilson, S. M.; Burton, R. A.; Doblin, M. S.; Stone, B. A.; Newbigin, E. J.; Fincher, G. B.; Bacic, A., *Planta* **2006,** *224*, 655-667.

Chapter 7: Enzymatic Degradation of Adsorbed Polysaccharide Layers

7.1 Abstract

Enzymatic degradation of two major plant cell wall polysaccharides, pectin and lichen MLG, were investigated using a quartz crystal microbalance with dissipation monitoring (QCM-D) and atomic force microscopy (AFM). Pectin model surfaces were prepared by pectin adsorption onto gold substrates from a citric phosphate buffer (50 mM, pH = 5.0) as described in Chapter 5. Enzymatic degradation of a series of pectins with different degrees of esterification (DE) by a pectinase from *Aspergillus niger* was studied. Enzymatic degradation was strongly affected by the DE of the pectin samples, with more complete degradation occurring for highly esterified pectins. Increased pectinase concentration also led to a more complete removal of pectins. The lichen MLG layers were prepared by adsorbing lichen MLG onto regenerated cellulose (RC) surfaces from a sodium acetate buffer (20 mM, pH = 5.5) as described in Chapter 6. The subsequent enzymatic degradation of lichen MLG films by a lichenase, an *endo*-(1→3), (1→4)-β-glucanase from *Bacillus subtilis*, was studied by QCM-D and AFM. Enzymatic degradation of lichen MLG layers was studied as a function of enzyme concentration, pH and temperature. Enzymatic degradation rates increased with increasing enzyme concentration, leading to greater removal of lichen MLG. Lichenase showed activity towards lichen MLG surface layers over a wide range of temperature (15 to 50 °C) and pH (pH = 5.5 to 7.5).

7.2 Introduction

Enzymatic degradation is involved in many fundamental applications, such as biology, industrial processing and human diseases.[1-3] Various enzymes in plants participate in degradation and modification of cell wall polysaccharides for the regulation of cell wall expansion and alteration.[1, 4] Degradation of plant cell wall polysaccharides is also extremely important to the food industry and for biofuel processes. As a result, knowledge of enzymatic degradation of cell wall polysaccharides is highly desirable.

Pectins, major components of type I cell walls, are the most complex biomacromolecules in nature, resulting in the presence of various forms of pectin related enzymes in plants. Details on different domains of pectin were discussed in Chapter 2.2.3. Simplified backbone structures of pectin and polygalacturonic acid (PGA) are provided in Figure 7.1. The backbone of pectin is mainly composed of galacturonic acid units through α-(1→4) linkages. Some of the carboxyl groups of galacturonic acid units are partially esterified by methyl groups. The degree of esterification (DE), which is defined as the percentage of carboxylic acids converted to methoxy esters along the pectin backbone, is one of the most important characteristics of pectins. De-esterified pectin, PGA, is a pectin degradation product and commercial PGA is prepared from citrus pectin by partial depolymerization and demethylation.

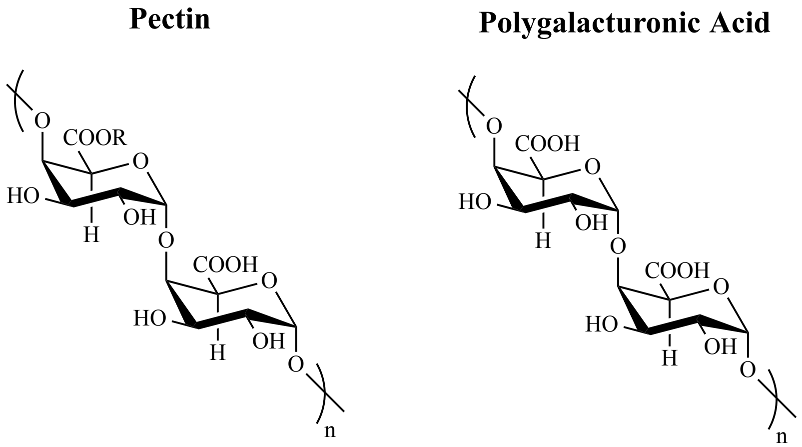

Figure 7.1 Simplified structures of a pectin backbone and PGA. Group R at a *C*6 position represents a methyl group. For the pectin molecular structure depicted here, the DE would be 50%.

Pectinase is a general term for related enzymes that hydrolyze pectic substances. Enzymatic regulation of pectins, including modification and degradation, is believed to control adhesion and permeability within a cell wall matrix.[5] Regulation of pectin by pectinases is also closely related to cell wall extension, softening of plant tissues during maturation and storage, abscission and pathogenesis.[6, 7] Pectinases account for about 25% of the global sales of food enzymes.[6] Most of the commercial pectinases are produced from fungal sources. For example, the *Aspergillus* family is the family of enzymes most commonly used for the industrial production of pectin products.[8] Polygalacturonases, lyases and pectinesterases are among the most extensively studied pectinases and show quite different modes of action as depicted in Figure 7.2. Pectinesterases catalyze the de-esterification of pectins through the removal of methoxy groups. Polygalacturonases and lyases are responsible for the breakdown of pectin backbones through two different degradation mechanisms. Polygalacturonases catalyze the hydrolytic cleavage of the polygalacturonic acid backbone by the addition of water, while lyases catalyze β-elimination of PGA backbones. Pectinases are tremendously important for biotechnology with wide applications in fruit juice extraction, wine production, waste water treatment, textiles, and the pulp and paper industry.[6]

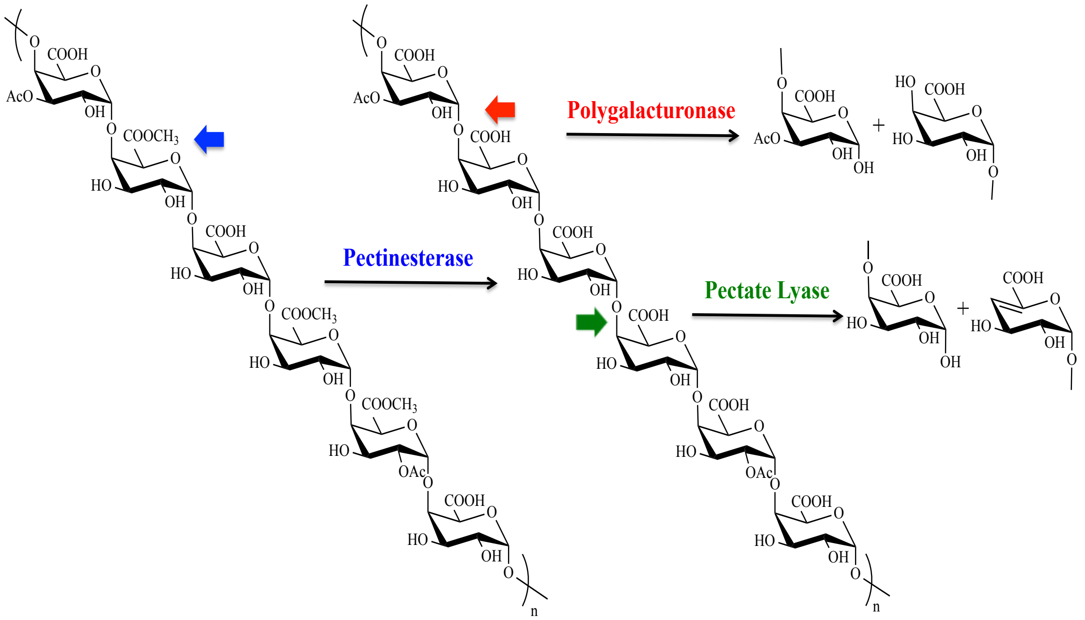

Figure 7.2 Different sites of pectinesterase, polygalacturonase and pectate lyase activity.

The activity of polygalacturonases can be measured through either the increase in the number of reducing groups or a decrease in substrate solution viscosity.[9] Most of the polygalacturonases have an optimal pH range of 3.5 to 5.5 and a temperature range of 30 to 50 °C.[6, 10] The activity of lyases can be measured by an increase in UV absorbance at 235 nm due to the formation of unsaturated double bonds during β-elimination.[11] Unlike polygalacturonases, lyases have an optimal pH in the alkaline range (pH = 7.5 to 10.0) and temperature optima of 40 to 50 °C.[6, 12] The activity of pectinesterases is most commonly measured by gel diffusion assays based upon the binding of ruthenium red to pectins.[13] Pectinesterases show their greatest activity towards pectins with 65 to 75% methylation over a pH range from 4.0 to 8.0 and a temperature range of 40 to 50 °C.[6, 14]

Mixed linkage glucans (MLG) are a major type of hemicellulose accounting for about 3 to 5% of the dry mass of biomass from Poales, cereals and some lichens (*Cetraria islandica*).[15] Lichen MLG is extracted from lichen species with a structure of an unbranched homopolymer of glucose units linked together by both β-(1→3) and β-(1→4) linkages. Several enzymes are responsible for the degradation of MLG in nature, for instance, β-(1→3),(1→4)-glucanases (lichenase EC 3.2.1.73), β-(1→4)-glucanases (cellulase, EC 3.2.1.4), β-(1→3)-glucanases (laminarinase, EC 3.2.1.39) and β-(1→3(4))-glucanases (EC 3.2.1.6).[16] Each enzyme shows great specificity, for instance, lichenase is a β-(1→3), (1→4)-D-glucan 4-glucanohydrolase which specifically cleaves the β-(1→4) linkages adjacent to a β-(1→3) linkage as depicted in Figure 7.3 and yields oligosaccharides with a single β-(1→3) linkage adjacent to the reducing end. These strict cleavage sites of lichenase arise from a number of specific hydrogen bonding interactions between the enzyme and the equatorial hydroxyl groups of the glucose units.[17] Lichenase has no detectable effect on β-(1→3)-glucans (laminaran), β-(1→4)-glucan (cellulose) or carboxymethyl cellulose.[18] This specificity of lichenase makes it useful in structural analyses of MLGs.[19]

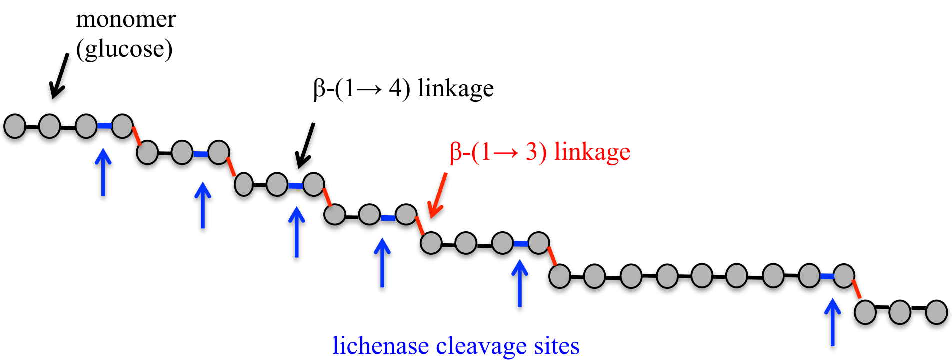

Figure 7.3 A schematic representation of the molecular structure of lichen MLG highlighting specific cleavage sites for lichenase. Blue arrows and bonds show the cleavage sites and bonds that are broken, respectively.

Previous studies of lichenase revealed that the enzyme is a retaining glycosyl hydrolase with a jellyroll β-sandwich structure and six subsites.[18, 20, 21] The active site of lichenase contains a conserved amino acid motif with two glutamic acid residues (Glu^{138} and Glu^{134}) involved in an acid/base (Glu^{138}) and nucleophile hydrolysis (Glu^{134}) mechanism.[22, 23] As depicted in Figures 7.4 and 7.5, the degradation process involves a glycosylation and deglycosylation step on the basis of a double displacement mechanism.[24] The major hydrolysis products released by a lichenase include 3-*O*-β-D-cellobiosyl-D-glucose (trisaccharide) and 3-*O*-β-D-cellotriosyl-D-glucose (tetrasaccharide), as well as longer cellodextrin-like oligosaccharides. Plants are not the only source of lichenase, a number of microorganisms, such as bacteria and fungi also produce lichenase. Although plant and microbial lichenase share no structural similarity, they show the same cleavage specificity.[21] The pH and temperature optima also depend upon the source of the β-(1→3), (1→4)-glucanase.[22] Lichenase used in this study was extracted from *Bacillus subtilis* which is a common source for the preparation of different enzymes, such as α-amylase.[25] The *Bacillus* lichenase is a monodomain protein with molar mass of 25 to 30 kDa, an optimal pH range of 6.0 to 7.5 and temperature range of 45 to 65 °C.[26] Lichenase shows extensive applications in the brewing industry for improving the production rate and clarity of beer, as well as in animal feed for enhancing food intake.[18] Enzyme-mediated saccharification also plays an important role in ethanol production during bioconversion.

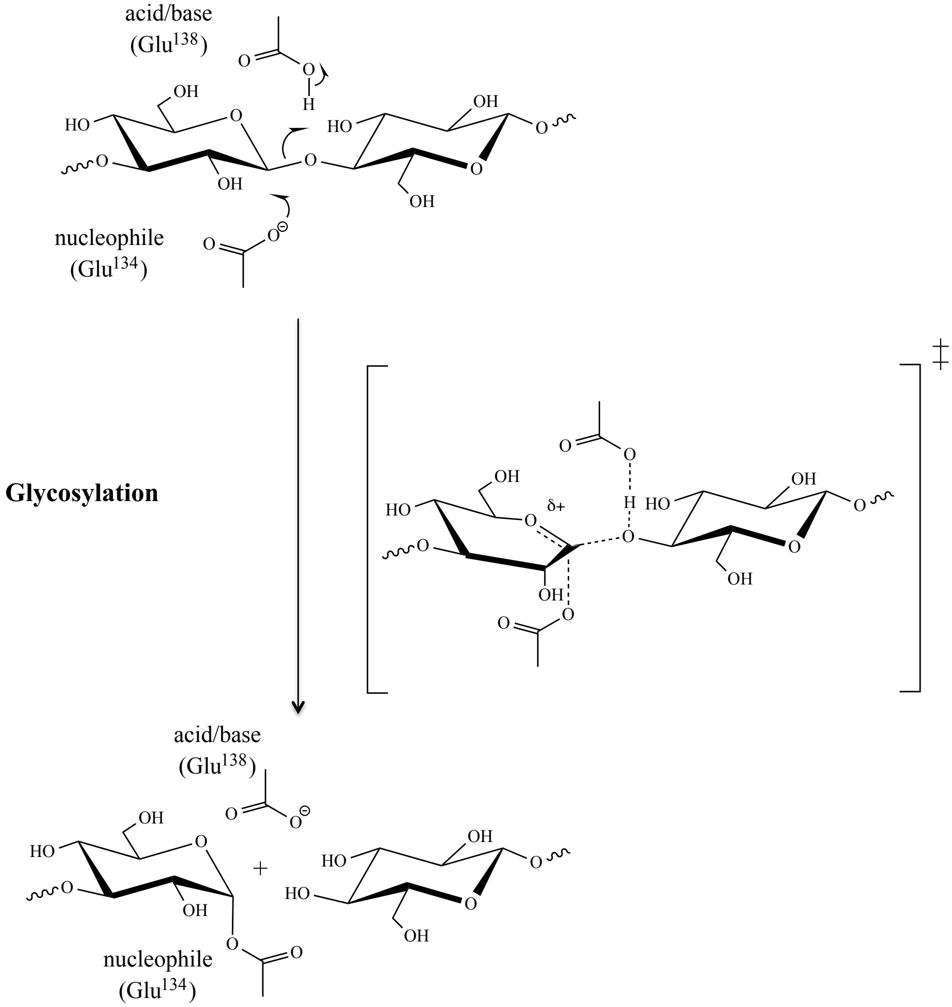

Figure 7.4 The first step (glycosylation) of the double displacement mechanism of a retaining lichenase. The second step is depicted in Figure 7.5. Adapted from Abel *et al.*[24]

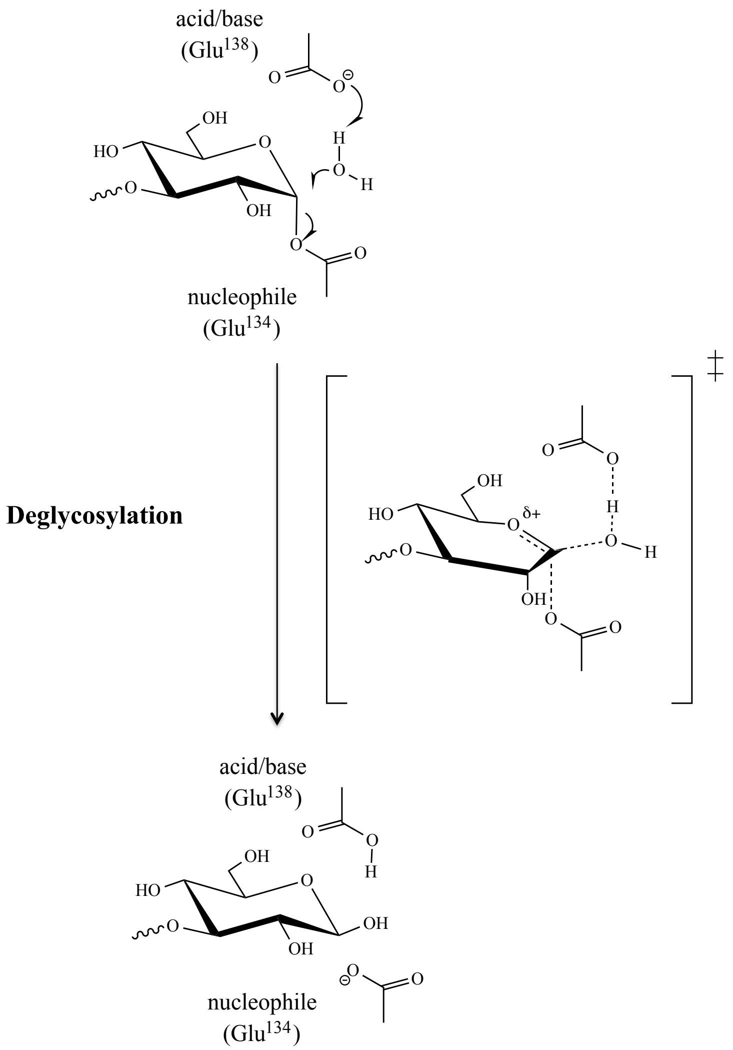

Figure 7.5 The second step (deglycosylation) of the double displacement mechanism of a retaining lichenase. The first step is depicted in Figure 7.4. Adapted from Abel *et al.*[24]

In this chapter, a quartz crystal microbalance with dissipation monitoring (QCM-D) was used for monitoring enzymatic degradation of two polysaccharide layers, including pectin and lichen MLG. Visualization of the polysaccharide surfaces before and after enzymatic degradation was accomplished through atomic force microscopy (AFM). The enzymatic degradation of pectin was investigated as a function of enzyme concentration, pH and the DE of the pectin samples. For lichen MLG layers, the effects of enzyme concentration, pH and temperature were studied.

7.3 Experimental

7.3.1 Materials

Four pectin samples with different DE were used in this study and are summarized in Table 7.1. For pectinase, one unit (1 U) of enzyme activity is defined as the amount of enzyme that releases 1 μmol•mL^{-1}•min^{-1} galacturonic acid under standard assay conditions (25 °C, pH = 4.0). Pectinase was dissolved in a sodium acetate (SA) buffer (50 mM) with different pH and fresh solutions were prepared at the beginning of each measurement. For lichenase, one unit (1 U) of enzyme activity is defined as the amount of enzyme that releases 1 μmol•mL^{-1}•min^{-1} glucose under standard assay conditions (40 °C, pH = 6.5). Lichenase was dissolved in a sodium phosphate (SP) buffer (20 mM) with different pH and fresh solutions were prepared at the beginning of each measurement. For pectinase degradation studies, a batch mode was used and the degradation of pectin was in the absence of flow. For lichenase degradation studies, the lichen MLG layers were subjected to a continuous flow of lichenase solution until a plateau in the degradation profiles occurred. The reason for different degradation modes was due to different enzyme-substrate interactions. Pectinase is known to strongly interact with a gold substrate and irreversibly adsorb onto gold, while lichenase only interacts weakly with cellulose and has no action on a cellulose substrate due to the absence of cleavage sites.

Table 7.1 Summary of pectin samples used in this chapter.[a]

	Supplier	**Source**	**Degree of Esterification**	**[a]Molar Mass /kDa**
Polygalacturonic Acid	Megazyme	Citrus	4%	-
Pectin	Sigma-Aldrich	Citrus	< 26%	23 to 71
Low DE Pectin	Sigma-Aldrich	Citrus	20 to 30%	17
High DE Pectin	Sigma-Aldrich	Citrus	55 to 70%	82

a. Weight average molar mass.

7.3.2 QCM-D Measurements

For pectin deposition and degradation, QCM-D sensors were placed in the flow cells. The preparation of pectin model surfaces with different DE was previously described in Chapter 5. After the preadsorption of pectin samples onto gold from citric phosphate (CP) buffer (50 mM, pH = 5.0) at 40.0 °C, SA buffer (50 mM) was subsequently introduced into the flow cells at the same temperature to change the surrounding pH for pectinase. For all pectinase degradation studies, 1 mL of pectinase solution was pumped into each flow cell, then the pump was stopped and the degradation was carried out in a batch mode. At the end of the degradation, SA buffer (50 mM, pH = 4.0) was flowed through the system for the removal of residual and reversibly adsorbed enzymes and products. Changes in scale frequency ($\Delta f/n$) and dissipation (ΔD) were recorded simultaneously. All measurements were performed at 40.0 °C in triplicate. The average values ± one standard deviation were calculated for each condition.

For lichen MLG deposition and degradation, RC-coated QCM-D sensors were placed in the flow cells. Deposition of lichen MLG layers was previously described in Chapter 6. After the preadsorption of lichen MLG onto RC surfaces from 0.05% (w/w) solutions in SA buffer (20 mM, pH = 5.5) at 50.0 °C, SP buffer (20 mM) was subsequently introduced into the flow cells at the same temperature. For all lichenase degradation studies, lichenase solutions were pumped into the flow cells under a continuous flow rate of 0.200 mL•min^{-1}. At the end of enzymatic degradation, SP buffer (20 mM) was flowed through the system for the removal of residual and reversibly adsorbed enzymes and products. Changes in $\Delta f/n$ and ΔD were recorded simultaneously. All measurements were performed under a continuous flow rate of 0.200 mL•min^{-1} at 50.0 °C in triplicate. The average values ± one standard deviation were calculated for each condition.

7.3.3 AFM Measurements

Before and after enzyme degradation, the QCM-D sensors were dried in an oven at 60 °C for 5 hours and then imaged with an MFP-3D-Bio atomic force microscope (MFP-3D-BIO, Asylum Research) in tapping mode. Images from AFM were collected under ambient conditions using a silicon tip (OMCL-AC 160TS, Olympus Corp.). The reported root-mean-square (RMS) roughnesses were determined from 2 μm × 2 μm scan areas.

7.4 Results and Discussion

7.4.1 Pectinase Degradation of Pectin Model Surfaces

Pectin model surfaces were prepared on QCM-D gold sensors by adsorbing pectin samples from solutions in citric phosphate (CP) buffer (50 mM, pH = 5.0) directly onto the gold at 40.0 °C as described in Chapter 5. As the optimal pH of the pectinase used in this study was around pH = 4.0, it was necessary to add an equilibrium step after film preparation at pH = 5.0. After pectin film formation, the pectin layers were exposed to SA buffer (50 mM, pH = 4.0). Representative adsorption profiles for the preparation of high DE pectin model surfaces with a switch to SA buffer (50 mM, pH = 4.0) are provided in Figure 7.6. After the gold sensor was equilibrated in ultrapure water, SA buffer was introduced into the flow cell. The decrease in scaled frequency ($\Delta f/n$) and increase in dissipation (ΔD) reflect differences in the density and viscosity between SA buffer and water. A decrease in $\Delta f/n$ and increase in ΔD indicated pectin adsorption onto the gold substrates from solutions in CP buffer (50 mM, pH = 5.0) at 40.0 °C. The switch back to CP buffer (50 mM, pH = 5.0) showed the initial adsorption was irreversible in the buffer. Next, the solution was switched to water. During this step, $\Delta f/n$ increased and ΔD decreased. Parts of these changes ($\Delta f/n \sim 8$ Hz and $\Delta D \sim 2 \times 10^{-6}$) were due to changes in the density and viscosity but some of the film also desorbed in water. Upon switching from water to SA buffer, there were small changes in $\Delta f/n$ and ΔD. These changes are comparable to changes observed when gold coated crystals were switched from water to SA buffer. Hence, the small changes in $\Delta f/n$ and ΔD upon the switch from water to SA buffer in Figure 7.6 only correspond to density and viscosity changes of the surrounding medium and not substantial desorption of the film. As such, the pectin layers were stable in SA buffer (50 mM, pH = 4.0). All four pectin samples tested in this chapter showed irreversible adsorption onto gold substrates and adsorbed amounts ($\Gamma_{QCM\text{-}D} = 4.5$ mg•m^{-2}) from the Sauerbrey equation (Equation 3.1) were similar for all four samples.[27]

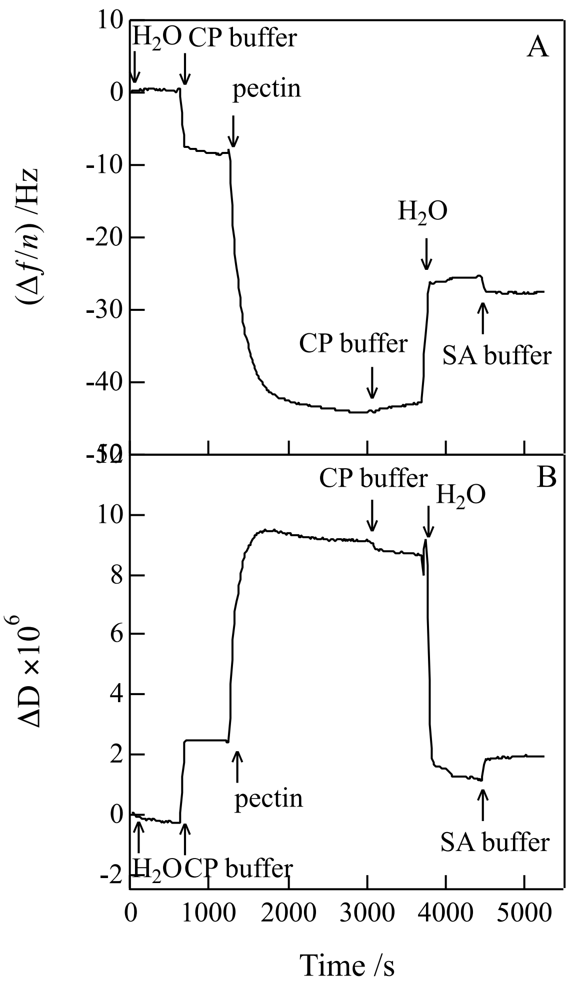

Figure 7.6 Representative time dependent (A) $\Delta f/n$ and (B) ΔD adsorption profiles for high DE pectin adsorbed onto gold substrates from 500 mg•L^{-1} solutions in CP buffer (50 mM, pH = 5.0) at 40.0 °C. An additional switch to SA buffer (50 mM, pH = 4.0) was performed to change the surrounding solution conditions for pectinase studies. Data correspond to the fifth overtone and arrows indicate where solutions were switched.

After the preadsorption of pectin onto gold substrates, the instrument was re-zeroed. Next, the pectin layers were exposed to a pectinase solution at the same temperature and $\Delta f/n$ and ΔD were monitored simultaneously. Representative QCM-D degradation profiles for high DE pectin layers exposed to pectinase as a function of enzyme concentration are provided in Figure 7.7. Unlike the adsorption process described in Figure 7.6, the enzymatic degradation process in Figure 7.7 was accompanied by a significant increase in $\Delta f/n$ and decrease in ΔD immediately after the injection of 1 mL of freshly prepared pectinase solution. The shapes of the profiles are different from cellulase degradation of cellulose[28] or chitinase activity on chitin model surfaces[29] measured by QCM-D. For these two cases, there was an initial decrease in $\Delta f/n$ and increase in ΔD that corresponds to cellulase adsorption. After the initial adsorption step, there were significant increases in $\Delta f/n$ and decreases in ΔD, as the cellulose was degraded, however, the initial rates for cellulase and chitinase were slower than those seen in Figure 7.7. In contrast to the cellulase and chitinase systems, initial enzyme adsorption was absent for the case of pectinase degradation. The absence of initial pectinase adsorption could be explained by greater water solubility of pectin oligosaccharides cut by pectinase which allowed them to diffuse away from the substrates. In essence, significant film degradation occurred as soon as enzyme arrived. For cellulose and chitin, only very small fragments of the chains are water soluble leading to a slower release of diffusible species and an accumulation of enzyme on the substrate. Pectinase degradation occurred rather fast and reached degradation equilibrium within 15 minute of degradation, indicating tremendous pectinase activity towards high DE pectin. Irreversible changes in $\Delta f/n$ and ΔD for pectinase degradation of high DE pectin layers are summarized in Table 7.2. The amount of high DE pectin removed by pectinase solution with a concentration of 2.3 U•mL^{-1} was about 3.0 mg•m^{-2} calculated from the Sauerbrey equation (Equation 3.1).[27] This showed that about 65% of the hydrated mass of high DE pectin was released during pectinase degradation. This value is a lower bound as any irreversibly adsorbed pectinase would replace released pectin degradation products. Possible incomplete degradation of pectin could arise from collapsed pectin residues that block further penetration of pectinase. Control experiments were conducted with a continuous flow of fresh pectinase, leading to more complete hydrolysis of the pectin, even though there was still a contribution from pectinase adsorption onto the gold substrates. The affinity of pectinase ($\Delta f/n \sim -20$ Hz and $\Delta D \sim 0.4 \times 10^{-6}$) for gold is the reason the pump was stopped after pectinase injection and the enzymatic degradation data in Figure 7.7 were obtained in the absence of flow.

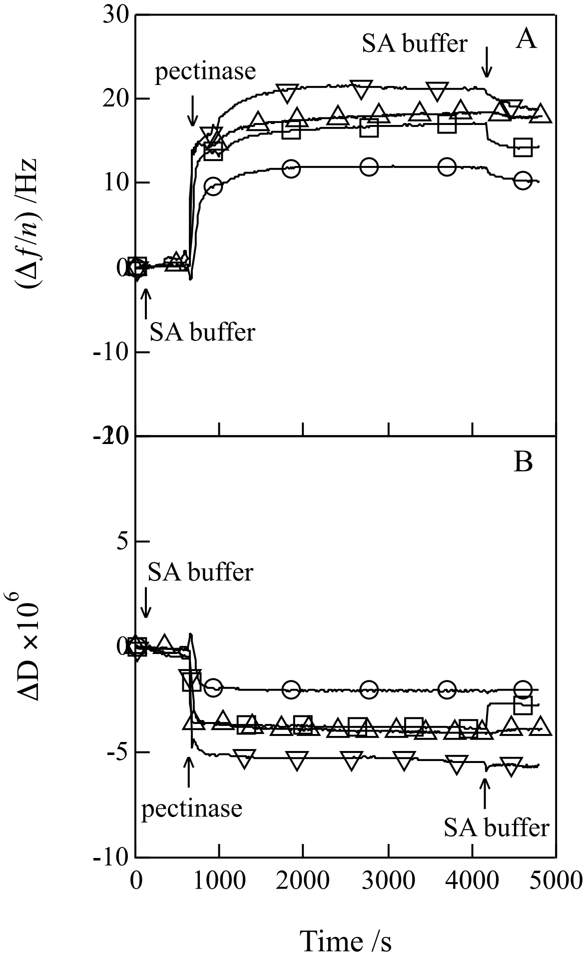

Figure 7.7 Representative time dependent (A) Δ*f*/*n* and (B) ΔD degradation profiles for pectinase action on high DE pectin layers in SA buffer (50 mM, pH = 4.0) at 40.0 °C. A series of enzyme concentrations were used, including (O) 0.1, (□) 0.5, (Δ) 1.0 and (∇) 2.3 U•mL^{-1}. Data correspond to the fifth overtone and arrows indicate where solutions were switched.

Table 7.2 Irreversible $\Delta f/n$ and ΔD for pectinase degradation of high DE pectin layers in SA buffer (50 mM, pH = 4.0) at 40.0 °C.

Pectinase Concentration /U•mL^{-1}	**$\Delta f/n$ /Hz**	**ΔD ×10^{6}**
0.1	10.7 ± 0.5	-2.0 ± 0.9
0.5	13 ± 1	-2.8 ± 0.4
1.0	13.6 ± 1.5	-3.4 ± 0.2
2.3	16.6 ± 0.9	-5.1 ± 0.3

Pectinase concentration effects on enzymatic degradation of high DE pectin layers were investigated using a series of enzyme concentrations, including 0.1, 0.5, 1.0 and 2.3 U•mL^{-1}. Representative time dependent QCM-D degradation profiles and irreversible changes in $\Delta f/n$ and ΔD for pectinase degradation of high DE pectin layers for different pectinase concentrations are provided in Figure 7.7 and Table 7.2, respectively. Greater changes in $\Delta f/n$ and ΔD were obtained with increasing pectinase concentration, indicating a greater mass loss at high pectinase concentrations. Lowering the pectinase concentration to 0.1 U•mL^{-1} resulted in slower degradation of high DE pectin layers compared to the degradation at 0.5 U•mL^{-1} and higher concentrations. Pectinase is known to break down pectin chains in an endo and random fashion. With the increase in pectinase concentration, pectinase molecules were subjected to more cleavage events, leading to a more rapid decrease in molar mass with an attendant enhancement of more soluble, low molar mass products. Similar behavior was also observed for the enzymatic degradation of polyelectrolyte multilayers containing poly-L-lysine and PGA.[30] A degradation plateau was also achieved at an early stage of enzymatic degradation. Representative AFM height images of high DE pectin layers before and after pectinase action for different pectinase concentrations as well as a bare gold substrate are provided in Figure 7.8. The AFM images before pectinase degradation (Figure 7.8B) showed that high DE pectin model surfaces appeared to be a heterogeneous network containing aggregated structures with small RMS roughnesses of about 2.1 nm. This was closely related to the high concentration of polysaccharide solution used for the preparation of pectin model surfaces. The height images obtained at the end of pectinase degradation showed a clear reduction in aggregate size. Changes in morphology and RMS roughness of high DE pectin model surfaces before and after enzymatic degradation confirmed the successful removal of high DE pectin layers from gold substrates. At moderate enzyme concentration (2.3 U•mL^{-1}, Figure 7.8C), aggregates with irregular shapes and sizes were observed compared to Figure 7.8B. At high enzyme concentration (5.0 U•mL^{-1}, Figure 7.8D), residues can be easily identified from AFM images and a smooth surface layer with RMS roughness of about 1.1 nm was obtained. The difference in surface morphology between high DE pectin layers after enzymatic degradation (Figure 7.8D) and the bare gold substrate (Figure 7.8A) suggests that enzymes as well as residues of degradation products are present on the gold substrate.

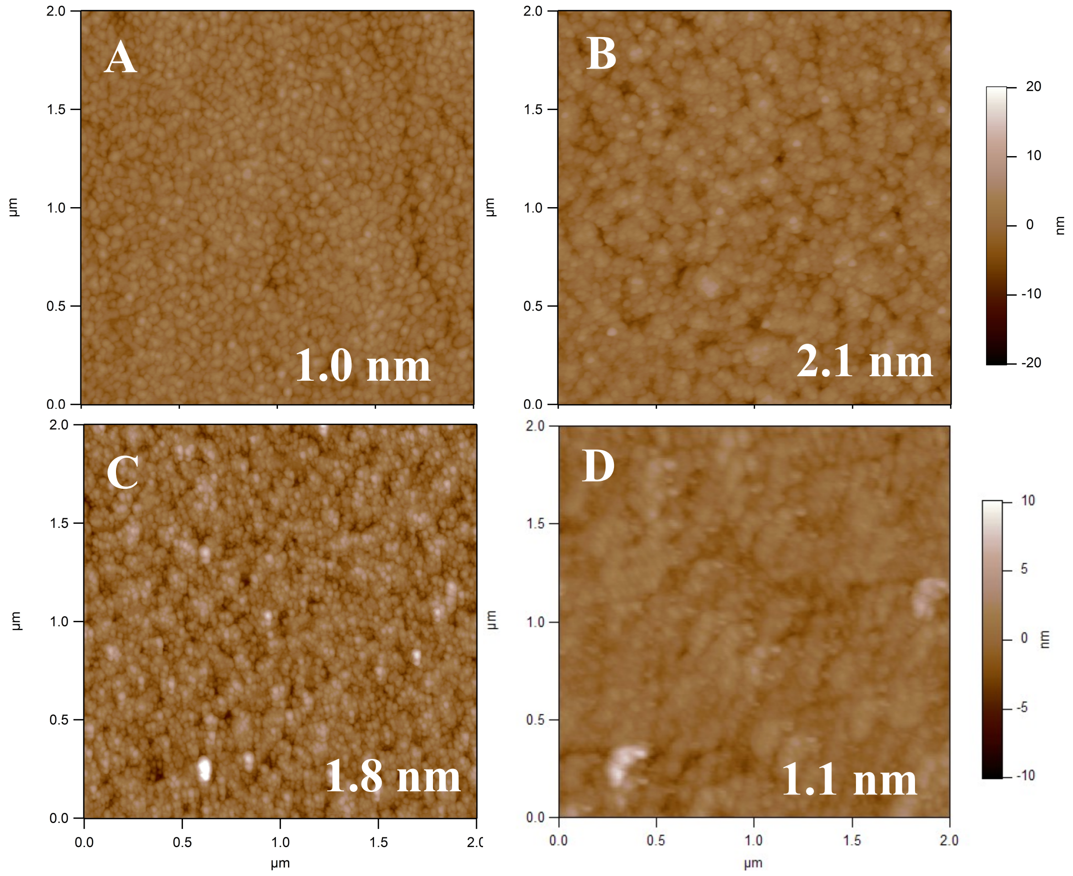

Figure 7.8 Representative AFM images of (A) a bare gold substrate, (B) a gold substrate with a high DE pectin layers before pectinase degradation and (C) and (D) high DE pectin layers after degradation by a pectinase from *Aspergillus niger* at 40.0 °C. The enzyme concentrations for the degraded films were (C) 2.3 U•mL^{-1} and (D) 5.0 U•mL^{-1} in SA buffer (50 mM, pH = 4.0). The RMS roughnesses (white numbers on images) were obtained from the entire 2 µm × 2 µm image areas with z range of 20 nm.

The effect of pH on pectinase degradation of high DE pectin layers was also examined by QCM-D. Representative time dependent degradation profiles for pectinase degradation of high DE pectin layers using pH = 4.0 and 6.0 at 40.0 °C are provided in Figure 7.9. Irreversible changes in $\Delta f/n$ and ΔD for pectinase degradation of high DE pectin layers under different pH conditions are summarized in Table 7.3. Greater changes in $\Delta f/n$ and ΔD were obtained at pH = 4.0, indicating a greater mass loss at pH = 4.0 compared to pH = 6.0. In addition, there was a significant difference in degradation kinetics of high DE pectin for different pH conditions. Degradation at low pH (pH = 4.0) occurred almost instantly (< 10 min). The degradation at high pH (pH = 6.0) appeared to remove pectin in a more gradual manner and changes in $\Delta f/n$ kept increasing even after a degradation time of 1 hour. This observation is in agreement with the information provided by the supplier that the optimal pH of pectinase was in the range of 4.0 to 5.0. This result was also consistent with the literature value of 4.0 for the optimal pH of pectinase.[6, 31] Representative AFM height images of high DE pectin layers before and after pectinase treatment at different pH conditions are provided in Figure 7.10. As is evident in Figure 7.10, pectinase degradation under different pH showed quite different surface morphologies after pectinase degradation. At pH = 4.0, a clear reduction in aggregate size was observed, while aggregates with greater sizes were easily identified for pectinase treatments at pH = 6.0. Similar morphologies and RMS roughnesses between degraded high DE pectin layers at pH = 6.0 (Figure 7.10B) and pectinase coated gold substrates (Figure 7.10C) indicated the presence of pectinase residues on gold substrates, especially at high pH conditions.

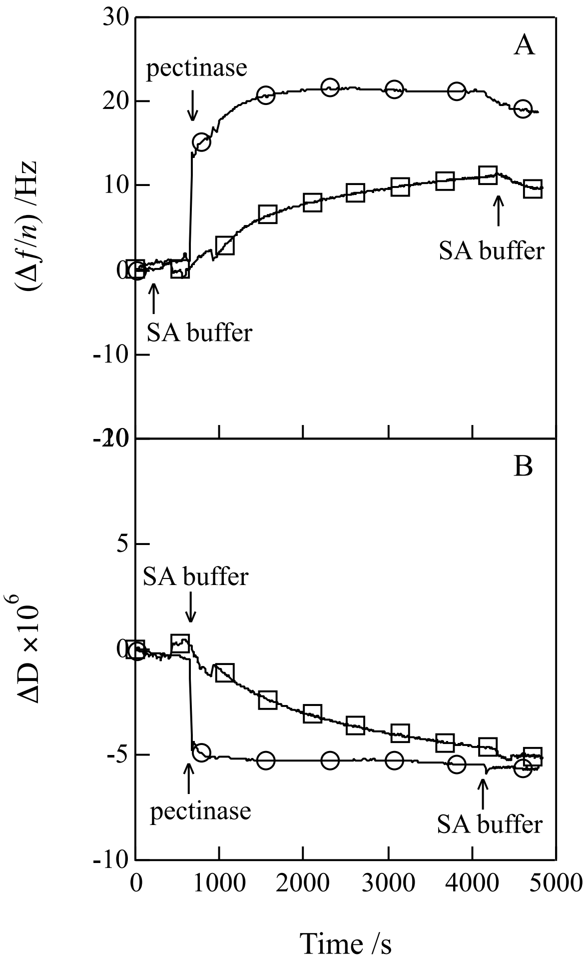

Figure 7.9 Representative time dependent (A) $\Delta f/n$ and (B) ΔD degradation profiles for pectinase action on high DE pectin layers using 50 mM SA buffer at 40.0 °C and different pH conditions: (O) pH = 4.0 and (☐) pH = 6.0. The enzyme concentration was 2.3 U•mL^{-1}. Data correspond to the fifth overtone and arrows indicate where solutions were switched.

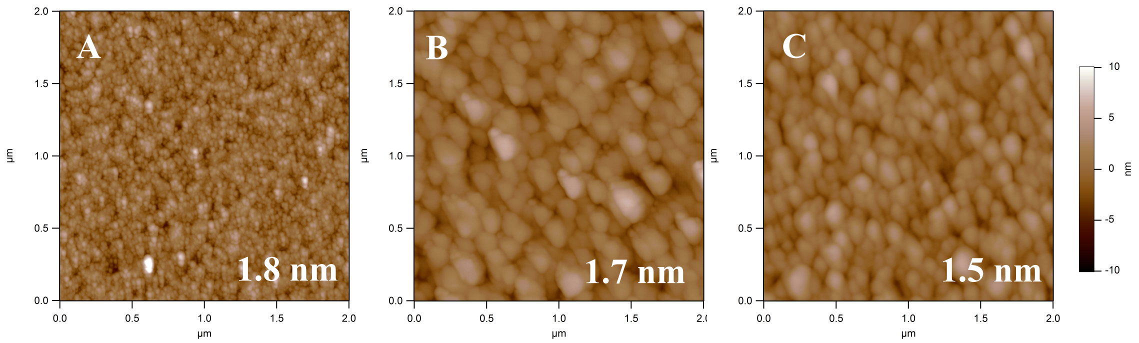

Figure 7.10 Representative AFM images of high DE pectin layers after degradation by a pectinase from *Aspergillus niger* at (A) pH = 4.0 and (B) pH = 6.0 and (C) a control experiment for pectinase adsorption onto bare gold substrates at 40.0 °C. The enzyme concentration was 2.3 U•mL^{-1} in SA buffer (50 mM). The RMS roughnesses (white numbers on images) were obtained from the entire 2 μm × 2 μm image areas with z range of 20 nm.

Table 7.3 Irreversible $\Delta f/n$ and ΔD for pectinase degradation of high DE pectin layers at 40.0 °C and different pH. The enzyme concentration was 2.3 U•mL^{-1} in SA buffer (50 mM).

pH	$\Delta f/n$ /Hz	ΔD ×10^6
4.0	16.6 ± 0.9	-5.1 ± 0.3
6.0	8.9 ± 0.5	-4.3 ± 0.6

In addition to effects of enzyme concentration and pH, DE effects on pectinase degradation were probed using the combination of QCM-D and AFM. Representative time dependent degradation profiles for pectinase action on PGA, pectin, low DE pectin and high DE pectin are provided in Figure 7.11. Irreversible changes in $\Delta f/n$ and ΔD for pectinase degradation of pectin layers with different DE at 40.0 °C are summarized in Table 7.4. Greater changes in both $\Delta f/n$ and ΔD were observed with increasing DE for pectin, indicating a greater degradation of highly esterified pectin layers. For pectins with relatively low DE (pectin and polygalacturonic acid), only the initial adsorption of enzyme was observed. Only slight degradation of the low DE pectins (pectin and polygalacturonic acid) occurred for incubation times in excess of 1 hour. These results contradict a previous study that claimed high DE pectins negatively affected the affinity of a pectinase from *Fusarium moniliforme* as well as their hydrolysis of pectins.[32] Some studies also showed that pectin with high DE was more stable than its corresponding acid form, PGA, under acidic pH (pH = 4.5) similar to the one used in this study[33] and could be explained by fewer free carboxyl groups for catalysis and the reduction of enzyme-substrate coupling for highly esterified pectin.[34] However, these results also contradict results obtained from QCM-D studies. Still other researchers have reported the existence of some pectinases exhibiting enhanced activity towards highly esterified pectins. For instance, a polymethylgalacturonase with an optimal pH between 4.0 and 5.0 that preferentially acts upon highly esterified pectin substrates has been reported.[31] This result is actually quite similar to our case, where the pectinase worked better on highly esterified pectin at an optimal pH of 4.0.

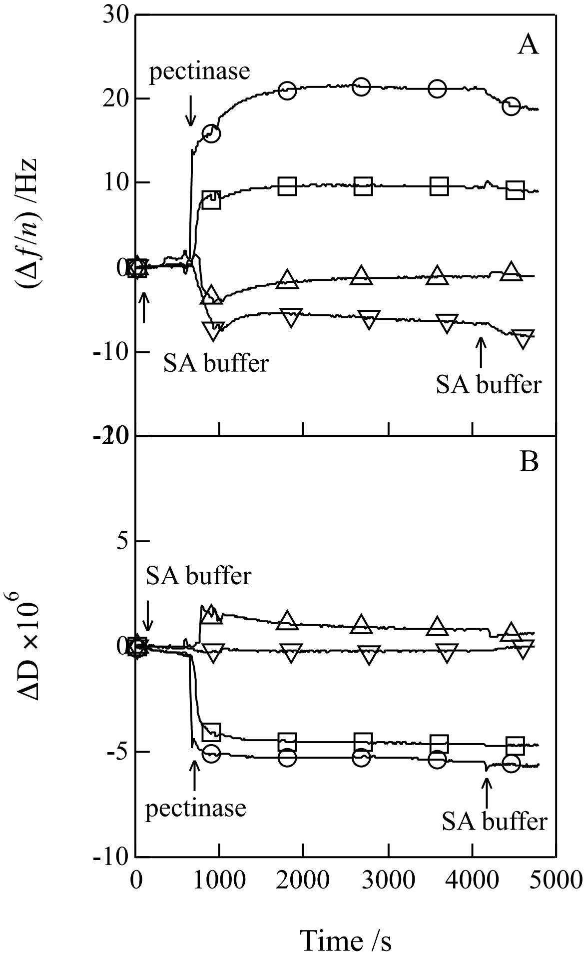

Figure 7.11 Representative time dependent (A) Δ*f*/*n* and (B) ΔD degradation profiles for pectinase action on pectin samples with different DE, including (O) high DE pectin, (☐) low DE pectin, (Δ) pectin and (∇) PGA with decreasing DE. The enzyme concentration was 2.3 U•mL^{-1} in SA buffer (50 mM, pH = 4.0) at 40.0 °C. Data correspond to the fifth overtone and arrows indicate where solutions were switched.

Table 7.4 Irreversible $\Delta f/n$ and ΔD for pectinase degradation of pectin layers with different DE at 40.0 °C. The enzyme concentration was 2.3 U•mL^{-1} in SA buffer (50 mM, pH 4.0).

Sample	**DE**	**$\Delta f/n$ /Hz**	**$\Delta D \times 10^6$**
PGA	4%	-8 ± 2	0.34 ± 0.04
Pectin	< 26%	-2.5 ± 0.6	0.8 ± 0.2
Low DE Pectin	20-34%	9.2 ± 0.6	-3.7 ± 0.6
High DE Pectin	55-70%	16.6 ± 0.9	-5.1 ± 0.3

Representative AFM height images of pectin layers with different DE before and after pectinase degradation are provided in Figures 7.12 and 7.13. Aggregates were easily identified in the AFM images before degradation and all of the pectin samples adsorbed as relatively smooth surface layers on gold substrates from CP buffer (50 mM, pH 5.0). For high DE pectin and low DE pectin layers, AFM height images obtained after degradation as seen in Figure 7.12, respectively, showed a clear reduction in aggregate size. Changes in RMS roughness and morphology of pectin model surfaces before and after enzymatic degradation confirmed the successful removal of pectin layers with relatively high DE from the gold substrates. Conversely, similar AFM images were obtained for pectin and PGA layers (Figure 7.13) before and after pectinase degradation. The images before and after "degradation" look nearly the same. This fact is consistent with insignificant enzymatic degradation of pectins with relatively low DE. These images are consistent with QCM-D data that showed pectinase exhibited greater activity towards highly esterified pectin, leading to more complete removal of pectin layers. Both QCM-D data and AFM images confirmed that pectinase worked better on highly esterified pectin samples, leading to more complete mass removal.

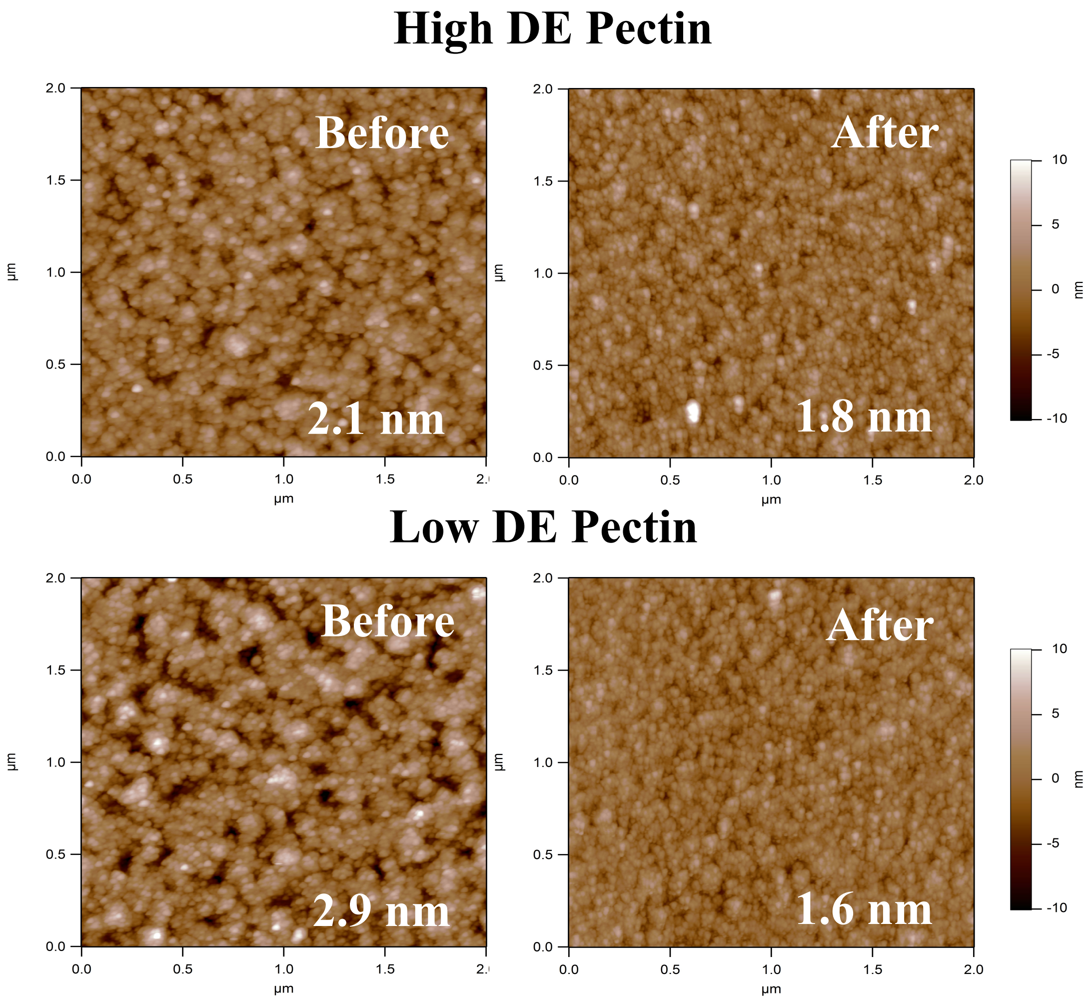

Figure 7.12 Representative AFM height images for the two pectin samples with relatively high DE before and after degradation by a pectinase solution with a concentration of 2.3 U•mL^{-1} in SA buffer (50 mM, pH = 4.0) at 40.0 °C. The RMS roughnesses (white numbers on images) were obtained from the entire 2 µm × 2 µm image areas with z range of 20 nm.

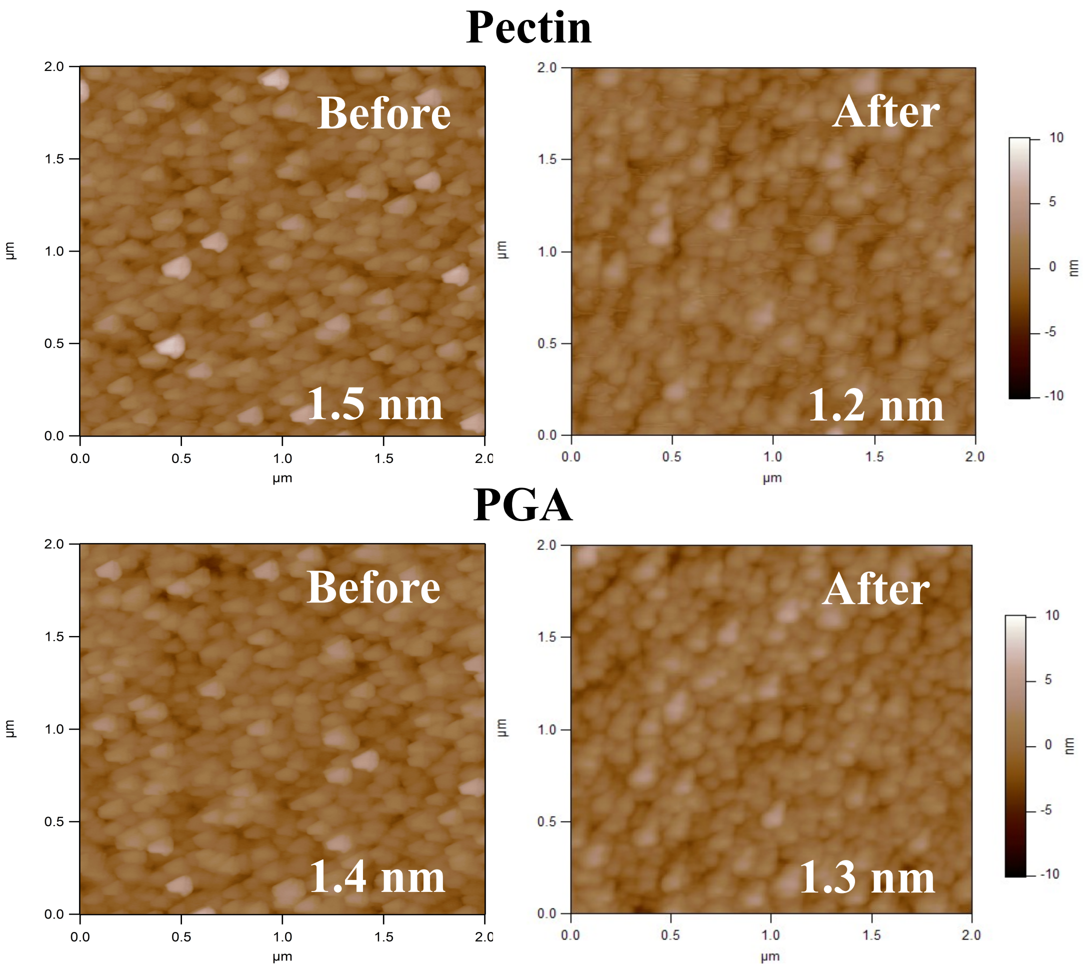

Figure 7.13 Representative AFM height images for the two pectin samples with relatively low DE before and after "degradation" by a pectinase solution with a concentration of 2.3 U•mL^{-1} in SA buffer (50 mM, pH = 4.0) at 40.0 °C. The RMS roughnesses (white numbers on images) were obtained from the entire 2 µm × 2 µm image areas with z range of 20 nm.

Surprisingly, the ease of degradation (*C*6 esterified > non-esterified) observed in our study followed the same trend expected for β-elimination under basic conditions. For a β-elimination mechanism, the activated hydrogen atoms at the *C*5 positions can be removed by suitable proton acceptors, leading to an unstable anionic intermediate that is stabilized by losing the C-O linkages in the β position. As seen in Figure 7.14, esterification at the *C*6 positions eliminates a local negative charge, thereby allowing easier hydrogen abstraction from the *C*5 postition.[35] Similar degradation in neutral or weakly acidic conditions has also been observed.[11] For non-basic conditions, β-elimination reactions have been stimulated by cations and anions in solution.[36] For instance, residual citrate ions from the preadsorption process as well as sodium ions used in CP and SA buffer conditions could stimulate β-elimination and promote pectin degradation via β-elimination even in weakly acidic conditions. A β-elimination mechanism is consistent with the pectinase activity observed in this study towards highly esterified pectin (Figure 7.14) rather than pectin with low DE and PGA (Figure 7.15).

Highly Esterified Pectin

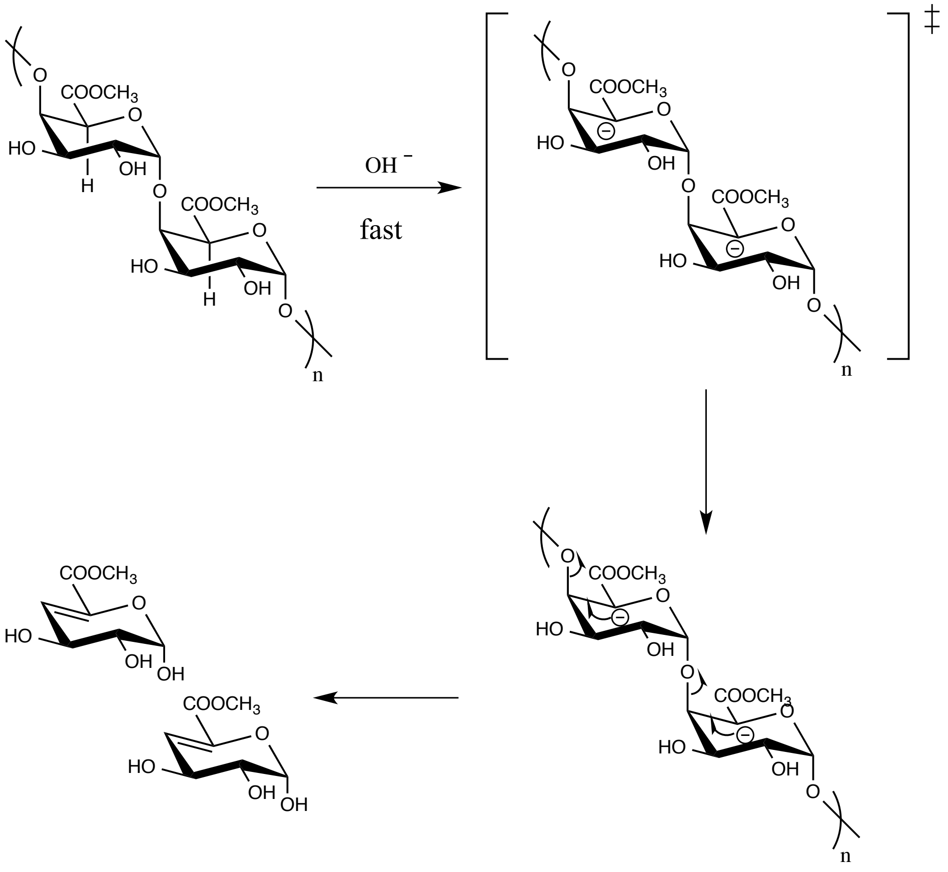

Figure 7.14 Depiction of a β-elimination mechanism for highly esterified pectin. The anionic intermediate is shown in brackets. Esterification at the *C*6 positions eliminates a local negative charge that inhibits hydrogen abstraction from the *C*5 position seen in Figure 7.15 for PGA.

Polygalacturonic Acid

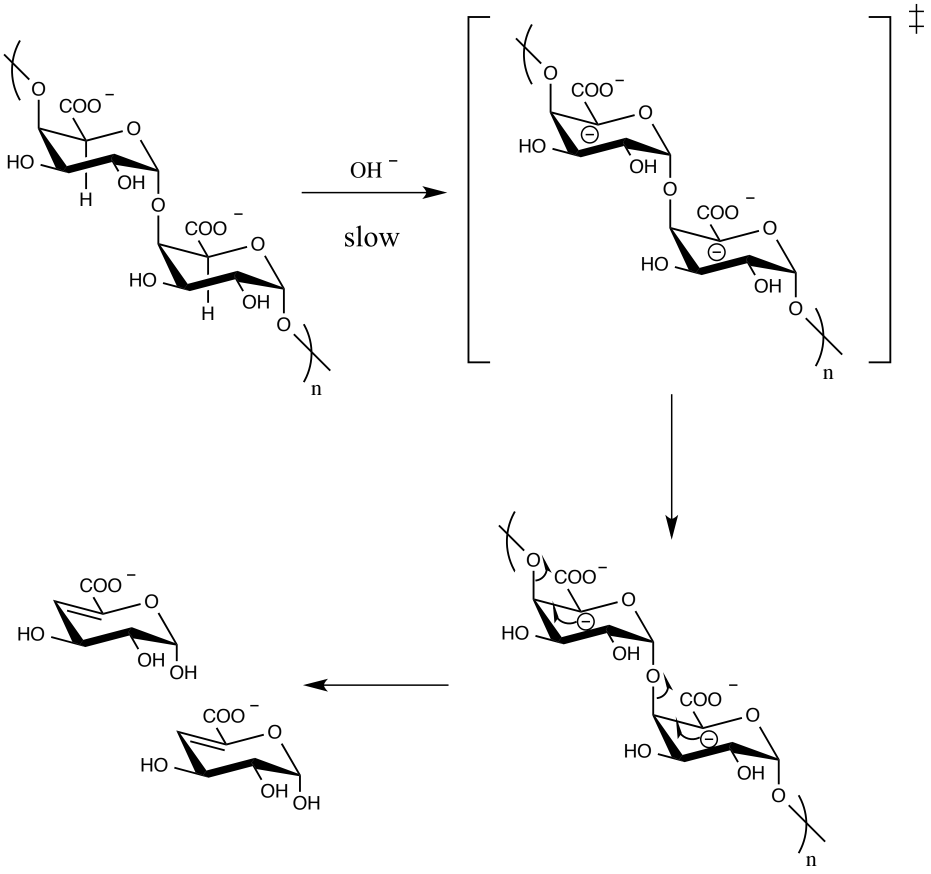

Figure 7.15 Depiction of a β-elimination mechanism for PGA. The anionic intermediates are shown in brackets. The presence of two negative changes in close proximity severely impedes β-elimination.

7.4.2 Lichenase Degradation of Lichen MLG Layers

Lichen MLG surface layers were prepared on RC-coated QCM-D sensors as described in Chapter 6. Representative time dependent adsorption profiles for lichen MLG adsorbed from 0.05% (w/w) solutions in SA buffer (20 mM, pH = 5.5) onto RC substrates are provided in Figure 7.16. As seen in Figure 7.16, there was a significant decrease in $\Delta f/n$ and increase in ΔD right after the injection of lichen MLG solution. Adsorption profiles did not return to the baseline, indicating an irreversible adsorption of lichen MLG onto RC substrates from SA buffer (20 mM, pH = 5.5) at 50.0 °C. Upon switching to water, $\Delta f/n$ increased and ΔD decreased. These changes ($\Delta f/n$ ~ -10 Hz and ΔD ~ 4×10^{-6}) were mainly due to the removal of reversibly bound lichen MLG. Upon switching from water to SP buffer, there were small changes in $\Delta f/n$ and ΔD. These changes were comparable to changes observed when RC coated sensors were switched from water to SP buffer. Hence, the small changes in $\Delta f/n$ and ΔD upon switch from water to SP buffer only correspond to changes in the density and viscosity of the surrounding medium rather than substantial desorption of the lichen MLG film. Hence, the lichen MLG layers were stable in SP buffer.

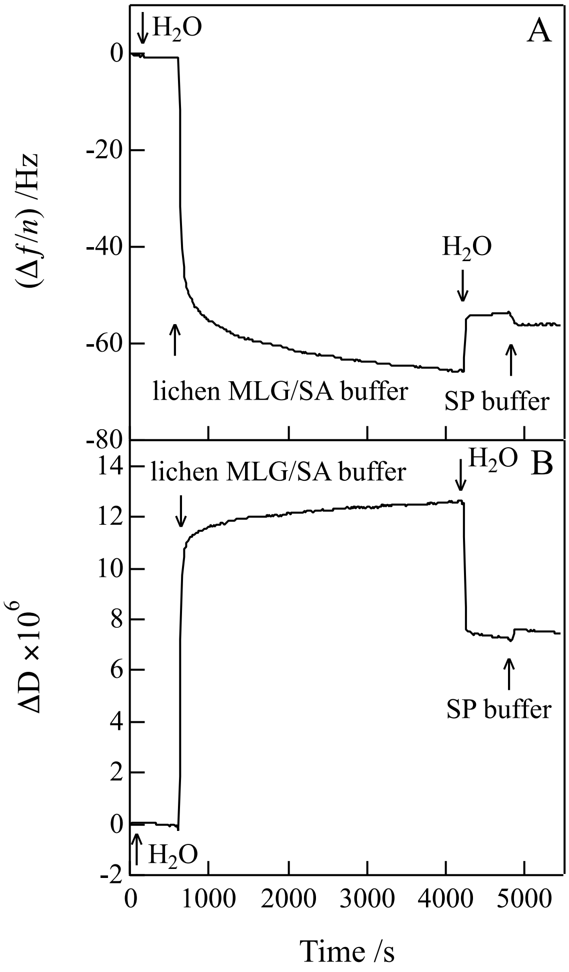

Figure 7.16 Representative time dependent (A) $\Delta f/n$ and (B) ΔD adsorption profiles for lichen MLG adsorption onto RC substrates from 0.05% (w/w) solutions in SA buffer (20 mM, pH = 5.5) at 50.0 °C. An additional switch to SP buffer (20 mM, pH =6.5) was performed to change the surrounding solution conditions for lichenase solutions. Data correspond to the fifth overtone and arrows indicate where solutions were switched.

Enzymatic degradation was examined using a lichenase from *Bacillus subtilis* at 50.0 °C by QCM-D and AFM. After adsorption of lichen MLG onto RC substrates, the lichen MLG layers were exposed to a lichenase solution and changes in $\Delta f/n$ and ΔD were monitored simultaneously. Representative time dependent degradation profiles for lichen MLG surface layers exposed to lichenase solutions in SP buffer (20 mM, pH = 6.5) with different lichenase concentrations are provided in Figure 7.17. In contrast to lichen MLG adsorption as depicted in Figure 7.16, enzymatic degradation of lichen MLG was accompanied by a significant increase in $\Delta f/n$ and a decrease in ΔD immediately after the injection of lichenase solution. These changes represented a significant reduction of hydrated mass and thus the removal of the lichen MLG layers. Unlike pectinase degradation, where the pump was stopped, lichenase degradation was carried out at a continuous flow rate of 0.200 $\mathrm{mL{\bullet}min^{-1}}$ and fresh lichenase solutions were provided until a plateau was obtained in the degradation profiles. Lichenase catalyzed degradation occurred quickly and significant mass loss was observed at early stages of degradation. On the basis of previous NMR studies, the majority of the hydrolysis products are cellotriosyl and cellotetraosyl units.[37, 38] The fast degradation kinetics were attributed to the more readily water-soluble cellotriosyl and cellotetraosyl units that could be easily removed from RC substrates. Due to the cleavage site specificity of lichenase, there were no significant interactions between lichenase and the RC substrate. Hence, adsorbed layers of lichen MLG on the RC substrates were perfect substrates for lichenase degradation studies.

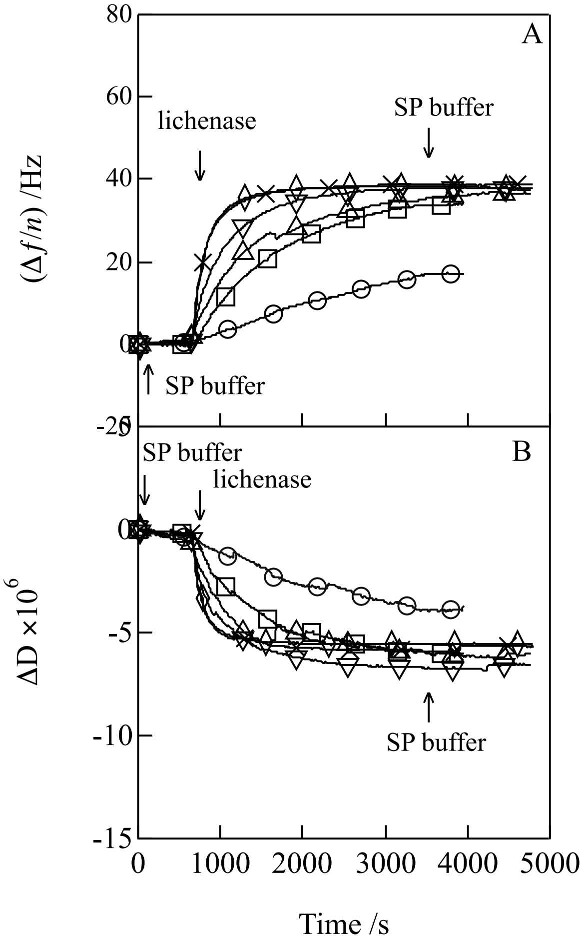

Figure 7.17 Representative time dependent (A) Δ*f*/*n* and (B) ΔD degradation profiles for lichenase action on lichen MLG layers adsorbed onto RC substrates at 50.0 °C. A series of enzyme concentrations were used, including (O) 0.1, (□) 0.5, (Δ) 1.0, (∇) 2.5, (×) 5.0 and (◊) 10 U•mL^{-1} in SP buffer (20 mM, pH = 6.5). Data correspond to the fifth overtone and arrows indicate where solutions were switched.

Enzyme concentration effects on lichenase degradation were examined using a series of enzyme concentrations, including 0.1 0.5, 1.0, 2.5, 5.0 and 10 U•mL^{-1}. Representative time dependent degradation profiles for lichenase action on lichen MLG layers using different enzyme concentrations are provided in Figure 7.17. Irreversible changes in Δ*f*/*n* and ΔD for lichenase degradation of lichen MLG layers at 50.0 °C using different enzyme concentrations are summarized in Table 7.5. At high enzyme concentrations, lichenase degradation occurred almost instantaneously with rapid $\Delta f/n$ increases and ΔD decreases, while $\Delta f/n$ and ΔD occurred more gradually for lower enzyme concentrations (e.g. 0.1 U•mL^{-1}). The QCM-D data also provided information about the initial hydrolysis rates which were obtained from the slopes of the $\Delta f/n$ curves at the very beginning of the hydrolysis. As is evident in Figure 7.17, initial hydrolysis rates increased with increasing lichenase concentration. Representative AFM height images of lichen MLG layers before and after lichenase action are provided in Figure 7.18. The AFM images before lichenase degradation showed that lichen MLG formed a rather smooth surface layer with a continuous network-like morphology and the RMS roughnesses was about 1.3 nm (Figure 7.18B). After lichenase degradation, AFM height images showed a slightly different morphology. At low lichenase concentrations (Figure 7.18C, 0.1 U•mL^{-1}), similar morphology as lichen MLG layer (Figure 7.18 B) was observed indicating incomplete degradation. At high lichenase concentrations (Figure 7.18D, 5.0 U•mL^{-1}), the morphology is similar to bare RC (Figure 7.18 A) indicating a more complete removal of lichen MLG layers.

Table 7.5 Irreversible $\Delta f/n$ and ΔD for lichenase degradation of lichen MLG layers at 50.0 °C. Lichenase solutions were made in SP buffer (20 mM, pH = 6.5).

Lichenase Concentration /U•mL^{-1}	**$\Delta f/n$ /Hz**	**ΔD ×10^{6}**
0.1	16.1 ± 0.5	-3.70 ± 0.05
0.5	33.8 ± 0.5	-6.0 ± 0.1
1.0	38 ± 2	-6.5 ± 0.9
2.5	39 ± 2	-7.0 ± 0.6
5.0	41 ± 1	-6.3 ± 0.2
10	43 ±2	-6.3 ± 0.5

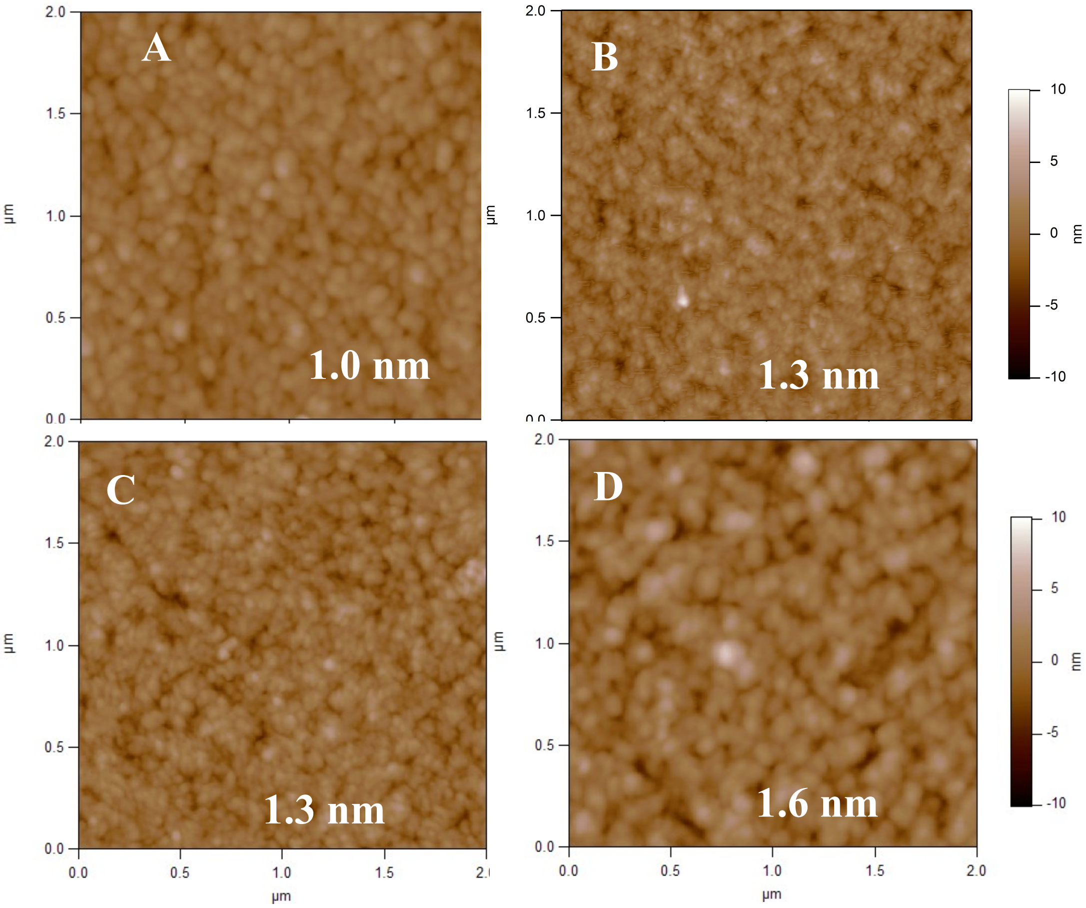

Figure 7.18 Representative AFM images of (A) a bare RC surface and (B) a lichen MLG layer on a RC surface before enzyme degradation and after degradation by a lichenase from *Bacillus subtilis* with an enzyme concentration of (C) 0.1 U•mL^{-1} and (D) 5.0 U•mL^{-1} in SP buffer (20 mM, pH = 6.5) at 50.0 °C. The RMS roughnesses (white numbers on images) were obtained from the entire 2 µm × 2 µm image areas with z ranges of 20 nm.

The effect of pH on lichenase degradation of lichen MLG layers was also examined by QCM-D and AFM. Representative time dependent degradation profiles for lichenase degradation with the same enzyme concentration (5 U•mL^{-1}) from different pH conditions are provided in Figure 7.19. Irreversible $\Delta f/n$ and ΔD for lichenase catalyzed degradation of lichen MLG layers under different pH are summarized in Table 7.6. Three different pH were investigated, including pH = 5.5, 6.5 and 7.5. As seen in Figure 7.19, QCM-D results showed that degradation of lichen MLG layers by lichenase occurred over the entire range of experimental pH with similar degradation profiles. Values of $\Delta f/n$ (~ 40 Hz) and ΔD (-5 $\times 10^6$) almost reached the same value for all the pH investigated. Likewise, similar degradation profiles were obtained from low enzyme concentration condition (1 U•mL^{-1}) for the same range of pH (5.5 to 7.5). These observations are consistent with recent bulk studies that showed these enzymes are endoglucanases with activity and stability over a broad pH range.[26, 39] A recent bulk study also showed similar results for a chimeric lichenase with high stability over pH range from 5 to 9.[40] The pH stability of lichenases makes them potential candidates for various industrial applications, especially detergent formulations.[41] Representative AFM height images of lichen MLG layers before and after action by lichenase at different pH are provided in Figure 7.20. Although similar degradation profiles were obtained for different pH, AFM height images showed slightly different surface morphologies with different RMS roughnesses. These images are in agreement with QCM-D studies which had similar degradation profiles from different pH conditions for both low (1 U•mL^{-1}) and high concentrations (5 U•mL^{-1}).

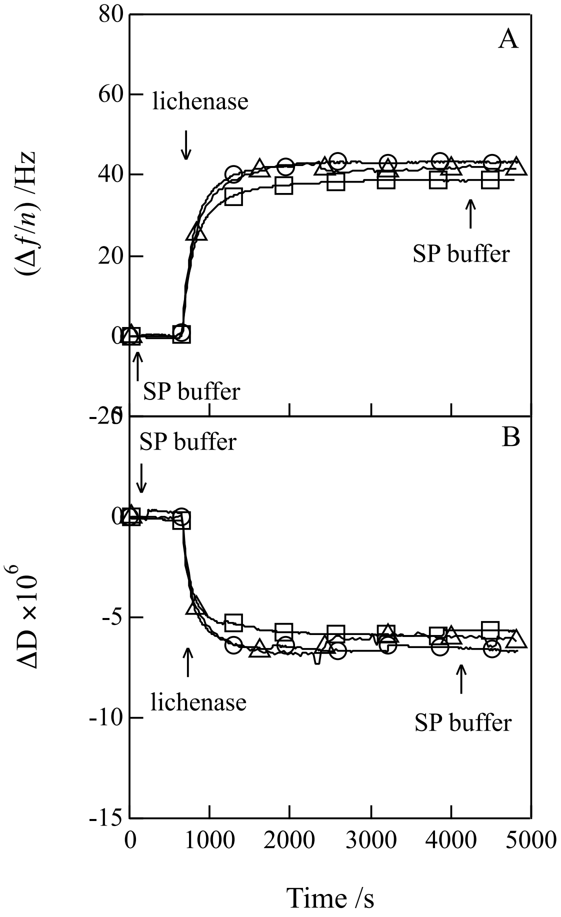

Figure 7.19 Representative time dependent (A) Δ*f*/*n* and (B) ΔD degradation profiles for lichenase action on lichen MLG surface layers for different pH: (O) 5.5, (☐) 6.5 and (Δ) 7.5 at 50.0 °C. The enzyme concentration was 5 U•mL^{-1} in SP buffer (20 mM). Data correspond to the fifth overtone and arrows indicate where solutions were switched.

Table 7.6 Irreversible Δ*f*/*n* and ΔD for lichenase degradation of lichen MLG at 50.0 °C and different pH. Lichenase concentration was 5 U•mL^{-1} from SP buffer (20 mM).

pH	**Δ*f*/*n* /Hz**	**ΔD ×10^{6}**
5.5	44 ± 1	-6 ± 1
6.5	40 ± 2	-6.3 ± 0.7
7.5	42 ± 2	-6.2 ± 0.6

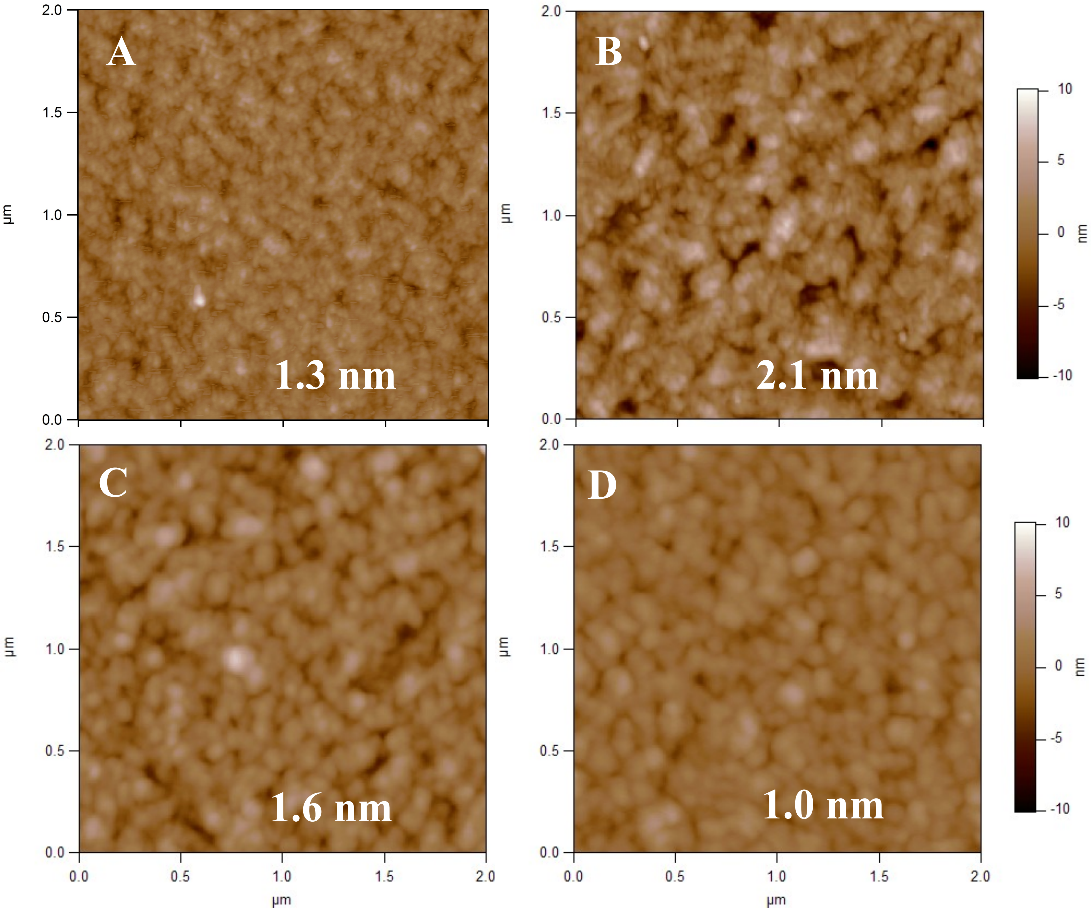

Figure 7.20 Representative AFM height images for lichen MLG layers (A) before and after lichenase degradation at (B) pH = 5.5, (C) pH = 6.5 and (D) pH = 7.5 at 50.0 °C. The enzyme concentration was 5 U•mL^{-1}. The RMS roughnesses (white numbers on images) were obtained from the entire 2 µm × 2 µm image areas with z ranges of 20 nm.

In addition to the effects of enzyme concentration and pH, temperature effects on lichenase degradation of lichen MLG layers were examined by QCM-D and AFM. Representative time dependent degradation profiles for lichenase degradation with the same enzyme concentration (5 U•mL^{-1}) at different temperatures are provided in Figure 7.21. Irreversible $\Delta f/n$ and ΔD for lichenase degradation of lichen MLG layers at different temperatures are summarized in Table 7.7. The QCM-D results showed similar degradation profiles for all the temperatures investigated, ranging from 15.0 °C to 50.0 °C. Although there was only a slight difference in degradation kinetics at 15.0 °C, changes in $\Delta f/n$ (~ 40 Hz) and ΔD (-5×10^{6}) almost reached the same value for all the temperatures investigated. Likewise, similar degradation profiles were obtained from low enzyme concentration condition (1 U•mL^{-1}) for the same range of temperature (15.0 °C to 50.0 °C). A recent study showed that β-(1→3), (1→4)-glucanases from *Bacillus subtilis* had limited thermotolerance at higher temperature, losing 60% of their activity after a 10-minute incubation at 60 °C.[22] However, there were no significant differences in degradation profiles for the temperature range investigated in this study. Some studies also found that lichenase showed a temperature optimum around 70 to 80 °C.[42, 43] As the E4 system (Q-Sense AB) used in this study has a temperature range of 15.0 to 50.0 °C, it was not possible to test temperatures greater than 50.0 °C. A recent study showed similar results for a chimeric lichenase with great stability over a wide range of temperature from 40 to 90 °C.[40] However, low temperature data (< 40 °C) were not available from this study. On the basis of a study in the literature, several members of the hydrolase family to which lichenase belongs were found to be active with optimal temperatures around 20 °C.[44] This finding is consistent with our low temperature data that lichenase showed similar activity at low temperatures. Representative AFM height images of lichen MLG layers before and after lichenase exposure are provided in Figure 7.22. Similar surface morphologies were obtained for all the temperatures investigated, which was in agreement with the fact that QCM-D results exhibited similar degradation profiles over the temperature range of 15.0 to 50.0 °C.

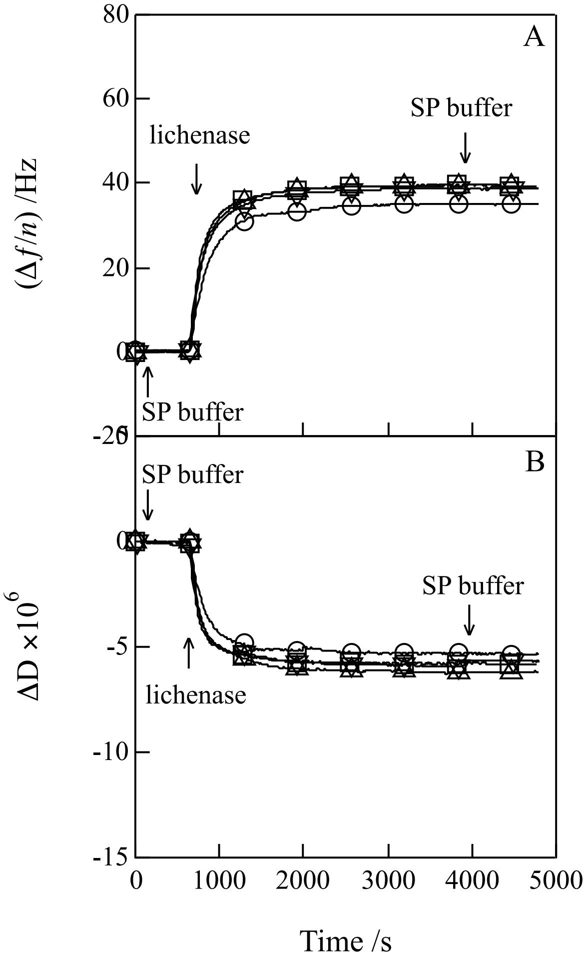

Figure 7.21 Representative time dependent (A) $\Delta f/n$ and (B) ΔD degradation profiles for lichenase action on lichen MLG layers at various temperatures: (O) 15.0 °C, (□) 30.0 °C, (Δ) 40.0 °C and (∇) 50.0 °C. The enzyme concentration was 5 U•mL^{-1} in SP buffer (20 mM, pH = 6.5). Data correspond to the fifth overtone and arrows indicate where solutions were switched.

Table 7.7 Irreversible $\Delta f/n$ and ΔD for lichenase degradation of lichen MLG layers at different temperatures. Lichenase concentration was 5 U•mL^{-1} in SP buffer (20 mM).

Temperature /°C	**$\Delta f/n$ /Hz**	**ΔD ×10^6**
15.0	36 ± 1	-5.4 ± 0.6
30.0	39.7 ± 0.5	-6.4 ± 0.5
40.0	40 ± 2	-6.13 ± 0.04
50.0	40 ± 2	-6.3 ± 0.7

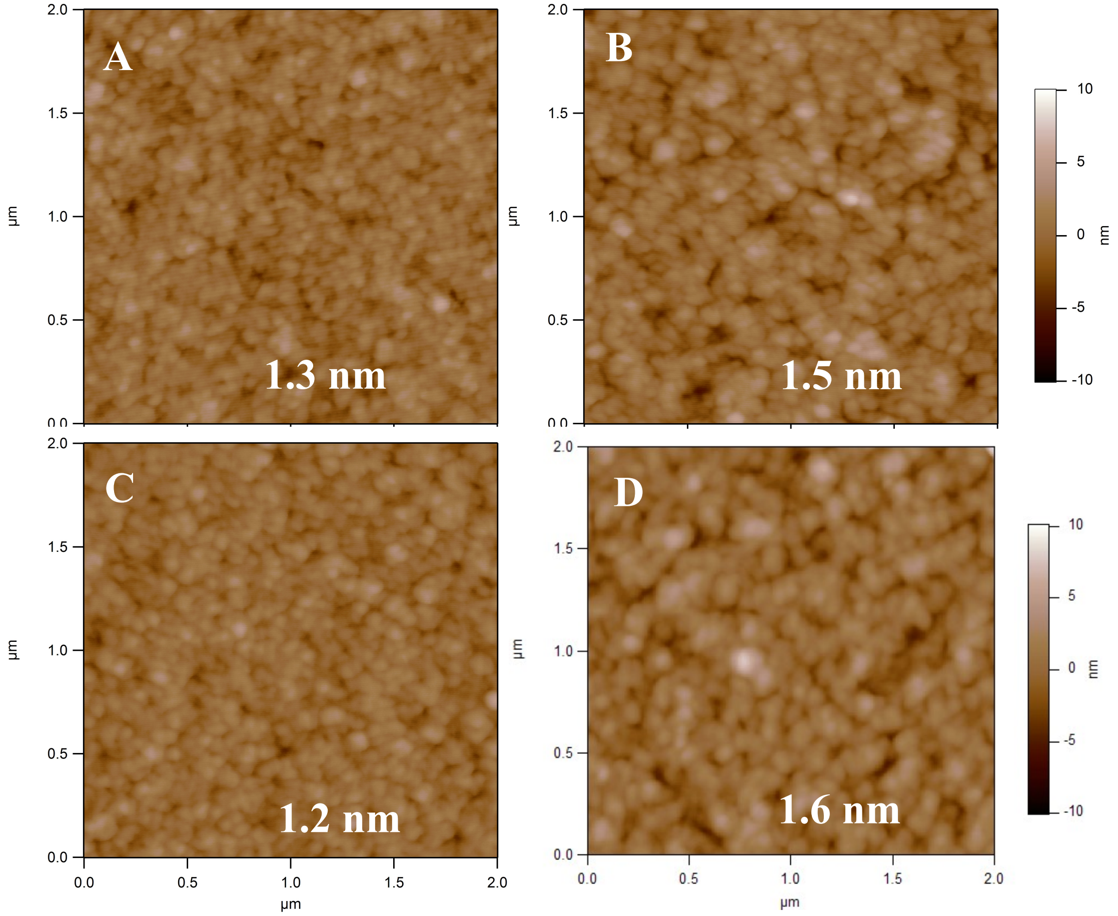

Figure 7.22 Representative AFM height images for lichen MLG layers after lichenase degradation at (A) 15.0 °C, (B) 30.0 °C, (C) 40.0 °C and (D) 50.0 °C. The enzyme concentration was 5 U•mL^{-1}. The RMS roughnesses (white numbers on images) were obtained from the entire 2 µm × 2 µm image areas with z ranges of 20 nm.

7.5 Conclusions

Well-defined pectin model surfaces were used for enzymatic degradation studies by a pectinase from *Aspergillus niger*. More complete removal of pectin layers was achieved for high pectinase concentration. Ease of degradation for highly esterified pectin compared to pectins with low DE followed the same trend as that for β-elimination under basic conditions. Esterification at *C*6 positions eliminates local negative charges, thereby allowing easier hydrogen abstraction from *C*5 positions.[35] Lichen MLG layers were successfully prepared on RC substrates and the subsequent enzymatic degradation by a lichenase was studied as a function of enzyme concentration, pH and temperature. Enzymatic degradation rates increased with increasing lichenase concentration, leading to a greater removal of the lichen MLG layers. Results from QCM-D and AFM showed lichenase had a wide range of thermal (15 to 50 °C) and pH (5.5 to 7.5) stability.

7.6 References

(1) Ward, O. P.; Moo-young, M.; Venkat, K., *Critical Reviews in Biotechnology* **1989,** *8*, 237-274.

(2) Kirk, O.; Borchert, T. V.; Fuglsang, C. C., *Current Opinion in Biotechnology* **2002,** *13*, 345-351.

(3) Tanzi, R. E.; Bertram, L., *Cell* **2005,** *120*, 545-555.

(4) Minic, Z.; Jouanin, L., *Plant Physiology and Biochemistry* **2006,** *44*, 435-449.

(5) Micheli, F., *Trends in Plant Science* **2001,** *6*, 414-419.

(6) Jayani, R. S.; Saxena, S.; Gupta, R., *Process Biochemistry* **2005,** *40*, 2931-2944.

(7) Gaffe, J.; Tiznado, M. E.; Handa, A. K., *Plant Physiology* **1997,** *114*, 1547-1556.

(8) de Vries, R. P.; Visser, J., *Microbiology and Molecular Biology Reviews* **2001,** *65*, 497-522.

(9) Rexová-Benková, Ľ.; Markovič, O., Pectic enzymes. In *Advances in Carbohydrate Chemistry and Biochemistry*, Tipson, R. S.; Derek, H., Eds. Academic Press: 1976; Vol. Volume 33, pp 323-385.

(10) Singh, S. A.; Appu Rao, A. G., *Biotechnology and Applied Biochemistry* **2002,** *35*, 115-123.

(11) Albersheim, P.; Neukom, H.; Deuel, H., *Archives of Biochemistry and Biophysics* **1960,** *90*, 46-51.

(12) Benen, J. A. E.; Kester, H. C. M.; Pařenicová, L.; Visser, J., *Biochemistry* **2000,** *39*, 15563-15569.

(13) Sterling, C., *American Journal of Botany* **1970,** *57*, 172-175.

(14) Maldonado, M. C.; Strasser de Saad, A. M., *Journal of Industrial Microbiology and Biotechnology* **1998,** *20*, 34-38.

(15) Wood, P. J., *Trends in Food Science & Technology* **2004,** *15*, 313-320.

(16) Chaari, F.; Bhiri, F.; Blibech, M.; Maktouf, S.; Ellouz-Chaabouni, S.; Ellouz-Ghorbel, R., *Process Biochemistry* **2012,** *47*, 509-516.

(17) Gaiser, O. J.; Piotukh, K.; Ponnuswamy, M. N.; Planas, A.; Borriss, R.; Heinemann, U., *Journal of Molecular Biology* **2006,** *357*, 1211-1225.

(18) McCleary, B. V., Lichenase from *Bacillus subtilis*. In *Methods in Enzymology*, Willis A. Wood, S. T. K., Ed. Academic Press: 1988; Vol. Volume 160, pp 572-575.

(19) Cui, W.; Wood, P. J.; Blackwell, B.; Nikiforuk, J., *Carbohyd Polym* **2000,** *41*, 249-258.

(20) Huber, D. J.; Nevins, D. J., *Plant Physiology* **1977,** *60*, 300-304.

(21) Planas, A., *Biochimica et Biophysica Acta (BBA) - Protein Structure and Molecular Enzymology* **2000,** *1543*, 361-382.

(22) Furtado, G. P.; Ribeiro, L. F.; Santos, C. R.; Tonoli, C. C.; de Souza, A. R.; Oliveira, R. R.; Murakami, M. T.; Ward, R. J., *Process Biochemistry* **2011,** *46*, 1202-1206.

(23) Koshland, D. E., *Biological Reviews* **1953,** *28*, 416-436.

(24) Abel, M.; Planas, A.; Christensen, U., *Biochem. J.* **2001,** *357*, 195-202.

(25) Bacic, A.; Stone, B. A., *Functional Plant Biology* **1981,** *8*, 475-495.

(26) Chaari, F.; Belghith-Fendri, L.; Blibech, M.; Driss, D.; Ellouzi, S. Z.; sameh, M.; Ellouz-Chaabouni, S., *Process Biochemistry* **2014,** *49*, 1040-1046.

(27) Sauerbrey, G., *Z. Phys* **1959,** *155*, 206-222.

(28) Turon, X.; Rojas, O.; Deinhammer, R., *Langmuir* **2008,** *24*, 3880-3887.

(29) Wang, C.; Kittle, J. D.; Qian, C.; Roman, M.; Esker, A. R., *Biomacromolecules* **2013,** *14*, 2622-2628.

(30) Westwood, M.; Roberts, D.; Parker, R., *Carbohyd Polym* **2011,** *84*, 960-969.

(31) Sharma, N.; Rathore, M.; Sharma, M., *Reviews in Environmental Science and Biotechnology* **2012**, 1-16.

(32) Bonnin, E.; Le Goff, A.; Körner, R.; Vigouroux, J.; Roepstorff, P.; Thibault, J. F., *Biochimica et Biophysica Acta (BBA) - Protein Structure and Molecular Enzymology* **2002,** *1596*, 83-94.

(33) Diaz, J. V.; Anthon, G. E.; Barrett, D. M., *Journal of Agricultural and Food Chemistry* **2007,** *55*, 5131-5136.

(34) Dinu, D., *Romanian Biotechnological Letters* **2001,** *6*, 397-402.

(35) Kravtchenko, T. P.; Arnould, I.; Voragen, A. G. J.; Pilnik, W., *Carbohyd Polym* **1992,** *19*, 237-242.

(36) Keijbets, M. J. H.; Pilnik, W., *Carbohydrate Research* **1974,** *33*, 359-362.

(37) Roubroeks, J. P.; Mastromauro, D. I.; Andersson, R.; Christensen, B. E.; Åman, P., *Biomacromolecules* **2000,** *1*, 584-591.

(38) Carpita, N. C., *Annual Review of Plant Biology* **1996,** *47*, 445-476.

(39) Ferreira, C.; Marana, S. R.; Silva, C.; Terra, W. R., *Comparative Biochemistry and Physiology Part B: Biochemistry and Molecular Biology* **1999,** *123*, 241-250.

(40) Fu, L.; Xu, Z.; Shuai, J.; Hu, C.; Dai, W.; Li, W., *Curr Microbiol* **2008,** *56*, 287-292.

(41) Kottwitz, B.; Maurer, K.-H. Detergent containing glucanase. 2002.

(42) Schimming, S.; Schwarz, W. H.; Staudenbauer, W. L., *Biochemical and Biophysical Research Communications* **1991,** *177*, 447-452.

(43) Yang, S.; Qiaojuan, Y.; Jiang, Z.; Fan, G.; Wang, L., *Journal of Agricultural and Food Chemistry* **2008,** *56*, 5345-5351.

(44) Piruzian, E.; Goldenkova, I.; Musiychuk, K.; Kobets, N.; Arman, I.; Bobrysheva, I.; Chekhuta, I.; Glazkova, D., *Mol Gen Genomics* **2002,** *266*, 778-786.

Chapter 8: Conclusions and Suggested Future Work

8.1 Overall Conclusions

This study probed the adsorption of polysaccharides as well as other biomacromolecules, such as enzymes, onto different polysaccharide model surfaces. Three major surface science techniques, including a quartz crystal microbalance with dissipation monitoring (QCM-D), surface plasmon resonance (SPR) and atomic force microscopy (AFM), were used in this dissertation. First, the adsorption of high molar mass xyloglucan, a major type of hemicellulose in dicot plants, and xyloglucan oligosaccharides onto cellulose were studied by QCM-D and SPR. Adsorbed amounts of xyloglucan strongly correlated to the porosity and roughnesses of the cellulose substrates and increased in the order of regenerated cellulose (RC) < nanocrystalline cellulose (NC) < Avicel cellulose. Dynamic adsorption isotherm studies showed that xyloglucan heptasaccharide adsorption onto RC followed a Langmuir adsorption isotherm, whereas Freundlich adsorption isotherms provided better fits for xyloglucan oligosaccharide and high molar mass xyloglucan adsorption onto RC. Additionally, the adsorption of carboxymethyl cellulose (CMC), a representative cellulose derivative, onto cellulose was studied. A Voigt-based viscoelastic model and the combination of QCM-D and SPR data confirmed the formation of soft and dissipative CMC layers on RC with average water contents > 90%. This study also demonstrated the adsorption of CMC onto RC was strongly affected by the addition of $CaCl_2$ as well as the degree of substitution (DS) and the degree of polymerization (DP) of the CMC samples. Adsorbed amounts of CMC increased with decreasing DS and increasing DP as well as increasing ionic strength.

This work also highlighted the preparation of pectin model surfaces and used them as platforms for interaction studies with xyloglucan. Preparation of pectin model surfaces was achieved by adsorbing pectin or polygalacturonic acid (PGA) from citric phosphate buffer. Adsorption was mainly based upon strong van der Waals interactions between polysaccharide backbones and gold substrates. Complete coverage of pectins was confirmed by AFM studies and the resulting films had root-mean-square (RMS) roughnesses of about 1.5 nm. Subsequent interaction studies with xyloglucan showed that there were no significant or negligible interactions between xyloglucan and pectins with high galacturonic acid content for solution condition study.

Additionally, we presented the adsorption of hemicelluloses from type II cell walls, mixed linkage glucans (MLGs), onto cellulose. Two MLG samples, barley and lichen MLG, were used for investigating how molecular structure affects MLG adsorption onto cellulose. Both experimental and viscoelastic modeling of adsorbed MLG layers suggested that lichen MLG formed softer layers compared to barley MLG due to a higher proportion of β-(1→3) linkages. Interaction studies between lichen MLG and other matrix polysaccharides suggested matrix polysaccharides inhibited subsequent deposition of lichen MLG onto cellulose. This result also provided some insight into the deposition order of type II cell wall components.

Finally, this work presented enzymatic degradation studies of pectin and lichen MLG layers. First, well-defined pectin model surfaces were used for enzymatic degradation studies by a pectinase from *Aspergillus niger*. Ease of degradation for highly esterified pectins compared to low DE pectins followed the same trend observed for β-elimination under basic conditions. Next, lichen MLG layers were used for enzymatic degradation by a lichenase from *Bacillus subtilis* as a function of enzyme concentration, pH and temperature. The QCM-D and AFM results showed that lichenase had a wide range of thermal (15 to 50 °C) and pH (pH = 5.5 to 7.5) stability with more complete removal of lichen MLG layers obtained at higher lichenase concentrations.

8.2 Suggestion for Future Work

8.2.1 Polysaccharide Layers for Controlled Protein Adsorption

Polysaccharides, as renewable, nontoxic biomacromolecules, have gained attention for the development of functional materials for diagnostic and medical applications[1] and have long been studied for controlled protein adsorption.[2] They can be used to enable the substrates with desired functionalities that have tremendous influence over the subsequent adsorption of proteins. For instance, a cellulose derivative, carboxymethyl cellulose (CMC) can form stable, hydrogel-like layers on cellulose.[3] These CMC layers can be used for the control of protein binding due to the elimination of nonspecific protein interactions.[4] They can also be used for the nucleation and growth of hydroxyapatite for subsequent tissue engineering.[5] Pectins are useful cell wall polysaccharides with negative charges that have been used together with proteins to form insoluble complexes for drug delivery applications.[6] Interfacial interactions between pectin and a model protein, bovine serum albumin (BSA), has been examined as a function of ionic strength using QCM-D.[7] Chitosan, composed of β-(1→4)-linked N-acetyl-D-glucosamine, is another useful polysaccharide that is obtained through the deacetylation of chitin. Unlike CMC and pectins that carry negative charges, chitosan has positive charges at an appropriate pH due to the presence of amine groups. Interactions between polysaccharides and proteins are mainly driven by electrostatic interactions.

These functionalities, especially ionic character, allow for the manipulation of interactions between polysaccharides and target proteins. For example, modified cellulose substrates have proven to serve as good platforms for controlled adsorption of human immunoglobulin G and BSA.[4] This application is expected to open new venues for biodetection or filtration of pathogens.

As a surface technique, QCM-D is extremely useful for studying interactions between different biomacromolecules, providing not only quantitative information on adsorbed amount ($\Gamma_{QCM\text{-}D}$) but also viscoelastic properties of adsorbed layers. A recent study has employed QCM-D for studying BSA interactions with mucin and their corresponding layer properties.[8] In this thesis, some preliminary results on CMC and pectin adsorption at solid/liquid interfaces have been discussed and these stable adsorbed polysaccharide layers serve as good platforms for subsequent protein adsorption. The ionic properties of the adsorbed layer can be controlled by surrounding conditions, especially pH, thereby controlling the electrostatic interactions between the polysaccharide layers and the target proteins.

8.2.2 Preparation of Pectins with Different Degrees of Methylation and Acetylation

Greater than 60% of pectins in the plant cell walls are homogalacturonans with a polygalacturonic acid (PGA) backbone and varying degrees of methylation (DM) and acetylation (DAc).[9] The DM and DAc of PGA, as well as the distribution of methyl and acetyl groups, play an important role in their interactions with other cell wall polysaccharides.[10, 11] Native pectins in plant cell walls are generally highly methylated but poorly acetylated.[12, 13] For the PGA, a model compound of pectin backbone, it could serve as a starting material for the modification of pectins with different DM and DAc. It can be esterified by methanol at the *C*6 position (carboxyl groups) and by acetyl groups at the *C*2 or *C*3 positions (hydroxyl groups). A common method for carboxyl group modification is esterification in acidic methanol.[14] Recently, reactions of tetrabutylammonium (TBA) salts of pectin with methyl iodide (CH_3I) in dimethyl sulfoxide (DMSO) have been proposed for the methylation of pectin under homogeneous reaction conditions with the resulting DM dependent upon the stoichiometric ratio of the reagents.[12] Acetylation of pectin can be obtained by reacting pectin with acetic anhydride in a solvent of formamide with pyridine as a catalyst, giving a DAc value up to 150% (3 of every four hydroxyl groups along the backbone).[15]

Extensive studies have been carried out on the effects of DM and DAc on gelation.[6, 16] Pectins can be further categorized into high methoxyl (HM) and low methoxyl (LM) pectin depending upon the DM values. The gelation mechanisms are based upon Ca^{2+} crosslinking and non-ionic interactions for HM and LM pectins, respectively.[17] Acetylation also plays an important role in the gelation of pectins. For instance, pectin from sugar beet with a high fraction of acetylation is not able to form gels under the same conditions as citrus or apple pectins with low fractions of acetylation.[18] However, the gelation properties can be restored by selectively removing acetyl groups.[16] Studies by QCM-D provide a good opportunity to test pectin gelation for pectins with different DM and DAc on different substrates. The viscoelastic properties of the resulting gels could be deduced through Voigt-based viscoelastic modeling of QCM-D data. As a complementary technique, SPR can be used together with QCM-D for monitoring interfacial behavior of pectins with different DM and DAc. It is also known that acetylation inhibits degradation of PGA by endopolygalacturonases as well as de-esterification by pectinesterases.[12, 13, 19] Studies on the effect of acetylation and methylation on pectin degradation are also of great interest and importance to obtain a more complete understanding of pectins.

8.2.3 Enzymatic Degradation of Pectin Using Different Enzymes

Enzymes can be extracted not only from plant sources, but also from microbial sources. In contrast to plant enzymes, microbial enzymes are characterized by better pH and thermal stability. In addition, their activity depends upon the species from which they are extracted. For instance, *Trichoderma reesei* produces many cellulose degrading enzymes, while *Aspergillus* species are highly involved in pectin degradation.[20] Pectinases account for about 25% of the global sales of food enzymes and most of the commercial pectinases are produced from microbial sources.[21] For instance, the *Aspergillus* family is the most commonly used family for the industrial production of pectin related enzymes.[22]

Enzymatic regulation of pectin, including modification and degradation, is believed to control adhesion and permeability within the cell wall matrix.[23] Pectinase is a general term for enzymes that are related to pectic substances and a pectinase is typically a mixture of polygalacturonases, pectinesterases and pectate lyases, synergistically and cooperatively breaking down pectins. For example, polygalacturonases catalyze the hydrolytic cleavage of the PGA backbone by addition of water, while pectinesterases catalyze the de-esterification of pectins. Enzymes isolated from different microbial sources are expected to be markedly different from each other with respect to their physicochemical and biological properties and their modes of action. Three commercially available pectin related enzymes, including a pectinase from *Aspergillus niger*, a pectinase from *Aspergillus aculeatus* and a polygalacturonase from *Aspergillus aculeatus*, can be used for the enzymatic degradation of pectins. Preliminary results for the enzymatic degradation of high DE pectin by three different enzymes are provided in Figure 8.1. Each enzyme showed different degradation kinetics as well as degrees of hydrolysis. It would be interesting to study the enzymatic degradation behavior of each enzyme as a function of pH, ionic strength as well as the degree of esterification (DE) of pectin substrates.

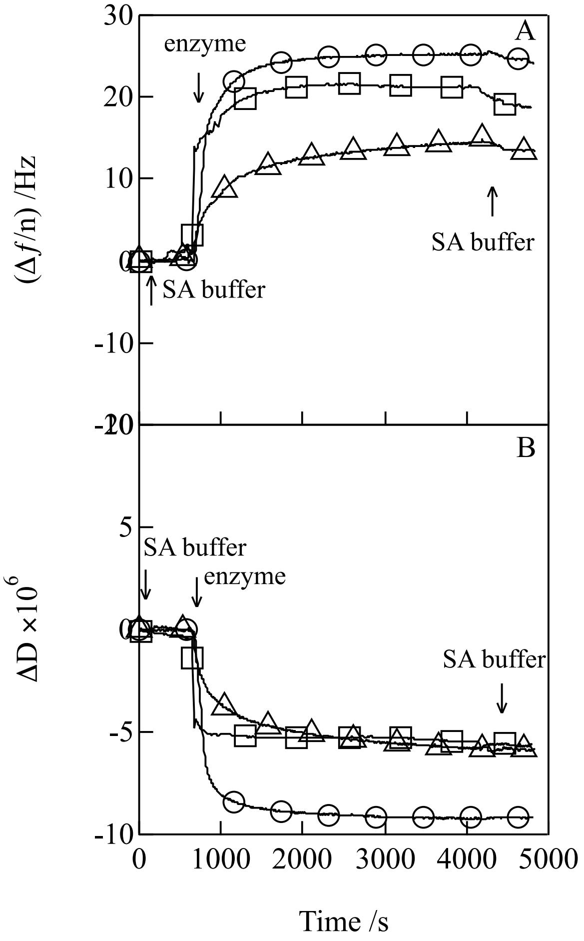

Figure 8.1 Representative time dependent (A) Δ*f*/*n* and (B) ΔD degradation profiles for (O) pectinase from *Aspergillus niger*, (☐) pectinase *Aspergillus aculeatus* and (Δ) a polygalacturonase from *Aspergillus aculeatus* acting upon high DE pectin layers. The enzyme concentration was 2.3 U•mL^{-1} in a sodium acetate buffer (50 mM, pH = 4.0).

8.3 References

(1) Pelton, R., *Trends in Analytical Chemistry* **2009,** *28*, 925-942.

(2) Ganzevles, R. A.; Cohen Stuart, M. A.; Vliet, T. v.; de Jongh, H. H. J., *Food Hydrocolloids* **2006,** *20*, 872-878.

(3) Liu, Z.; Choi, H.; Gatenholm, P.; Esker, A. R., *Langmuir* **2011,** *27*, 8718-8728.

(4) Orelma, H.; Filpponen, I.; Johansson, L.-S.; Laine, J.; Rojas, O. J., *Biomacromolecules* **2011,** *12*, 4311-4318.

(5) Zimmermann, K. A.; LeBlanc, J. M.; Sheets, K. T.; Fox, R. W.; Gatenholm, P., *Materials Science and Engineering: C* **2011,** *31*, 43-49.

(6) Liu, L.; Fishman, M.; Hicks, K., *Cellulose* **2007,** *14*, 15-24.

(7) Wang, X.; Ruengruglikit, C.; Wang, Y.-W.; Huang, Q., *Journal of Agricultural and Food Chemistry* **2007,** *55*, 10425-10431.

(8) Feiler, A. A.; Sahlholm, A.; Sandberg, T.; Caldwell, K. D., *J Colloid Interf Sci* **2007,** *315*, 475-481.

(9) Caffall, K. H.; Mohnen, D., *Carbohydrate Research* **2009,** *344*, 1879-1900.

(10) Thibault, J. F.; Rinaudo, M., *Biopolymers* **1986,** *25*, 455-468.

(11) Ralet, M. C.; Crépeau, M. J.; Buchholt, H. C.; Thibault, J. F., *Biochemical Engineering Journal* **2003,** *16*, 191-201.

(12) Renard, C. M. G. C.; Jarvis, M. C., *Carbohyd Polym* **1999,** *39*, 201-207.

(13) Renard, C. M. G. C.; Jarvis, M. C., *Carbohyd Polym* **1999,** *39*, 209-216.

(14) Jansen, E. F.; Jang, R., *Journal of the American Chemical Society* **1946,** *68*, 1475-1477.

(15) Carson, J. F.; Maclay, W. D., *Journal of the American Chemical Society* **1946,** *68*, 1015-1017.

(16) Oosterveld, A.; Beldman, G.; Searle-van Leeuwen, M. J. F.; Voragen, A. G. J., *Carbohyd Polym* **2000,** *43*, 249-256.

(17) Sriamornsak, P., *Silpakorn University International Journal* **2003,** *3*, 206-228.

(18) Kertesz, Z. I., *The pectic substances*. Interscience Publishers New York: 1951; Vol. 1.

(19) Buchholt, H. C.; Christensen, T. M. I. E.; Fallesen, B.; Ralet, M.-C.; Thibault, J.-F., *Carbohyd Polym* **2004,** *58*, 149-161.

(20) van den Brink, J.; de Vries, R., *Appl Microbiol Biotechnol* **2011,** *91*, 1477-1492.

(21) Jayani, R. S.; Saxena, S.; Gupta, R., *Process Biochemistry* **2005,** *40*, 2931-2944.

(22) de Vries, R. P.; Visser, J., *Microbiology and Molecular Biology Reviews* **2001,** *65*, 497-522.

(23) Micheli, F., *Trends in Plant Science* **2001,** *6*, 414-419.